



HAL
open science

Simulateurs supraconducteurs de modèles d'impuretés quantiques

Théo S epulcre

► **To cite this version:**

Th eo S epulcre. Simulateurs supraconducteurs de mod eles d'impuret es quantiques. Syst emes m e-
soscopiques et effet Hall quantique [cond-mat.mes-hall]. Universit e Grenoble Alpes [2020-..], 2021.
Fran ais. NNT : 2021GRALY074 . tel-03581262v2

HAL Id: tel-03581262

<https://theses.hal.science/tel-03581262v2>

Submitted on 10 Mar 2022

HAL is a multi-disciplinary open access archive for the deposit and dissemination of scientific research documents, whether they are published or not. The documents may come from teaching and research institutions in France or abroad, or from public or private research centers.

L'archive ouverte pluridisciplinaire **HAL**, est destin ee au d ep ot et  a la diffusion de documents scientifiques de niveau recherche, publi es ou non,  emanant des  tablissements d'enseignement et de recherche fran ais ou  trangers, des laboratoires publics ou priv es.

THÈSE

Pour obtenir le grade de

Docteur de l'Université Grenoble Alpes

Spécialité : Physique Théorique

Arrêté ministériel : 25 mai 2016

Présentée par **Théo Sépulcre**.

Thèse dirigée par **Serge Florens** (UGA),

Préparée au sein de l'**Institut Néel du CNRS**,

Avec l'**École doctorale de physique de Grenoble**.

Superconducting Simulators for Quantum Impurity Models

Simulateurs Supraconducteurs de Modèles d'Impureté Quantiques

Thèse soutenue publiquement le **19 novembre 2021**,

Devant le jury composé de :

M. Serge Florens, Directeur de recherche à l'Institut Néel.	Directeur
Mme Audrey Cottet, Directrice de recherche à l'École Normale Supérieure.	Rapporteur
Mme Milena Grifoni, Professeure de l'Université de Regensburg.	Rapporteur
M. Sergey Skipetrov, Directeur de recherche au Laboratoire de Physique et Modélisation des Milieux Condensés.	Président du jury
M. Nicolas Dupuis, Directeur de recherche à Sorbonne Université.	Examineur
M. Carles Altimiras, Ingénieur chercheur au Service de Physique de l'État Condensé du CEA.	Examineur



Gloire et louange à toi, Satan, dans les hauteurs
Du ciel, où tu régnas, et dans les profondeurs
De l'Enfer, où, vaincu, tu rêves en silence !
Fait que mon âme un jour, sous l'Arbre de Science
Près de toi se repose, à l'heure où sur ton front
Comme un Temple nouveau ses rameaux s'épandront.

Baudelaire, *Prière*.

Glory and praise to thee, in heaven above
Where thou didst reign, and in the abysses of
Thy Hell, where thou art brooding, silently!
Grant that with thee my soul, beneath the Tree
Of Knowledge may find rest, when, o'er thy brows,
Like a new Temple it puts forth its boughs.

Transl. Lewis Piaget Shanks.

Contents

Acknowledgements	5
Abstract	6
Résumé	7

Introduction

1 Quantum light and matter	10
1.1 Quest for stronger couplings	10
1.2 The quantum many-body problem	13
1.3 Simulating nature	15

Part I

Roadmap to many-body physics in cQED

2 Macroscopic quantum variables	20
2.1 Cooper pair box	21
2.2 Plasma oscillations	22
3 Canonical quantization of large circuits	25
3.1 Many degrees of freedom	25
3.2 Charge-boson model	27
3.3 Spectral density	32
4 Review of impurity models	35
4.1 Dissipative environments	35
4.2 Spin-boson model	36
4.3 Numerical renormalization group	39
4.4 Extended phase	42

4.5	Schmid transition	44
-----	-----------------------------	----

Part II
Physics of compact phases

5 	A compact ansatz	48
5.1	Periodic wave-function	48
5.2	Transmon regime.	51
6 	Application to charge-boson	54
6.1	Vacuum energy.	54
6.2	Charge fluctuations.	57
6.3	Phase fluctuations	59
6.4	Numerical optimization.	61
7 	Perspectives on the compact ansatz	64
7.1	Many-body excited states.	64
7.2	Josephson junction chains	65

Part III
Boundary Sine-Gordon simulator

8 	Experimental simulator modeling	69
8.1	Circuit diagram and phenomenology	69
8.2	Transmission and Green's functions	73
8.3	Transmission spectroscopy	75
9 	Analytical insights from the continuum limit	79
9.1	BSG Spectral density.	79
9.2	Diagrammatic expansion	81
9.3	Self-energy power law.	84
10 	Microscopic analysis	91
10.1	Equations of motion inversion	91
10.2	Finite temperature	94
10.3	High frequency and skeleton expansion.	98
10.4	Peak forests at low frequency	101
10.5	Adjusting to experimental data	104

Conclusion

11 Perspectives on many-body simulation	109
Bibliography	111

Acknowledgements

To work properly, a PhD student needs a whole supporting ecosystem. Without these many people who helped me, pushed me forward, fed me with science and allowed me to vent frustrations, this manuscript would never have seen the light of day. It is a great pleasure to thank here everyone who helped and contributed, one way or another.

My first acknowledgements go to the members of the jury; Audrey Cottet and Milena Grifoni who accepted to assess the manuscript, and attended the defense together with Sergey Skipetrov, Nicolas Dupuis and Carles Altimiras. Thank you for the very stimulating discussions that followed the questions.

I am especially grateful to Serge, my PhD advisor, for everything he did during the last three years. Having your office next to mine was quite a dangerous situation for you; and yet, everytime I came to you for guidance, looking for a computation trick, a master plan for paper writing or simply to discuss physics, you always found the time to help me.

During the course of the PhD, I had many occasions to meet and discuss with confirmed researchers, who helped me make my way through the maze of modern science. I was very glad to meet with Izak, when he visited Grenoble, and took some evenings to walk me through his computations. Many thanks to Soumya and Kuljeet, who welcomed me warmly at IIT Mumbai. Soumya kindly guided us through the city streets, allowing me to discover a bit of India. I am also grateful to Denis, who agreed on so many meetings to keep our project moving forward. Finally, I would like to thank Nicolas R. and Sebastien, the bright experimentalists who provided us with data and saved this work from being all pipe dreams and pure abstractions. Their cheerfulness was precious to go through the ups and downs of scientific life.

I felt lucky to meet with extraordinary people at the institute, who made me feel at home in Bâtiment M. I am indebted to the whole M209 team for all the good vibes in this office. I missed you all dearly when covid came. Many thanks to Nicolas G. for your warm welcome when I started my internship, and being ever patient when helping me untangle my fortran code. Thanks to Massimiliano for the cheerfulness and coding advices, and of course to Miguel-Angel who told me how to properly swear in Spanish and tolerated my butchering of the rest of the language. I am also deeply grateful to Katee, who was there everytime I needed a cheeky wine-based after work. With you in the office, yeares flashed by like monthes.

Merci à la fine équipe de M202, qui a supporté mes incursions récurrentes à la recherche d'une astuce d'intégration comme d'une pause café. Merci à Quentin, à qui je n'ai jamais osé dire que je ne sais même pas à quoi ressemble un basson, et à Serguei, véritable grand frère des thésards, jamais avare de bon conseils.

Merci enfin à ceux de M214, Maxime et Guillaume, qui m'ont appris à perdre aux échecs avec panache. Des remerciements particuliers vont à mon petit frère de thèse. Même si tu as la drôle d'idée de préférer les fermions aux bosons, je crois qu'on s'est entendu sur tout le reste. Ton scherzo c'est une dinguerie, mais n'oublie pas la ballade pour autant.

Une part significative de ces années a été dédiée à un projet un peu fou, écrire un manuel de physique sur notre "temps libre". Merci à toute l'équipe Jolidon, pour son enthousiasme pour la physique autant que pour son souci du détail. Merci en particulier à Camille, mon infatigable camarade de Fabry-Perot. On finira par l'avoir, cet effet anormal ! Et aussi à Benjamin, pour ta curiosité de tout, qui jour après jour a rendue notre cohabitation si riche.

A ma famille enfin, qui m'a fait le grand plaisir de venir endurer la soutenance, et surtout déboucher le champagne. Je ne saurais lister ce que je vous dois. Je me suis reposé sur votre soutien et votre bienveillance, et elles ne m'ont jamais défaut.

Abstract

Condensed matter physics is the branch of quantum mechanics which studies large assemblies of interacting particles. It sprouted from solid state physics: the study of the electron sea hosted by a metallic material was the earliest representative of the theoretical hardships encountered when predicting the behavior of such a myriad of quantum particles. The field was soon enriched by many other models describing other types of quantum matter, from magnetism to superconductivity, Dirac materials or quantum fluids of light. All these seemingly different applications are united by one ubiquitous aspect of many-body problems: the interplay of many elementary particles, electrons, photons, magnetic moments, leads to emergent collective behaviors, such as quasi-particles and phase transitions. As Anderson famously wrote, “more is different”.

In the recent years, important technological advances in the nanofabrication of superconducting circuits allowed to recreate all the ingredients of a condensed matter system in a finely controlled experimental setup. The quantum particles are emulated by excitations of the circuit, while quantum coherence is ensured by the absence of dissipation of the superconducting state as well as the low temperatures in the milliKelvin range. Finally, interactions are created *via* the Josephson effect, a by-product of superconducting phase rigidity across a tunnel barrier, which introduces non-linearity in the circuit. Such a device is called a quantum simulator.

This thesis has been motivated by the urge to review well known impurity models, the spin-boson and boundary sine-Gordon models, in the light of their recent implementation by superconducting circuits. Starting from an exhaustive modelisation of a generic microscopic circuit, we formulated a novel model taking into account the multi-level structure of charge qBits, that we called the “charge boson Hamiltonian”. Only in some regions of its parameter space this model indeed reduces to the sought-after spin boson or boundary sine-Gordon Hamiltonian. We then established its phase diagram by numerical renormalisation group, and explored the experimentally relevant regions by newly devised theoretical tools.

A striking aspect of the charge boson model is that the number of Cooper pairs on the impurity superconducting island is discrete, or equivalently that its superconducting phase is compact. We introduced a variational ansatz — nicknamed the compact ansatz — to study the relevance of this charge granularity. It allowed us to reach quantitative prediction on ground state observables in the experimentally pertinent region, and to describe compactness fading in the overdamped, strong coupling regime.

One can shunt the impurity capacitive coupling to its environment to reach this highly interacting regime shielded from charge noise by decompactification. The circuit then reduces to the celebrated boundary sine-Gordon model. Recent experiments allowed to probe the dissipative response of such a system, which displays spectacularly high inelastic cross-sections. Armed with a microscopic model of the system, we showed analytically and numerically how the plasma frequency introduces an ultraviolet cutoff which spoils the anomalous power laws of dissipative response that are known from the study of the Tomonaga-Luttinger liquid. Finally, a diagrammatic self-consistent technique performed at finite temperature allowed us to demonstrate how a smooth dissipative response emerges from a system in the mesoscopic size range, formed by a few thousand narrow Fabry-Perot modes, by overcrowding of thermally assisted multi-photons resonances.

Résumé

La physique de la matière condensée est une branche de la mécanique quantique qui étudie les grandes assemblées de particules quantiques en interaction. Elle a germé à partir de la physique de l'état solide : l'étude de la mer d'électrons contenue dans un métal fut le premier exemple des difficultés rencontrées par le théoricien voulant prédire le comportement d'une telle myriade de particules quantiques. Le domaine fut rapidement enrichi par de nombreux autres modèles, décrivant d'autres types de matière quantique, depuis le magnétisme jusqu'à la supraconductivité, les matériaux de Dirac et les fluides de lumière quantique. Toutes ces applications apparemment différentes se retrouvent unies par l'aspect essentiel du problème à N-corps quantique : l'interaction d'un grand nombre de particules élémentaires, électrons, photons, moments magnétiques, conduit à l'émergence de phénomènes collectifs, comme les quasi-particules ou les transitions de phase. Comme l'écrivait Anderson, "*more is different*".

Ces dernières années, d'importantes avancées technologiques dans la nanofabrication de circuits supraconducteurs ont permis de recréer tous les ingrédients d'un système de matière condensée dans un dispositif expérimental finement contrôlé. Les particules quantiques sont émulées par les excitations du circuit, tandis que la cohérence quantique est maintenue par l'absence de dissipation de l'état supraconducteur autant que par les basses températures employées, aux environs de la dizaine de milliKelvins. Enfin, les interactions sont suscitées par effet Josephson, une conséquence de la rigidité de la phase supraconductrice à travers une barrière tunnel, qui introduit des non-linéarités dans le circuit. Une telle plateforme expérimentale est appelée un simulateur quantique.

Cette thèse a été motivée par la nécessité de revoir certains modèles d'impuretés bien connus, modèle spin boson et modèle sine-Gordon à bord, à l'aune de leur implémentation récente sous forme de circuits supraconducteurs. Commenant par une modélisation complète d'un circuit microscopique générique, nous formulons un nouvel Hamiltonien prenant en compte la structure multi-niveaux des qBits de charge, et que nous baptisons l'Hamiltonien charge boson. Celui-ci ne se réduit aux modèles standards de la littérature que dans certaines limites que nous précisons. Nous traçons son diagramme de phase complet à l'aide du groupe de renormalisation numérique, et explorons ses régions expérimentalement pertinentes par des outils théoriques nouvellement créés.

Un aspect frappant du modèle charge boson est que le nombre de paires de Cooper occupant l'îlot supraconducteur de l'impureté est un entier, ou bien de façon équivalente que sa phase supraconductrice est compacte. Nous présentons un ansatz variationnel, que nous appelons l'ansatz compact, pour étudier la pertinence de cet aspect granulaire de la charge. Cela nous a permis d'obtenir des prédictions quantitatives des observables de l'état de vide, pour les régimes de paramètres utiles à l'expérience, et ainsi de décrire la disparition des effets compacts dans le régime suramorti à fort couplage.

Il est possible de court-circuiter le couplage capacitif de l'impureté à son environnement, pour atteindre ce régime d'interaction forte, que la décompactification protège du bruit de charge. Le circuit se réduit alors à simuler le fameux modèle sine-Gordon à bord. Des expériences récentes ont sondé la réponse dissipative d'un tel circuit, qui présente une section efficace inélastique spectaculairement élevée. Armé d'un modèle microscopique détaillé du système, nous montrons que la fréquence plasma introduit une coupure ultraviolette qui supprime les lois de puissance anormales de la réponse dissipative, bien connues par l'étude des liquides de Tomonaga-Luttinger. Enfin, une technique diagrammatique auto-cohérente, entreprise à température finie, a permis de démontrer comment une réponse dissipative lisse en fréquence peut émerger d'un système de taille mésoscopique, par surpopulation de resonances multi-photons assistée par excitations thermiques.

List of commonly used symbols

Symbol	Meaning
\dot{A}	Differential with respect to time.
$A(\omega)$	Fourier transform of $A(t)$, using $A(t) = \int_{\mathbb{R}} \frac{d\omega}{2\pi} e^{-i\omega t} A(\omega)$ and $A(\omega) = \int_{\mathbb{R}} dt e^{i\omega t} A(t)$.
\hat{A}	Operator on an Hilbert space.
\mathbf{A}	$N \times N$ matrix, N a finite number of sites or modes.
\mathbb{A}	2×2 matrix of Keldysh components.
G	Green's function
R, A, F, K	Retarded, Advanced, Feynman or Keldysh definition for a Green's function.
Σ	Self-energy.
$\hat{\varphi}, \hat{\phi}, \hat{\theta}$	Superconducting phase.
\hat{n}, \hat{N}	Number of Cooper pairs.
\hat{a}, \hat{b}	Annihilation operators for bosonic mode.
E_J	Josephson energy.
E_c	Charging energy.
ω_c	A generic cutoff frequency.
T, β	Temperature, and $\hbar/(k_B T)$, inverse temperature scale.
g_k	coupling between impurity and environment mode k .
γ_k	g_k/ω_k .
R_q	$\hbar/(2e)^2$ the resistance quantum, often set to one.
Φ_q	$\hbar/2e$ the flux quantum, often set to one.

Introduction

1 | Quantum light and matter

Alors commença la bousculade échevelée,
vers le rayonnant midi du corps noir.

René Depestre, *Minerai Noir*.

And so they began jostling
madly, towards the radiant
noon of the blackbody.

The quantum theory has an history worth telling. Born laboriously more than a hundred years ago under the pen of puzzled physicists, it grew into the spine of modern physics. Created as the theory of an inaccessible, microscopic world, pondering on the whereabouts of electrons and photons, it came to explain the inner clockwork of stars and produced our worldwide society of consumer electronics.

Over the course of the century, the initial ideas of the 1920s ramified into many directions. One important line of work has been to put the foundations of quantum mechanics to the test, by designing clever experiments which probed the more drastic parts of the theory. Another crucial research direction extended the original concepts to complex systems of many interacting particles. It produced quantum field theory, a common framework for physical systems with infinitely many degrees of freedom, immensely deepening our understanding of the quantum world along the way.

In this introductory chapter, we aim at sketching the broad historical context of this manuscript, especially showing how the search for experimental simulators for the quantum many-body problem stands at the intersection of these two long standing lines of research.

1.1 Quest for stronger couplings

One of the earliest testbed for quantum mechanics was atomic physics. The wavelike behavior of an electron orbiting a nucleus was the key element to explain discrete atomic spectra, made of well separated lines corresponding to transitions between well defined energy levels of the electron, in the same fashion a cord produces well defined notes. The special case of the hydrogen atom, the simplest atom composed of a single electron orbiting a single proton, allowed fine predictions of its spectrum. Exact solution of its Schrödinger equation, and latter its Dirac equation, could be reached, and correctly predicted the Lyman, Balmer and other series of lines, as well as their fine structure.

In total, the explanation of atomic spectra by quantum mechanics was a bright success. Yet, it did not put to the test the strangest aspects of the theory. To see quantum coherence in action, one would have to experiment with only one — or a few — quantum particles. It could only be a *gedankenexperiment* in the early days of quantum mechanics¹. Great technological advances brought them to reality a few decades latter only. The preferred experimental technique was still optics, creating the field of quantum optics^{2,3}.

¹ Schrödinger, for example, recognized that: “it is fair to state that we are not experimenting with single particles, any more than we can raise Ichtyosauria in the zoo. We are scrutinizing records of events long after they have happened.” *cf.*

E. Schrödinger. **1952**. *Br. J. Philos. Sci.* 3, 233.

² For an introduction to quantum optics, *cf.*

M. Fox. **2006**. *Quantum Optics*;

S. Haroche & J.-M. Raimond. **2006**. *Exploring the Quantum*.

³ A quick summary of the field history is given by

S. Haroche. **2013**. *Rev. Mod. Phys.* 85, 1083.

Rabi oscillations

The most straightforward hallmark of quantum coherence are Rabi oscillations. Consider the simplest model for an atom, where only two levels are considered, $|g\rangle$ and $|e\rangle$ the ground and excited states. In the presence of an external excitation, able to pump energy from $|g\rangle$ to $|e\rangle$, the system Hamiltonian writes¹

$$\hat{H} = \begin{bmatrix} E_g & 0 \\ 0 & E_e \end{bmatrix} + g \cos(\omega t) \begin{bmatrix} 0 & 1 \\ 1 & 0 \end{bmatrix}, \quad (1.1)$$

the interaction part representing the field of a coherent source of light oscillating at pulsation ω , a laser electric field most of the time². g , the interaction strength, is typically proportional to the electric dipole of the transition and to the oscillating field amplitude. The amplitude for both states is written as $a_{g/e}(t) = c_{g/e}(t) \exp(-iE_{g/e}t)$ to factor out the free evolution of the system (we could say we placed ourselves in the field frame of reference), and Schrödinger's equation is then

$$\begin{cases} \dot{c}_g(t) = -ig (e^{i(\omega-\omega_0)t} + e^{-i(\omega+\omega_0)t}) c_e(t) \\ \dot{c}_e(t) = -ig (e^{i(\omega+\omega_0)t} + e^{-i(\omega-\omega_0)t}) c_g(t) \end{cases}, \quad \text{where } \omega_0 = E_e - E_g. \quad (1.2)$$

To solve this coupled differential equation, we first use the *rotating wave approximation*³ which neglects the fast rotating terms at $\omega + \omega_0$. This approximation is crucial to produce analytical results. Next, we also assume perfect resonance, *i.e.* $\omega - \omega_0 = 0$, for simplicity. We can now solve Eq. (1.2) to get the probability to hop from ground to excited state $P_{g \rightarrow e}(t) = \sin^2(gt)$. The frequency of this Rabi oscillation is called the Rabi frequency, $\Omega_R = g$. Of course, any incoherent desexcitation mechanism will break the Rabi oscillation. One can list spontaneous emission towards $|g\rangle$, but also any transition to other, unconsidered atomic level. This adds up with dephasing mechanisms, as elastic collisions with other atoms, which too will break phase coherence of the wavefunction. Let's pack the two mechanisms into an inverse relaxation time, Γ . If $\Gamma > g$, decoherence happens faster than the oscillations, and they cannot be observed, as represented on Fig. 1.1. To beat decoherence, one needs high laser field intensity to raise g , which was done for the first time in 1972⁴.

The next question was whether the light itself could display such a well controlled quantum phenomenon. The simplest model would be to couple our two-levels atom to a single mode of the electromagnetic field,

$$\hat{H} = \frac{\Delta}{2} \hat{\sigma}_z + \omega_0 \hat{a}^\dagger \hat{a} + g(\hat{\sigma}_+ + \hat{\sigma}_-)(\hat{a}^\dagger + \hat{a}), \quad (1.3)$$

which is called the quantum Rabi model. Δ is the energy splitting between the two levels, while ω_0 is the characteristic frequency of the light mode and g is their coupling. Only recently an exact solution of the model was found⁵. We commonly simplify it in the same spirit than the earlier RWA, by suppressing the terms that do not conserve energy at resonance, $\hat{a}^\dagger \hat{\sigma}_+$ and $\hat{a} \hat{\sigma}_-$, to reach the Jaynes-Cummings Hamiltonian⁶:

$$\hat{H} = \frac{\Delta}{2} \hat{\sigma}_z + \omega_0 \hat{a}^\dagger \hat{a} + g(\hat{\sigma}_- \hat{a}^\dagger + \hat{\sigma}_+ \hat{a}), \quad (1.4)$$

which is exactly solvable. We are now on the lookout for the same Rabi oscillation phenomenon, but between the atom and the light, which would prove the electromagnetic field quantum nature. The difficulty is that we cannot raise g by dialing up a laser pump: the emission is solely due to the vacuum fluctuations of the light mode. The solution is to place the atom into a Fabry-Perot cavity. First, it allows to isolate

¹ We set $\hbar = 1$.

² The same Hamiltonian appears in many contexts, as nuclear magnetic resonance.

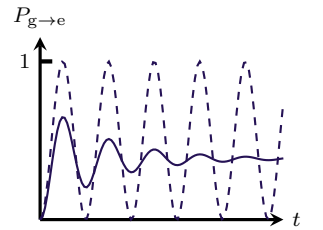


Figure 1.1: Rabi oscillations, (—) $\Gamma/g = 0$, (---) $\Gamma/g = 0.1$.

³ Often abbreviated RWA.

⁴ H. M. Gibbs. **1972**. *Phys. Rev. Lett.* **29**, 459; H. M. Gibbs. **1973**. *Phys. Rev. A* **8**, 446.

⁵ D. Braak. **2011**. *Phys. Rev. Lett.* **107**, 100401.

⁶ E. Jaynes & F. Cummings. **1963**. *Proc. IEEE* **51**, 89.

one resonant mode of the cavity, to obtain a faithful representation of the Rabi model. Better, the Purcell effect allows to engineer the atoms rate of spontaneous emission into the cavity mode: it especially grows with the cavity quality factor and diminishes with its volume¹. Again, the figure of merit of the experiment is the Γ/g ratio, with Γ the losses of the cavity to the external environment. $\Gamma/g > 1$ defines the **strong coupling regime**, where quantum coherence effects can be seen. The requirements of such an experiment have been especially difficult to match, such that the effect has been demonstrated only twenty five years ago for a single atom².

The fine control of a few quantum degrees of freedom also allowed to put to the test the models of decoherence theoreticians built to explain the crossover between quantum and classical behaviors³. The cavity can play the role of the environment, while being monitored. One can then follow its evolution while superposed states of the atom starts evolving toward a statistical, classical mixture⁴.

Ultra-strong coupling

The strong coupling regime was described still within the Jaynes-Cummings approximation. The RWA relied on the assumption that the cavity field is oscillating faster than the atom/cavity exchange of energy, $g/\omega_0 \ll 1$. We can then define an **ultra-strong coupling** regime, reached for $g \sim \omega_0$. Would it differ drastically from the strong coupling case, or, in other words, which qualitative physics the off-resonant terms add to the picture? To answer, one has to examine these models spectra⁵. Let's suppose for simplicity $\Delta = \omega_0$, such that excitations of the atom and of the cavity bear the same energy. When the coupling is turned off, all the states of the form $|g, N\rangle$ and $|e, N-1\rangle$ are degenerate, as represented on Fig. 1.2. In time independent perturbation theory, we know that the degeneracies are lifted if the perturbation operator, \hat{V} , has non-vanishing matrix element between the two states. The prototypical example is given by the eigenstates of

$$\hat{H}_0 + \hat{V} = \begin{bmatrix} -E_0 & 0 \\ 0 & E_0 \end{bmatrix} + \begin{bmatrix} 0 & g \\ g & 0 \end{bmatrix}, \quad (1.5)$$

which has eigenvalues $E_{\pm} = \pm\sqrt{E_0^2 + g^2}$; the splitting is important when the initial levels are close of one another. When dialing E_0 , we see an avoided crossing at $E_0 = 0$, as represented on Fig. 1.3. In the Jaynes-Cummings model, only the degenerate levels are connected by the interaction term: we only have splittings between pairs of states having the same number of excitations. The ground state is unchanged.

When entering the ultra-strong coupling regime, the off-resonant terms participate in the structure of the spectrum, and the simple picture of the Jaynes-Cummings ladder is lost. The ground state undergoes an especially striking change, since it turns into photonic Schödinger cats entangled with the atom⁶. To demonstrate having reached the ultra-strong coupling regime, the simplest experimental evidence is an avoided crossing between states that do not interact under the Jaynes-Cummings Hamiltonian. As an example, states $|e, 0\rangle$ and $|g, 3\rangle$ do not have the same excitation number, and so should not interact, but they are connected *via* non-RWA terms. Explicitly,

$$|g, 3\rangle \xrightarrow[\text{RWA}]{\hat{a}\hat{\sigma}_+} |e, 2\rangle \xrightarrow[\text{non RWA}]{\hat{a}\hat{\sigma}_-} |g, 1\rangle \xrightarrow[\text{RWA}]{\hat{a}\hat{\sigma}_+} |e, 0\rangle. \quad (1.6)$$

When the interaction strength g is dialed up, they are expected to cross; observing an anti-crossing is a demonstration of beyond RWA effects⁷.

¹ E. M. Purcell, H. C. Torrey, & R. V. Pound. **1946**. *Phys. Rev.* **69**, 37.

² M. Brune, F. Schmidt-Kaler, *et al.* **1996b**. *Phys. Rev. Lett.* **76**, 1800; A. Boca, R. Miller, *et al.* **2004**. *Phys. Rev. Lett.* **93**, 233603.

³ M. A. Schlosshauer. **2007**. *Decoherence*.

⁴ M. Brune, E. Hagley, *et al.* **1996a**. *Phys. Rev. Lett.* **77**, 4887.

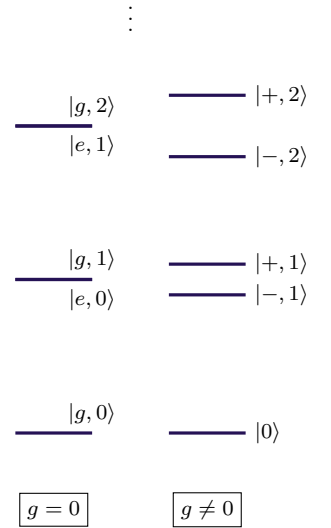


Figure 1.2: Jaynes-Cummings ladder for $\Delta = \omega_0$.

⁵ For a complete review of theoretical methods on Rabi model, *cf.*

A. L. Boité. **2020**. *Adv. Quantum Technol.* **3**, 1900140.

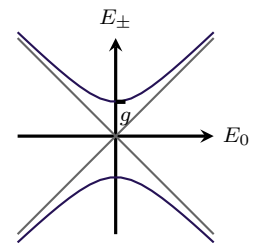


Figure 1.3: Avoided eigenstates crossing.

(\circ) : $g = 0$,

(\bullet) : $g \neq 0$.

⁶ S. Ashhab & F. Nori. **2010**. *Phys. Rev. A* **81**, 042311.

⁷ T. Niemczyk, F. Deppe, *et al.* **2010**. *Nature Phys.* **6**, 772.

Reaching this regime demanded to change radically the experimental system. Indeed, optical setups are intrinsically limited by the smallness of the light-matter coupling, given by the fine-structure constant $\alpha \simeq 1/137$. Strong competitors to quantum optics appeared in the last decades, especially in the domain of solid-state devices. They usually trade the excellent coherence times of isolated atoms for the higher couplings of electronic systems. We focus here on superconducting circuits, which we introduce in Sec. 1.3, and discuss further in Chaps. 2 & 3. Several recent reviews document the various experimental platforms and recent advances on the topic of ultra-strong coupling¹.

We remark that when testing the quantum theory of light and matter, modern physics changed several times its experimental platform, using high-power optics, cavity QED, trapped ions or solid state devices when they suited best the inquired phenomenon.

1.2 The quantum many-body problem

The quantum vacuum, a radically non-classical concept², was a key part of the vacuum Rabi oscillations between the atom and the cavity. Yet, 1996 experiments at ENS³ and NIST⁴ were far from the first time the physicists heard about the fluctuations of electromagnetic field vacuum. In 1947 was reported the measure of a shift in frequency — the Lamb shift — between the $^2S_{1/2}$ $^2P_{1/2}$ energy levels of the hydrogen atom⁵. It could not be explained by Dirac’s equation, demonstrating once more the richness of the hydrogen spectrum for quantum theory. The role of vacuum fluctuations was soon anticipated, but the theorists computing the shift value battled for years against divergent sums over the infinite continuum of modes of the electromagnetic field⁶. A solution to the problem came piece by piece. It first consisted in tricks to hide the infinities away by introducing counter-terms in Hamiltonians and Lagrangians. A mean to physically interpret these infinities was found in the renormalization group concept⁷. Importantly, these efforts created one unified language, quantum field theory, encompassing the seemingly different domains of particle physics, condensed matter and nuclear physics. The common denominator was the infinite number of degrees of freedom to take care of, and the correlated tendency of integrals over these degrees of freedom to blow up.

Electrons in interaction

In condensed matter, the most important puzzle to solve in the early times of quantum mechanics was the Fermi liquid⁸. The properties of solids, like electric and thermal conduction, could be explained by assuming the electrons are quantum fermionic particles, but non-interacting with respect to each other — it is known as the Sommerfeld theory — while the Coulomb interaction happens to be strong. Worst, any attempt to correct the result by perturbation theory ended up with infinite corrections at all orders, a meaningless result. The solution was formulated by Landau, who introduced his famous concept of quasi-particles. Close to the Fermi surface, electrons do not have a lot of opportunities to scatter. When the interactions are turned on, we can then still describe electrons as “almost particles”, albeit with a finite lifetime: quasi-particles. In the process, the mass of the quasi-particle is drastically changed. We say the mass is renormalized by the interactions. After Landau, the same ideas were reached by diagrammatic methods, which used Feynman’s diagrams to rearrange the perturbative expansion and reach a finite result. This proved both the genius of Landau and its insightful phenomenological theory, and the ability of diagrammatic techniques to evade the shortcomings of bare perturbation theory.

¹ A. F. Kockum, A. Miranowicz, *et al.* **2019**. *Nat. Rev. Phys.* **1**, 19; P. Forn-Díaz, L. Lamata, *et al.* **2019**. *Rev. Mod. Phys.* **91**, 025005; X. Gu, A. F. Kockum, *et al.* **2017**. *Phys. Rep.* **718**==719, 1.

² An in-depth analysis of the concept together with its historical perspective can be found at P. W. Milonni. **2013**. *The Quantum Vacuum*.

³ M. Brune, F. Schmidt-Kaler, *et al.* **1996b**. *Phys. Rev. Lett.* **76**, 1800.

⁴ D. M. Meekhof, C. Monroe, *et al.* **1996**. *Phys. Rev. Lett.* **76**, 1796.

⁵ W. E. Lamb & R. C. Retherford. **1947**. *Phys. Rev.* **72**, 241.

⁶ The situation was made even more obscure by relativistic covariance, which forbade simple regularization schemes. For an historic perspective, *cf.*

D. Kaiser. **2005**. *Drawing Theories Apart*; S. S. Schweber. **2020**. *QED and the Men Who Made It*.

⁷ M. Gell-Mann & F. E. Low. **1954**. *Phys. Rev.* **95**, 1300.

⁸ For an introduction to solid state physics, and field theory in condensed matter, *cf. resp.*

S. Simon, H. **2013**. *The Oxford Solid State Basics*; P. Coleman. **2015**. *Introduction to Many-Body Physics*.

The key element of the quasi-particle concept is the possibility to reach the interacting system from the non-interacting one by adiabatically turning on the interaction strength. In other words, there must be no phase transition separating the free and interacting system. In that sense, the concept of phase transition became an essential part of field theory: a phase transition separates regions of the parameter space where the ground state have different symmetries. This change of symmetry completely drives the qualitative physics observed in the various phases. Inside one phase, one can expect one special point in parameter space where the interaction strength vanishes, making the model exactly solvable. The system behavior in the rest of the phase can be explained by perturbation — and/or diagrammatic — method around this point. Finding these points, called fixed points, and the phase transition boundaries, is the purpose of the renormalization group.

A spectacular illustration of this mechanism can be found in the Bardeen, Cooper & Schrieffer theory of superconductivity. At low temperature, a phase transition separates the Fermi liquid from a superconducting phase, characterized by its ground state of condensed Cooper pairs¹.

Impurity models

In the 1960s emerged a new type of problems in condensed matter. The puzzle was the influence of diluted magnetic impurities in metallic hosts, which had a drastic effect on the sample resistivity at low temperature. The resistivity was expected to smoothly vanish, but instead went through a minimum, before growing again, in strong contradiction with known mechanisms of electrical conductivity. The problem at hand was soon recognized to be the interaction of the electronic sea with the free orbitals of the impurity², often a magnetic ion. A first explanation of the resistivity minimum was given by Kondo, who showed that the electron/impurity scattering rate at 2nd order in perturbation theory displayed a logarithmic divergence at low temperature, $1/\tau \sim 2(J\rho)^2 \ln(D/(k_B T))$, with J the coupling strength, ρ the electronic density of states and D their bandwidth^{3,4}. Still, the logarithmic law cannot hold all the way down to $T = 0$, but perturbation, and latter diagrammatic resummation⁵, ran into troubles, again in the form of diverging corrections. The next important step was made by Anderson, who connected the problem with the ideas of the renormalization group, and especially with scaling laws⁶. The idea is to eliminate perturbatively the high energy modes lying above a certain cutoff Λ , to integrate them in an effective model. We then monitor the evolution of the model parameters when Λ is lowered, providing scaling laws of the system. However, at some Λ , the coupling strength grows so much that renormalized perturbative theory still breaks down: this scale is the Kondo temperature, T_K . The next step was to extend the computation below T_K , where non-perturbative methods are needed. A solution was given by Wilson⁷: using a numerical method, the **numerical renormalization group**, he followed the renormalization flow of the coupling strength beyond perturbative analysis, and thus below T_K .

Other impurity systems appeared over the years. The most famous one is probably the spin-boson system, which describes a two-level system coupled to a bath of harmonic oscillators, which are well known to host bosonic excitations. It can be seen as the minimal extension of the Rabi model to the many-body realm. The corresponding Hamiltonian reads:

$$\hat{H} = \frac{\Delta}{2} \hat{\sigma}_x + g \hat{\sigma}_z \sum_k \left(g_k \hat{a}_k^\dagger + \bar{g}_k \hat{a}_k \right) + \sum_k \omega_k \hat{a}_k^\dagger \hat{a}_k. \quad (1.7)$$

¹ More context and references on the topic are given in Chap. 2.

² A. Blandin & J. Friedel. **1959**. *J. Phys. Radium* 20, 160.

³ J. Kondo. **1964**. *Prog. Theor. Phys.* 32, 37.

⁴ For introduction and in-depth discussion, cf. resp. P. Coleman. **2015**. *Introduction to Many-Body Physics*; A. C. Hewson. **1993**. *The Kondo Problem to Heavy Fermions*.

⁵ cf. corresponding chapter of R. D. Mattuck. **1976**. *A Guide to Feynman Diagrams in the Many-body Problem*.

⁶ P. W. Anderson. **1970**. *J. Phys. C: Solid State Phys.* 3, 2436.

⁷ K. Wilson & J. Kogut. **1974**. *Phys. Rep.* 12, 75; K. G. Wilson. **1975**. *Rev. Mod. Phys.* 47, 773.

We recognize the Rabi Hamiltonian, simply extended to several oscillator modes. This model is quite ubiquitous in quantum physics, since the spin degree of freedom is the approximation of many systems: atoms, molecules hopping between two conformations, polarization of light or quantum numbers of exotic particles. In turn, the bosonic field is the most common environment one can expect, describing phonons in solid state systems, photons for atoms in a vacuum, *etc.* Several analytical tools could be imported from the analysis of the Kondo model, as the renormalization group¹, numerical renormalization group², and the search for phase transitions³. More specific tools were also devised for the situation, based on variational ansätze⁴ or specific approximation schemes, as the non-interacting blip approximation⁵. Among the various regimes and findings, the most striking is perhaps the localization transition⁶: at strong coupling between the spin and the oscillators, a phase transition suddenly localizes the spin in an eigenstate of $\hat{\sigma}_z$ dressed by bosonic excitations. All tunneling to the other dressed eigenstate is suppressed. This localization especially suppresses any quantum superposition between the two states, and can be seen as a quantum to classical transition. Indeed, the spin-boson system has been a playground to formulate decoherence mechanisms.

These impurity models provided good explanation for several experimental evidence, from the resistance minimum of the Kondo model to the quantum to classical transition. Nonetheless, it has proven hard to check the full extent of their predictions, a situation quite similar to early quantum mechanics, as we exposed in Sec. 1.1. A typical example is perhaps the important spatial correlations that develop themselves at strong coupling. For example, in the Kondo model, an exponentially large screening cloud of length scale $\xi_k = v_F/T_K$ (v_F the Fermi velocity) appears around the impurity⁷. Experimental evidences of this exponential length scale are scarce on electronic systems⁸, and the spin correlation structure has never been observed. As a response, alternative experimental setups have been proposed *e.g.* with quantum circuits⁹.

Similarly to few-body quantum theory a few decades ago, the theory of quantum many-body systems exhibits intriguing phenomena that are hard to study on the experimental setups that initially triggered the study of these many-body models. The next step is then to search for new experimental platforms which could simulate the same physics, while easing the experimental demonstration of these predicted phase transitions, long distance correlations, and other hallmarks of collective behavior of the quantum particles.

1.3 Simulating nature

Many experimental platforms are currently put forward as candidates for emulating models with strong interactions amongst many particles. The focus of this thesis is on superconducting circuits¹⁰. Solid state devices built with superconducting materials for low dissipation have been noticed long ago as a promising platform to observe quantum effects¹¹. The first devices were aimed at isolating a single electron or a single Cooper pair in a superconducting island. Even though the discreteness of electrons is well established, it is not so easy to harness in a solid state device, where the electron wavefunctions spreads, making the local electrical charge — the charge of a capacitor, for example — a continuous variable.

The solution is to employ a device based on the tunnel effect: tunneling is an all or nothing process, since the electron wavefunction is evanescent in the insulating

¹ V. Hakim, A. Muramatsu, & F. Guinea. **1984**. *Phys. Rev. B* **30**, 464.

² R. Bulla, N.-H. Tong, & M. Vojta. **2003**. *Phys. Rev. Lett.* **91**, 170601; R. Bulla, H.-J. Lee, *et al.* **2005**. *Phys. Rev. B* **71**, 045122.

³ M. Vojta. **2006**. *Phil. Mag.* **86**, 1807.

⁴ R. Silbey & R. A. Harris. **1984**. *J. Chem. Phys.* **80**, 2615.

⁵ A. J. Leggett, S. Chakravarty, *et al.* **1987**. *Rev. Mod. Phys.* **59**, 1.

⁶ We discuss this topic in Sec. 4.2.

⁷ J. E. Gubernatis, J. E. Hirsch, & D. J. Scalapino. **1987**. *Phys. Rev. B* **35**, 8478; V. Barzykin & I. Affleck. **1996**. *Phys. Rev. Lett.* **76**, 4959.

⁸ I. V. Borzenets, J. Shim, *et al.* **2020**. *Nature* **579**, 210.

⁹ I. Snyman & S. Florens. **2015**. *Phys. Rev. B* **92**, 085131.

¹⁰ For an introduction and a complete review, *cf. resp.* U. Vool & M. Devoret. **2017**. *Int. J. Circuit Theory Appl.* **45**, 897; A. Blais, A. L. Grimsmo, *et al.* **2021**. *Rev. Mod. Phys.* **93**, 025005.

¹¹ P. W. Anderson. **1964**. in *Lectures on the Many-body Problems*, ed. E. R. Caianiello, 113; A. J. Leggett. **1992**. in *Quantum Tunneling in Condensed Media*, ed. Y. Kagan & A. J. Leggett.

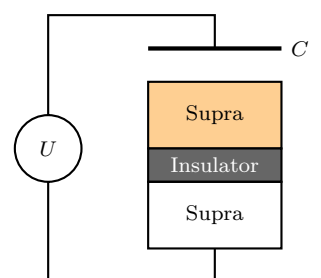


Figure 1.4: Single Cooper pair circuit. The top superconductor (•) forms an island.

region. The same is valid for Cooper pairs in a superconducting material. We then design a superconducting island, biased by an external voltage through a capacitor, and connected to the ground by a small insulating layer through which the charge carriers can tunnel. The device is represented on Fig. 1.4 (Such a device is analyzed further in Sec. 2.1). When the bias voltage varies, we expect sudden jumps in the island charge that we can measure from monitoring the current¹. The device can be seen as a single charge sensitive electrometer².

The next step was to observe quantum coherence effects on a single Cooper pair, and it was done a few years later³ by reaching a superposition state of 0 and 1 Cooper pairs on the island. Interestingly, the applications to manipulation of quantum information in a digital machine was already emphasized in these early works. In this spirit, the coherence time of this device was soon measured by a charge echo method⁴, imported from the spin echo technique. It was found that the coherence time was mostly limited by the charge noise, which displayed a $1/f$ power spectrum. Limiting the charge noise is a constant concern in charge based systems.

An other line of work towards quantum effects in superconducting devices uses superconducting rings containing a Josephson junction. More details on this system are given in Sec. 4.4. Here, we only state that the quantum variable is now the superconducting current running around the loop. By tuning the external flux through the loop, it has been possible to realize quantum superposition of currents running clockwise and anti-clockwise⁵, quite similarly to the superposition of 0 and 1 Cooper pairs we saw earlier. In fact, these two experiments are the two faces of the same coin, as the general framework of circuit quantum electrodynamics we employ in the manuscript will show.

These two devices for manipulation of quantum information are now known as the charge and flux qBit⁶ respectively. A technological race was then started⁷, fueled by advances in microfabrication techniques, to find, fabricate and operate the best circuit design for a superconducting qBit. Important milestones are the transmon qBit⁸, which exploits a trade-off between charge noise and non-linearity that we explore in depth in Part. II. Next, the fluxonium qBit⁹ entered the realm of single qBit designed with many Josephson junctions: the proposal shunts a charge qBit with a long chain of $\sim 10^2$ Josephson junctions, which behave together like a superinductance, an inductor reaching L values orders of magnitude above what a geometric inductor could accomplish. The goal is to quench the low frequency charge noise, while keeping unaltered the AC response of the charge system. Finally, a recent nanofabrication tour de force must be signaled: the production of a quasi-charge qBit¹⁰. This circuit concludes the “periodic table of superconducting circuits”: while the transmon exploits weakly non-linear phase oscillations of a charge qBit with low charging energy, the quasi-charge qBit exploits weakly non-linear phase oscillations of a flux qBit with low inductive energy.

Superconducting circuits and the many-body regime

A strong appeal of superconducting circuits is that once one has a good design for simulating one quantum particle, is it relatively easy to repeat it many times on a chip and hope to simulate a many-body model¹¹. Of course, we only expect non-trivial effects to develop when the interaction strength between the simulated particles is high enough, but this is precisely the strong advantage of solid state experimental

¹ M. H. Devoret, D. Esteve, & C. Urbina. **1992**. *Nature* **360**, 547.

² Which has been put forward for exotic applications, V. Bouchiat, G. Chardin, *et al.* **1997**. *Hyperfine Interact.* **109**, 345.

³ V. Bouchiat, D. Vion, *et al.* **1998**. *Phys. Scr.* **1998**, 165.

⁴ Y. Nakamura, Y. A. Pashkin, *et al.* **2002**. *Phys. Rev. Lett.* **88**, 047901.

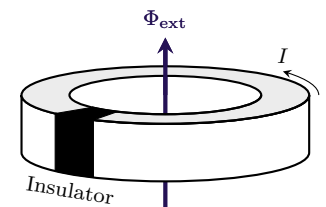


Figure 1.5: A superconducting ring threaded by a magnetic flux Φ_{ext} and interrupted by a Josephson junction.

⁵ C. H. van der Wal, A. C. J. ter Haar, *et al.* **2000**. *Science* **290**, 773; J. R. Friedman, V. Patel, *et al.* **2000**. *Nature* **406**, 43.

⁶ I. Chiorescu, Y. Nakamura, *et al.* **2003**. *Science* **299**, 1869.

⁷ D. Vion, A. Aassime, *et al.* **2002**. *Science* **296**, 886.

⁸ J. Koch, T. M. Yu, *et al.* **2007**. *Phys. Rev. A* **76**, 042319.

⁹ V. E. Manucharyan, J. Koch, *et al.* **2009**. *Science* **326**, 113.

¹⁰ I. V. Pechenezhskiy, R. A. Mencia, *et al.* **2020**. *Nature* **585**, 368.

¹¹ In that regard, cold atoms are a strong competitor to circuits, *cf. e.g.* T. Giamarchi. **2017**. *Physics* **10**, 115.

platforms.

Such proposals appeared several times during the two last decades, especially towards simulating aspects of Kondo physics¹. They exploit the bosonisation of the Kondo model² to match the bosonic systems we typically obtain by quantization of the excitations of a junction chain. The impurity models are a natural target for the first proposals of many-body simulators, since they simplify greatly the circuit design and operation; they require one qBit — or atom-like degree of freedom — only. Still, one can anticipate that superconducting circuits are fit for the simulation of the (bulk) quantum sine-Gordon model, due to the cosine potential of the Josephson energy³. The closely related Luttinger liquid has been recently explored by means of superconducting circuits⁴. Disorder seems to be the key conceptual ingredient to link the experimental output of such a device with its expected behavior.

Still, making the connection with experimental work asks to pinpoint a good observable that could be accessed experimentally, while carrying hallmarks of non-trivial many-body effects. For a simulator composed of a long chain of junctions hosting bosonic excitations, *i.e.* photons⁵, coupled to a qBit emulating the impurity, one could study the photon scattering off the impurity⁶. Experimental attempts on impurity model simulation focused on spectroscopic quantities, the easiest to measure. The renormalization of the spin-boson tunneling amplitude has been obtained from a superconducting simulator⁷, as well as the Josephson energy renormalization in the boundary sine-Gordon model⁸, a related impurity model the analysis of which we devote the Part. III of this manuscript. Scattering processes in this same boundary sine-Gordon simulator has been recently investigated⁹. From these experiments, we can hope to demonstrate the universal properties that link the low-energy properties of many quantum impurity systems¹⁰.

The exploration of the quantum many-body problem has steadfastly entered the stage of simulation: versatile experimental platforms have been designed to reproduce the physics of broad interest theoretical models. On the theoretical side, this state of affairs now requires to review these models in light of their new experimental realizations, together with their practical limitations. The purpose of this thesis is to perform such an analysis on Josephson based simulators.

Organisation of the manuscript

In Part. I, we set the stage by presenting the physical system of interest and the theoretical methods widely used in the field. We introduce the canonical quantization of a generic superconducting circuit, and show, on general grounds, how to reach from there the standard models, spin-boson and boundary sine-Gordon. As an intermediate step, we introduce a more general model, which we nicknamed the charge-boson model. It interpolates between these two previous models, which appear as specific limits of the charge-boson Hamiltonian. We also raise the question of the impact of the superconducting phase compact nature, a long debated topic¹¹ intricated with the experimental hardships caused by charge noise. We present novel numerical renormalization group analysis of the charge-boson model. We map its phase diagram to guide our following inquiry. For both the spin-boson and the boundary sine-Gordon model, we then present well established analyses of their many-body properties, and especially of the phase transition they display. The poor man’s scaling, simple implementation of the renormalization group ideas on the boundary sine-Gordon model,

¹ S. Camalet, J. Schrieffer, *et al.* **2004**. *EPL* **68**, 37; K. Le Hur. **2012**. *Phys. Rev. B* **85**, 140506; I. Snyman & S. Florens. **2015**. *Phys. Rev. B* **92**, 085131.

² For the specific derivation and a review of the method, *cf. resp.* F. Guinea, V. Hakim, & A. Muramatsu. **1985a**. *Phys. Rev. B* **32**, 4410; J. von Delft & H. Schoeller. **1998**. *Ann. Phys. (Berlin)* **7**, 225.

³ A. Roy, D. Schuricht, *et al.* **2021**. *Nucl. Phys. B* **968**, 115445.

⁴ K. Cedergren, R. Ackroyd, *et al.* **2017**. *Phys. Rev. Lett.* **119**, 167701.

⁵ The typical parameters of a superconducting circuit result in these photons to be in the microwave frequency range.

⁶ M. Goldstein, M. H. Devoret, *et al.* **2013**. *Phys. Rev. Lett.* **110**, 017002; N. Gheeraert, X. H. H. Zhang, *et al.* **2018**. *Phys. Rev. A* **98**, 043816.

⁷ P. Forn-Díaz, J. J. García-Ripoll, *et al.* **2017**. *Nat. Phys.* **13**, 39; L. Magazzù, P. Forn-Díaz, *et al.* **2018**. *Nat. Commun.* **9**, 1403.

⁸ S. Leger, J. Puertas-Martinez, *et al.* **2019**. *Nat. Commun.* **10**, 5259.

⁹ R. Kuzmin, N. Grabon, *et al.* **2021**. *Phys. Rev. Lett.* **126**, 197701.

¹⁰ A. Anthore, D. M. Kennes, *et al.* **2020**. *Eur. Phys. J. Spec. Top.* **229**, 663.

¹¹ A. Murani, N. Bourlet, *et al.* **2020**. *Phys. Rev. X* **10**, 021003.

will especially drive our development in the next sections. It predicts an emergent energy scale, the renormalized Josephson energy, that separates between perturbative and non-perturbative regions.

Part. II focuses on the question of the compact superconducting phase variable. Here we propose a new variational ansatz as a tool to diagnose the relevance of the phenomenon and test decompactification mechanisms that neutralize phase compactness together with charge noise. The ansatz is constructed and tested on the one-body case of the isolated Josephson junction — or charge qBit — to get to know the method and assess its accuracy on a simple situation. We then move to the charge-boson case, where the compact ansatz method gives a simple, physical understanding of the decompactification at strong coupling, and demonstrates its ability to quantitatively describe the system in a vast region of parameter space, containing all the experimentally relevant situations. The benchmark is conducted against numerical renormalization group.

We then specialize in Part. III to the decompactified case, relevant for the experiments at hand, where the general charge-boson description reduces to the boundary sine-Gordon model. We especially focus on the circuit designed by N. Roch's experimental team¹ to measure inelastic scattering processes. We re-employ the methods of Part. I to derive a careful modelization of the experimental situation, and reduce the observables to the model response functions. The situation is then analyzed using a diagrammatic technique, versatile enough to produce important analytical results in the limit of a continuous sea of bosonic modes, and carry numerical computations at finite temperature using the Keldysh formalism, fully resolved in frequency, without any drastic approximation on the microscopic model. The analytic section predicts anomalous power laws in the perturbative region, a strong hallmark of many-body physics, provided the ultraviolet cutoff is high enough. The numerical section introduces a resummation technique, the skeleton expansion, which explains how a small number of narrow multi-photon resonances can produce a smooth dissipative response alike to a continuum of modes. The section ends up with quantitative comparison between theoretical predictions and experimental results, which shows good agreement together with intriguing discrepancy in the non-perturbative regime. This raises questions on the validity of the diagrammatic method at very low pinning of the superconducting phase variable.

The last chapter is devoted to sketch some perspectives on this work. We argue on paths to follow to tackle the non-perturbative regime discrepancy between theoretical and experimental data. The work done to carry the computations using the Keldysh formalism allows to envision new applications of the method to out-of-equilibrium and transient dynamics, a domain where the superconducting phase compactness could retrieve some influence.

¹ J. Puertas Martínez, S. Léger, *et al.* **2019**. *npj Q. Info.* 5, 1; S. Léger. **2021**, *Electrodynamique Quantique d'une Jonction Josephson Couplée à Un Environnement Fortement Dissipatif*, Ph.D thesis, UGA.

Part I

Roadmap to many-body physics in cQED

2 | Macroscopic quantum variables

On appelait cela le principe d'incertitude, parce qu'il y avait une chose dont on était sûr, c'est que c'était faux. Ou alors si c'était juste, c'était vraiment par hasard, ou bien qu'il y avait une erreur quelque part.

Jacques Rouxel, *L'ordinateur Shadok*.

Superconductivity is one of the most striking phenomena of condensed matter physics. Its study has uncovered a wealth of spectacular effects, such as zero resistance, Meissner effect, quantum coherence in electric currents, *etc.* A microscopic theory explaining these observations was built up by Bardeen, Cooper and Schrieffer in 1957¹. We will not go into details of this theory here, and will only mention the qualitative elements needed to explain the behavior of superconducting circuits.

Many metals are subject to an instability of their Fermi sea at low temperature, due to an attractive interaction between electrons mediated by crystal phonons. This is signaled by a divergence in the electron-electron scattering cross-section². After the instability occurs, the many-body ground state is composed of paired electrons, the so-called Cooper pairs, which all condense into the same state. The finite energy needed to break Cooper pairs is given by the superconducting gap, Δ . Its finite value ensures that, at a low temperature, the condensate gathers a macroscopic number of electrons. The whole electron fluid is then described by a macroscopic wave function,³ $\psi(x) = \sqrt{\rho(x)} \exp(i\varphi(x))$.

The fact that this macroscopic wavefunction could lead to tests of quantum mechanics on a new scale, beyond what *e.g.* atomic physics permitted, was noticed as soon as 1964⁴. In a bulk superconductor, the superconducting phase φ is a classical variable, free from quantum fluctuations due to the high energy cost of phase gradients. This phenomenon is called phase rigidity. We will see that a quantum uncertainty relation relates this phase to the number of Cooper pairs. As a consequence, the Cooper pair number is undefined⁵ in a bulk superconductor, and the dynamic of the phase is classical. This state of affairs can be ultimately be linked to a breaking of electromagnetic gauge invariance⁶.

To observe macroscopic quantum effects, we need to find an intermediate regime, where neither the charge nor the phase are classical. This is the case inside a small superconductor grain: if the grain is small enough, Coulomb repulsion between Cooper pairs will forbid their number to fluctuate too much. We now examine a phenomenological model of such a situation, that will serve as the cornerstone for our description of superconducting circuits.

It was called the uncertainty principle, because one thing we knew for sure was that it was wrong. Or if it was right, it was really by accident, or by someone's mistake.

¹ L.-P. Levy. **2000**. *Magnetism and Superconductivity*.

² H. Bruus & K. Flensberg. **2004**. *Many-Body Quantum Theory in Condensed Matter Physics*.

³ R. P. Feynman, R. B. Leighton, & M. Sands. **2011**. *The Feynman Lectures on Physics, Vol. III*.

⁴ P. W. Anderson. **1964**. in *Lectures on the Many-body Problems*, ed. E. R. Caianiello, 113; A. J. Leggett. **2019**. in *Fundamentals and Frontiers of the Josephson Effect*, ed. F. Tafuri, 63.

⁵ In the quantum mechanical sense: its fluctuations are very strong, as it can be seen in the usual BCS ground state wavefunction.

⁶ S. Weinberg. **1986**. *Prog. Theor. Phys. Supp.* 86, 43.

2.1 Cooper pair box

The Cooper pair box is a superconducting device composed of a tiny superconducting island separated from a ground plane by an insulator layer thin enough to allow tunneling of Cooper pairs in and out of the island. An external generator imposes an external charge n_g on the island. Let's assume that a finite number n of Cooper pairs occupy the island in a state $|n\rangle$. The Coulomb energy is then zero if this number balances the external charge. Otherwise, it evolves quadratically in the charge number, because of Coulomb repulsion. The Hamiltonian of the system is then^{1,2}

$$\hat{H} = \frac{E_c}{2}(\hat{n} - n_g)^2 - \frac{E_J}{2} \sum_{n \in \mathbb{Z}} |n\rangle\langle n+1| + |n\rangle\langle n-1|. \quad (2.1)$$

The second term describes tunneling of Cooper pairs in and out of the island. E_c and E_J are characteristic Coulomb³ and tunneling energy. The situation can be summarized by an electric diagram using lumped elements, as in Fig. 2.1. The cross represents the tunnel barrier, which is called a **Josephson Junction**.

Let's derive the spectrum of the system in the $E_J \ll E_c$ limit. At $E_J = 0$, the Hamiltonian is already diagonal. At every charge n corresponds an energy parabola with respect to n_g , as shown on Fig. 2.2. The system displays level degeneracy at $n_g = 1/2 + n \quad \forall n \in \mathbb{Z}$. This degeneracy is lifted by the tunneling term. The splitting is estimated by first order degenerate perturbation theory to be of width E_J .

Charge qBit

At the degeneracy point, the Cooper pair box displays a two-level structure that can be used as a qBit to store and manipulate quantum information⁴. This is one of the oldest design of a superconducting qBit. It is mainly flawed by its sensibility to experimental noise on the n_g variable. This **charge noise** is believed to originate from fluctuating two level systems in the circuit substrate, which affects the superconducting island electrostatic environment. It results in a so-called $1/f$ noise power spectrum⁵. Operating at $n_g = 1/2$ suppress the sensibility to n_g at first order, thus improving the charge qBit coherence time. Yet, rare tunneling events of unpaired electrons can suddenly shift n_g of $\pm 1/2$, and scramble irremediably the computation basis of the qBit⁶. The physics of n_g is discussed further in part II.

Superconducting phase

It is now clear that, at finite E_J/E_c ratios, eigenstates of the superconducting island are not charge eigenstates, such that the charge is fluctuating. This can be examined further by introducing its quantum conjugated variable, the superconducting phase $\hat{\varphi}$, defined by⁷

$$[\hat{\varphi}, \hat{n}] = i\hat{1}. \quad (2.2)$$

Via Baker-Campbell-Hausdorff formula, one can show that \hat{n} is the generator of translations along φ (and *vice versa*),

$$\hat{\varphi} e^{i\phi \hat{n}} |\varphi\rangle = (\varphi + \phi) e^{i\phi \hat{n}} |\varphi\rangle \Rightarrow e^{i\phi \hat{n}} |\varphi\rangle = |\varphi + \phi\rangle. \quad (2.3)$$

Then, if we choose $\phi = 2\pi$, we obtain

$$\begin{aligned} e^{i2\pi \hat{n}} &= \sum_{j=0}^{\infty} \frac{1}{j!} \left(\sum_{n \in \mathbb{Z}} i2\pi n |n\rangle\langle n| \right) = \sum_{n \in \mathbb{Z}} e^{i2\pi n} |n\rangle\langle n| = \hat{1} \\ &\Rightarrow |\varphi\rangle = |\varphi + 2\pi\rangle. \end{aligned} \quad (2.4)$$

¹ The 1/2 prefactor of E_c is a matter of convention. E_c and $4E_c$ are often found in literature.

² The charge being discrete,

$$\hat{n} = \sum_{n \in \mathbb{Z}} n |n\rangle\langle n|.$$

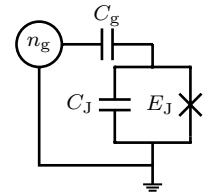


Figure 2.1: Diagram of a Cooper pair box. The cross symbolizes the tunnel probability.

³ We will see how to relate it to capacitances of the model in Sec. 3.1.

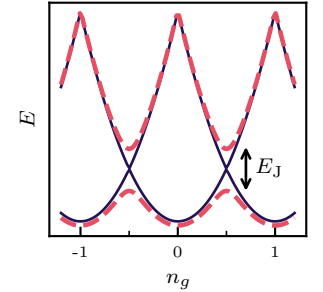


Figure 2.2: 2 lowest energy levels at (●) $E_J = 0$ and (○) $E_J \neq 0$.

⁴ V. Bouchiat, D. Vion, *et al.* **1998**. *Phys. Scr.* **1998**, 165.

⁵ Y. Nakamura, Y. A. Pashkin, *et al.* **2002**. *Phys. Rev. Lett.* **88**, 047901.

⁶ In certain cases, it is possible to monitor such events and post-select experimental data free from such tunnelings, *cf.*

J. J. Viennot, X. Ma, & K. W. Lehnert. **2018**. *Phys. Rev. Lett.* **121**, 183601.

⁷ As we will see, the compact nature of $\hat{\varphi}$ renders this equation somewhat ill-defined. It could be rewritten using $\exp i\hat{\varphi}$ only.

These two states are indistinguishable, as a consequence of the Cooper pair number being an integer. This relationship between number and phase is quite general¹. We must then see φ as an angular variable, in the sense that $\hat{\varphi} = \int_0^{2\pi} d\varphi \varphi |\varphi\rangle\langle\varphi|$. The Eq. (2.3) can be differentiated to derive the scalar product

$$\langle\varphi|n\rangle = \frac{1}{\sqrt{2\pi}} e^{in\varphi}. \quad (2.5)$$

In turn, this result allows us to rewrite the tunneling term in Eq. (2.1) as

$$\hat{H} = \frac{E_c}{2} (\hat{n} - n_g)^2 - E_J \cos \hat{\varphi}. \quad (2.6)$$

This is the standard Hamiltonian for a single junction. Although non-trivial, it can be exactly solved: the associated Schrödinger equation is a Mathieu equation, the solution of which is exactly known. Even if this Hamiltonian as been obtained heuristically, it could have been derived from microscopic BCS theory².

2.2 Plasma oscillations

A simple mechanical analog of Eq. (2.6) is a pendulum, the kinetic energy and potential corresponding respectively to charging energy and Josephson energy. Accordingly, a regime of small oscillations must exist at $E_J/E_c \gg 1$ ³. The corresponding Hamiltonian is

$$\hat{H} = \frac{E_c}{2} \hat{n}^2 + \frac{E_J}{2} \hat{\varphi}^2. \quad (2.7)$$

In this regime, energy must oscillate between storage in charge and phase. The charge energy storage mechanism is given by the capacitance of the junction. For a capacitance C , we have $2en = CU$, e the electron charge and U the voltage between sides of the junction, so we can relate $E_c = (2e)^2/C$ to match the classical energy of a condensator.

By analogy with an LC-oscillator, we would expect the other energy storage mode to be inductive. Indeed, using the equation of motion for the charge in the small oscillations regime, we can derive a relation between phase and current \hat{I} ,

$$\hat{I} = 2e \frac{d\hat{n}}{dt} = 2e \frac{i}{\hbar} \left[\frac{E_J}{2} \hat{\varphi}^2, \hat{n} \right] = -\frac{2e}{\hbar} E_J \hat{\varphi}. \quad (2.8)$$

The Josephson energy is then equivalent to the energy of an inductance $L = (\hbar/2e)^2/E_J$. We call it a kinetic inductance, to differentiate it from the geometric inductance provided by a circuit loop. We then expect oscillations at $\omega_p = 1/\sqrt{LC} = \sqrt{E_J E_c}/\hbar$. We call it the plasma frequency of the junction, because it describes charges oscillating back and forth the tunnel element. The equivalent circuit is represented on Fig. 2.3.

The equation of motion for \hat{n} and $\hat{\varphi}$ with full Hamiltonian (2.6) produces the **Josephson relations**:

$$\hbar \frac{d\varphi}{dt} = 2eU \quad (2.9)$$

$$I = 2e \frac{E_J}{\hbar} \sin \varphi = I_0 \sin \varphi. \quad (2.10)$$

These equations hold in the classical limit⁴. Although we will not use them further, they reveal important phenomena, *e.g.* the DC Josephson effect⁵, which predicts that a Josephson junction biased in voltage displays current oscillations. This prediction and the subsequent experimental discovery gave the 1973 Nobel prize to Esaki, Giaever and Josephson.

¹ N. Nagaosa. 1999. *Quantum Field Theory in Condensed Matter Physics*.

² J. M. Martinis & K. Osborne. 2004. arXiv:cond-mat/0402415.

³ One would rather expect $\langle\varphi^2\rangle \ll 1$ to represent small oscillations. These requirements are in fact equivalent.

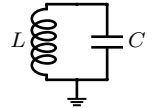


Figure 2.3: When $E_J \gg E_c$, the junction reduces to an LC circuit.

⁴ which is shown by invoking Ehrenfest theorem.

⁵ M. Tinkham. 2004. *Introduction to Superconductivity*; P. Mangin & R. Kahn. 2017. *Superconductivity*.

Orders of magnitude and real devices

One could wonder what a Josephson device displaying a cross-over between charging effects at $E_J \ll E_c$ and superconductivity at $E_J \gg E_c$ would actually look like. We consider an Al/Al₂O₃/Al junction, of thickness d and surface S . The situation is illustrated on Fig. 2.4, where the superconducting island is represented on the left. The island is biased in voltage through a capacitor.

The charging energy is estimated by $E_c = (2e)^2/C$, and $C \simeq \varepsilon S/d$ for a planar capacitor filled with insulator with dielectric constant ε . For aluminium, $\varepsilon \simeq 10\varepsilon_0$ at low temperatures, ε_0 the vacuum permittivity. Microfabrication techniques result in typical surfaces of $S \simeq 10\ \mu\text{m}^2$ and oxide layer in the 1 nm range, resulting in capacitances in the 1 fF range.

The Josephson energy can be determined by the famous Ambegaokar & Baratoff relation¹,

$$E_J = \frac{h\Delta}{8e^2 R_n}, \quad (2.11)$$

where Δ is the superconducting gap ($\Delta = 0.175\ \text{meV}$ for aluminum) and R_n is the normal resistance of the junction, due to normal electron tunneling. It evolves roughly as $R_n \sim 1/S$, which implies that the characteristic energy ratio evolves as $E_J/E_c \sim S^2$ with the junction surface: **charging effects take place for small junctions**. For the same surface, one can expect a kinetic inductance in the 10 nH range. The plasma frequency of this typical junction is then $f_p \simeq 10\ \text{GHz}$, such that AC measurements that probe the dynamical response of a circuit of junctions will lie in the microwave range².

If we want a system to display quantum mechanical behavior, we must check, among many things, that thermal excitations of the system are not too probable. For a harmonic oscillator, the first excited level start being thermally populated for a temperature verifying $\hbar\omega/k_B T \simeq 1$. This limit is at $T = 50\ \text{mK}$ for a 1 GHz oscillator typical of circuit QED. Dilution fridges can reach $\sim 20\ \text{mK}$ routinely, which makes them good tools to attain the quantum regime. Yet, the gap to thermal excitations is narrow, and one must stay aware that bad thermalization or lowering of circuit characteristic frequencies could bridge it. Thermal fluctuations are notoriously hard to distinguish from quantum fluctuations, such that many quantum effects would then be smeared.

Finally, the high frequencies³ question the lumped element approximation in use throughout this manuscript. Retardation effects in electromagnetic signals appear at lengths above $\ell = v/\omega$, v the wave velocity. In high impedance superconducting chains, $v \simeq c/10$, such that $\ell \sim 3\ \text{mm}$. While well above the μm size of a single Josephson junction, arrays of 10^3 junctions or above will behave as waveguides rather than electrical circuits.

Natural units

In the rest of the manuscript, a more convenient system of units is used, **where \hbar and $2e$ are set to one**. This amounts to measuring all fluxes in unit of the flux quantum $\Phi_q = \hbar/2e = 3.29 \times 10^{-16}\ \text{Tm}^2$, and all impedances in units of the resistance quantum, $R_q = \hbar/(2e)^2 = 1027\ \Omega$ ⁴. Using these units, the Hamiltonian

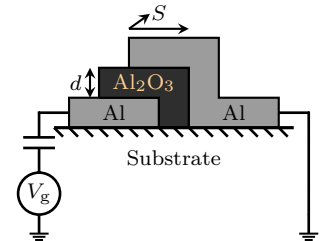


Figure 2.4: A Josephson junction made of aluminium superconductors sandwiching an oxide layer.

¹ V. Ambegaokar & A. Baratoff. **1963**. *Phys. Rev. Lett.* **10**, 486.

² U. Vool & M. Devoret. **2017**. *Int. J. Circuit Theory Appl.* **45**, 897.

³ One could compare it to the few GHz that are the top limit of current electronics and microprocessors.

⁴ The quantum of resistance can sometimes be defined as $h/(2e)^2$, and is closely related to the Von Klitzing constant $R_K = h/e^2$ used in quantum Hall effect.

(2.7) is recast in the usual harmonic oscillator form:

$$\hat{H} = \frac{1}{2C}\hat{n}^2 + \frac{1}{2L}\hat{\varphi}^2 = \omega_p \left(\hat{a}^\dagger \hat{a} + \frac{1}{2} \right) \quad (2.12)$$

where

$$\begin{cases} \omega_p = 1/\sqrt{LC} \\ Z = \sqrt{L/C} \end{cases}, \begin{cases} \hat{a}^\dagger = 1/\sqrt{2Z}(\hat{\varphi} - iZ\hat{n}) \\ \hat{a} = 1/\sqrt{2Z}(\hat{\varphi} + iZ\hat{n}) \end{cases} \Leftrightarrow \begin{cases} \hat{\varphi} = \sqrt{Z/2}(\hat{a}^\dagger + \hat{a}) \\ \hat{n} = i/\sqrt{2Z}(\hat{a}^\dagger - \hat{a}) \end{cases}. \quad (2.13)$$

From the last set of equations, we deduce that Z represents the zero point fluctuations of the phase, since $\langle 0|\hat{\varphi}^2|0\rangle = Z/2$.

3 | Canonical quantization of large circuits

“Il se produit alors un système d’ondes statiques présentant des noeuds et des ventres, ce qui ne contribue pas peu à créer l’atmosphère de la salle de danse.”

Boris Vian, *L’Écume des Jours*.

“A system of static waves is produced, displaying nodes and bumps, with no little influence on the dancefloor good vibe.”

3.1 Many degrees of freedom

In the previous section, we quantized one degree of freedom of a superconducting circuit. We could alternatively say we dealt with one quantum particle. To tackle the quantum theory of a full circuit, we need a more systematic procedure. We construct a classical Lagrangian for the circuit, keeping in mind the general idea that capacitance energy is equivalent to a kinetic term, and that inductances are potential energies, and may be non-linear. The main difficulty is that Kirchhoff’s law will introduce redundancies that need to be accounted for. The method presented there¹ is focused on nodes of the circuit. A dual description focused on loops can be formulated².

Method of nodes

Let us consider a generic circuit like the one on Fig. 3.1. Each branch carries a flux defined via induction law, $\dot{\phi}_b = v_b$, v_b the branch voltage. Kirchhoff’s loop rule requires that the voltage drop along a loop in the circuit is zero. This is automatically satisfied if branch fluxes derive from a discrete gradient, *i.e.* if we define nodes fluxes such that for the branch b between nodes i and $i+1$, $\phi_b = \phi_{i+1} - \phi_i$. The redundancy in this description is eliminated by choosing a ground node, the flux of which is set to 0.

The circuit dynamical variables can be packed into one vector of fluxes, $\vec{\phi}$. The quadratic part of the Lagrangian is then built with a capacitance matrix \mathbf{C} ³, verifying

$$\begin{cases} C_{ij} = C_{ji} = -C_{ij}, \text{ the capacitance between nodes } i \text{ and } j, \\ C_{ii} = -\sum_{j \neq i} C_{ij}. \end{cases} \quad (3.1)$$

Similar definitions hold for $1/L$, the matrix of inverse inductances⁴. The quadratic part of the circuit Lagrangian is then

$$\mathcal{L} = \frac{1}{2} \dot{\vec{\phi}}^T \mathbf{C} \dot{\vec{\phi}} - \frac{1}{2} \vec{\phi}^T 1/L \vec{\phi}. \quad (3.2)$$

Up until now, we ignored the possibility of an external magnetic flux threading a loop of the circuit. This would modify Kirchhoff’s loop rule, which requires that the sum of fluxes along a closed loop matches the external magnetic flux. This is taken into account using a spanning tree for the network of capacitances: it is a set of branches that connect every node to the ground through capacitance branches⁵, without mak-

¹ U. Vool & M. Devoret. 2017. *Int. J. Circuit Theory Appl.* 45, 897; B. Yurke & J. S. Denker. 1984. *Phys. Rev. A* 29, 1419.

² J. Ulrich & F. Hassler. 2016. *Phys. Rev. B* 94, 094505.

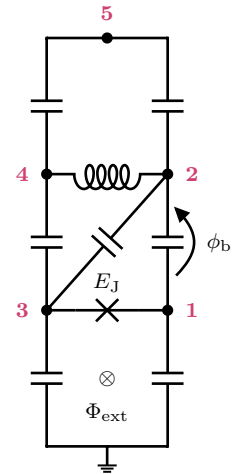


Figure 3.1: A generic circuit with 6 nodes, threaded by an external flux and containing a Josephson junction. A branch flux is indicated.

³ Matrices acting on vectors of variables will be denoted by bold symbols.

⁴ We emphasize that $1/L \neq L^{-1}$.

⁵ If a node cannot be reached via capacitance branches, it corresponds to a node having no kinetic energy. Thus, it is not a true degree of freedom and can be removed.

ing loops. Then, every inductance branch closes a loop in the spanning tree: the external flux threading this loop is affected to this branch via a supplementary term

$$\sum_{\text{inductive branches } b} \frac{1}{L_b} (\phi_{i+1} - \phi_i) \Phi_{\text{ext}}. \quad (3.3)$$

This is equivalent to adding a generator to these branches. Finally, the non-quadratic part of the Lagrangian, generated by the Josephson junctions, is simply added *via* a $\cos(\phi_{i+1} - \phi_i + \Phi_{\text{ext}})$ term, with Φ_{ext} still defined by the spanning tree. As an example, the circuit from Fig. 3.1 is described by

$$\mathcal{L} = \frac{C}{2} \dot{\vec{\phi}}^\top \begin{bmatrix} 2 & -1 & 0 & 0 & 0 \\ -1 & 3 & -1 & 0 & -1 \\ 0 & -1 & 3 & -1 & 0 \\ 0 & 0 & -1 & 2 & -1 \\ 0 & -1 & 0 & -1 & 2 \end{bmatrix} \dot{\vec{\phi}} - \frac{1}{2L} (\phi_4 - \phi_2 + \Phi_{\text{ext}})^2 + E_J \cos(\phi_3 - \phi_1 + \Phi_{\text{ext}}). \quad (3.4)$$

where we assumed the same capacitance C for all capacitors. At last, it is clear that ϕ_5 has no potential energy: it is a cyclic variable in the sense of Lagrangian mechanics. It can be replaced, as obvious from the circuit diagram itself, by a $C/2$ capacitance.

We can now return to the charge qBit circuit on Fig. 2.1, and derive from this procedure $E_c = 1/(C_g + C_J)$.

Hamiltonian form

We derive the classical Hamiltonian of the system by Legendre transform. The conjugate momenta to the phases are charges, defined by¹

$$n_i = \frac{\partial \mathcal{L}}{\partial \dot{\phi}_i} = C_{ij} \dot{\phi}_j \quad (3.5)$$

which allows to compute the Hamiltonian

$$\mathcal{H} = n_i \dot{\phi}_i - \mathcal{L} = \frac{1}{2} \vec{n}^\top \mathbf{C}^{-1} \vec{n} + \frac{1}{2} \vec{\phi}^\top \mathbf{1}/L \vec{\phi} + \sum_{\text{junctions}} \cos \Delta \phi. \quad (3.6)$$

Canonical quantization is trivial, and simply promotes n_i and ϕ_i to operators with a commutator derived from the Poisson bracket, $[\hat{\phi}, \hat{n}] = i\hat{1}$. Although this expression is quite general, the inverse capacitance matrix is often full, with no simple structure, while \mathbf{C} is often simpler to work with. It is then preferable to simplify the Lagrangian first by finding the eigenmodes of its quadratic part².

It is noteworthy that the charge offset can be incorporated in this quantization procedure, by adding $n_{gi} \dot{\phi}_i$ term in the Lagrangian. This important feature is absent from different quantization routes³.

Eigenmodes

The main difference between this electrokinetic Hamiltonian and some mechanical system Hamiltonian is the presence of a matrix with off-diagonal terms in the kinetic term. Thus, it is not enough to diagonalize one matrix to uncover the independent eigenmodes of the system: we have to solve the *generalized eigenvalue problem*⁴, which asks for \mathbf{P} and a diagonal matrix $\boldsymbol{\omega}$ such that

$$\mathbf{P}^\top \mathbf{C} \mathbf{P} = \mathbf{1} \quad \text{and} \quad \mathbf{1}/L \mathbf{P} = \mathbf{C} \mathbf{P} \boldsymbol{\omega}^2. \quad (3.7)$$

¹ We make use of Einstein's summation convention: summation over repeated dummy indices is implied.

² Another way would be to employ path integral quantization, which is directly formulated in terms of the Lagrangian.

³ S. E. Nigg, H. Paik, *et al.* **2012**. *Phys. Rev. Lett.* **108**, 240502.

⁴ A. Ruhe & H. van der Vorst. **2000**. *Templates for the Solution of Algebraic Eigenvalue Problems*.

The problem is well defined only if both \mathbf{C} and $1/L$ are symmetric and \mathbf{C} is definite positive. If one sets $\mathbf{C} = \mathbf{1}$, we recover an eigenvalue problem, with \mathbf{P} the matrix of eigenvectors and ω^2 the eigenvalues. Once provided with a solution \mathbf{P} , it is clear that the system can be rewritten in terms of eigenmodes, by the change of variables $\mathbf{P}\vec{\varphi} = \vec{\phi}$ in the Lagrangian¹ leading to

$$\mathcal{L} = \frac{1}{2} (\dot{\varphi}_q \dot{\varphi}_q - \omega_q^2 \varphi_q \varphi_q), \quad (3.8)$$

which is now straightforward to convert into Hamiltonian form and diagonalize.

It is in fact guaranteed that such a \mathbf{P} exists: since \mathbf{C} is definite positive, it can be written with a Gram matrix \mathbf{G} , $\mathbf{C} = \mathbf{G}^\top \mathbf{G}$. Then, the generalized eigenvalue problem can be recast into

$$(\mathbf{G}^{-1} \mathbf{1} / L \mathbf{G}^{-1}) (\mathbf{G} \mathbf{P}) = (\mathbf{G} \mathbf{P}) \omega^2, \quad (3.9)$$

a standard eigenvalue problem. Finally, since $[\mathbf{P}^\top \mathbf{C} \mathbf{P}, \omega] = 0$, $\mathbf{P}^\top \mathbf{C} \mathbf{P}$ is diagonal. It can furthermore be set to identity by a rescaling of the columns of \mathbf{P} . Even if this proof is constructive, it is in practice inefficient to solve an explicit problem.

Adding external fluxes or charge offsets do not pose any further difficulty, but it is noteworthy that non-quadratic terms from Josephson potentials become quite involved, at least for a general circuit.

3.2 Charge-boson model

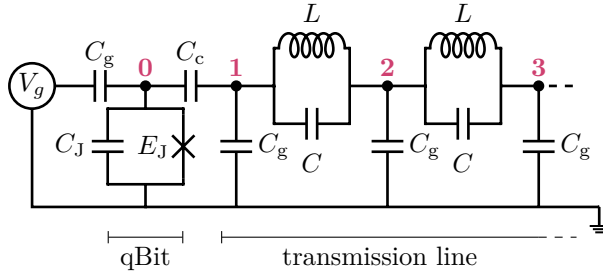


Figure 3.2: The charge-boson circuit. The site zero is the atom-like degree of freedom, capacitively coupled to a high-impedance transmission line, and subject to charge noise *via* the generator V_g .

The most common setup to simulate light-matter coupling with superconducting circuits is to couple a charge qBit, *i.e.* a superconducting island coupled to ground with a Josephson junction in the non-linear regime, with a transmission line that simulates the electromagnetic environment. The diagram for such a system is represented on Fig. 3.2. which has been successfully implemented experimentally². Here, the transmission line is represented in its lumped elements form. It could stand for a regular line, a coaxial cable or a planar long resonator^{3,4}. To achieve high coupling, it is more efficient to actually design such a chain on chip, using large Josephson junctions as inductors, thus drastically raising the chain impedance, and ultimately its coupling to the impurity (*cf.* Sec. 3.3). Using arrays of Josephson junctions as a meta-material is a very promising approach⁵, thanks to the resulting high-impedance as well as the tunability⁶ and bulk non-linearity⁷ they provide.

Before working out the details of this circuit, it is instructive to give a rough sketch of the different physical scales we expect to appear. The discrete transmission line will host propagative modes at low energy, with impedance $Z_c = \sqrt{L/C_g}$. In the lowest mode, all N sites oscillate in phase: the whole chain behaves as one island of effective capacitance NC_g , and inductance NL , thus oscillating at $\omega_{\min} = 1/(N\sqrt{LC_g})$. At

¹ In the Hamiltonian, one has to conserve canonical commutation, which imposes that charges transform as $CP\vec{N} = \vec{n}$.

² J. Puertas Martínez, S. Léger, *et al.* **2019**. *npj Q. Info.* **5**, 1.

³ P. Forn-Díaz, J. J. García-Ripoll, *et al.* **2017**. *Nat. Phys.* **13**, 39.

⁴ In the limit of infinite number of sites and long wavelength.

⁵ P. Jung, A. V. Ustinov, & S. M. Anlage. **2014**. *Supercond. Sci. Technol.* **27**, 073001.

⁶ M. Mirhosseini, E. Kim, *et al.* **2018**. *Nat. Commun.* **9**, 3706.

⁷ Y. Krupko, V. D. Nguyen, *et al.* **2018**. *Phys. Rev. B* **98**, 094516.

high frequency, the discrete chain has a natural cutoff at the Brillouin zone edge of $\omega_{\max} = 2/\sqrt{LC_g}$. With current technology, arrays of $10^3 - 10^4$ sites can be nano-fabricated, but the parasitic capacity of the junctions will impose a much lower bandwidth to the system: at high frequency, neighboring sites oscillate in phase opposition, at a frequency imposed by the plasma resonance of the junctions, $\omega_p \simeq 1/\sqrt{LC}$. As we will see, the boundary condition on site 0 adds yet another high-frequency cutoff. The corresponding dispersion relation is sketched on Fig. 3.3. The plasma pulsation is usually around 20 GHz. The qBit characteristic frequency can be controlled using a SQUID instead of a simple junction, which allows to swipe $\sqrt{E_J E_c}$ across the range 1 – 20 GHz.

Circuit Hamiltonian

We now apply the method of Sec. 3.1. Notations are taken from Fig. 3.2. Site 0 is singled out, since we want to describe its coupling to the environment. Its coupling energy $(\dot{\phi}_0 - \dot{\phi}_1)^2/2C_c$ is developed and splitted such that

$$\mathcal{L} = (C_c + C_J) \frac{\dot{\phi}_0^2}{2} + E_J \cos(\phi_0) - C_c \dot{\phi}_0 \dot{\phi}_1 + \frac{1}{2} \left(\vec{\phi}^\top \mathbf{C} \vec{\phi} - \vec{\phi}^\top \mathbf{1}/L \vec{\phi} \right), \quad (3.10)$$

where $\vec{\phi} = (\phi_1, \phi_2, \dots)$, and

$$\mathbf{C} = \begin{bmatrix} C_g + C_c + C & -C & & & \\ -C & 2C + C_g & -C & & \\ & -C & 2C + C_g & -C & \\ & & & \ddots & \\ & & & & \ddots \end{bmatrix}, \mathbf{1}/L = \frac{1}{L} \begin{bmatrix} 1 & -1 & & & \\ -1 & 2 & -1 & & \\ & -1 & 2 & -1 & \\ & & & \ddots & \ddots \end{bmatrix}. \quad (3.11)$$

Let's call \mathbf{P} the solution to the generalized eigenvalue problem (3.7). The change of variables $\vec{\phi} = \mathbf{P} \vec{\varphi}$ brings the environment in diagonal form

$$\mathcal{L} = (C_c + C_J) \frac{\dot{\phi}_0^2}{2} + E_J \cos(\phi_0) - C_c \dot{\phi}_0 \mathbf{P}_{1\ell} \dot{\varphi}_\ell + \frac{1}{2} (\dot{\varphi}_k \dot{\varphi}_k - \omega_k^2 \varphi_k \varphi_k). \quad (3.12)$$

We will use P_ℓ as a shorthand for $\mathbf{P}_{1\ell}$. The conjugate momenta to ϕ_0 and φ_k are

$$\begin{cases} n_0 = (C_J + C_c) \dot{\phi}_0 - C_c P_\ell \dot{\varphi}_\ell \\ n_k = \dot{\varphi}_k - C_c P_k \dot{\phi}_0 \end{cases} \Rightarrow \dot{\phi}_0 = \frac{n_0 + C_c P_\ell n_\ell}{C_c + C_J - C_c^2 P_\ell P_\ell}. \quad (3.13)$$

Reporting this in \mathcal{H} provides, after some algebra:

$$\begin{aligned} \mathcal{H} &= \dot{\phi}_0 n_0 + \dot{\varphi}_q n_q - \mathcal{L} \\ &= (C_c + C_J) \frac{\dot{\phi}_0^2}{2} - C_c \dot{\phi}_0 P_\ell \dot{\varphi}_\ell + \frac{1}{2} (\dot{\varphi}_k \dot{\varphi}_k - \omega_k^2 \varphi_k \varphi_k) - E_J \cos(\phi_0) \\ &= \frac{(n_0 + C_c P_\ell n_\ell)^2}{2(C_c + C_J - C_c^2 P_\ell P_\ell)} - E_J \cos(\phi_0) + \frac{1}{2} (n_k n_k + \omega_k^2 \varphi_k \varphi_k). \end{aligned} \quad (3.14)$$

This Hamiltonian has a clear interpretation: the two first terms describe the atom-like degree of freedom, $(\hat{n}_0, \hat{\varphi}_0)$, with a renormalized capacitance¹ $C_{\text{eff}} = C_c + C_J - C_c^2 P_\ell P_\ell$. It has a minimal coupling to a scalar electromagnetic field, represented by the third term.

The $P_\ell P_\ell$ term can be expressed in terms of capacitances. Since $\mathbf{P}^\top \mathbf{C} \mathbf{P} = \mathbf{1}$, $P_\ell P_\ell = (\mathbf{C}^{-1})_{00}$. To extract a specific element of a matrix inverse, we make use of Cramer's rule, $\mathbf{C}^{-1} = \mathbf{C}_o^\top / \det \mathbf{C}$, \mathbf{C}_o the comatrix of \mathbf{C} ². We first assume that $C_c = C$, and

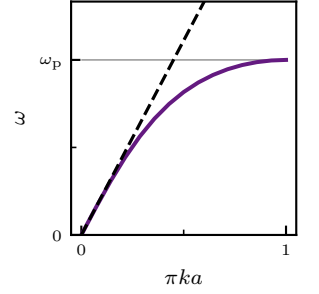


Figure 3.3: The expected dispersion relation as a function of adimensional wavenumber (a is the size of a junction). (—) $\omega = f(\pi ka)$, (---) Long wavelength approximation.

¹ Or renormalized mass, in particle physics language.

² The comatrix of A is the matrix of determinants of submatrices formed by removing one line and one column to A .

will correct this using Sherman-Morrison formula at the end. Let D_n be the following determinant:

$$D_n = \left| \begin{array}{cccc} 2C + C_g & -C & & \\ -C & 2C + C_g & -C & \\ & -C & 2C + C_g & \ddots \\ & & -C & 2C + C_g \end{array} \right|_n \quad (3.15)$$

Then, Cramer's rule asserts that $\mathbf{C}_{00}^{-1} = D_{n-1}/D_n$ (for n sites). Expanding the first line of the determinant, we obtain the recursion $D_n = (2C + C_g)D_{n-1} - C^2D_{n-2}$. To find the $n \rightarrow \infty$ limit, we reduce the recursion to degree one by defining $u_n = D_n/D_{n-1}$. Then, $u_n = (2C + C_g) - C^2/u_{n-1}$. If this sequence has a limit, it verifies $u_\infty = (2C + C_g) - C^2/u_\infty$, from which we deduce $u_\infty = C + C_g(1 + \sqrt{1 + 4C/C_g})/2$. Finally, Sherman-Morrison formula corrects the inverse of a matrix \mathbf{A} under a rank one perturbation \vec{u} by:

$$(\mathbf{A} + \vec{u}\vec{u}^\top)^{-1} = \mathbf{A}^{-1} - \frac{\mathbf{A}^{-1}\vec{u}\vec{u}^\top\mathbf{A}^{-1}}{1 + \vec{u}^\top\mathbf{A}^{-1}\vec{u}}. \quad (3.16)$$

Here, $\vec{u} = (C_c - C, 0, \dots)$, such that the correction simply is $\mathbf{C}_{00}^{-1} = C_c - C + \mathbf{C}_{00}^{-1}(C_c - C)$ ¹. Finally,

$$C_{\text{eff}} = C_c + C_J - \frac{C_c^2}{C_c + \frac{C_g}{2} \left(1 + \sqrt{1 + \frac{4C}{C_g}}\right)}. \quad (3.17)$$

The diamagnetic term

When facing a minimal coupling Hamiltonian like (3.14), a standard treatment in atomic physics is to expand the momenta squared as a kinetic energy, a linear atom-field coupling, and

$$\frac{C_c^2}{C_{\text{eff}}}(P_\ell n_\ell)^2, \quad (3.18)$$

the diamagnetic term². This last part is then removed, since it is irrelevant in perturbation theory. Nonetheless, its importance has been widely debated³: it is especially necessary to preserve the gauge invariance of the theory. The question of its relevance was raised again in the context of the Dicke model: the ultra-strong coupling between an assembly of electric dipoles and a cavity mode was believed to lead to a superradiant phase transition⁴, that could be prevented by taking the diamagnetic term into account⁵.

In our context, the diamagnetic term has been suspected to modify the coupling strength⁶ and to regularize the continuum limit of the theory⁷. To avoid any pitfall, we will now take a detour to slightly reformulate the model to automatically take care of the diamagnetic term. In practice, it only adds quadratic corrections to the free field Hamiltonian: it must be possible to find new field eigenmodes that account for it. In fact, it is even possible to massage it into the diagonalization we already did. We will then be able to discuss the impact of the diamagnetic term on the system behavior.

Extended circuit Hamiltonian

In contrast to Eq. (3.10), we now include the site 0 in the capacitance and inductance matrices, in order to perform the complete diagonalisation in one shot. We will be able to separate again the impurity site afterwards. The Lagrangian assumes the form

$$\mathcal{L} = \frac{1}{2} \left(\dot{\vec{\phi}}^\top \mathbf{C} \dot{\vec{\phi}} - \vec{\phi}^\top \mathbf{1}/L \vec{\phi} \right) + E_J \cos(\phi_0) \quad (3.19)$$

¹ The similarity with Dyson's formula is no coincidence, cf. Sec. 8.2.

² In regular electromagnetism, this term is indeed responsible for atomic diamagnetism.

³ W. E. Lamb, R. R. Schlicher, & M. O. Scully. **1987**. *Phys. Rev. A* **36**, 2763; C. Cohen-Tannoudji, J. Dupont-Roc, & G. Grynberg. **1987**. *Photons et Atomes*.

⁴ P. Nataf & C. Ciuti. **2010**. *Phys. Rev. Lett.* **104**, 023601.

⁵ O. Viehmann, J. von Delft, & F. Marquardt. **2011**. *Phys. Rev. Lett.* **107**, 113602; C. Ciuti & P. Nataf. **2012**. *Phys. Rev. Lett.* **109**, 179301; G. M. Andolina, F. M. D. Pellegrino, *et al.* **2019**. *Phys. Rev. B* **100**, 121109.

⁶ J. J. García-Ripoll, B. Peropadre, & S. De Liberato. **2015**. *Sci. Rep.* **5**, 16055.

⁷ M. Malekakhlagh, A. Petrescu, & H. E. Türeci. **2017**. *Phys. Rev. Lett.* **119**, 073601.

where $\vec{\phi} = (\phi_0, \phi_1, \dots)$, and

$$\mathbf{C} = \begin{bmatrix} C_J + C_c & -C_c & & & & \\ -C_c & C_g + C_c + C & -C & & & \\ & -C & 2C + C_g & -C & & \\ & & -C & 2C + C_g & -C & \\ & & & & \ddots & \\ & & & & & \ddots \end{bmatrix}, \quad \mathbf{1/L} = \frac{1}{L} \begin{bmatrix} 0 & & & & & \\ & 1 & -1 & & & \\ & -1 & 2 & -1 & & \\ & & -1 & 2 & -1 & \\ & & & & \ddots & \\ & & & & & \ddots \end{bmatrix}. \quad (3.20)$$

Still calling \mathbf{P} the solution to the generalized eigenvalue problem (3.7), we can jump directly to the Hamiltonian form

$$\hat{H} = \frac{1}{2} (\hat{n}_k \hat{n}_k + \omega_k^2 \hat{\varphi}_k \hat{\varphi}_k) - E_J \cos(\mathbf{P}_{0\ell} \hat{\varphi}_\ell). \quad (3.21)$$

While exact, this expression is quite obscure, since the impurity mode is no longer apparent. We have to detail the structure of \mathbf{P} to understand it. Eq. (3.7) can be expanded, row by row, into¹

$$\text{row } i = 0: \quad \mathbf{P}_{1\ell} = \frac{C_J + C_c}{C_c} \mathbf{P}_{0\ell} \quad \text{or} \quad \omega_\ell = 0. \quad (3.22)$$

$$\text{row } i = 1: \quad \mathbf{P}_{2\ell} = \mathbf{P}_{1\ell} \left(1 - \frac{C_f}{C} \frac{\omega_\ell^2}{\omega_0^2 - \omega_\ell^2} \right), \quad (3.23)$$

$$\text{with } C_f = \frac{C_c C_J}{C_c + C_J} + C_g \quad \text{and} \quad \omega_0 = \frac{1}{\sqrt{LC}}.$$

$$\text{rows } i > 1: \quad \mathbf{P}_{i+1,\ell} + \mathbf{P}_{i-1,\ell} = \mathbf{P}_{i\ell} \left(2 - \frac{C_g}{C} \frac{\omega_\ell^2}{\omega_0^2 - \omega_\ell^2} \right). \quad (3.24)$$

Let first inspect the $\omega_\ell = 0$ eigenvalue. The eigenproblem reduces to $(\mathbf{1/L})_{ij} \mathbf{P}_{j0} = 0$. Then, $\mathbf{P}_{10} = \mathbf{P}_{20}$, and the bulk relation reduces to $\mathbf{P}_{i+1,0} + \mathbf{P}_{i-1,0} = 2\mathbf{P}_{i0}$. By recursion, $\mathbf{P}_{i0} = \mathbf{P}_{10} \quad \forall i > 1$. If we also consider that $\mathbf{P}^\top \mathbf{C} \mathbf{P} = \mathbf{1}$, the resulting row vector is

$$\mathbf{P}_{00} = \frac{1}{\sqrt{C_J + C_c}}, \quad \text{and} \quad \mathbf{P}_{i0} = 0 \quad \forall i > 0. \quad (3.25)$$

This means that the zero frequency mode is completely localized on site 0: we found the qBit mode. This is a hint that we should change our variables, since $\mathbf{P}_{0\ell} \varphi_\ell$ is the qBit degree of freedom. Let us use again the shorthand $\mathbf{P}_{0\ell} = P_\ell$, and write²

$$\begin{cases} \hat{\theta} = P_\ell \hat{\varphi}_\ell \\ \hat{\theta}_\ell = \hat{\varphi}_\ell \quad \forall \ell > 0 \end{cases}, \quad \begin{cases} \hat{N} = \hat{n}_0 / P_0 \\ \hat{N}_\ell = \hat{n}_\ell - P_\ell \hat{n}_0 / P_0 \quad \forall \ell > 0 \end{cases}. \quad (3.26)$$

Inverting these equations gives $\hat{n}_0^2 = (P_0 \hat{N})^2$, $\hat{n}_\ell^2 = (\hat{N}_\ell + P_\ell \hat{N})^2 \quad \forall \ell > 0$, and most importantly, $\hat{\varphi}_0^2 = (\hat{\theta} - P_\ell \hat{\theta}_\ell)^2 / P_0^2$. This residue of the diamagnetic term is no trouble, since $\omega_0 = 0$. It disappears of the Hamiltonian, which assumes the form

$$\hat{H} = \frac{P_\ell P_\ell}{2} \hat{N}^2 - E_J \cos(\hat{\theta}) + \hat{N} P_k \hat{N}_k + \frac{1}{2} (\hat{N}_q \hat{N}_q + \omega_q \hat{\theta}_q \hat{\theta}_q). \quad (3.27)$$

We recognize an atom-like part, with renormalized capacitance $1/P_\ell P_\ell$, capacitively coupled³ to a scalar electromagnetic field. The diamagnetic term has effectively been absorbed into the P_ℓ . One could track down where exactly the \mathbf{P} matrix has been modified: the two differences are the expression of the qBit renormalized capacitance, and the C_f capacitance, that would simply be $C_f = C_c + C_g$, were the diamagnetic term neglected.

We can at last rewrite the field in terms of creation and annihilation operators⁴, and

¹ Our convention is to let indices i, j, n, m label sites, while k, q, ℓ label eigenmodes.

² This transformation is valid since it preserves the commutation relations.

³ which means coupled *via* their charges.

⁴ Here,

$$\begin{cases} \hat{\theta}_k = \sqrt{1/2\omega_k} (\hat{a}_k^\dagger + \hat{a}_k) \\ \hat{N}_k = i\sqrt{\omega_k/2} (\hat{a}_k^\dagger - \hat{a}_k) \end{cases}.$$

reintroduce the offset charge:

$$\hat{H} = \frac{E_c}{2} (\hat{N} - n_g)^2 - E_J \cos(\hat{\theta}) + i(\hat{N} - n_g) \sum_k g_k (\hat{a}_k^\dagger - \hat{a}_k) + \sum_k \omega_k \hat{a}_k^\dagger \hat{a}_k, \quad (3.28)$$

where we called $g_k = P_k \sqrt{\omega_k/2}$ the coupling to mode k and E_c the junction effective charging energy. The task remains to find an expression for these parameters as function of the microscopic capacitances and inductances. The Hamiltonian Eq. (3.28) generalizes the spin-boson model to a multi-state version. We nickname it the **charge-boson model**. It has not been studied so far in the litterature.

Expression for the coupling strength

The system is almost invariant by discrete translations¹, apart from the boundary conditions. We then expect a static wave solution:

$$P_{i\ell} = N_\ell \cos((i-1)k_\ell + \delta_\ell) \quad \forall i > 0. \quad (3.29)$$

The equation for site 0 is already given by (3.22). k_ℓ is a wavenumber, those exact determination depends on the unspecified other boundary condition, at the other end of the chain. We expect that in the $N \rightarrow \infty$ limit, it varies continuously in the Brillouin zone, *i.e.* $k_\ell \in [0, \pi)$. δ_ℓ is a phase shift at reflection, mixing ingoing and outgoing waves, and N_ℓ is a norm.

Concerning the field modes, we obtain their dispersion relation by injecting the P ansatz in the bulk relation, Eq. (3.24), to obtain²

$$\omega_\ell^2 = \frac{4}{LC_g} \frac{\sin^2(k_\ell/2)}{1 + \frac{4C}{C_g} \sin^2(k_\ell/2)}. \quad (3.30)$$

This results agrees with the sketch of the Fig. 3.3, and allows to compute precisely the plasma pulsation to be $\omega_p = \omega_0/\sqrt{1 + C_g/4C}$. The phase shift is then obtained by plugging the ansatz in the boundary condition (3.23). After some trigonometry, we get

$$\tan(\delta_\ell) = \tan\left(\frac{k_\ell}{2}\right) \left(\frac{2C_f}{C_g} - 1\right). \quad (3.31)$$

Finally, the ansatz is completely determined by finding the norms N_ℓ *via* the normalization $P^\top C P = \mathbf{1}$. For $q, \ell \neq 0$, it writes

$$\begin{aligned} P_{iq} C_{ij} P_{j\ell} &= \\ & P_{1q} ((C + C_c + C_g) P_{1\ell} - C_c P_{0\ell} - C P_{2\ell}) \\ & + \sum_{i=2}^N P_{iq} \left((2C + C_g) P_{i\ell} - C P_{i\ell} \left(2 - \frac{C_g}{C} \frac{\omega_\ell^2}{\omega_0^2 - \omega_\ell^2} \right) \right) \end{aligned} \quad (3.32)$$

$$= \left(C_g \sum_{i=1}^N P_{iq} P_{i\ell} + \frac{C_c C_J}{C_c + C_J} P_{1q} P_{1\ell} \right) \left(1 + \frac{4C}{C_g} \sin^2(k_\ell/2) \right) = \delta_{k\ell}. \quad (3.33)$$

We retain only terms scaling as N , neglecting the others. In this large chain limit, we expand

$$\begin{aligned} \sum_{i=1}^N P_{iq} P_{i\ell} &= \frac{N_k N_\ell}{2} \sum_{i=1}^N \cos(i(k_q + k_\ell)) \cos(\delta_k + \delta_\ell) - \sin(i(k_q + k_\ell)) \sin(\delta_k + \delta_\ell) \\ & + \cos(i(k_q - k_\ell)) \cos(\delta_k - \delta_\ell) - \sin(i(k_q - k_\ell)) \sin(\delta_k - \delta_\ell) \end{aligned} \quad (3.34)$$

¹ With periodic boundary conditions, the symmetry is exact, which is equivalent to C and $1/L$ being circulant matrices: their diagonalization is closely related to the Discrete Fourier Transform.

² Another useful form is

$$4 \sin^2\left(\frac{k_\ell}{2}\right) = \frac{C_g}{C} \frac{\omega_\ell^2}{\omega_0^2 - \omega_\ell^2}.$$

Since $\sum_{i=1}^N \cos(jk) \rightarrow -1/2 + N\delta(k)$ when $N \rightarrow \infty$, we only retain

$$N_\ell^2 = \frac{2}{N} \frac{1}{C_g + 4C \sin^2(k_\ell/2)}. \quad (3.35)$$

We now have all the components of P_ℓ :

$$P_0^2 = \frac{1}{C_c + C_J}, \quad \text{and} \quad P_\ell^2 = \frac{2}{NC_g} \left(\frac{C_c}{C_c + C_J} \right)^2 \frac{1}{\left(1 + \frac{4C}{C_g} \sin^2(k_\ell/2)\right) \left(1 + \left(2\frac{C_f}{C_g} - 1\right)^2 \tan^2(k_\ell/2)\right)}. \quad (3.36)$$

3.3 Spectral density

Quite often, one is only concerned with the $N \rightarrow \infty$ limit, where the environment is composed of a continuum of modes. Then, its characteristics can be packed into one function, the spectral density, defined as $J(\omega) = \pi \sum_\ell g_\ell^2 \delta(\omega - \omega_\ell)$ ¹. All sums over modes can be recast as integrals over frequency², which will include $J(\omega) = Ng^2(\omega)dk/d\omega$ in the integrand. J will be used intensively in Chap. 4. Turning our previous expressions into functions of ω requires some algebra. Using Eqs. (3.30) & (3.35),

$$N_\ell^2 = \frac{2}{NC_g} \frac{\omega_0^2 - \omega_\ell^2}{\omega_0^2}. \quad (3.37)$$

Aside, $\tan^2(k_\ell/2) = \sin^2(k_\ell/2)/(1 - \sin^2(k_\ell/2))$. Using the plasma pulsation expression,

$$\cos^2(\delta_\ell) = \frac{\omega_p^2 - \omega_\ell^2}{\omega_p^2 - (1 - \chi)\omega_\ell^2}, \quad \chi = \left(\frac{2C_f}{C_g} - 1 \right)^2 / (1 + 4C/C_g). \quad (3.38)$$

The inverse group velocity is also obtained through the dispersion relation:

$$2 \frac{d}{d\omega} \left(\arcsin \sqrt{\frac{C_g \omega_\ell^2}{4C \omega_0^2} - \omega_\ell^2} \right) = \frac{1}{\sqrt{1 + 4C/C_g}} \frac{2\omega_0^2}{(\omega_0^2 - \omega_\ell^2) \sqrt{\omega_p^2 - \omega_\ell^2}}. \quad (3.39)$$

Combining these results, the spectral density is

$$J(\omega) = \left(\frac{C_c}{C_c + C_J} \right)^2 \sqrt{\frac{L}{C_g}} \omega \frac{\sqrt{1 - \omega^2/\omega_p^2}}{1 + \omega^2(1/\omega_\chi^2 - 1/\omega_p^2)}, \quad 1/\omega_\chi^2 = LC_g \left(\frac{C_f}{C_g} - \frac{1}{2} \right)^2. \quad (3.40)$$

At low frequencies, the spectral density is linear with ω ³, with a slope $2\pi\alpha$, α being the *coupling strength*⁴. It is proportional to the line impedance, and is maximized when $C_c \gg C_J$. One can verify that taking the diamagnetic term into account reduced α ^{5,6}.

The rest of the expression provides a high-frequency cutoff. Of course, the discrete chain model imposes a first cutoff, pinpointed in the next paragraph. The plasma frequency imposes a second one, usually much lower. Finally, a third characteristic frequency appears, related to the phase shift, ω_χ ⁷.

Continuum limit

The value and form of the cutoff is most important to prevent diverging integrals, especially in perturbation theory. It is well known that these divergences plagued the early days of quantum electrodynamics⁸. It is then instructive to investigate the limit of no discretization of the scalar electromagnetic field. This would correspond to the environment being an infinite, continuous waveguide.

¹ See Eq. (3.28) for g_k definition.

² Using the integral definition

$$\sum_{\ell=1}^N F(k_\ell) = \frac{N}{\pi} \int_0^\pi F(k) dk.$$

³ This linearity labels our environment as Ohmic. Other possibilities exists, cf.

U. Weiss. **2008**. *Quantum Dissipative Systems*.

⁴ Reading the last expression,

$$\alpha = \sqrt{\frac{L}{C_g}} \left(\frac{C_c}{C_c + C_J} \right)^2.$$

⁵ J. J. García-Ripoll, B. Peropadre, & S. De Liberato. **2015**. *Sci. Rep.* **5**, 16055.

⁶ We stress that the weight of the diamagnetic term is not an independent parameter in this model, and cannot be tuned.

⁷ Especially, both δ_ℓ and $1/\omega_\chi$ vanish if $2C_f = C_g$.

⁸ For pedagogical text on the physical content of divergences and and historical approach, cf.

P. W. Milonni. **2013**. *The Quantum Vacuum*;
D. Kaiser. **2005**. *Drawing Theories Apart*.

Let's simplify our previous computation of J in this case. We take $C = 0$ to neglect plasma oscillations ($\omega_p \rightarrow \infty$), which reduces the dispersion relation to the standard optical branch, $\omega = \omega_m \sin(k/2)$, with $\omega_m = 2/\sqrt{LC_g}$ the maximum frequency. The spectral density follows:

$$J(\omega) = \left(\frac{C_c}{C_c + C_J} \right)^2 \sqrt{\frac{L}{C_g}} \omega \frac{\sqrt{1 - \omega^2/\omega_m^2}}{1 + (\chi - 1)\omega^2/\omega_m^2}. \quad (3.41)$$

We must have $\omega_m \rightarrow \infty$ in the continuum limit, while the chain impedance $Z_c = \sqrt{L/C_g}$ must remain finite. We then scale both L and C_g by an adimensional scale ϵ^1 , and take the $\epsilon \rightarrow 0$ limit. Then,

$$\omega_m/\sqrt{\chi - 1} \xrightarrow{\epsilon \rightarrow 0} \omega_M = \frac{1}{Z_c} \frac{C_c + C_J}{C_c C_J}, \quad (3.42)$$

and the spectral density acquires a finite, natural Lorentzian cutoff:

$$J(\omega) = \frac{2\pi\alpha\omega}{1 + \omega^2/\omega_M^2}, \quad \alpha = \frac{Z_c}{2\pi} \left(\frac{C_c}{C_c + C_J} \right)^2. \quad (3.43)$$

This cutoff has been provided by the boundary condition of the eigenvalue problem, and can be seen as being partly related to the diamagnetic term².

Effective charging energy

We now turn to the other emergent parameter in the charge-boson Hamiltonian of Eq. (3.28), the effective charging E_c . In terms of our microscopic model parameters, it writes

$$E_c = \frac{1}{C_c + C_J} + \frac{2}{\pi} \int_0^\infty \frac{J(\omega)}{\omega} d\omega. \quad (3.44)$$

It is a sum of on-site charging energy and a circuit charging energy, that grows at high-coupling. As we will see, this prevents us to set α , E_c and ω_M as independent parameters.

Working in the continuum limit provided by Eq. (3.43), the integral is evaluated to

$$4\alpha \int_0^\infty \frac{d\omega}{1 + \omega^2/\omega_M^2} = 2\pi\alpha\omega_M = \frac{C_c}{C_J} \frac{1}{C_c + C_J}. \quad (3.45)$$

The final result is quite simple, we have $E_c = 1/C_J$. The renormalized charging energy especially does not depend on the coupling capacitor, C_c . Furthermore, the charge-boson parameters are related by

$$2\pi\alpha = \frac{C_c}{C_c + C_J} \frac{E_c}{\omega_M}. \quad (3.46)$$

The coupling strength saturates at a value $\alpha_{\max} = E_c/(2\pi\omega_M)$, as illustrated on Fig. 3.4. The bound is reached for $C_c \gg C_J$. In this limit, the coupling strength further simplifies to $2\pi\alpha = Z_c$. The exact form of the bound is of course linked to the cutoff form, and would be modified by numerical prefactor when considering *e.g.* a plasma pulsation cutoff. Yet, the existence of a maximum coupling at given E_c and ω_M is a general result. To reach higher couplings, only two routes are possible. Lowering the cutoff drives the system out of the universal regime defined by ω_M greater any energy scale, to a trivial regime where the atom-like element decouples from the environment, when $\sqrt{E_J E_c} \gg \omega_M$. Cranking up E_c would lead to the same difficulty, and would strengthen charge noise on top of it.

¹ We could employ a , a chain junction length, instead. We would need to introduce lineic values of L , C and C_g .

² M. Malekakhlagh, A. Petrescu, & H. E. Türeci. **2017**. *Phys. Rev. Lett.* **119**, 073601.

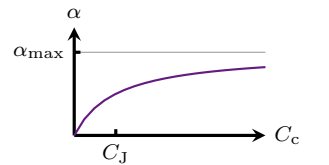


Figure 3.4: The coupling strength as a function of C_c , saturating at α_{\max} when $C_c \rightarrow \infty$.

In this chapter, we have reduced the microscopic model presented by Fig. 3.2, with many various microscopic parameters, to a generic charge-boson Hamiltonian characterized by a simple spectral density (Ohmic with ultraviolet cutoff), and only two independent parameters. The next chapter will clarify the connection with other well-known many-body models from the literature, summarize the main results from these models, and inquire about the importance of the bound coupling strength concerning the apparition of phase transitions in experimental setups simulating the spin-boson system.

4 | Review of impurity models

“Je vais pas vous citer Aristote ... – Qui ça ? – Aristote. Non non, vous connaissez pas, c’est pas grave. – C’est pas celui qui a écrit *La Poétique* ? – Euh ... Si. Si, carrément. – Non, mais je savais, ça. – Mais vous l’avez lue ? – Non, je sais pas lire.”

Astier, *Kaamelott*.

The charge-boson Hamiltonian established from a microscopic model (*cf.* Eq. (3.28)) is an example of an impurity model, where a local degree of freedom is coupled to a field made of many-degrees of freedom¹. It is thus closely related to a whole family of impurity models well known from the literature, especially the spin-boson and the boundary sine-Gordon models. In this chapter, we review these connections, and the main results known on these theoretical neighbors.

Dissipative models were historically introduced to explore the notion of quantum dissipation², which studies how quantum effects such as wavefunction coherence can be lost when a macroscopic number of degrees of freedom interact together. In the thermodynamic limit, the bosonic field — often called the environment in this context — act as a reservoir, which absorbs energy and quantum coherence from the charge qBit without ever giving it back. If the qBit/field interaction is strong enough, a phase transition is encountered, which discriminates between quantum and classical behaviors.

Evidences for these critical phenomena are still hard to find in the laboratory, since *in situ* control of the system parameters is difficult to achieve. Thus an experimental platform that is easily tunable and can display these quantum phase transitions, *i.e.* a simulator, is a critical tool to explore this physics.

4.1 Dissipative environments

The dissipative properties of a macroscopic number of harmonic oscillators linearly coupled to a local degree of freedom, harmonic oscillator, spin or quantum rotor³, has been explored first by Caldeira & Leggett⁴. They were following a pioneering work of Feynman & Vernon⁵. The first take home message of these early studies is that, due to linear coupling, the dynamic of the environment can be exactly eliminated⁶, and replaced by an effective self-interaction of the local degree of freedom. We will show this at equation of motion level. Let’s consider the charge-boson Hamiltonian, denoting the superconducting phase and charge as $\hat{\varphi}$ and \hat{n} :

$$\hat{H} = \frac{E_c}{2} \hat{n}^2 - E_J \cos(\hat{\varphi}) + i\hat{n} \sum_k g_k (\hat{a}_k^\dagger - \hat{a}_k) + \sum_k \omega_k \hat{a}_k^\dagger \hat{a}_k, \quad (4.1)$$

The equation of motion for $\hat{\varphi}$ is provided by Heisenberg’s equation⁷:

$$\dot{\hat{\varphi}} = i[\hat{H}, \hat{\varphi}] = E_c \hat{n} + ig_k (\hat{a}_k^\dagger - \hat{a}_k). \quad (4.2)$$

“I won’t quote Aristotle, but ... – Who ? – You don’t know him, don’t worry – Isn’t he the guy who wrote *Poetics* ? – Well ... yes. Yes he is. – I knew that. – Did you read it ? – No, I don’t know how to read.”

¹ The environment is here bosonic, but examples of fermionic environments are numerous, *e.g.* the Kondo model.

² M. A. Schlosshauer. 2007. *Decoherence*.

³ Equivalent to a charge qBit.

⁴ A. J. Leggett, S. Chakravarty, *et al.* 1987. *Rev. Mod. Phys.* 59, 1.

⁵ R. P. Feynman & F. L. Vernon. 1963. *Ann. Phys.* 24, 118.

⁶ ‘traced out’ when working in density matrix framework, or ‘integrated over’ when dealing with path integrals.

⁷ We again use Einstein’s sum convention in intermediate computations.

The bosonic field equation of motion, in turn, is:

$$\dot{\hat{a}}_k = g_k \hat{n} - i\omega_k \hat{a}_k, \quad \dot{\hat{a}}_k^\dagger = g_k \hat{n} + i\omega_k \hat{a}_k^\dagger. \quad (4.3)$$

By Fourier transform¹, in the frequency domain,

$$\hat{a}_k(\omega) = \frac{ig_k \hat{n}}{\omega - \omega_k}, \quad \hat{a}_k^\dagger(\omega) = \frac{ig_k \hat{n}}{\omega + \omega_k} \quad (4.4)$$

which is plugged back into Eq. (4.2), resulting in

$$-i\omega \hat{\varphi}(\omega) = \left(E_c - \sum_k \frac{2g_k^2 \omega_k}{\omega_k^2 - \omega^2} \right) \hat{n}(\omega). \quad (4.5)$$

This sum is evaluated in the continuum limit, corresponding here to a thermodynamic limit for the bosonic bath, with $J(\omega) = 2\pi\alpha\omega$.

$$\sum_k \frac{2g_k^2 \omega_k}{\omega_k^2 - \omega^2} = 4\alpha \int_0^\infty d\nu \frac{\nu^2}{\nu^2 - \omega^2} = 4\alpha\omega_c + 4\alpha \int_0^\infty d\nu \frac{\omega^2}{\nu^2 - \omega^2}. \quad (4.6)$$

The real part was ultraviolet-divergent, we parametrized it using a cutoff ω_c . It renormalizes the charging energy, $E_c \rightarrow E_c - 4\alpha\omega_c$. The imaginary part is finite when $\omega_c \rightarrow \infty$, but has poles in $\omega = \pm\nu$. We evaluate it by adding a small imaginary part to the frequency $\omega \rightarrow \omega + i\epsilon$, $\epsilon > 0$ ². We then evaluate

$$\int_0^\infty \frac{d\nu}{\nu^2 - (\omega + i\epsilon)^2} = \frac{1}{2\omega} \int_0^\infty \left(\frac{1}{\nu - \omega - i\epsilon} - \frac{1}{\nu + \omega + i\epsilon} \right) d\nu. \quad (4.7)$$

We make use of the Sokhotski-Plemelj formula³

$$\lim_{\epsilon \rightarrow 0^+} \frac{1}{x + i\epsilon} = \text{p.v.} \left(\frac{1}{x} \right) - i\pi\delta(x), \quad (4.8)$$

which holds in the sense of distributions. The first fraction provides

$$\int_0^\infty \frac{d\nu}{\nu - \omega - i\epsilon} = \int_0^\infty \frac{d\nu}{\nu - \omega} + i\pi \int_0^\infty \delta(\nu - \omega) d\nu. \quad (4.9)$$

The real part of the two fractions cancels, and the imaginary parts combine to give

$$\sum_k \frac{2g_k^2 \omega_k}{\omega_k^2 - \omega^2} = -(-i\omega)2\pi\alpha. \quad (4.10)$$

Back to φ equation of motion, since $\dot{\hat{n}} = -E_J \sin \hat{\varphi}$, using an inverse Fourier transform, the full equation of motion is

$$\ddot{\varphi} + \left(E_J E_c + 2\pi\alpha E_J \frac{d}{dt} \right) \sin \varphi = 0 \quad (4.11)$$

This equation of motion is the same as the classical electrokinetic equation of the circuit on Fig. 4.1, where the chain has been replaced by a purely Ohmic resistor of resistance $Z_c = 2\pi\alpha$ (and $C_J \ll C_c$ suppressed)⁴. The damped harmonic oscillator is finally retrieved by $\sin \varphi \simeq \varphi$, with frequency $\omega_0 = \sqrt{E_J E_c}$, and quality factor $Q = Z_0/Z_c$, $Z_0 = \sqrt{E_c/E_J}$. Strong dissipation occurs if $Q \ll 1$, *i.e.* $Z_c \gg Z_0$.

4.2 Spin-boson model

When the superconducting island of Fig. 3.2 circuit is biased in charge, with a resulting charge $n_g = V_g C_g$, the Lagrangian is supplemented with a $-n_g \dot{\phi}_0$ term. In turn, the Hamiltonian form is modified by the substitution $\hat{n}_\ell \rightarrow \hat{n}_\ell + P_\ell n_g$. The change of

¹ The convention is

$$f(t) = \int_{\mathbb{R}} \frac{d\omega}{2\pi} e^{-i\omega t} f(\omega).$$

² This choice of regularization will be made clearer in the context of Green's functions, *cf.* Sec. 8.2.

³ W. Appel. 2007. *Mathematics for Physics and Physicists*.

⁴ This is not to say that we solved the dynamics of the system: Eq. 4.11 still represents a hard problem.

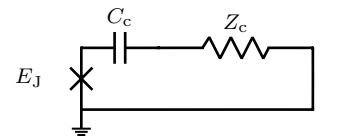


Figure 4.1: An Ohmic bath of oscillators as the environment is equivalent to a Ohmic resistor.

variables performed to isolate the charge degree of freedom is not affected by this new term; the final result is modified by the substitution $\hat{N} \rightarrow \hat{N} + n_g$. The Hamiltonian is then

$$\hat{H} = \frac{E_c}{2}(\hat{n} - n_g)^2 - E_J \cos(\hat{\varphi}) + i(\hat{n} - n_g)g_k(\hat{a}_k^\dagger - \hat{a}_k) + \omega_k \hat{a}_k^\dagger \hat{a}_k. \quad (4.12)$$

Depending on the E_J/E_c ratio, the terminal junction physics is quite different. As already discussed in Sec. 2.1, when $E_J/E_c \ll 1$, the junction is very sensitive to external charge n_g . At $n_g = 1/2$, the charge states $|n = 0\rangle$ and $|n = 1\rangle$ are almost degenerate, while the other charge states are well separated in energy. It is acceptable to truncate the Hilbert space to these states only. If $\hat{\Pi}$ is the projector for the truncation,

$$\hat{\Pi}(\hat{n} - 1/2)\hat{\Pi} = -\hat{\sigma}_z/2 \quad \text{and} \quad \hat{\Pi}(\cos \hat{\varphi})\hat{\Pi} = \hat{\sigma}_x/2. \quad (4.13)$$

The charging energy reduces to a meaningless constant. We absorb the minuses into a redefinition of Pauli matrices¹, and obtain

$$\hat{H} = \frac{E_J}{2}\hat{\sigma}_x + \frac{i}{2}\hat{\sigma}_z g_k(\hat{a}_k^\dagger - \hat{a}_k) + \omega_k \hat{a}_k^\dagger \hat{a}_k. \quad (4.14)$$

This is the famous **spin-boson Hamiltonian**. The two-level approximation is so ubiquitous in quantum physics that it appears in many occasions. One can list many quantum chemistry processes², like the inversion of NH₃ molecule tetrahedron, flavor oscillations of mesons or neutrinos, or small particle tunneling in metals, as applications of the spin-boson model.

The model phenomenology is the following. The two eigenstates of $\hat{\sigma}_z$, often denoted $|\downarrow\rangle$ and $|\uparrow\rangle$, can be pictured as spatial states located at the left and right bottom of a double well. $\hat{\sigma}_x$ is responsible for tunnel effect, a drastic quantum effect which turns the ground state into a superposition of left and right states. When decoupled from the environment, eigenstates are binding and anti-binding orbitals, $(|\uparrow\rangle + |\downarrow\rangle)/\sqrt{2}$ and $(|\uparrow\rangle - |\downarrow\rangle)/\sqrt{2}$, separated by an energy E_J .

The environment interacts *via* $\hat{\sigma}_z$, which means it works against the tunnel effect, and tries to locate the system into one of the two wells. Since the whole system is symmetric under $|\downarrow\rangle \leftrightarrow |\uparrow\rangle$, such a localization would break a symmetry of the Hamiltonian (4.14). Should it happen, a phase transition must separate the localized and delocalized behavior. We can expect the binding/anti-binding energy separation E_J^* ³ to vanish in the localized phase, since left and right orbitals become uncoupled. The situation is summarized on Fig. 4.2.

Silbey-Harris ansatz

When $E_J = 0$, the Hamiltonian (4.14) is exactly solvable. The ground state is degenerate, $|\uparrow\rangle$ or $|\downarrow\rangle$, together with a displaced bosonic vacuum. Let us rewrite the Hamiltonian at $E_J = 0$ in this displaced basis, using the unitary transformation

$$\hat{U} = \exp\left(-\frac{i}{2}\hat{\sigma}_z f_k(\hat{a}_k^\dagger + \hat{a}_k)\right). \quad (4.15)$$

The f_k will be determined in order to diagonalize the problem. One can check that $\hat{U}^\dagger \hat{U} = \hat{1}$. If one solves the spectrum of $\hat{H}' = \hat{U}^\dagger \hat{H} \hat{U}$, by finding its eigenstates $|E'\rangle$, \hat{H} has $|E\rangle = \hat{U}|E'\rangle$ as eigenstates, with same spectrum as \hat{H}' . In the displaced basis,

$$\hat{H}'(E_J = 0) = \omega_k \hat{a}_k^\dagger \hat{a}_k + \frac{i}{2}\hat{\sigma}_z(g_k - \omega_k f_k)(\hat{a}_k^\dagger - \hat{a}_k) + \frac{1}{4}f_k(\omega_k f_k - 2g_k). \quad (4.16)$$

The problem is solved by $f_k = g_k/\omega_k$. The vacuum is then a coherent state.

¹ Since $[\hat{\sigma}_i, \hat{\sigma}_j] = 2i\epsilon_{ijk}\hat{\sigma}_k$, changing the sign of two Pauli matrices preserves the commutation relations.

² R. A. Marcus. **1956**. *J. Chem. Phys.* **24**, 966.

³ $E_J^* < E_J$ according to our current discussion. We will soon compute it.

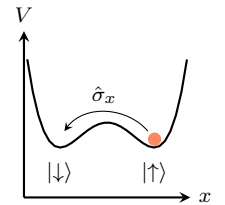


Figure 4.2: Tunneling process of a particle (•) in a double-well potential $V(x)$. $\hat{\sigma}_x$ hops between left and right states, denoted $|\uparrow\rangle$ and $|\downarrow\rangle$.

The case with non-zero tunneling is much richer. Perturbation theory is a natural first attempt to describe the effect of the environment on the system. Let us compute the correction to E_J^* , the energy separation between binding and anti-binding orbitals. The coupling term is treated as a perturbation. At first order, the correction is zero. The second order is given by

$$\Delta E_{\pm} = \frac{1}{4} \sum_k \frac{g_k^2}{E_J \mp \omega_k}, \quad (4.17)$$

where ΔE_{\pm} is the correction to binding and anti-binding energy respectively. We take the continuum limit of bosonic modes and Ohmic dispersion¹, resulting in

$$E_J^* = E_J + \Delta E_+ - \Delta E_- = E_J \left(1 - \alpha \int_0^{\infty} \frac{x^2}{x^2 - 1} dx + O(\alpha^2) \right). \quad (4.18)$$

As expected, the energy gap is reduced by the environment, and the result organizes itself as a perturbation series in α . The integral is divergent in the ultraviolet region. Realistic models come with built-in ultraviolet cutoffs, as we saw in Sec. 3.3, and we expect its value to be relevant to our computation. We do not expect bare perturbation theory to reveal a phase transition anyway, so we will not deal with the integral now: we turn to another method.

Another idea, first implemented by Silbey & Harris², is to build on the interpretation given by the exact diagonalisation we previously performed. We saw that the two left and right states dress with coherent states of the bosonic field, an image often found when dealing with quasi-particles called polarons³. We want to understand how this cloud of displaced bosons change when tunneling is turned on. Let us first express the tunneling term in the displaced basis:

$$\hat{U}^\dagger \hat{\sigma}_x \hat{U} = e^{\frac{i}{2} \hat{\sigma}_z \hat{B}} \hat{\sigma}_x e^{-\frac{i}{2} \hat{\sigma}_z \hat{B}}, \quad (4.19)$$

where $\hat{B} = f_k(\hat{a}_k^\dagger + \hat{a}_k)$, the bosonic part of the displacement, commutes with any $\hat{\sigma}_i$. The displacement formula gives⁴

$$\begin{aligned} e^{\frac{i}{2} \hat{\sigma}_z \hat{B}} \hat{\sigma}_x e^{-\frac{i}{2} \hat{\sigma}_z \hat{B}} &= \hat{\sigma}_x - i\hat{B}[\hat{\sigma}_x, \frac{\hat{\sigma}_z}{2}] + \frac{1}{2!}(-i\hat{B})^2 \left[[\hat{\sigma}_x, \frac{\hat{\sigma}_z}{2}], \frac{\hat{\sigma}_z}{2} \right] + \dots \\ &= \hat{\sigma}_x \left(1 - \frac{1}{2!} \hat{B}^2 + \dots \right) - \hat{\sigma}_y \left(\hat{B} - \frac{1}{3!} \hat{B}^3 + \dots \right) \\ &= \hat{\sigma}_+ e^{i\hat{B}} + \hat{\sigma}_- e^{-i\hat{B}}. \end{aligned} \quad (4.20)$$

Then,

$$\hat{H}' = \frac{E_J}{2} \left(\hat{\sigma}_+ e^{i\hat{B}} + \hat{\sigma}_- e^{-i\hat{B}} \right) + \frac{i}{2} \hat{\sigma}_z (g_k - \omega_k f_k) (\hat{a}_k^\dagger - \hat{a}_k) + \omega_k \hat{a}_k^\dagger \hat{a}_k + \frac{1}{4} f_k (\omega_k f_k - 2g_k). \quad (4.21)$$

There no longer is an exact solution for the f_k ; we can choose them *via* the variational method⁵, that consists in minimizing the ground state expectation energy with respect to the parameters of a family of trial states⁶. The trial state is $\hat{U}|0, -\rangle$, where $|0, \pm\rangle = (|\uparrow\rangle \pm |\downarrow\rangle)/\sqrt{2} \otimes |0_{\text{bosons}}\rangle$. We first compute the ground state expected energy⁷

$$\langle 0, - | \hat{U}^\dagger \hat{H}' \hat{U} | 0, - \rangle = \langle 0, - | \hat{H}' | 0, - \rangle = -\frac{E_J}{2} e^{-f_k f_k / 2} + \frac{1}{4} f_k (\omega_k f_k - g_k), \quad (4.22)$$

And the variational principle translates as

$$\frac{\partial}{\partial f_k} \langle 0, - | \hat{H}' | 0, - \rangle = 0 \quad \Rightarrow \quad f_k = \frac{g_k}{\omega_k + E_J e^{-f_k f_k / 2}}. \quad (4.23)$$

¹ $J(\omega) = 2\pi\alpha\omega$ for the purely Ohmic model, without cutoff.

² R. Silbey & R. A. Harris. **1984**. *J. Chem. Phys.* **80**, 2615.

³ G. D. Mahan. **2000**. *Many-Particle Physics*; M. I. Dykman & E. I. Rashba. **2015**. *Phys. Today* **68**, 10.

⁴

$$\begin{cases} \hat{\sigma}_+ = (\hat{\sigma}_x + i\hat{\sigma}_y)/2 \\ \hat{\sigma}_- = (\hat{\sigma}_x - i\hat{\sigma}_y)/2 \end{cases}$$

are the raising/lowering spin operators.

⁵ M. Le Bellac. **2006**. *Quantum Physics*.

⁶ More advanced versions of the variational principle have been developed, especially at finite temperature, *cf.*

R. Feynman. **1972**. *Statistical Mechanics*; J. da Providencia & C. Fiolhais. **1987**. *Eur. J. Phys.* **8**, 12.

⁷ The expectation value is simple to evaluate with

$$e^{\alpha \hat{a}^\dagger + \alpha \hat{a}} = e^{\alpha^2/2} e^{\alpha \hat{a}^\dagger} e^{\alpha \hat{a}}.$$

This is a self-consistency equation for the f_k . As a matter of fact, several methods lead to this same equation; self-consistent Hartree-Fock approximation would provide a similar result, as well as enforcing that the one excitation spectrum is orthogonal to the ground state, which constitute an avenue to improve this ansatz systematically¹.

The self-consistent equation can be rewritten on the effective energy gap:

$$E_J^* = \langle 0, + | \hat{H}' | 0, + \rangle - \langle 0, - | \hat{H}' | 0, - \rangle = E_J e^{-f \epsilon f \epsilon / 2}, \quad (4.24)$$

Plugging in Eq. (4.23),

$$E_J^* = E_J \exp \left(-\frac{1}{2} \sum_k \frac{g_k^2}{(\omega_k + E_J^*)^2} \right). \quad (4.25)$$

The sum is evaluated in the continuum limit. The cutoff, noted ω_c , is a relevant scale, as we mentioned earlier. We replace the Lorentzian cutoff of Sec. 3.3 by a hard cutoff. One can check this simplification does not change the $\omega_c \gg E_J$ limit. Then,

$$-\frac{1}{2} \sum_k \frac{g_k^2}{(\omega_k + E_J^*)^2} = -\alpha \int_0^{\omega_c/E_J^*} \frac{x}{(1+x)^2} dx = \alpha \left(\frac{\omega_c}{\omega_c + E_J^*} - \ln \left(1 + \frac{\omega_c}{E_J^*} \right) \right). \quad (4.26)$$

Note that Eq. (4.23) recovers the $E_J = 0$ case we previously examined. With this simpler solution for the f_k , the integral of Eq. (4.26) would have been infrared divergent: the self-consistency provides a low energy cutoff that would have been absent of a perturbative approach in E_J . In the limit $\omega_c \gg E_J > E_J^*$ (and $e \simeq 1$), the self-consistent equation can be solved, to

$$E_J^* = E_J \left(\frac{\omega_c}{E_J} \right)^{\frac{\alpha}{\alpha-1}}. \quad (4.27)$$

This renormalized tunneling amplitude E_J^* is plotted in Fig. 4.2. At $\alpha = 1^2$, provided that $\omega_c > E_J$, it vanishes, faster than any power law. A transition occurs, between a delocalized quantum particle that tunnels (even slightly) between $|\uparrow\rangle$ and $|\downarrow\rangle$ states, such that the ground state is (anti)-symmetric, and a localized particle prevented to tunnel due to the strong coupling to the environment. In this phase, the left-right symmetry breaks. This ansatz method to diagnose a transition will be put to work many times in this manuscript, albeit in different contexts. After the transition, our ansatz breaks down, and cannot describe the system anymore: symmetry breaking must be enforced on the ansatz to go on.

The spin-boson model has been studied in much more detail in the litterature. The time-resolved spin dynamics is interesting to analyse, as it changes from under-damped to over-damped at $\alpha = 1/2^3$, a phenomenon reminiscent of classical physics. Other dissipative environment, especially sub-Ohmic ones, also provide different critical phenomena⁴ and spin dynamics, but no superconducting circuit design is known to produce such dispersion relations. We will now return to the full charge-boson problem, to inquire the fate of the localization transition when the two-levels approximation fails.

4.3 Numerical renormalization group

In the derivation of the spin-boson Hamiltonian from the microscopic circuit model, we projected out all charge states other than $|n = 0\rangle$ and $|n = 1\rangle$. We argued that in the $E_J/E_c \ll 1$ limit, these eliminated states are higher in energy, and cannot be accessed.

¹ S. He, L. Duan, & Q.-H. Chen. **2018**. *Phys. Rev. B* **97**, 115157.

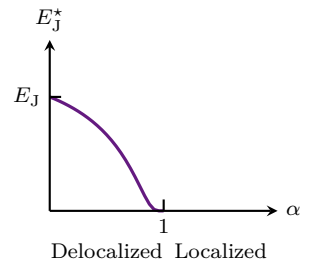


Figure 4.3: Energy gap E_J^* renormalized as a function of the boson field interaction strength α .

² Note that this estimation of the critical α is crude: a *bona fide* perturbative renormalization group analysis would find corrections, *cf*

V. Hakim, A. Muramatsu, & F. Guinea. **1984**. *Phys. Rev. B* **30**, 464.

³ A. J. Leggett, S. Chakravarty, *et al.* **1987**. *Rev. Mod. Phys.* **59**, 1.

⁴ S. Florens, A. Freyn, *et al.* **2011**. *Phys. Rev. B* **84**, 155110.

One could object that in quantum mechanics, classically inaccessible states can significantly contribute to the physics at hands. Heisenberg's undetermination on energy, $\Delta E \Delta t > \hbar/2$, authorizes the system to hop to a forbidden state for a small time, an event called a virtual process. As an example, in QED, virtual photons are responsible for electron-electron scattering. In condensed matter, a famous example is the reduction of the Anderson model to the Kondo model, where virtual transitions of the d-orbital to doubly occupied or empty state provides a mechanism for spin flips¹. The Schieffer-Wolff transformation² allows a perturbative treatment of these virtual processes at the Hamiltonian level.

In the charge-boson Hamiltonian, only $\cos \hat{\varphi}$ allows transitions to higher charge states. At first order, its projection on the spin Hilbert space only produces a $(E_J/2E_c)\hat{1}$ term, that does not change the physics. We then have confidence that the spin-boson analysis stays relevant at small but finite E_J/E_c . We then expect the critical point of the spin-boson localization transition to extend into a vertical critical line in the charge-boson phase diagram, see Fig. 4.3. In the opposite limit, $E_J/E_c \gg 1$, the charge qBit reduces to a harmonic oscillator, as we discussed in Sec. 2.2. In this limit, all charge states are accessible, and are close enough in energy for their discreteness not to be observed anymore. The model is purely harmonic, and no phase transition occurs. In between these two limits, the spin-boson paradigm must lose its relevance: to understand how, we would like to follow the transition line to arbitrary values of E_J/E_c .

To do so, it is possible to extend the Silbey-Harris ansatz to charge states³. We will rather use a numerical method devised to investigate phase transitions of impurity models, the *Numerical renormalization Group*. The method builds on Wilson's understanding of the renormalization group⁴ to avoid a perturbative treatment of the renormalization, and instead follows numerically the renormalization flow. It was first used to study the Kondo problem⁵. It was the first method to describe correctly the strong coupling limit of the model.

The method employs a discretization of bosonic modes on a logarithmic grid, such that $\omega_n = \omega_c/\Lambda^n$, Λ the Wilson parameter usually set to 2. Each mode stands for a whole energy scale. This choice of grid is represented on Fig. 4.5. Starting by high energy modes, the renormalization flow is followed by successively diagonalizing the Hamiltonian of the mode considered coupled to the charge qBit, and then truncating the resulting spectrum and eigenstates to its lowest part. Then, the next to highest mode can be added, diagonalized and truncated. Each step retains the effect of high energy modes on the low-energy physics. The process allows to compute low-energy spectrum as well as vacuum expectation values. To diagnose the phase transition, we need to guess an order parameter to be evaluated from these observables.

At $n_g = 1/2$, by analogy with the spin-boson case, we expect the symmetry ($\hat{n} \rightarrow 1 - \hat{n}$, $\hat{a}_k^\dagger \rightarrow -\hat{a}_k^\dagger$) to break at the localization transition. If the vacuum state preserves the symmetry, $\langle \hat{n} - n_g \rangle = 0$ ⁶, whereas $\langle \hat{n} - n_g \rangle \neq 0$ in the broken phase: this observable plays the role of order parameter.

Since we now consider any E_J/E_c , one must recall the results of Sec. 3.3: E_c , ω_c and α are not independent parameters, but rather obey⁷

$$\alpha < \alpha_{\max} = E_c/\omega_c. \quad (4.28)$$

¹ P. Coleman. **2002**. *AIP Conf. Proc.* **629**, 79.

² J. R. Schieffer & P. A. Wolff. **1966**. *Phys. Rev.* **149**, 491.

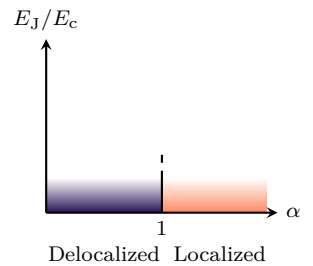


Figure 4.4: The spin-boson localization transition point extends to a transition line at small but finite E_J/E_c .

³ I. Snyman, personal communication.

⁴ K. Wilson & J. Kogut. **1974**. *Phys. Rep.* **12**, 75.

⁵ K. G. Wilson. **1975**. *Rev. Mod. Phys.* **47**, 773.

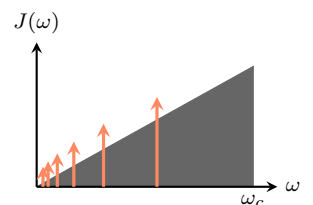


Figure 4.5: (•) Spectral function of the model with hard cutoff at ω_c , and (•) discretised modes on the Wilson grid.

⁶ The average is done over the vacuum.

⁷ This bound was irrelevant in the spin-boson limit where $E_c \rightarrow \infty$.

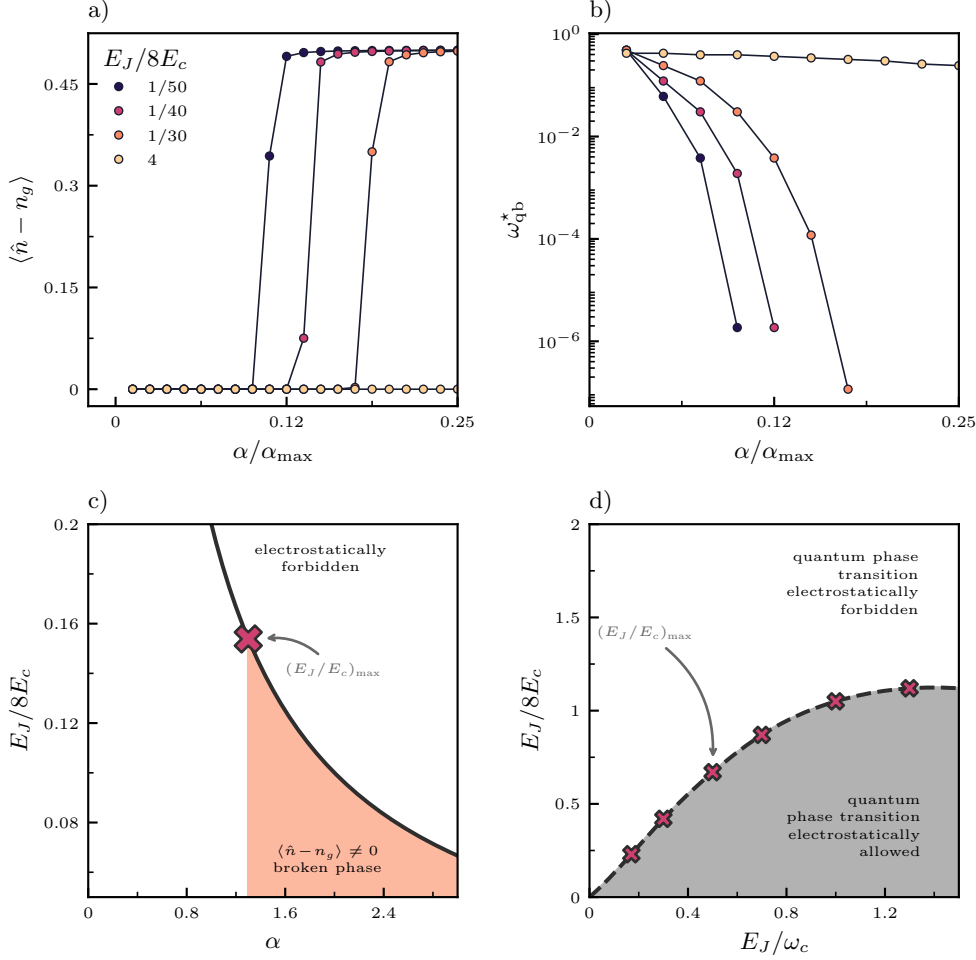


Figure 4.6: **a)** Order parameter as a function of dissipation strength for various E_J/E_c , at $E_J = \omega_c/10$, and degeneracy point $n_g = 1/2$. A critical point is only observed for $E_J/E_c < 1$. **b)** Renormalized qBit frequency for the same parameters, which vanishes at the critical point. **c)** Charge-boson phase diagram at $E_J = \omega_c/10$ showing the localization transition boundary together with the parameter region forbidden by the underlying microscopic circuit. The maximum E_J/E_c still displaying a transition is indicated by a red cross. **d)** Evolution of the maximum E_J/E_c displaying a quantum phase transition with E_J , ruling out the possibility of observing a phase transition when $E_J/E_c \gtrsim 1$.

The results of the NRG simulations¹ are displayed on Fig. 4.6. Panels a) and b) confirms the presence of a localization transition, signaled by a sudden jump of the order parameter from 0 to finite value, while the effective frequency of the qBit, ω_{qb}^* ² collapses to 0. The various curves are plotted at $E_J = \omega_c/10$ fixed, while E_c , and thus α_{\max} , varies. The phase diagram is represented on panel c). The boundary with the region forbidden by the electrostatic constraints of the underlying circuit is also represented. A transition separates the symmetric and broken phase at finite E_J/E_c , confirming the simple Schieffer-Wolff argument, but disappears into the forbidden region when E_J/E_c rises too much. Finally, one could hope to extend the broken domain by varying E_J : on panel d), we see how evolves the lowest E_J/E_c ratio that displays a transition when E_J/ω_c changes: no transition can be seen above $E_J/E_c \simeq 1$.

Finally, the NRG analysis reveals no sharp transition between spin-boson and harmonic oscillator behavior. There is instead a large cross-over region, that cannot be understood simply with either picture. Furthermore, this is the only region accessible to experimental setups, since charge noise become prominent in the low E_J/E_c region. Part II will address the question of building a physically appropriate image of this cross over regime.

¹ K. Kaur, T. Sépulcre, *et al.* **2021**. *Phys. Rev. Lett.* **127**, 237702.

² This quantity is defined by analogy with E_J^* in the spin-boson model.

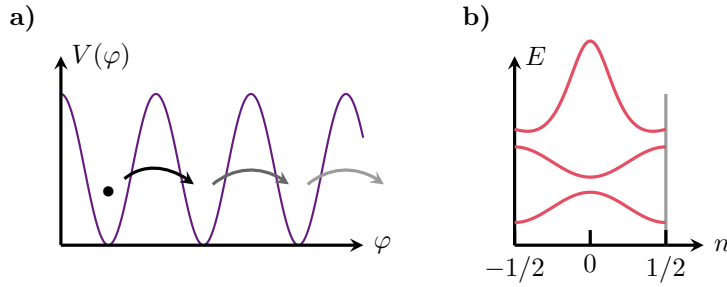


Figure 4.7: Extended phase picture.
a) The Josephson term translates as a periodic potential. Quantum tunneling allows hopping between minima.
b) The Bloch theorem ensures that energies arrange in Bloch bands. In a band, eigenstates are labeled by a quasi-momenta n .

4.4 Extended phase

The charge noise has been invoked many times as the main experimental issue to observe non-trivial many-body effects. As we underlined, it is tightly connected with the compact phase space and the quantification of charge. We can rightfully ask how to get rid of it.

Let us first insist on the different physics at play with compact and extended superconducting phase¹. The difference is also relevant for few degrees of freedom qBits². In the extended case, as represented on Fig. 4.7, the system is a quantum particle moving in a periodic, cosine potential. States localized at φ and $\varphi + 2\pi$ are distinguishable. The Bloch theorem applies, which means that the eigenstates are labeled by a quasi-momentum, n , and the energy levels are arranged in bands. In our conventions, the Brillouin zone extends from $n = -1/2$ to $n = 1/2$. Adding an external n_g parameter only shifts the quasi-momenta, and can be absorbed into a redefinition of n .

In the compact picture, sketched on Fig. 4.8, states $|\varphi\rangle$ and $|\varphi + 2\pi\rangle$ cannot be distinguished: we deal with a quantum rotor³ (or pendulum). The spectrum is discrete, since the boundary conditions on the wavefunction $\psi(\varphi) = \psi(\varphi + 2\pi)e^{i2\pi n_g}$ imposes quantification on its own. The Bloch bands are only retrieved when the external parameter n_g is varied between $n_g = -1/2$ and $n_g = 1/2$. For a fixed n_g , the rest of the Bloch band is inaccessible. Phase compactness is equivalent to quantification of the charge, since the Fourier transform relation between the two reduces to the charge being the Fourier series of the phase. Finally, one should notice that it is not

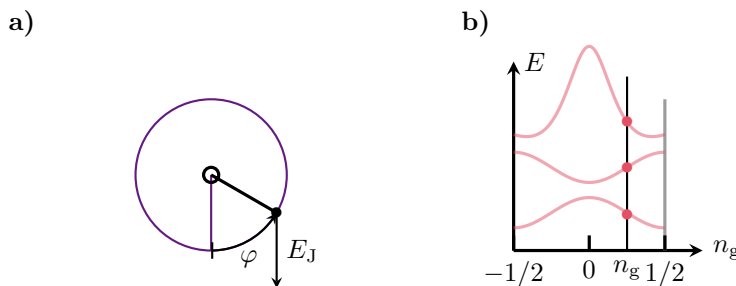


Figure 4.8: Extended phase picture.
a) The Josephson term adds a gravity like term to a quantum pendulum.
b) At fixed n_g , the spectrum is discrete.

possible to discriminate between extended and compact phase when only a Hamiltonian is provided. It is rather a property of the underlying Hilbert space⁴. A compact description is chosen if the energy separation between charge states is pertinent at the energy scale experimentally probed⁵. We now review a few scenarios for phase decompactification, *i.e.*, situations where charge discreteness becomes irrelevant.

¹ G. Schön & A. Zaikin. **1990**. *Phys. Rep.* **198**, 237.
² J. Koch, V. Manucharyan, *et al.* **2009**. *Phys. Rev. Lett.* **103**, 217004.
³ At $E_J = 0$, its eigenstates, called charge states in this manuscript, could as well be called angular momentum states.
⁴ The situation is clearer in path integral formulation. In the compact case, the sum over other trajectories must take into account windings around $[0, 2\pi)$. *cf* Appendix E of G. Schön & A. Zaikin. **1990**. *Phys. Rep.* **198**, 237.
⁵ R.-P. Riwar. **2021**. *SciPost Phys.* **10**, 093.

Flux qBit

A simple solution to get rid of charge noise is to explicitly break the 2π -periodicity of the Hamiltonian, by shunting the superconducting island with an inductor. The resulting circuit is represented on Fig. 4.9. The corresponding Hamiltonian reads

$$\hat{H} = \frac{E_c}{2}(\hat{n} - n_g)^2 - E_J \cos \hat{\varphi} + \frac{1}{2L}(\hat{\varphi} - \Phi/\Phi_0)^2, \quad (4.29)$$

with Φ/Φ_0 the adimensional external magnetic flux piercing the inducting loop. The charge can continuously flow through the inductor. The phase is extended, so that n_g can be eliminated by a gauge transform $\hat{U} = \exp(in_g \hat{\varphi})$. The quantum particle evolves in a potential represented on Fig. 4.10. At $\Phi/\Phi_0 = \pi$, we find once again a symmetrical double well. The left and right eigenstates corresponds here to permanent currents circulating clockwise and anti-clockwise in the inductor loop. The general spectrum of such a device is quite rich beyond this two-level approximation¹. The shielding from offset charge noise came at a price. Φ/Φ_0 is a new parameter to fine tune instead of n_g , that can be noisy: the device is sensitive to flux noise.

A spin-boson simulator based on a superconducting device using a flux qBit has been tested already². The renormalization of Eq. (4.27) has been tested in the delocalized phase.

Orthogonality catastrophe

It is perhaps a trivial observation that at $E_J \gg E_c$, the phase decompactifies. Indeed, in this regime, one can use a harmonic approximation for the Josephson potential, in which case $\langle \hat{\varphi}^2 \rangle = \sqrt{E_c/E_J} \ll 2\pi$ (cf. Sec. 2.2). The phase fluctuations are small compared to the potential period, which means that the boundary conditions are lifted. Conversely, the charge loses its quantification. At the spectrum level, the energy bands flatten, so that the energy does not depend over n_g anymore³.

In this limit, the vanishing of compact effects is linked to the disappearance of overlap (and such, of interference) between neighboring minima. A similar orthogonality catastrophe can be triggered by the environment, as it has been shown in a path integral formalism⁴. Part II will discuss a method to study this orthogonality catastrophe between winding numbers.

Phase freezing

Concerning the complete charge-boson model, the $E_J \gg E_c$ limit is more involved. It is easier to examine it on a transformed Hamiltonian. Using

$$\hat{U} = \exp\left(-i\hat{n} \frac{g_k}{\omega_k} (\hat{a}_k^\dagger - \hat{a}_k)\right) = \exp(-i\hat{n}\hat{B}), \quad (4.30)$$

the Josephson term transforms as

$$\begin{aligned} \hat{U}^\dagger \cos \hat{\varphi} \hat{U} &= \cos \hat{\varphi} \left(1 - \frac{\hat{B}^2}{2!} + \dots\right) - \sin \hat{\varphi} \left(\hat{B} - \frac{\hat{B}^3}{3!} + \dots\right) \\ &= \cos(\hat{\varphi} + \hat{B}). \end{aligned} \quad (4.31)$$

The rest of the Hamiltonian has simpler transforms. Overall, the rotated Hamiltonian is

$$\hat{H}' = \frac{1}{2} \left(E_c - 2g_\ell \frac{g_\ell}{\omega_\ell}\right) (\hat{n} - n_g)^2 - E_J \cos\left(\hat{\varphi} + \frac{g_k}{\omega_k} (\hat{a}_k^\dagger - \hat{a}_k)\right) + \omega_q \hat{a}_q^\dagger \hat{a}_q. \quad (4.32)$$

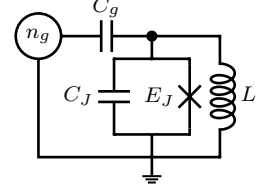


Figure 4.9: The flux qBit electric diagram.

¹ J. Koch, V. Manucharyan, *et al.* **2009**. *Phys. Rev. Lett.* **103**, 217004.

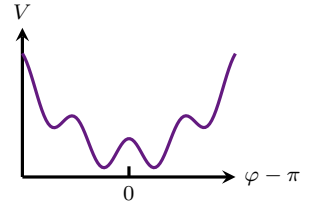


Figure 4.10: Potential from inductor and Josephson term for the flux qBit.

² P. Forn-Díaz, J. J. García-Ripoll, *et al.* **2017**. *Nat. Phys.* **13**, 39.

³ This limit is seen as trivial since, starting from an extended phase, it would correspond to a tight-binding model where the hopping parameter vanishes. There is therefore no difference between compact and extended.

⁴ W. Zwerger, A. T. Dorsey, & M. P. A. Fisher. **1986**. *Phys. Rev. B* **34**, 6518.

The new, effective charging energy is nothing more than the bare charging energy, as we can see from Eq. (3.44): $E_c - 2ge\ell/\omega_\ell = 1/(C_c + C_J)$.

In the $C_c \rightarrow \infty$ limit, the (bare) charging energy vanishes. The $(\hat{\varphi}, \hat{n})$ degree of freedom has no dynamic anymore, it freezes out and can be removed to reach the *boundary sine-Gordon* Hamiltonian¹,

$$\hat{H} = -E_J \cos \left(\sum_k \frac{g_k}{\omega_k} (\hat{a}_k^\dagger + \hat{a}_k) \right) + \sum_k \omega_k \hat{a}_k^\dagger \hat{a}_k. \quad (4.33)$$

Since the charge degree of freedom has disappeared, it seems that the phase compactness (and charge quantization) vanished too. The mechanism is the following: at $C_c \rightarrow \infty$, the coupling capacitance in circuit of Fig. 3.2 is replaced by a wire. The same model will indeed be re-derived from a microscopic circuit using such a galvanic coupling in Part III. The nodes 0 and 1 are then merged, and we indeed lose one degree of freedom. The small superconducting island is wire-connected to the infinite chain, so its charge is not quantized anymore. Upon closer inspection, the full circuit with a finite chain is now a superconducting island. The total charge must then be quantized, but the associated charging energy is much lower. Charge states are not well separated, and we can expect a continuous charge (and extended phase) description to hold.

4.5 Schmid transition

The Hamiltonian (4.33) has been intensively studied in the literature, where it is usually used to describe a dissipative quantum particle in a periodic potential. It is also believed to describe a single Josephson junction, with dissipation provided by normal electron tunneling². The kinetic energy of the particle only appears in the model cutoff, ω_c which is thus supposed finite. It has been shown that this model too displays a quantum phase transition, also leading to the localization, or self-trapping, of the quantum particle at strong dissipation. The phase diagram has been studied at length using renormalization groups analysis³. We will give the most naive version of the argument, but more detailed analysis only confirms the main result⁴. Path integral versions of the argument are common textbook material⁵, but we will rather employ the Schrieffer-Wolff method⁶ to perform a simple *Poor man's scaling* on the model and extract the scaling law.

As already discussed in Sec. 4.3, the Schrieffer-Wolff transformation allows to perturbatively project a Hamiltonian on a low-energy subspace. It fits nicely in the renormalization group analysis, which amounts to determine how the coupling constants of a given Hamiltonian evolves when the energy scale Λ varies. Let's suppose that the procedure has been applied already from ω_c to $\Lambda + \delta\Lambda$, and we want to pursue it down to Λ . We separate the boson modes between low-energy modes, $\omega_k < \Lambda$, and high-energy modes $\Lambda < \omega_k < \Lambda + \delta\Lambda$. The projection of these modes provide a non-vanishing result already at first order, which simplifies greatly the Schrieffer-Wolff approach. We first expand the Josephson term by⁷:

$$\cos \left(\gamma_k (\hat{a}_k^\dagger + \hat{a}_k) \right) = \frac{1}{2} \sum_{\pm} \left(\prod_{k=0}^{\Lambda+\delta\Lambda} e^{\pm i\gamma_k \hat{a}_k^\dagger} \right) \left(\prod_{k=0}^{\Lambda+\delta\Lambda} e^{\pm i\gamma_k \hat{a}_k} \right) \left(\prod_{k=0}^{\Lambda+\delta\Lambda} e^{-\frac{1}{2}\gamma_k^2} \right). \quad (4.34)$$

Then, projected on states of the form $|i\rangle \otimes |0\rangle$, i any state of the low energy oscillators, and $|0\rangle$ the high energy oscillators vacuum,

¹ The name originates from the *sine-Gordon model*, a scalar field obeying the wave equation

$$(\partial_t^2 - c^2 \partial_x^2) \phi + g \sin \phi = 0.$$

It famously hosts soliton solutions, *cf.*

T. Dauxois & M. Peyrard. **2006**. *Physics of Solitons*.

² G. Schön & A. Zaikin. **1990**. *Phys. Rep.* **198**, 237.

³ A. Schmid. **1983**. *Phys. Rev. Lett.* **51**, 1506; S. Bulgadaev. **1984**. *ZhETF Pisma Redaktsiiu*.

⁴ F. Guinea, V. Hakim, & A. Muramatsu. **1985b**. *Phys. Rev. Lett.* **54**, 263.

⁵ N. Nagaosa. **1999**. *Quantum Field Theory in Condensed Matter Physics*; A. Altland & B. D. Simons. **2010**. *Condensed Matter Field Theory*.

⁶ P. Coleman. **2002**. *AIP Conf. Proc.* **629**, 79.

⁷ It will prove itself useful to define $\gamma_k = g_k/\omega_k$ as a shorthand.

$$\langle i | \otimes \langle 0 | \cos \left(\gamma_k (\hat{a}_k^\dagger + \hat{a}_k) \right) | j \rangle \otimes | 0 \rangle = \langle i | \cos \left(\sum_{k=0}^{\Lambda} \gamma_k (\hat{a}_k^\dagger + \hat{a}_k) \right) | j \rangle \exp \left(-\frac{1}{2} \sum_{q=\Lambda}^{\Lambda+\delta\Lambda} \gamma_q^2 \right). \quad (4.35)$$

The last sum is computed in the continuum limit, and evaluates to¹

$$-\frac{1}{2} \sum_{q=\Lambda}^{\Lambda+\delta\Lambda} \gamma_q^2 = -\alpha \int_{\Lambda}^{\Lambda+\delta\Lambda} \frac{d\omega}{\omega} = -\alpha \ln \left(1 + \frac{\delta\Lambda}{\Lambda} \right) \quad (4.36)$$

We see that the low energy Hamiltonian will take the same form as the original one, with E_J renormalized to

$$E_J(\Lambda) = E_J(\Lambda + \delta\Lambda) e^{-\alpha\delta\Lambda/\Lambda} \Rightarrow E_J(\Lambda + \delta\Lambda) = E_J(\Lambda) \left(1 + \alpha \frac{\delta\Lambda}{\Lambda} + \dots \right) \quad (4.37)$$

We form the adimensional ratio $e_J = E_J/\Lambda$, and compute the differential equation governing its evolution when the cutoff is changed.

$$\begin{aligned} \frac{de_J}{d\ln \Lambda} &= \Lambda \frac{dE_J}{d\Lambda} = \frac{\Lambda}{\delta\Lambda} \left(\frac{E_J(\Lambda + \delta\Lambda)}{\Lambda + \delta\Lambda} - \frac{E_J(\Lambda)}{\Lambda} \right) \\ \Rightarrow \frac{de_J}{d\ln \Lambda} &= (\alpha - 1)e_J = \beta(e_J). \end{aligned} \quad (4.38)$$

The right-hand side of this last equation is the β -function of the renormalization flow, computed perturbatively at first order in the regime of small e_J . The corresponding flow is represented on Fig. 4.11.

At $\alpha < 1$, $\beta < 0$, so e_J increases when the cutoff is lowered, *i.e.* along the renormalization flow. The potential becomes more and more important, and the quantum particle comes to rest in one of the minima of the potential. The superconducting phase is localized, charge is delocalized, so this phase could be labeled as superconducting. This sign of β -function is associated with *asymptotic freedom*, since e_J is small at high energy, validating perturbation expansions for high-energy processes only².

If $\alpha > 1$, the situation is reversed: at low energies, the effect of the potential vanishes, leaving the quantum particle extended over many minima: superconducting phase is delocalized, charge is localized, so this phase is insulating. Between the two, a quantum transition occurs at $\alpha = 1$.

The flow equation can be integrated:

$$E_J(\Lambda) = E_J \left(\frac{\Lambda}{\omega_c} \right)^\alpha. \quad (4.39)$$

The cutoff has been reintroduced by asking that the running constant $E_J(\Lambda)$ equates the bare value E_J at the beginning of the flow, $\Lambda = \omega_c$ ³. A characteristic energy scale emerges as the one below which perturbation theory fails. Let us call it E_J^* . It verifies

$$e_J(E_J^*) = 1 \Rightarrow E_J^* = E_J \left(\frac{\omega_c}{E_J} \right)^{\frac{\alpha}{\alpha-1}}. \quad (4.40)$$

This equation is reminiscent of the spin-boson scaling law, Eq. 4.27, even if the context is quite different.

¹ Consistency asks to keep the same definition for $2\pi\alpha = Z_c/R_q = Z_c$, but the literature often uses $1/\alpha$ as the coupling strength.

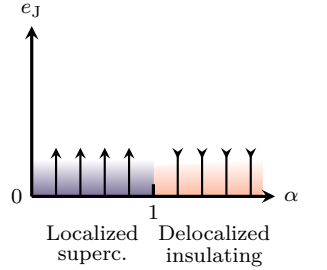


Figure 4.11: renormalization flow indicated by arrows obtained by perturbation in the $e_J \rightarrow 0$ region.

² The Kondo model and QCD are in the same situation, while QED is rather perturbative at small energy.

³ With a more realistic cutoff scheme, like the Lorentzian cutoff of Sec. 3.3, the flow equation is modified, and the flow starts at $\Lambda = \infty$.

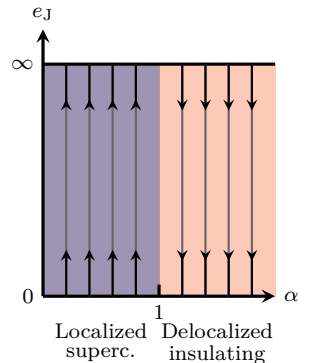


Figure 4.12: The full phase diagram of the Schmid transition.

Half of the work only has yet been done. To complete the phase diagram, it is possible to perform a perturbative renormalization group analysis at $e_J \rightarrow \infty$, the strong coupling limit. A duality indeed connects the weak and strong coupling cases. This can be done in a path integral formalism¹ and instanton techniques, or with a tight-binding approximation². The resulting phase diagram is presented on Fig. 4.12. The flow and the boundary has been demonstrated to stay straight between the two known limit of strong and weak coupling.

The quantum particle dynamic has also been studied in both phases³, and at zero and finite temperature. Even if the Schmid model is theoretically well known, experimental evidences for the phase transition are still elusive. In Part III, we will detail an experimental superconducting circuit which displays many-body physics at intermediate coupling in the superconducting phase. Especially, the scaling law (4.40) will be re-derived using a diagrammatic expansion method, taking into account higher order corrections, finite temperature and detailed microscopic model.

We now have a good grasp on the several regimes the charge-boson model can display. This model was introduced to better model Josephson-based impurity simulators, using a general derivation that could be applied to a large class of circuits beyond the one we focus on. Clearly, we only provided an hand-waving picture of the compact superconducting phase role. The next part will elaborate on the topic, with two questions in mind: how to quantitatively capture its effect in the crossover region $E_J \simeq E_c$ in a simple formalism, and how to describe its fading when the boundary phase freezes out and the model reduces to boundary sine-Gordon. The last part of the manuscript focuses on this regime, shielded from charge noise effects, which has been effectively simulated in the laboratory. We will inquire about many-body physics hallmarks that can be witnessed in these experiments.

¹ N. Nagaosa. 1999. *Quantum Field Theory in Condensed Matter Physics*.

² F. Guinea, V. Hakim, & A. Muramatsu. 1985b. *Phys. Rev. Lett.* 54, 263.

³ M. P. A. Fisher & W. Zwerger. 1985. *Phys. Rev. B* 32, 6190; C. Aslangul, N. Pottier, & D. Saint-James. 1985. *Phys. Lett. A* 111, 175.

Part II

Physics of compact phases

5 | A compact ansatz

“I’m tired of running in circles.”

Bob-Wacksberg, *Bojack Horseman*.

In the previous section, the isolated Josephson junction modeled by

$$\hat{H} = \frac{E_c}{2} (\hat{n} - n_g)^2 - E_J \cos(\hat{\varphi}), \quad (5.1)$$

has proven its deceptive simplicity hides many interesting physical regimes. We especially separated two regions, an harmonic oscillator behavior at $E_J/E_c \gg 1$, and a charge qBit region at $E_J/E_c \ll 1$, where phase compactness drives the physics and where the spectrum is strongly dependent on n_g . The crossover in between is difficult to capture with simple approximations, while these two approximate descriptions quickly lose relevance when $E_J/E_c \sim 1$. Still, this intermediate region contains the transmon regime, one of the most common superconducting qBit designs¹. Its fine understanding is thus important, to guide many-body regime experiments as well as to provide understanding of the dissipative properties of qBit designs.

When dealing with an isolated junction, this intermediate regime is of course well described by the analytic solution to the Schrödinger equation obtained using Mathieu functions. Still, this method cannot hold when more complicated systems are considered, involving several junctions or many degrees of freedom, as we did when building the charge-boson model in Part I of this manuscript.

The main difficulty when devising an approximation scheme in the intermediate regime is the contradiction between the quadratic approximation, that is the starting point of perturbation theory around the cosine potential minimum, and the periodicity of the wavefunction. We propose to circumvent this difficulty by introducing a wavefunction ansatz², that preserves this property by construction. It serves at a starting point for an optimization procedure, very similar to the Silbey-Harris ansatz optimization of Sec. 4.2 and to the self-consistent harmonic approximation we will employ in Sec. 9.2. This chapter constructs the ansatz on the isolated junction case, where exact results provide simple benchmarks. Chap. 6 then applies it to the many-body situation of the charge-boson Hamiltonian detailed in Sec. 3.2. Finally, Chap. 7 will propose some extensions of this theoretical tool.

5.1 Periodic wave-function

Let us call \hat{H}_0 the quadratic approximation of the isolated junction Hamiltonian. It corresponds to an LC-oscillator³,

$$\hat{H}_0 = \frac{E_c}{2} \hat{n}^2 + \frac{E_J}{2} \hat{\varphi}^2 = \omega_0 (\hat{a}^\dagger \hat{a} + 1/2). \quad (5.2)$$

¹ J. Koch, T. M. Yu, *et al.* **2007**. *Phys. Rev. A* **76**, 042319.

² K. Kaur, T. Sépulcre, *et al.* **2021**. *Phys. Rev. Lett.* **127**, 237702.

³ As a reminder,

$$\begin{cases} \hat{\varphi} = 1/\sqrt{2y}(\hat{a}^\dagger + \hat{a}) \\ \hat{n} = i\sqrt{y/2}(\hat{a}^\dagger - \hat{a}) \end{cases} .$$

$\omega_0 = \sqrt{E_J E_c}$,
and $y = \sqrt{E_J/E_c} = 1/Z$ is the oscillator admittance.

Its eigenstates are the Fock states $|i\rangle$ ¹. $|0\rangle$, the ground state, is Gaussian. Indeed, when computing its wavefunction ψ_0 , we obtain

$$\langle\varphi|\hat{n}|0\rangle = iy\langle\varphi|\hat{\phi}|0\rangle = iy\varphi\psi_0(\varphi) = -i\frac{d}{d\varphi}\psi_0(\varphi). \quad (5.3)$$

Solving this differential equation provides

$$\psi_0(\varphi) = (y/\pi)^{1/4}e^{-\frac{y}{2}\varphi^2}, \quad (5.4)$$

with normalization to unity. Note that we use mainly the admittance $y = 1/Z$ in this part, since it is an increasing function of the E_J/E_c ratio. This wavefunction is plotted on Fig. 5.1. 2π -periodicity can be enforced by summing the same wavefunction, displaced by $2\pi w$, with $w \in \mathbb{Z}$. Such a displacement is provided by the operator $\hat{O} = \sum_{w \in \mathbb{Z}} \exp(i2\pi\hat{n}w)$. The ground state periodized wavefunction is then

$$\psi_0^\circ(\varphi) = \langle\varphi|\hat{O}|0\rangle = \sum_{w \in \mathbb{Z}} \int_{\mathbb{R}} d\theta \langle\varphi|e^{i2\pi\hat{n}w}|\theta\rangle\langle\theta|0\rangle = \sum_{w \in \mathbb{Z}} \psi_0(\varphi - 2\pi w). \quad (5.5)$$

The resulting compact ansatz for the ground state wavefunction is plotted on Fig. 5.2. It is indeed periodic. Interestingly, it seems to converge to a plane wave with periodic boundary conditions, which is indeed the eigenstate of the system in the charge qBit limit. Another expression for this wavefunction can be reached *via* Fourier series relation. Setting aside the normalization factor for now, we evaluate the Fourier transform

$$\psi_0^\circ(\varphi) = \frac{1}{2\pi} \int_{\mathbb{R}} dk a(k)e^{-ik\varphi} \quad \text{where} \quad a(k) = \int_{\mathbb{R}} d\varphi e^{in\varphi} \psi_0^\circ(\varphi). \quad (5.6)$$

Plugging in the result of Eq. (5.5), we use Gaussian integration² and Poisson's summation formula³, we obtain

$$\psi_0^\circ(\varphi) \propto \sum_{n \in \mathbb{Z}} e^{-n^2/(2y)} e^{-in\varphi} = \vartheta\left(2\pi\varphi; \frac{i}{2\pi y}\right). \quad (5.7)$$

The last equation made connection with Jacobi's ϑ function. This special function is known to be defined over the whole complex plane, which confirms that the infinite sum is convergent for any y and φ . Moreover, we will sometime derive duality relations linking $y \leftrightarrow 1/y$ formulae that could be seen as a special case of Jacobi's identity. Jacobi's ϑ functions already appeared in the closely related context of coherent states on a circle⁴.

The explicit expression is quite rich in itself, since the sum can be interpreted as a sum over charge states, which are plane waves in phase representation. When $y \rightarrow 0$, only the $n = 0$ state contributes to the ground state, thus retrieving that the ground state of the charge qBit is a pure charge state. Since the ansatz is constructed to capture the harmonic limit, it interpolates between high and low E_J/E_c regimes. Following this interpretation, we called the dummy variable n , since it represent the discrete charge levels, whereas sums in phase domain are performed over a winding number, w , a notation that comes from path integrals over the circle⁵.

Normalization

The last expression emphasizes a norm problem in the ansatz. Since it is expressed as a sum over plane waves, its norm is infinite, even if it is supposed to describe a bound state. In fact, there is no point in defining the wavefunction over \mathbb{R} , since it should

¹ Not to be confused with charge stated, denoted $|n\rangle$ in Part. I. In this part, Fock states are implied, unless explicitly stated otherwise.

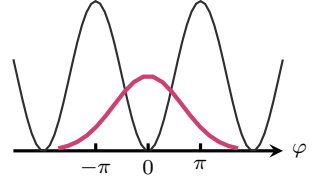


Figure 5.1:

- (●) : Gaussian wave-packet, plotted for $E_J/E_c = 0.5$.
- (●) : Josephson potential.

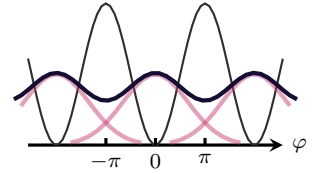


Figure 5.2:

- (●) : Displaced Gaussian wave-packets, plotted for $E_J/E_c = 0.5$.
- (●) : The compact ansatz, obtained by sum over displaced wave-packets.
- (●) : Josephson potential.

² As a reminder,

$$\int_{\mathbb{R}} dx e^{-ax^2+bx} = \sqrt{\frac{\pi}{a}} e^{\frac{b^2}{4a}}.$$

³ In the sense of distributions,

$$\sum_{w \in \mathbb{Z}} e^{i2\pi wn} = \sum_{w \in \mathbb{Z}} \delta(w - n).$$

⁴ K. Kowalski, J. Rembielinski, & L. C. Papaloucas. **1996**. *J. Phys. A: Math. Gen.* **29**, 4149; J. A. González & M. A. del Olmo. **1998**. *J. Phys. A: Math. Gen.* **31**, 8841.

⁵ L. S. Schulman. **2012**. *Techniques and Applications of Path Integration*.

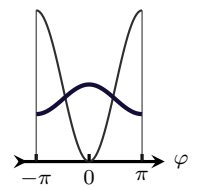


Figure 5.3: To normalize properly the wavefunction, it is restricted to the interval $(-\pi, \pi]$.

only take values over $(-\pi, \pi]$. In that spirit, we simply restrict the wavefunction over this interval, as represented on Fig. 5.3. Its norm is then evaluated using Parseval's identity,

$$\int_0^{2\pi} d\varphi |\psi_0^\circ|^2 = \sum_{n \in \mathbb{Z}} e^{-n^2/y}. \quad (5.8)$$

In an algebraic language, the state norm would be

$$\langle 0|\hat{\mathcal{O}}^\dagger \hat{\mathcal{O}}|0\rangle = \sum_{v,w \in \mathbb{Z}} \langle 0|e^{i2\pi(v-w)}|0\rangle = \sum_{n \in \mathbb{Z}} \langle 0|e^{i2\pi n}|0\rangle \left(\sum_{m \in \mathbb{Z}} 1 \right). \quad (5.9)$$

Dropping the infinite, constant factor is equivalent to restrict the phase to $(-\pi, \pi]$. As a rule, every time an expectation value of the form $\langle i|\hat{\mathcal{O}}^\dagger \hat{A} \hat{\mathcal{O}}|j\rangle$ presents itself, we distinguish two cases. Either $[\hat{\mathcal{O}}, \hat{A}] = 0$; \hat{A} is said to be 2π -periodic. We commute \hat{A} and $\hat{\mathcal{O}}$, rearrange the sum over winding numbers and drop the infinite factor, so only $\langle i|\hat{A} \hat{\mathcal{O}}|j\rangle$ is left to evaluate. If \hat{A} is not periodic, its restriction to the circle is not well defined. If the quantity must be computed nonetheless, the commutator must be added, and the restriction to $(-\pi, \pi]$ done explicitly.

Aharonov-Casher phases

Up until now, we have set the charge offset n_g aside. In the harmonic oscillator limit, It has indeed no effect on the physics. To see this, let's consider the Hamiltonian

$$\hat{H}_0(n_g) = \frac{E_c}{2} (\hat{n} - n_g)^2 + \frac{E_J}{2} \hat{\varphi}^2. \quad (5.10)$$

We move to the rotated basis given by the gauge transform $\hat{U} = e^{in_g \hat{\varphi}}$:

$$\hat{H}'_0(n_g) = \hat{U}^\dagger \hat{H}_0(n_g) \hat{U} = \hat{H}_0(0). \quad (5.11)$$

We know right away that n_g does not change the spectrum of \hat{H}_0 , it is simply gauged away. Now, if the system is restricted to the circle, the situation is different, since the gauge transform also changes the boundary conditions. If $\psi(\varphi)$ is an eigenwavefunction, the corresponding eigenvalue problem derived from the Schrödinger equation writes

$$\frac{E_c}{2} \left(-i \frac{d}{d\varphi} - n_g \right)^2 \psi(\varphi) + V(\varphi) \psi(\varphi) = E \psi(\varphi), \quad (5.12)$$

valid for any potential $V(\varphi)$. The gauge transformed wave function is $\Psi(\varphi) = \exp(-in_g \varphi) \psi(\varphi)$, which obeys

$$-\frac{E_c}{2} \frac{d^2 \Psi}{d\varphi^2} + V(\varphi) \Psi(\varphi) = E \Psi(\varphi), \quad (5.13)$$

and the boundary condition is now

$$\psi(\varphi) = \psi(\varphi + 2\pi) \quad \Rightarrow \quad \Psi(\varphi) = \Psi(\varphi + 2\pi) e^{i2\pi n_g}. \quad (5.14)$$

The effect of these new boundary conditions for $n_g = 0$ are represented on Fig. 5.4, and Fig. 5.5 for $n_g = 1/2$, both in the $V = 0$ case. From here, we can recover the spectrum of the charge qBit as discussed in Sec. 2.1, and represented on Fig. 2.2.

We can now apply compactification on a gauge transformed state:

$$\hat{\mathcal{O}} \hat{U} |\psi\rangle = \sum_{w \in \mathbb{Z}} e^{i2\pi w \hat{n}} e^{in_g \hat{\varphi}} |\psi\rangle = e^{in_g \hat{\varphi}} \sum_{w \in \mathbb{Z}} e^{i2\pi w (\hat{n} - n_g)} |\psi\rangle, \quad (5.15)$$

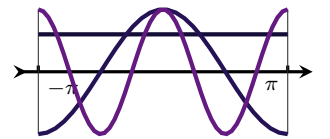


Figure 5.4: First eigenstates at $n_g = 0$ and $y = 0$.

(●) : Ground state,
(●) : 1st and 2nd excited states,
(●) : 3rd and 4th excited states.

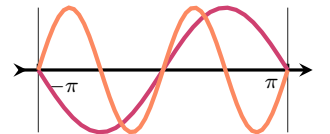


Figure 5.5: First eigenstates at $n_g = 1/2$ and $y = 0$.

(●) : two degenerate ground states,
(●) : 1st and 2nd excited states.

such that any expectation value over gauge transformed states assumes the form

$$\langle i|\hat{U}^\dagger\hat{\mathcal{O}}\hat{A}\hat{\mathcal{O}}\hat{U}|j\rangle = \langle i|\left(\sum_{w\in\mathbb{Z}}e^{i2\pi w(\hat{n}-n_g)}\right)\hat{A}'\left(\sum_{w\in\mathbb{Z}}e^{i2\pi w(\hat{n}-n_g)}\right)|j\rangle. \quad (5.16)$$

with \hat{A}' the gauge transformed of \hat{A} . We re-define the compactification operator to include the n_g phase factor, such that the expectation value of \hat{A} is simply $\langle i|\hat{A}'\hat{\mathcal{O}}|j\rangle$, provided that \hat{A} is 2π -periodic.

We illustrate the effect of n_g by computing the ground state ansatz norm:

$$\langle 0|\hat{\mathcal{O}}|0\rangle = \sum_{w\in\mathbb{Z}}e^{-i2\pi wn_g}\langle 0|e^{-2\pi w(\hat{a}^\dagger-\hat{a})\sqrt{y/2}}|0\rangle = \sum_{w\in\mathbb{Z}}e^{-y\pi^2 w^2-i2\pi wn_g}. \quad (5.17)$$

We, again, recognize Jacobi's ϑ function, which indicates one can reach a dual $y \leftrightarrow 1/y$ expression. We express the Gaussian weight as the result of a Gaussian integral¹. The sum over winding numbers is transformed using Poisson's summation formula to reach

$$\langle 0|\hat{\mathcal{O}}|0\rangle = \frac{1}{\sqrt{\pi y}}\sum_{n\in\mathbb{Z}}e^{-\frac{1}{y}(n-n_g)^2}. \quad (5.18)$$

The interpretation in terms of charge states is again clear: the charge n is displaced by the charge offset n_g .

The charge offset being a gauge parameter, we can see its influence on a non simply connected set as the circle as a close relative to the Aharonov-Bohm effect, the Aharonov-Casher effect. It has been experimentally demonstrated² with a charge qBit, by measuring the periodicity of the spectrum with respect to n_g .

5.2 Transmon regime

A first application of the ansatz is to recover the first excited levels of the isolated junction. Since we aim at describing the crossover region $y \simeq 1$, we should especially be able to recover the characteristics of the transmon qBit. This device is a Josephson junction shunted by a large capacitor, which allows to tune the E_J/E_c ratio around 10 to 100. Here, the anharmonicity is quite weak, but vanishes slowly, following a weak power law³, while the charge dispersion vanishes exponentially. Therefore, there is a sweet spot at intermediate E_J/E_c , where anharmonicity is strong enough to operate the system as a qBit, at least at short times, and where the charge noise is suppressed.

To estimate anharmonicity, we must assess the energy of the three first levels. We estimate the energy by computing the Hamiltonian expectation value. We first need to express the wavefunction of the N^{th} level of the harmonic oscillator. It is written out with Hermite polynomials denoted H_N ,

$$\psi_N(\varphi) = \left(\frac{y}{\pi}\right)^{1/4} H_N(\sqrt{y}\varphi)e^{-\frac{y}{2}\varphi^2} \quad \text{and} \quad \psi_N(n) = H_N\left(\frac{n}{\sqrt{y}}\right)e^{-\frac{1}{2y}n^2}. \quad (5.19)$$

The second result is reached by Fourier transform of the first. The Hamiltonian expectation value expand as

$$\frac{\langle N|\hat{H}'_0\hat{\mathcal{O}}|N\rangle}{\langle N|\hat{\mathcal{O}}|N\rangle} = \frac{E_c}{2}\frac{\langle N|\hat{n}^2\hat{\mathcal{O}}|N\rangle}{\langle N|\hat{\mathcal{O}}|N\rangle} - E_J\frac{\langle N|\cos\hat{\varphi}|N\rangle}{\langle N|\hat{\mathcal{O}}|N\rangle}. \quad (5.20)$$

Note that we indeed compute the average of the gauge transformed Hamiltonian, with no explicit n_g dependence, and that both terms are 2π -periodic.

¹ Exactly,

$$e^{-y\pi^2 w^2} = \frac{1}{\sqrt{y\pi}}\int_{\mathbb{R}}e^{-\frac{x^2}{y}+i2\pi wx}dx.$$

² M. T. Bell, W. Zhang, *et al.* **2016**. *Phys. Rev. Lett.* **116**, 107002.

³ J. Koch, T. M. Yu, *et al.* **2007**. *Phys. Rev. A* **76**, 042319.

The expectation values are reached by inserting the identity¹

$$\langle N | \hat{\mathcal{O}} | N \rangle = \sum_{w \in \mathbb{Z}} \int_{\mathbb{R}} dn e^{i2\pi w(n-n_g)} |\langle n | N \rangle|^2 = \sum_{n \in \mathbb{Z}} |\psi_N(n - n_g)|^2, \quad (5.21)$$

where $|N\rangle$ denotes a Fock state. Similarly,

$$\langle N | \hat{n}^2 \hat{\mathcal{O}} | N \rangle = \sum_{n \in \mathbb{Z}} (n - n_g)^2 |\psi_N(n - n_g)|^2. \quad (5.22)$$

Finally, the expectation value of $\cos \hat{\varphi}$ is computed using the displacement relation, $\exp(\pm i\hat{\varphi})|n\rangle = |n \pm 1\rangle$:

$$\begin{aligned} \langle N | \cos \hat{\varphi} | N \rangle &= \sum_{n \in \mathbb{Z}} \text{Re} (\psi_N(n - n_g) \bar{\psi}_N(n - n_g + 1)) \\ &= \sum_{n \in \mathbb{Z}} \psi_N(n - n_g) \psi_N(n - n_g + 1). \end{aligned} \quad (5.23)$$

The resulting energy estimates are represented as functions of admittance and charge offset on Fig. 5.6 and Fig. 5.7 respectively. By comparison to the exact result, we see that the harmonic oscillator levels are well described in the $y \rightarrow \infty$ region. In the intermediate, $y \sim 1$ region, only qualitative agreement is obtained, with some numerical discrepancy between the exact result and the ansatz. The result can be refined by variational principle. While the two limits $y \rightarrow \infty$ and $y \rightarrow 0$ seem correct for levels 0 and 1, starting at level 2, the ansatz fails in the $y \rightarrow 0$ limit.

Compact self-consistent harmonic approximation

As we advertised in the chapter introduction, the ansatz can be improved by variational principle, very much like the Silbey-Harris ansatz exposed in Sec. 4.2. Once again, the most natural parameter to optimize is the E_J parameter of the quadratic approximation, since we expect that when the phase starts to explore the cosine potential, the effective stiffness of the potential will diminish.

We devise a family of ansatz wavefunctions for the ground state as the compactified vacuum wavefunctions of the quadratic approximation

$$\hat{H}_0(E_J^*) = \frac{E_c}{2} (\hat{n} - n_g)^2 + \frac{E_J^*}{2} \hat{\varphi}^2 \quad (5.24)$$

This corresponds to the wavefunction computed at Eq. (5.5) where $E_J \rightarrow E_J^*$ is a variational parameter. By theorem, the true ground state has the smallest energy expectation value of the Hilbert space, so we assume that finding the smallest energy expectation value of the ansatz family is a correct approximation for the true ground state. We minimize the function

$$\frac{E(E_J^*)}{\omega_0} = \frac{1}{2y} \frac{\sum_{n \in \mathbb{Z}} (n - n_g)^2 e^{-\frac{1}{y^*} (n - n_g)^2}}{\sum_{n \in \mathbb{Z}} e^{-\frac{1}{y^*} (n - n_g)^2}} - y e^{-\frac{1}{4y^*}} \frac{\sum_{n \in \mathbb{Z}} e^{-\frac{1}{y^*} (n - n_g + 1/2)^2}}{\sum_{n \in \mathbb{Z}} e^{-\frac{1}{y^*} (n - n_g)^2}}. \quad (5.25)$$

with respect to $y^* = \sqrt{E_J^*/E_c}$. This process would be tedious to perform by hand, so we resort to a numerical minimization routine. Since we only have one parameter to optimize, this numerical technique is simple, stable and computationally efficient.

Excited levels

The variational principle is most often applied to ground state computations. Yet, if the system displays discrete, well separated levels, they can be accessed too². The

¹ $\hat{\mathcal{O}}$ operator already enforces compactness: all other operators are defined on \mathbb{R} , such that

$$\hat{1} = \int_{\mathbb{R}} dn |n\rangle \langle n|.$$

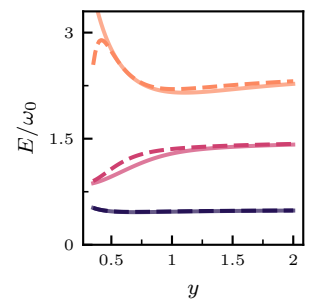


Figure 5.6: (●) Ground state, (●) first and (●) second excited levels energy for $n_g = 0.5$ as a function of y . (---) ansatz, (—) exact result.

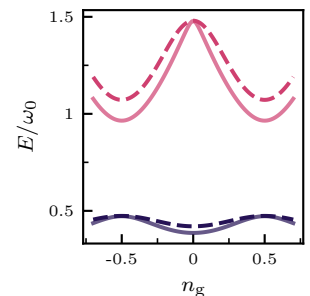


Figure 5.7: (●) Ground state and (●) first excited level energy for admittance $y = 0.5$ as a function of n_g . (---) ansatz, (—) exact result.

² M. Le Bellac. 2006. *Quantum Physics*.

method consists in finding first the variational ground state. We then project it out of the search space. Indeed, the true spectrum verifies $\langle g|e_1\rangle = 0$, for $|g\rangle = |e_0\rangle$ the ground state and $|e_1\rangle$ the first excited level. Furthermore, this prevents the minimization algorithm to retrieve the ground state while looking for $|e_1\rangle$. The same constrained minimization process can be iterated to find higher and higher excited states, imposing, when looking for state $|e_i\rangle$, that $\langle e_i|e_j\rangle = 0 \quad \forall j < i$.

In our context, this procedure will provide different E_j^* for each excited level. Indeed, since excited states explore larger regions of the cosine potential, we expect a stronger renormalization of the potential. This is reminiscent of the renormalization group approach, where coupling parameter renormalization depends on the energy scale.

Energy levels computed with this optimization method are presented on Fig. 5.8 and Fig. 5.9 for admittance and charge offset dependence respectively. There is excellent agreement between the exact result and the optimized ansatz, in the whole y and n_g range. The discrepancy rises to a few percents in intermediate regions, $y \sim 1$ and $n_g \sim 1/4$. The ground state is best described, with rising discrepancy for higher levels. The issue concerning the 2nd excited level at $y \rightarrow 0$ has been fixed by the orthonormalization procedure.

On this result, we recognize the different regimes and behaviors of the isolated junction, especially the evenly spaced levels of the harmonic oscillator when $y \rightarrow \infty$, and the strong anharmonicity that appears in the $y \rightarrow 0$ region. Fig. 5.9 is similar to the charge qBit spectrum on Fig. 2.2, with band dispersion and a level splitting at $n_g = 1/2$. No other approximation scheme, neither perturbation theory, nor non-compact self-consistent approximation, or Brillouin-Kramers-Wentzel approximation, produce such accurate results for all regions of parameter space.

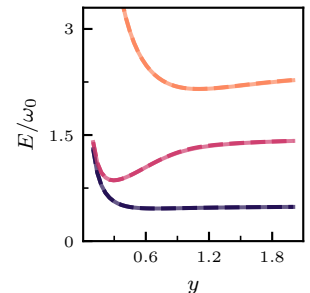


Figure 5.8: (●) Ground state, (●) first and (●) second excited levels energy for $n_g = 0.5$ as a function of y . (---) optimized ansatz, (—) exact result.

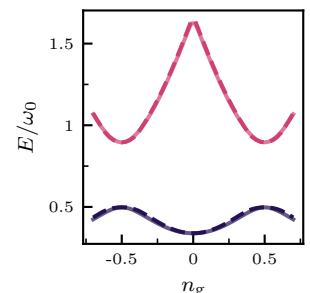


Figure 5.9: (●) Ground state and (●) first excited level energy for admittance $y = 0.4$ as a function of n_g . (---) optimized ansatz, (—) exact result.

6 | Application to charge-boson

And, so I dreamed that if I were clever, I would find a formula for the amplitude of a path that was beautiful and simple [...]. I have never succeeded in that either. But, I did want to mention some of the unsuccessful things on which I spent almost as much effort, as on the things that did work.

Feynman, *Nobel Lecture*.

We apply the compact ansatz method developed in the last chapter to the many-body charge-boson Hamiltonian we discussed in Sec. 3.2. Some results were already obtained by mapping its low E_J/E_c region on the spin-boson model in Sec. 4.2, and by means of the numerical renormalization group (NRG) in Sec. 4.3. We used it to put in evidence the presence of the spin-boson phase transition (at $n_g = 1/2$), driven by the renormalization of tunneling amplitude E_J^* that reaches 0 on the transition line.

For higher values of E_J/E_c , we highlighted a line of maximum coupling strength, on which the system is believed to decompactify, *i.e.*, where the relevance of the discreteness of charge states is lost. Only two significant parameters are left, α and E_J , and we are led to the boundary sine-Gordon Hamiltonian. This model also displays a phase transition, namely the Schmid transition, which was detailed in Sec. 4.5. Decompactification leading to vanishing charge noise, the Part. III will be devoted to the simulation of a realistic simulator for the boundary sine-Gordon problem using superconducting circuits. These various regions are represented on Fig. 6.1.

The compact ansatz is a good candidate to provide insights on the crossover region $E_J/E_c \sim 1$ of the charge-boson model. We can anticipate it will capture the vanishing compactness effects on the many-body ground state when E_J/E_c is raised, smoothly transiting from spin-boson to the damped harmonic oscillator through a damped transmon region. We also await for the decompactification mechanism in the $\alpha \rightarrow \alpha_{\max}$ limit to show itself.

Adapting the ansatz to a many-body problem will require some more computations, to express the vacuum expectation energy. We then explore the decompactification mechanism, in the continuous limit, and make connection with the non-compact self-consistent harmonic approximation. Finally, we provide numerical results to compare the algorithm accuracy with the numerical renormalization group as a benchmark.

6.1 Vacuum energy

We remind the charge-boson Hamiltonian,¹

$$\hat{H} = \frac{E_c}{2}(\hat{n} - n_g)^2 - E_J \cos \hat{\varphi} + (\hat{n} - n_g) \sum_k i g_k (\hat{a}_k^\dagger - \hat{a}_k) + \sum_\ell \omega_\ell \hat{a}_\ell^\dagger \hat{a}_\ell. \quad (6.1)$$

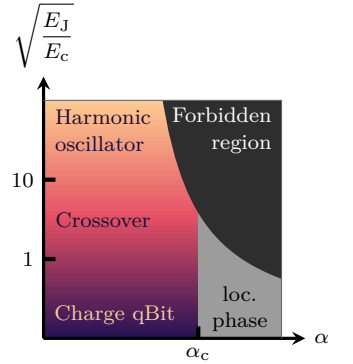


Figure 6.1: The various parameter regions of the charge-boson model at fixed E_J , sketched from Sec. 4.3. The spin-boson line separates the localized phase. In the delocalized/superconducting region, a smooth crossover connects the damped harmonic oscillator to the damped charge qBit.

¹ We resume employing Einstein's summation convention at intermediary steps.

The corresponding quadratic approximation, after gauge transformation which removes n_g , reads

$$\hat{H}'_0 = \frac{E_c}{2} \hat{n}^2 + \frac{E_J^*}{2} \hat{\phi}^2 + \hat{n} i g_k (\hat{a}_k^\dagger - \hat{a}_k) + \omega_\ell \hat{a}_\ell^\dagger \hat{a}_\ell. \quad (6.2)$$

We need to diagonalize it to produce its vacuum explicitly¹. We use a modified harmonic oscillator definition, to boil the computation down to one matrix diagonalization only.

$$\begin{cases} \hat{n} = i/\sqrt{2\omega}(\hat{a}^\dagger - \hat{a}) \\ \hat{\phi} = \sqrt{\omega/2}(\hat{a}^\dagger + \hat{a}) \end{cases} \Rightarrow \omega(\hat{a}^\dagger \hat{a} + 1/2) = \frac{1}{2}(\omega^2 \hat{n}^2 + \hat{\phi}^2), \quad (6.3)$$

which exploit the $\hat{n} \leftrightarrow \hat{\phi}$ symmetry of the harmonic oscillator. In this basis,

$$\hat{H}'_0 = \frac{E_J^* E_c}{2} \left(\frac{\hat{n}}{\sqrt{E_J^*}} \right)^2 + \frac{1}{2} \left(\sqrt{E_J^*} \hat{\phi} \right)^2 + \frac{\hat{n}}{\sqrt{E_J^*}} g_k \sqrt{2\omega_k E_J^*} \hat{n}_k + \frac{1}{2} (\omega_k^2 \hat{n}_k \hat{n}_k + \hat{\phi}_k \hat{\phi}_k). \quad (6.4)$$

We package all degrees of freedom into two charge and phase vectors, $(\hat{n}/\sqrt{E_J^*}, \hat{n}_1, \hat{n}_2, \dots)$ and $(\sqrt{E_J^*} \hat{\phi}, \hat{\phi}_1, \hat{\phi}_2, \dots)$, and set aside Greek indices to specify sums over these extended vectors. Then²,

$$\hat{H}'_0 = \frac{1}{2} (\hat{n}_\sigma \mathbf{M}_{\sigma\rho} \hat{n}_\rho + \hat{\phi}_\mu \hat{\phi}_\mu), \quad \mathbf{M} = \begin{bmatrix} \omega_J^2 & \dots & g_k \sqrt{2E_J^* \omega_k} & \dots \\ \vdots & \ddots & & (0) \\ g_k \sqrt{2E_J^* \omega_k} & & \omega_k^2 & \\ \vdots & (0) & & \ddots \end{bmatrix}. \quad (6.5)$$

This \mathbf{M} matrix has the arrowhead form, which indicates we are dealing with the bosonic version of the resonant model, a solvable model ubiquitous in condensed matter³, which was first introduced in the context of dilute magnetic impurities^{4,5}. The simple matrix form allows for fast, reliable diagonalization algorithms to be employed for numerical diagonalization⁶. We will assume such a diagonalization has been performed, and postpone an analytical derivation in the continuum limit to the next section.

We write $\mathbf{M} = \mathbf{V}^\top \mathbf{\Omega}^2 \mathbf{V}$ with $\mathbf{\Omega}$ a diagonal matrix of eigenfrequencies, and \mathbf{V} a matrix of eigenvectors⁷. We perform the basis change $\hat{N}_\mu = \mathbf{V}_{\mu\nu} \hat{n}_\nu$, together with $\hat{\phi}_\mu = \mathbf{V}_{\mu\nu} \hat{\phi}_\nu$ ⁸, which leads to the standard form

$$\hat{H}'_0 = \frac{1}{2} \left(\Omega_\nu \hat{N}_\nu \hat{N}_\nu + \hat{\phi}_\mu \hat{\phi}_\mu \right) = \Omega_\nu \hat{b}_\nu^\dagger \hat{b}_\nu, \quad (6.6)$$

where the operators $\hat{b}_\mu^\dagger, \hat{b}_\nu$ describe a new set of bosonic particles, which are eigenmodes of the quadratic approximation to the whole impurity + chain system. The last form has been obtained using again the modified relations Eq. (6.3). We build the many-body ansatz by compactification of the \hat{b}_ν vacuum state, denoted $|0\rangle$. Still, only one degree of freedom, the impurity Josephson junction, has to be compactified. The compactification operator retains its expression,

$$\hat{\mathcal{O}} = \sum_{w \in \mathbb{Z}} e^{i2\pi w(\hat{n} - n_g)}, \quad (6.7)$$

where \hat{n} is the charge of the junction. It will be convenient to express it in the eigenmodes basis: the various changes of basis we performed result in

$$\begin{cases} \hat{n} = i v_\mu (\hat{b}_\mu^\dagger - \hat{b}_\mu) \\ \hat{\phi} = u_\mu (\hat{b}_\mu^\dagger + \hat{b}_\mu) \end{cases}, \quad \text{where } v_\mu = \mathbf{V}_{\mu 0} \sqrt{\frac{E_J^*}{2\Omega_\mu}}, \quad u_\mu = \mathbf{V}_{\mu 0} \sqrt{\frac{\Omega_\mu}{2E_J^*}}. \quad (6.8)$$

¹ One could imagine simply adding an $L^* = 1/E_J^*$ inductor to the matrices of Eq. (3.20), but the new finite Josephson frequency ω_J reintroduces the diamagnetic term: the extra arrowhead matrix diagonalization cannot be avoided.

² We use the shorthand $\omega_J^2 = E_c E_J^*$.

³ J. W. Gadzuk. **1981**. *Phys. Rev. B* **24**, 1651.

⁴ A. Blandin & J. Friedel. **1959**. *J. Phys. Radium* **20**, 160.

⁵ P. W. Anderson. **1961**. *Phys. Rev.* **124**, 41.

⁶ N. Jakovčević Stor, I. Slapničar, & J. L. Barlow. **2015**. *Linear Algebra Appl.* **464**, 62.

⁷ Since $\mathbf{M}_{\mu\sigma} \mathbf{V}_{\nu\sigma} = \mathbf{V}_{\nu\mu} \Omega_\nu^2$, $\mathbf{V}_{\nu\mu}$ is interpreted as the μ^{th} component of the ν^{th} eigenvector of \mathbf{M} .

⁸ Which makes a canonical change of variable: $[\hat{\phi}_\sigma, \hat{N}_\rho] = i \mathbf{V}_{\sigma\mu} \mathbf{V}_{\rho\mu} = i \delta_{\mu\nu}$ since \mathbf{V} is orthogonal, \mathbf{M} being real and symmetric.

The orthogonality of \mathbf{V} translates into the relation $u_\nu v_\nu = 1/2$. In the following, we extensively use the norms $u_\nu u_\nu = u^2$, $v_\nu v_\nu = v^2$. We can evaluate right away the compact vacuum state ansatz norm¹ :

$$\begin{aligned} \langle 0|\widehat{\mathcal{O}}|0\rangle &= \sum_{w \in \mathbb{Z}} e^{-2\pi^2 u^2 w^2} \langle 0|e^{-2\pi w v_\nu \hat{b}_\nu^\dagger} e^{2\pi w v_\mu \hat{b}_\mu} |0\rangle e^{-i2\pi w n_g} \\ &= \sum_{w \in \mathbb{Z}} e^{-2\pi^2 u^2 w^2 + i2\pi w n_g}. \end{aligned} \quad (6.9)$$

It should be noted that the many-body nature of the problem did not make the expectation values form more involved: we still perform one sum only. The only difference with the isolated junction is the expression of the Boltzmann-like factor weighting the contribution of the winding numbers: $1/y$ has been replaced by $2u^2$, which encodes the contribution of all modes.

Expectation values

We recast the Hamiltonian in the form

$$\hat{H}' = \hat{H}'_0 - \frac{E_J^*}{2} \hat{\varphi}^2 - E_J \cos \hat{\varphi}, \quad (6.10)$$

and compute separately the expectation values of the three pieces². First,

$$\langle 0|\hat{H}'_0 \widehat{\mathcal{O}}|0\rangle = \Omega_\nu \langle 0|\hat{b}_\nu^\dagger \hat{b}_\nu \widehat{\mathcal{O}}|0\rangle = 0. \quad (6.11)$$

Second, the $\hat{\varphi}^2$ expectation is evaluated as³

$$\langle 0|\hat{\varphi}^2 \widehat{\mathcal{O}}|0\rangle = u_\mu u_\nu \sum_{w \in \mathbb{Z}} e^{i2\pi w n_g} \langle 0|\left(\hat{b}_\mu \hat{b}_\nu^\dagger + \hat{b}_\mu^\dagger \hat{b}_\nu\right) e^{-2\pi w v_\sigma (\hat{b}_\sigma^\dagger - \hat{b}_\sigma)} |0\rangle. \quad (6.12)$$

The first term in parenthesis is computed by commuting the two operators, and reduces to $u^2 \langle 0|\widehat{\mathcal{O}}|0\rangle$. The second term is managed by commuting the two annihilation operators through the displacement operator. The commutation is⁴

$$\left[\hat{b}_\nu, e^{2\pi w v_\sigma \hat{b}_\sigma^\dagger}\right] = \sum_m \frac{1}{m!} (2\pi w)^m [\hat{b}_\nu, (v_\sigma \hat{b}_\sigma^\dagger)^m] = 2\pi w v_\nu e^{2\pi w v_\sigma \hat{b}_\sigma^\dagger}. \quad (6.13)$$

Together with $u_\rho v_\rho = 1/2$, we end up with

$$\langle 0|\hat{\varphi}^2 \widehat{\mathcal{O}}|0\rangle = u^2 \langle 0|\widehat{\mathcal{O}}|0\rangle + \sum_{w \in \mathbb{Z}} (\pi w)^2 e^{-2\pi^2 w^2 v^2 + i2\pi w n_g}. \quad (6.14)$$

We are left with the cosine expectation value, for which we split the cosine into exponentials, and commute them through the displacement operator^{5,6}.

$$\begin{aligned} \langle 0|\cos \hat{\varphi} \widehat{\mathcal{O}}|0\rangle &= \frac{1}{2} e^{-u^2/2} \sum_{\pm, w \in \mathbb{Z}} e^{i2\pi w n_g} \langle 0|e^{\pm i u_\rho \hat{b}_\rho} e^{-2\pi w v_\sigma (\hat{b}_\sigma^\dagger - \hat{b}_\sigma)} |0\rangle \\ &= e^{-u^2/2} \sum_{w \in \mathbb{Z}} (-1)^w e^{-2\pi^2 w^2 v^2 + i2\pi w n_g}. \end{aligned} \quad (6.15)$$

The sought-after expression for the variational energy is

$$\frac{\langle 0|\hat{H}' \widehat{\mathcal{O}}|0\rangle}{\langle 0|\widehat{\mathcal{O}}|0\rangle} = -\frac{E_J^*}{2} \left(u^2 + \frac{\sum_{w \in \mathbb{Z}} (\pi w)^2 e^{-2\pi^2 w^2 v^2 + i2\pi w n_g}}{\sum_{w \in \mathbb{Z}} e^{-2\pi^2 w^2 v^2 + i2\pi w n_g}} \right) - E_J e^{-\frac{u^2}{2}} \frac{\sum_{w \in \mathbb{Z}} (-1)^w e^{-2\pi^2 w^2 v^2 + i2\pi w n_g}}{\sum_{w \in \mathbb{Z}} e^{-2\pi^2 w^2 v^2 + i2\pi w n_g}}. \quad (6.16)$$

¹ We can show by expanding the exponentials that

$$\begin{aligned} e^{\beta \hat{b}} |0\rangle &= |0\rangle, \\ \langle 0|e^{\beta \hat{b}^\dagger} &= \langle 0| \quad \forall \beta \in \mathbb{C}. \end{aligned}$$

² Note that the two first terms are no longer 2π -periodic; only their sum is. This is no trouble, since we restricted the wavefunctions to $[-\pi, \pi]$ already.

³ As a reminder, $\langle 0|\hat{b}_\mu^\dagger = 0 \quad \forall \mu$.

⁴ Remind that if $[\hat{A}, \hat{B}] \in \mathbb{C}$, $[\hat{A}, \hat{B}^n] = n\hat{B}^{n-1}[\hat{A}, \hat{B}]$.

⁵ \sum_{\pm} implies a sum over the two values, $\pm = -, +$.

⁶ Remind that if $[\hat{A}, \hat{B}] \in \mathbb{C}$, $e^{\hat{A}} e^{\hat{B}} = e^{\hat{B}} e^{\hat{A}} e^{[\hat{A}, \hat{B}]}$.

The interpretation of this expression is quite clear: only the two parameters u^2 and v^2 enter the formula, they respectively renormalize E_J and weight the importance of the winding numbers contribution. It is still possible to reach a duality form, which is quickly converging in the regime where the winding number weight become larger than 1. It would be closely related to Eq. (5.25), albeit with admittance y replaced by the many-body weights u^2 and v^2 . We will now analyze these two parameters in the continuous limit to provide some insight on the physics this last equation contains. The Sec. 6.4 will then resort to numerical techniques to carry the variational principle, and provide observables to compare with the Numerical Renormalization Group.

Both the u^2 and v^2 weights have a simple interpretation: they are the vacuum phase and charge fluctuations. Indeed,

$$\langle 0|\hat{n}^2|0\rangle = -v_\mu v_\nu \langle 0|(\hat{b}_\mu^\dagger - \hat{b}_\mu)(\hat{b}_\nu^\dagger - \hat{b}_\nu)|0\rangle = v^2, \quad \text{and} \quad \langle 0|\hat{\varphi}^2|0\rangle = u^2. \quad (6.17)$$

In turn, we will express these fluctuations in the language of Green's function. That will allow us to use their equation of motion, which will bypass the arrowhead matrix diagonalization¹ and will allow us to reach analytical expressions for these quantities.

Let

$$\begin{cases} G_{nn}^R(t-t') = -i\theta(t-t')\langle 0|[\hat{n}(t), \hat{n}(t')]|0\rangle \\ G_{nn}^F(t-t') = -i\langle 0|\mathcal{T}\hat{n}(t)\hat{n}(t')|0\rangle \end{cases} \quad (6.18)$$

be the retarded and Feynman Green's functions for charge operators. \mathcal{T} is the time ordering symbol². Similar definitions hold for any couple of operators, especially for $G_{\varphi\varphi}^F$. We derive the equation of motion for the retarded functions. In frequency domain, they differ simply by a symmetry prescription, so we will obtain easily the Feynman functions we need. Finally, the vacuum fluctuations are obtained as the $t \rightarrow 0$ limit of G^F . Precisely,

$$\langle 0|\hat{n}^2|0\rangle = iG_{nn}^F(t=0), \quad \langle 0|\hat{\varphi}^2|0\rangle = iG_{\varphi\varphi}^F(t=0). \quad (6.19)$$

6.2 Charge fluctuations

The equations of motion on the Green's function are obtained by successive derivation with respect to time. This will produce relations between various Green's functions. If the Hamiltonian is quadratic, it must be possible to close and solve them. It is here the case, the Hamiltonian being given at Eq. (6.5) (note that $\hat{n}_0 = \hat{n}/\sqrt{E_J^*}$ and $\hat{\varphi}_0 = \sqrt{E_J^*}\hat{\varphi}$). This procedure is close to explicitly find an inverse for the arrowhead matrix. We successively find^{3,4}

$$\begin{aligned} i\partial_t G_{n_0 n_0}(t-t') &= \delta(t-t')[\hat{n}_0(t), \hat{n}_0(t')]\langle 0|0\rangle - i\theta(t-t')\langle 0|[i\partial_t \hat{n}_0(t), \hat{n}_0(t')]|0\rangle \\ &= -iG_{\varphi_0 n_0}(t-t'), \end{aligned} \quad (6.20)$$

In the same fashion,

$$\begin{aligned} \partial_t G_{\varphi_0 n_0}(t-t') &= \delta(t-t') + \omega_J^2 G_{n_0 n_0}(t-t') + \sum_k g_k \sqrt{2\omega_k E_J^*} G_{n_k n_0}, \\ \partial_t G_{n_k n_0}(t-t') &= -G_{\varphi_k n_0}(t-t'), \\ \partial_t G_{\varphi_k n_0}(t-t') &= \omega_k^2 G_{n_k n_0}(t-t') + g_k \sqrt{2\omega_k E_J^*} G_{n_0 n_0}(t-t'). \end{aligned} \quad (6.21)$$

Taking the Fourier transform and collecting and extracting $G_{n_0 n_0}$, we reach

$$G_{n_0 n_0}(\omega) = \frac{1}{\omega^2 - \omega_J^2 - E_J^* \sum_k \frac{2\omega_k g_k^2}{\omega^2 - \omega_k^2}}. \quad (6.22)$$

¹ Equation of motion rather need an inversion of the arrowhead matrix, which is easier to perform. This difference is illustrated again between Sec. 8.2 and Sec. 10.1. The two operations yield different information, but they are equivalent in the continuum limit, *cf.*

J. W. Gadzuk. 1981. *Phys. Rev. B* 24, 1651.

² It sorts the operators such that earlier times are placed on the right.

³ Equations of motion are valid for any prescription, so we omit the R symbol.

⁴ We use Heisenberg's equation of motion for operators,

$$i \frac{d\hat{A}}{dt} = [\hat{A}, \hat{H}].$$

This form is also standard in the description of resonant levels, bosonic or fermionic. The sum in the denominator is often called the hybridization function. In Part. III, we will see that it is also the (exact) self-energy of the free bosonic field. Such sums have been dealt with, in Sec. 3.3, using the spectral function to reach an integral representation,

$$\sum_k \frac{2\omega_k g_k^2}{\omega^2 - \omega_k^2} = 4\alpha \int_0^\infty d\nu \frac{\nu^2}{\omega^2 - \nu^2} \frac{1}{1 + (\nu/\omega_M)^2}. \quad (6.23)$$

We retained the Lorentzian cutoff derived in the continuum limit. We separate the part linear in ω_M ,

$$\begin{aligned} \sum_k \frac{2\omega_k g_k^2}{\omega^2 - \omega_k^2} &= -4\alpha \int_0^\infty \frac{d\nu}{1 + (\nu/\omega_M)^2} + 4\alpha\omega^2 \int_0^\infty \frac{d\nu}{(\omega^2 - \nu^2)(1 + (\nu/\omega_M)^2)} \\ &= -2\pi\alpha\omega_M + 4\alpha\omega^2 \int_0^\infty \frac{d\nu}{(\omega^2 - \nu^2)(1 + (\nu/\omega_M)^2)}. \end{aligned} \quad (6.24)$$

The second integral has poles, which need an explicit prescription. We use Feynman's prescription, in order to obtain Feynman Green's function, as represented on Fig. 6.2. The $\omega_M \rightarrow \infty$ limit of this integral is well defined: it is evaluated by partial fraction decomposition, and Sokhotski-Plemelj formula, to give

$$\begin{aligned} \int_0^\infty \frac{\omega^2 d\nu}{\omega^2 - \nu^2 - i\epsilon} &= \frac{\omega}{2} \left(\int_0^\infty \frac{d\nu}{\nu + \omega - i\epsilon} - \int_0^\infty \frac{d\nu}{\nu - \omega - i\epsilon} \right) \\ &= \frac{\omega}{2} \left(\int_0^\infty \frac{d\nu}{\nu + \omega} - \int_0^\infty \frac{d\nu}{\nu - \omega} + i\pi \int_0^\infty (\delta(\nu + \omega) - \delta(\nu - \omega)) d\nu \right). \end{aligned} \quad (6.25)$$

The principal parts cancel each other, and the sign of ω selects one of the δ functions. All in all, in the continuum limit,

$$G_{n_0 n_0}^F(\omega) = \frac{1}{\omega^2 - E_J^*(E_c - 2\pi\alpha\omega_M) + i2\pi\alpha E_J^*|\omega|}. \quad (6.26)$$

Several comments are in order. First, we reached the Feynman's function, as it can be checked from its imaginary part parity. Second, we see that the charging energy is displaced by the bath. In fact, this displacement exactly counterbalances the environmental part in E_c we highlighted in Sec. 3.2, and computed in the continuum limit in Sec. 3.3. We conclude that, independently of the details of the model, $E_c - 2\pi\alpha\omega_M = E_c^0 = 1/(C_c + C_J)$ is an exact relation. Finally, we simply reached the response function of a damped oscillator. Its pulsation is $\omega_0^2 = E_J^* E_c^0$, its admittance $y_0 = \sqrt{E_J^*/E_c^0}$, and quality factor $1/Q_0 = 2\pi\alpha y_0$.

The end of the charge fluctuations computation is reached by

$$\langle 0|\hat{n}^2|0\rangle = iE_J^* \int_{\mathbb{R}} d\omega G_{n_0 n_0}^F(\omega) = i2E_J^* \int_0^\infty \frac{d\omega}{2\pi} \frac{1}{\omega^2 - \omega_0^2 + i\omega\omega_0/Q_0}. \quad (6.27)$$

We factorize the denominator into the product of two complex poles. They are found as the zeros of the denominator. The associated discriminant is $\Delta = 4\omega_0^2(1 - 1/(2Q_0)^2)$. We focus on the two regimes, over-damped and under-damped, which correspond to $Q \ll 1/2$ and $Q \gg 1/2$ respectively. The poles are located at

$$\begin{cases} \omega_{\pm} = \omega_0 (\pm 1 - i/2Q_0) & (Q_0 \gg 1/2) \\ \omega_+ = -i\omega_0/Q_0, \text{ and } \omega_- = -i\omega_0 Q_0 & (Q_0 \ll 1/2) \end{cases}, \quad (6.28)$$

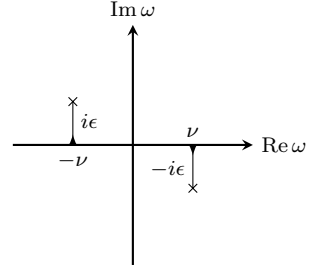


Figure 6.2: Pole displacements with Feynman's prescription.

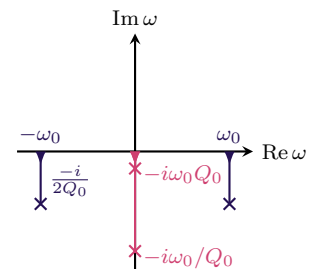


Figure 6.3: Poles position in complex ω plane. (●) $Q \gg 1/2$, (●) $Q \ll 1/2$.

as represented on Fig. 6.3. independently of the values of the poles, we can compute the integral:

$$\begin{aligned} \langle 0|\hat{n}^2|0\rangle &= i2E_J^* \lim_{\Lambda \rightarrow \infty} \int_0^\Lambda \frac{d\omega}{2\pi} \frac{1}{(\omega - \omega_+)(\omega - \omega_-)} \\ &= \frac{iE_J^*}{\pi(\omega_+ - \omega_-)} \left(\lim_{\Lambda \rightarrow \infty} \ln \left(\frac{\Lambda - \omega_+}{\Lambda - \omega_-} \right) + \ln \left(\frac{\omega_-}{\omega_+} \right) \right) = \frac{iE_J^*}{\pi(\omega_+ - \omega_-)} \ln \left(\frac{\omega_-}{\omega_+} \right). \end{aligned} \quad (6.29)$$

Underdamped case

In the under-damped case, the angle between the two complex poles tends to $-\pi$, while their *moduli* are equal. The complex logarithm thus evaluates to $\ln(\omega_-/\omega_+) \simeq -i\pi$, as represented on Fig. 6.4. We obtain

$$\langle 0|\hat{n}^2|0\rangle = \frac{y_0}{2}. \quad (6.30)$$

This is the isolated junction result. As we could have expected, in this limit, the Josephson junction decouples from the array, and we lose the many-body contribution to compactification.

Overdamped case

If $Q_0 < 1/2$, the angle between poles is strictly zero, while the poles are purely imaginary, so the charge fluctuation is purely real, as it should be. Its value is

$$\langle 0|\hat{n}^2|0\rangle = \frac{E_J^* Q_0}{\pi \omega_0} \frac{1}{1 - Q_0^2} \ln \left(\frac{1}{Q} \right) \simeq \frac{1}{\pi^2 \alpha} \ln(2\pi\alpha y_0). \quad (6.31)$$

This result is logarithmically divergent in the $y_0 \rightarrow 0$ and $y_0 \rightarrow \infty$ limits. We rather study the Boltzmann-like weight for winding number w . For $w = 1$ the maximum weight, we obtain

$$e^{-2\pi^2 v^2} = (2\pi\alpha y_0)^{-\frac{2}{\alpha}}. \quad (6.32)$$

The weight is a strictly decreasing function of the admittance y_0 , as plotted for several α on Fig. 6.5. We then have a hint on the decompactification mechanism: when $\alpha \rightarrow \alpha_{\max}$, $C_c \rightarrow \infty$, as stated in Sec. 3.3. This means that $E_c^0 = 1/(C_c + C_J) \rightarrow 0$. As long as E_J^* stays finite, $y_0 \rightarrow \infty$, such that the winding number weight vanishes, following a power law given by α . Still, we expect E_J^* to also be renormalized downwards, such that the limit of y_0 at strong coupling is still undecided, and the fate of compactification is still in the balance.

When the winding number weight exceeds 1, high winding numbers are contributing more than small ones. Yet, the analysis does not fail: it only signals that we should use a duality formula, to move to a charge picture. The sum over charge numbers will be involving a small number of charge states only. This charge regime is reached for $2\pi\alpha < 1/y_0$, *i.e.* in the under-damped regime, such that this power law do not hold. Only the winding number picture is relevant at strong coupling. The environment suppresses interference effects between different windings, and tends to decompactify the system. A similar result has been reached using Feynman's influence theory¹. The three possible regimes are represented on Fig. 6.6.

6.3 Phase fluctuations

The same method is applicable for the phase fluctuations, which will provide the u^2 parameter. It will allow us to interpret completely Eq. (6.16), and discuss the self-consistent procedure given by the variational principle.

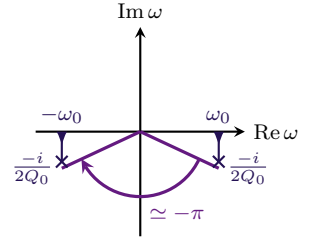


Figure 6.4: The complex logarithm imaginary part.

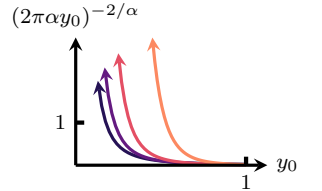


Figure 6.5: Winding weight for several α .

- (●) $\alpha = 0.9$,
- (●) $\alpha = 0.7$,
- (●) $\alpha = 0.5$,
- (●) $\alpha = 0.3$.

¹ W. Zwerger, A. T. Dorsey, & M. P. A. Fisher. **1986**. *Phys. Rev. B* **34**, 6518.

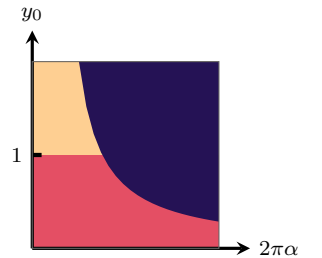


Figure 6.6: Various regions in the $(2\pi\alpha, y_0)$ plane. Note that y_0 itself is a function of α .

- (●) : extended, over-damped,
- (●) : extended, under-damped,
- (●) : compact, under-damped.

We aim at the phase Green's function, $G_{\varphi\varphi}^F(\omega)$. We can relate it to the charge Green's function by equation of motion technique. We already established that

$$\partial_t G_{n_0 n_0}(t-t') = -G_{\varphi_0 n_0}(t-t'). \quad (6.33)$$

Deriving with respect to the other time variable, we reach

$$\partial'_t G_{\varphi_0 n_0}(t-t') = \delta(t-t') - G_{\varphi_0 \varphi_0}(t-t'). \quad (6.34)$$

We change to only one time variable, $\tau = t-t'$, which implies $\partial_t = \partial_\tau$ and $\partial'_t = -\partial_\tau$, and so,

$$G_{\varphi_0 \varphi_0} = \omega^2 G_{n_0 n_0}(\omega) - 1. \quad (6.35)$$

Remembering $\hat{\varphi}_0 = \sqrt{E_J^*} \hat{\varphi}$, the phase fluctuation is then

$$u^2 = i \int_0^\infty \frac{d\omega}{\pi} \frac{E_c^0 - i2\pi\alpha\omega}{\omega^2 - \omega_0^2 + i\omega\omega_0/Q_0}. \quad (6.36)$$

Underdamped case

When the coupling is weak, $2\pi\alpha \ll 1$, only the first part of the numerator contributes. We retrieve the harmonic oscillator result,

$$\langle 0 | \hat{\varphi}^2 | 0 \rangle = \frac{E_c^0}{E_J^*} \langle 0 | \hat{n}^2 | 0 \rangle = \frac{1}{2y_0}. \quad (6.37)$$

We so have that Eq. (6.16) completely reduces to Eq. (5.25). The environment decouples from the Josephson junction, which can be compactified as an isolated junction.

Overdamped case

The first part of u^2 can still be recast into a charge fluctuation, so we write

$$u^2 = \frac{v^2}{y_0^2} + 2\alpha \int_0^{\omega_M} d\omega \frac{\omega}{\omega^2 - \omega_0^2 + i\omega\omega_0 Q_0}. \quad (6.38)$$

The remaining integral is logarithmically divergent, so we reintroduced a cutoff¹. We employ the same trick: we separate the poles by partial fraction decomposition², to obtain

$$\begin{aligned} u^2 &= \frac{v^2}{y_0^2} + 2\alpha \frac{1}{\omega_+ - \omega_-} \left(\omega_+ \ln \left(1 - \frac{\omega_M}{\omega_+} \right) - \omega_- \ln \left(1 - \frac{\omega_M}{\omega_-} \right) \right) \\ &= \frac{2\alpha}{2\pi^2 \alpha^2 y_0^2} \ln(2\pi\alpha y_0) + 2\alpha \ln \left(\frac{\omega_M}{2\pi\alpha E_J^*} \right), \end{aligned} \quad (6.39)$$

obtained with the poles expression given at Eq. (6.28). In the over-damped regime, the $1/(\pi\alpha y_0)^2$ is very weak, such that we can safely neglect the first term in front of the second. We end up with

$$\langle 0 | \hat{\varphi}^2 | 0 \rangle = 2\alpha \ln \left(\frac{\omega_M}{2\pi\alpha E_J^*} \right). \quad (6.40)$$

We are now equipped to return to the vacuum energy, Eq. (6.16), considered in the framework of variational principle. In this over-damped case, we know that the contribution of winding numbers are small, so we reduce the energy to the $w = 0$ contribution. The self-consistent equation for E_J^* reduces to

$$\frac{d\langle \hat{H} \rangle}{dE_J^*} = 0 \quad \Rightarrow \quad E_J^* = E_J e^{-u^2/2} - u^2 \left(\frac{du^2}{dE_J^*} \right)^{-1}. \quad (6.41)$$

¹ There is no reason the Lorentzian shape we derived for sums over modes would be valid here. We content ourselves with a sharp cutoff at a same energy scale.

² We obtain

$$\frac{\omega}{(\omega - \omega_+)(\omega - \omega_-)} = \frac{1}{\omega_+ - \omega_-} \left(\frac{\omega_+}{\omega - \omega_+} - \frac{\omega_-}{\omega - \omega_-} \right),$$

which avoids linearly divergent terms.

Using the previous result for u^2 ,

$$E_J^* \left(1 + \ln \left(\frac{2\pi\alpha E_J^*}{\omega_M} \right) \right) = E_J \left(\frac{2\pi\alpha E_J^*}{\omega_M} \right)^\alpha. \quad (6.42)$$

Neglecting the logarithmic correction on the left hand side, we recognize the result derived for the Schmid transition,

$$E_J^* = E_J \left(\frac{\omega_M}{2\pi\alpha E_J} \right)^{\frac{\alpha}{\alpha-1}}. \quad (6.43)$$

At $\alpha = 1$, this predicts that the scale E_J^* is renormalized to zero, faster than any power law.

We can then finish the description of the decompactification mechanism. Suppose that we crank up the coupling capacitance, C_c , to infinity. If E_c/ω_M is chosen such that $\alpha_{\max} < 1$, E_J^* stays finite in the $C_c \rightarrow \infty$ limit. On the contrary, $E_c^0 = 1/(C_c + C_J) \rightarrow 0$, such that $y_0 = \sqrt{E_J^*/E_c^0} \rightarrow \infty$. Compactification becomes irrelevant. At $\alpha = \alpha_{\max}$, the charging energy is effectively suppressed, the system is completely decompactified, and the model reduces to boundary sine-Gordon, as discussed in Sec. 4.4.

This scenario can be modified in two ways:

- At $E_J/E_c < 1$, compact effects becomes relevant in the under-damped regime (and even at $\alpha = 0$). The system reduces to spin-boson model for all α , and follows a different trajectory when C_c is dialed up.
- If $\alpha_{\max} > 1$, near the Schmid transition, E_J^* vanishes while E_c^0 is non-zero, such that $y_0 \rightarrow 0$. Compactification becomes relevant, the system reduces to a few charge states. If, furthermore, $n_g = 1/2$, it will encounter the spin-boson transition, at $\alpha > 1$.

6.4 Numerical optimization

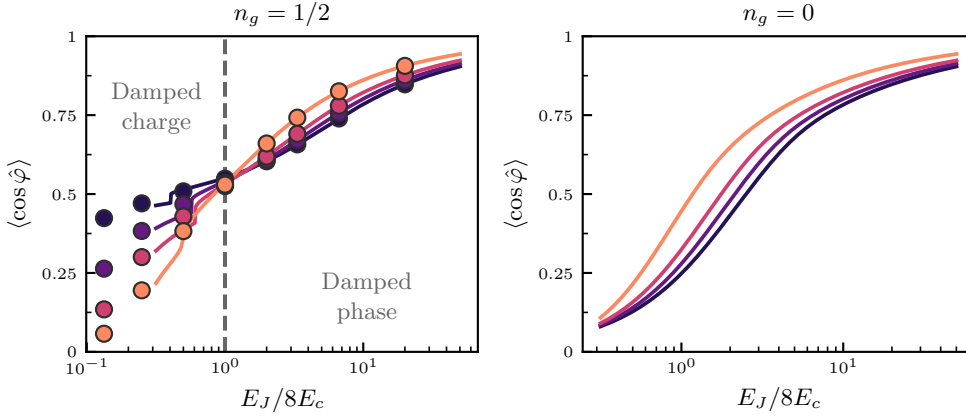
The previous discussion can be enriched by resorting to numerical computation to find the optimum E_J^* , by minimizing Eq. (6.16). By doing so, we can test the effect of compactification on the self-consistent harmonic approximation in the regimes where it is relevant.

Furthermore, since the whole method rests on the variational principle, its validity strongly depends on the quality of the initial wavefunction guess. It is then crucial to benchmark the method against well established non-perturbative numerical methods, as the numerical renormalization group.

Phase fluctuations at small α

Up until now, we focused on the over-damped region. The question of the interplay of small α and compactness is still open. Two *scenarii* are in competition:

- (i) If phase fluctuations are enhanced by α , the SCHA will lower $E_J^* \propto \exp(-u^2/2)$, thus lowering y_0 . If the effect is strong enough, it could prevent the system to ever enter the strong coupling regime.
- (ii) If the superconducting phase is localized by the interactions, E_J^* will rise. Eventually, the collapse of E_c^0 will lead to entering the over-damped regime, and later to decompactification, as we previously described.



Since $\hat{\varphi}^2$ is not a 2π -periodic operator, its average value over a compact state is not well defined, as we discussed in Sec. 5.1¹. We rather study $\langle 0 | \cos \hat{\varphi} | 0 \rangle$, which is well defined and encapsulate the same information. It is represented on Fig. 6.7 as a function of E_J/E_c , for several α and n_g .

For simple comparison to NRG, this computation is realised on the same logarithmic grid for environmental modes, $\omega_k = \omega_M/2^k$, cf. Sec. 4.3. Typically 20 modes are enough to reach the continuum limit in this scheme. At every step of the minimization algorithm, the arrowhead matrix Eq. (6.5) is diagonalized, u^2 and v^2 computed, and plugged into Eq. (6.16). Since only one parameter, E_J^* , is optimized, the minimum is reached within a few tens of steps. Overall, the computational cost is very low. We see that excellent agreement between NRG and compact ansatz is reached from high E_J/E_c down to $E_J/E_c \sim 0.5$ for $n_g = 1/2$. At this value, the minimization becomes unstable, as illustrates the sudden jumps in $\langle \cos \hat{\varphi} \rangle$. This signals that the ansatz is not matching the system wavefunction correctly anymore, and should not be trusted below the jumps. At $n_g = 0$, the system is described correctly in all regimes.

From this figure, we can separate between two regimes. At $E_J/E_c > 1$, phase fluctuations are damped² by the interaction with the environment. This corresponds to *scenario* (ii). Below $E_J/E_c = 1$, phase fluctuations are enhanced by the interactions. This is typical of spin-boson physics, as discussed in Sec. 4.2: tunnel amplitude between neighboring charge states will renormalize downwards, and finally vanish at the spin-boson phase transition. This corresponds to *scenario* (i), where over-damped regime is never reached and decompactification never happens when α is raised.

The E_J^* scale can be extracted from the numerical computation, as represented on Fig. 6.8 in the $E_J > E_c$ regime. The result is compared to the optimization conducted with the $w = 0$ term only, *i.e.* without compactification. Several regimes already discussed can be highlighted: when $\alpha \rightarrow \alpha_{\max}$, decompactification occurs, and compact and extended self-consistent harmonic approximation agree. In the harmonic limit $E_J \gg E_c$, compactness never contributes. E_J^* slowly rises, which is linked with phase fluctuation being damped by the interactions. In the crossover regime $E_J \sim E_c$, the low α region is strongly affected by compactness, while decompactification happens latter, when entering the over-damped regime.

This concludes our demonstration of the compact ansatz capabilities to unveil, analytically or at low computational cost, the physics of Josephson systems. Applied to

Figure 6.7: Phase fluctuations for several coupling strength, at $n_g = 0$ and $n_g = 1/2$. The later displays two regimes: localized charge at $E_J/E_c < 1$, localized phase otherwise. E_J is fixed at $\omega_M/10$.

(●) : $\alpha/\alpha_{\max} = 0.1$,
 (●) : $\alpha/\alpha_{\max} = 0.3$,
 (●) : $\alpha/\alpha_{\max} = 0.5$,
 (●) : $\alpha/\alpha_{\max} = 0.8$,
 (●) : NRG result,
 (—) : compact ansatz result.

¹ One could be surprised, then, to see it appeared in our computation of the vacuum state energy, in Sec. 6.1. It was then a part of \hat{H} , which itself, in total, is 2π -periodic.

² If $\langle \cos \hat{\varphi} \rangle = 0$, the system explores the whole cosine, so it is completely delocalized in phase.

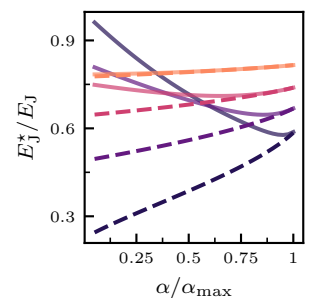


Figure 6.8: E_J^* as a function of the coupling strength, computed with and without $w \neq 0$ winding numbers. $E_c = \omega_M/10$ is fixed, and $n_g = 1/2$.

(●) : $E_J/E_c = 1$,
 (●) : $E_J/E_c = 2$,
 (●) : $E_J/E_c = 4$,
 (●) : $E_J/E_c = 10$,
 (---) $w = 0$ only,
 (—) all w .

the charge-boson model together with a realistic microscopic modelization, it shows that the most prominent many-body effects are hidden by an interplay of coupling strength limitation, decompactification mechanism, and charge noise, which would obscure experimental measures in the spin-boson regime. In the next section, we sketch some possible applications of the compact ansatz method to related systems, and anticipate new developments of its toolbox.

7 | Perspectives on the compact ansatz

“Est-ce qu'on peut s'en servir pour donner de l'élan à un pigeon ?”

Astier, *Kaamelott*.

“Can it be used to give momentum to a pigeon ?”

The main asset of the compact ansatz method is its ability to describe many regimes of the isolated junction in a simple framework, which can be extended to more involved circuits. We demonstrated earlier such an application to the charge-boson model. In this chapter, we give rough sketches of foreseen applications for the compact ansatz.

7.1 Many-body excited states

In the previous chapter, we set aside the ability of the variational principle to tackle excited states and focused on vacuum state properties. Still, we demonstrated this ability on the isolated junction in Sec. 5.2, and it is generally a very well known method in atomic physics¹ and quantum chemistry, where it is the cornerstone of many numerical methods for determination of discrete spectra, as the Hückel molecular orbital theory.

The race for efficient superconducting qBit designs produced a whole series of atom-like circuits, with spectra ranging from fairly simple, as the charge qBit, to complex, as the fluxonium² or the $0 - \pi$ qBit³. These spectra structures are relevant for quantum computing protocols: the proliferation of atomic states with no strong selection rules to suppress transitions leads to sizable effects *e.g.* for dispersive measurements⁴. High lying levels are also relevant for QND measurements through a readout cavity, which can be improved by raising the photon number in the readout cavity⁵. High lying levels are usually outside of Josephson potential cosine well, as represented on Fig. 7.1. Consequently, they are more sensitive to charge noise and compactness in general. A quantitative estimate of this charge noise could be obtained in a systematical way *via* the compact ansatz.

It has recently been demonstrated that a driven transmon is subject to instabilities, during which it escapes the potential well⁶. This physics is also related to restoration of compactness at high energy; one could then wonder if the decompactification mechanism would provide a simple picture of this dynamical instability.

Excited states expectation values

The main ingredient to perform such computations is to evaluate the expectation value of a Hamiltonian over excited states. We here only test the feasibility of such a procedure, without final result to exhibit. Assume for now that one state of \hat{H}_0 is populated only. Its index is ν . The corresponding Fock states are denoted $|n_\nu\rangle$, for n photons. We focus on the norm, $\langle n_\nu | \hat{\mathcal{O}} | m_\nu \rangle = \langle 0 | \hat{b}_\nu^n \hat{\mathcal{O}} \hat{b}_\nu^\dagger{}^m | 0 \rangle$. The powers of

¹ G. W. F. Drake & Z.-C. Van. **1994**. *Chem. Phys. Lett.* **229**, 486.

² V. E. Manucharyan, J. Koch, *et al.* **2009**. *Science* **326**, 113.

³ P. Brooks, A. Kitaev, & J. Preskill. **2013**. *Phys. Rev. A* **87**, 052306.

⁴ G. Zhu, D. G. Ferguson, *et al.* **2013**. *Phys. Rev. B* **87**, 024510.

⁵ D. Gusenkova, M. Spiecker, *et al.* **2021**. *Phys. Rev. Applied* **15**, 064030.

⁶ R. Lescanne, L. Verney, *et al.* **2019**. *Phys. Rev. Applied* **11**, 014030.

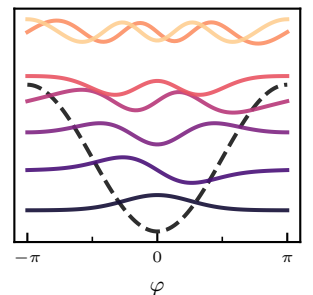


Figure 7.1: First levels wavefunctions of the isolated junction at $y = 1.5$. They are shifted up according to their energy.

(- -) Josephson potential,
Ground High energies

creation/annihilation operators can be represented with an exponential generating function,

$$\hat{b}^n = (-i)^n \left. \frac{d^m}{dx^m} e^{ix\hat{b}} \right|_{x=0}. \quad (7.1)$$

This allows the usage of displacement operators algebra to compute the bracket. The derivative is evaluated at the end of the computation. It produces

$$\langle n_\nu | \hat{\mathcal{O}} | m_\nu \rangle = (-i)^{m+n} \sum_{w \in \mathbb{Z}} e^{-2\pi^2 w^2 v^2} \left. \frac{d^m}{dx^m} \frac{d^n}{dy^n} \langle 0 | e^{ix\hat{b}_\nu} e^{-2\pi w v_\sigma \hat{b}_\sigma^\dagger} e^{2\pi w v_\rho \hat{b}_\rho} e^{iy\hat{b}_\nu^\dagger} | m_\nu \rangle \right|_{x,y=0}. \quad (7.2)$$

We commute the exponential operators¹, and obtain

$$\langle n_\nu | \hat{\mathcal{O}} | m_\nu \rangle = (-i)^{m+n} \sum_{w \in \mathbb{Z}} e^{-2\pi^2 w^2 v^2} e^{(2\pi w v_\nu)^2} \left. \frac{d^m}{dx^m} \frac{d^n}{dy^n} e^{-(x-i2\pi w v_\nu)(y+i2\pi w v_\nu)} \right|_{x,y=0}. \quad (7.3)$$

The derivative is similar to Wick's theorem². Using $f_\nu = -i2\pi w v_\nu$ as a placeholder, it takes the form

$$\begin{aligned} & (-1)^n e^{f_\nu^2} \left. \frac{d^m}{dx^m} (x + f_\nu) e^{-(x+f_\nu)(y+f_\nu^*)} \right|_{x,y=0} = P_n^m(f) \\ & = n! f^{n-m} \sum_k \frac{(-1)^k}{k!} \binom{m}{n-k} f^{2k}. \end{aligned} \quad (7.4)$$

This result is essentially combinatoric, and amounts at counting, for a given power of f , the number of derivatives leading to it. The final polynomial has the combinatoric structure of a rook polynomial³, with provide simple evaluation algorithms and useful recursion relations, *e.g.* $P_n^m(f_\nu) = (-1)^{n-m} P_m^n(f)$, which proves that our result is symmetric under $n_\nu \leftrightarrow m_\nu$ exchange. The resulting expectation value is

$$\langle n_\nu | \hat{\mathcal{O}} | m_\nu \rangle = \sum_{w \in \mathbb{Z}} e^{-2\pi^2 w^2 v^2} P_{n_\nu}^{m_\nu}(2\pi w v_\nu). \quad (7.5)$$

With some more effort, it is extended to any two Fock states given by two lists of occupation numbers, $\vec{n} = (n_1, \dots, n_\nu, \dots)$ and $\vec{m} = (m_1, \dots, m_\nu, \dots)$:

$$\langle \vec{n} | \hat{\mathcal{O}} | \vec{m} \rangle = \sum_{w \in \mathbb{Z}} e^{-2\pi^2 w^2 v^2} \prod_\nu P_{n_\nu}^{m_\nu}(2\pi w v_\nu). \quad (7.6)$$

Similar expressions can be reached for the others expectation values needed to compute the full Hamiltonian. One can notice that the bracket we evaluated shows non-zero overlaps between different ansatz states. Similarly to the procedure we applied in Sec. 5.2, a Gram-Schmidt orthonormalization process must be performed together with the variational method.

7.2 Josephson junction chains

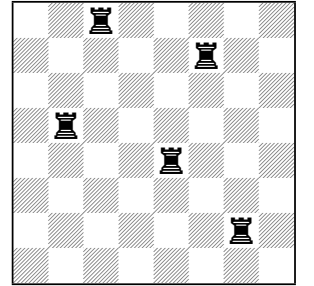
The charge boson model is related to a larger family of impurity models: a unique degree of freedom, either a fermion, a spin, a boson, a rotor, is coupled to a continuum of modes. These models are often encountered in condensed matter, the Kondo problem and the spin-boson model being the most prominent examples. Nonetheless, many interacting models are instead homogeneous in space, with a non-linearity distributed over whole space, sometimes in the form of an interaction between several fields. All models of particle physics are organized in such a way; one can call them bulk models. They tend to be harder to solve⁴ than their impurity counterpart.

¹ using that if $[\hat{A}, \hat{B}] \in \mathbb{C}$,

$$e^{\hat{A}} e^{\hat{B}} = e^{\hat{B}} e^{\hat{A}} e^{[\hat{A}, \hat{B}]}$$

² In the path integral version of the theorem, related to Gaussian integration.

³ The (n, m) rook polynomial, often appearing in combinatorics problems, is defined as $\sum_k r_{k,n,m} x^k$, $r_{m,n,k}$ the number of positions where k rooks do not attack each-other on a n by m checkerboard. An example position counted in $r_{5,8,8}$ is:



⁴ As an example, a famous condensed matter technique, dynamical mean field theory, reduces a bulk model to an impurity model, which is simpler to deal with and cheaper for numerical computations.

Superconductor/insulator transition

Superconducting circuits are well adapted to experimentally emulate bulk Hamiltonians. The simplest case is the one of a 1-dimensional Josephson junctions array, where the junctions geometry is chosen such that $E_J/E_c \sim 1$ for the individual junction. Such a chain is represented on Fig. 7.2. Historically, this area of study emerged as a part of low dimensional superconductivity. We discussed in Chap. 2

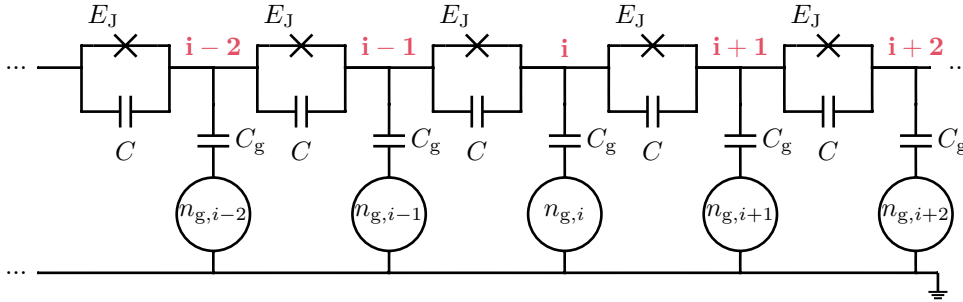


Figure 7.2: A one dimensional array of Josephson junctions. Each superconducting island is biased by a different charge offset $n_{g,i}$.

that Coulomb interaction can suppress superconductivity for small structures, the superconducting island with Josephson junction being the 0-dimensional representative of the phenomenon. Nanowires have long been studied as a continuous 1-dimensional superconducting systems¹, together with Josephson junction chains as its discrete counterpart. They display a phase transition, between a superconducting state and an insulating, Coulomb blockade phase.^{2,3} This model can be mapped onto the quantum sine-Gordon model⁴, which shows that the transition is of Kosterlitz-Thouless type⁵. Only recently, this transition was studied numerically by quantum Monte Carlo technique in the whole parameter space⁶.

The influence of disorder on the transition has been an active topic of research^{7,8}. An important source of disorder is the charge offsets, represented on Fig. 7.2, which can vary from site to site.

Quantum phase slips

The mechanism driving the quantum phase transition is the proliferation of tunneling events called phase slips. Consider the Hamiltonian of Fig. 7.2 circuit without charge offset:

$$\hat{H} = \frac{1}{2} \sum_{ij} \hat{n}_i C_{ij}^{-1} \hat{n}_j - E_J \sum_i \cos(\hat{\varphi}_{i+1} - \hat{\varphi}_i). \quad (7.7)$$

We can first consider classical, static solutions to this problem. the Josephson potential prevents phase variations over short distances. The minimal energy configuration is given by $\varphi_i = 0 \quad \forall i$. An other possible configuration is represented on Fig. 7.3. The phase winds one time over $[-\pi, \pi)$. For $\varphi_0 = \varphi_N = 0$ fixed boundary conditions, it is not possible to unwind the configuration without ‘breaking the thread’, *i.e.* having one junction tunneling suddenly from 0 to 2π . A high energy barrier forbids such transitions at the classical level, but they can be activated by thermal or quantum fluctuations. We can build an effective Hamiltonian to describe the situation: let $|w\rangle$ be the state of w windings around the cylinder. To evaluate the energy of a w windings configuration, we assume that each junction supports the same phase difference, $(2\pi w + \varphi_{\text{ext}})/N \ll 2\pi$ for N junctions and a phase difference φ_{ext} between boundaries. The lineic inductance, for N junctions over a distance d , is $\ell = NL/d$.

¹ A. Bezryadin, C. N. Lau, & M. Tinkham. **2000**. *Nature* 404, 971.

² R. M. Bradley & S. Doniach. **1984**. *Phys. Rev. B* 30, 1138.

³ For a review, *cf.* R. Fazio & H. van der Zant. **2001**. *Phys. Rep.* 355, 235.

⁴ V. Gurarie & A. M. Tsvelik. **2004**. *J. Low Temp. Phys.* 135, 245.

⁵ N. Nagaosa. **1999**. *Quantum Field Theory in Condensed Matter Physics*.

⁶ D. M. Basko, F. Pfeiffer, *et al.* **2020**. *Phys. Rev. B* 101, 024518.

⁷ D. M. Basko & F. W. J. Hekking. **2013**. *Phys. Rev. B* 88, 094507.

⁸ A. E. Svetogorov & D. M. Basko. **2018**. *Phys. Rev. B* 98, 054513.

For small phase differences, we obtain an energy $d/(2\ell)(\varphi_{\text{ext}} + 2\pi w)^2$, such that the effective Hamiltonian writes

$$\hat{H}_{\text{eff}} = \sum_{w \in Z} \frac{d}{2\ell N} (\varphi_{\text{ext}} + 2\pi w)^2 |w\rangle\langle w| - Nt \sum_{w \in Z} |w\rangle\langle w+1| + |w\rangle\langle w-1|. \quad (7.8)$$

the last term represent the tunnel effect, with t the tunneling amplitude for one junction. It is quite noteworthy that this effective Hamiltonian is completely analogous to the one of the charge qBit. The offset charge has been replaced by the total phase difference φ_{ext} . Its spectrum is represented on Fig. 7.4.

Using such a phase slip element in the design of superconducting qBits, to generate non-linearity without charge noise, is a promising route¹. The spectrum periodicity with respect to φ_{ext} of a chain of 6 junctions has been demonstrated², and encountered again in the fluxonium³.

Proliferating winding numbers

The compact ansatz can be adapted to such a situation, to study the quantum phase transition in the presence of charge noise disorder, as well as to provide simple and accurate estimates for spectrum and charge noise of few junctions designs⁴ for qBit oriented circuits.

The main difficulty is that a new winding numbers must be introduced for every junction. The sum over winding numbers then grows exponentially in the number of junctions. This is an important limitation to scale the system towards continuum limit. With a list of winding numbers $\vec{w} = (w_0, \dots, w_\nu, \dots)$, we expect expressions of the form

$$\langle 0 | \hat{C} | 0 \rangle = \sum_{\vec{w} \in Z^N} \exp(-2\pi^2 w_\nu v_{\nu\sigma} v_{\mu\sigma} w_\mu), \quad (7.9)$$

with $v_{\nu\sigma}$ an extension of the v_μ encountered in the impurity problem. The exponential factor has the form of a Boltzmann weight. To compute numerically this sum, we can import the Monte Carlo techniques developed for statistical mechanics, and bypass the exponential growth problem. If ground state observables can be computed this way, it could provide a mean to diagnose the insulator/superconductor transition, especially in the presence of n_{g_i} random charge noise.

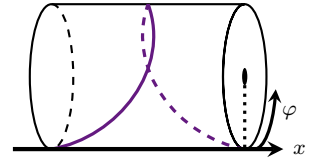


Figure 7.3: A winded field configuration, represented in the continuum limit.

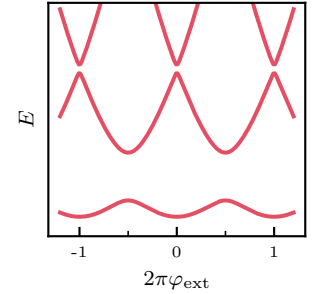


Figure 7.4: Spectrum of a phase slip element composed of a Josephson junction array.

- ¹ H. P. Büchler, V. B. Geshkenbein, & G. Blatter. **2004**. *Phys. Rev. Lett.* **92**, 067007; J. E. Mooij & Y. V. Nazarov. **2006**. *Nat. Phys.* **2**, 169.
- ² I. M. Pop, I. Protopopov, *et al.* **2010**. *Nat. Phys.* **6**, 589.
- ³ H. Meier, R. T. Brierley, *et al.* **2015**. *Phys. Rev. B* **92**, 064516.
- ⁴ A. Mizel & Y. Yanay. **2020**. *Phys. Rev. B* **102**, 014512.

Part III

Boundary Sine-Gordon simulator

8 | Experimental simulator modeling

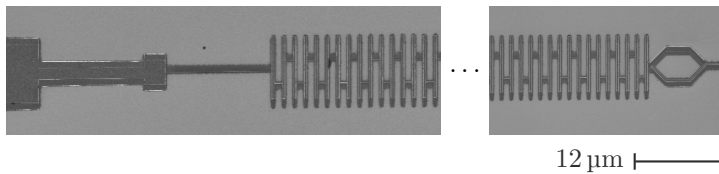
... came Nyarlathotep, swarthy, slender and sinister, always buying strange instruments of glass and metal and combining them into instruments yet stranger. He spoke much of the sciences, and gave exhibitions of power which sent his spectators away speechless.

Lovecraft, *Nyarlathotep*.

Part I discussed several routes to observe many-body effects in superconducting circuits, through the simulation of well known models as spin-boson or boundary sine-Gordon. We characterized the different energy scales and focused on quantum phase transitions as hallmarks of many-body physics. These are properties of the system ground state. Other characterizations of many-body effects are possible, and often easier to access experimentally. In this first chapter on the experimental sine-Gordon simulator, we discuss the expected phenomenology of such a device. We link experimental observables obtained in spectroscopy experiments with the many-body properties of this interacting system, encapsulated in its self-energy function.

Cross-sections of scattering events are often a good tool to probe the non-linear response of a system, since one can easily discriminate between elastic and inelastic scattering events, the latter involving particle creation or annihilation¹. We will see how spectroscopic data can be predicted from calculations beyond perturbative expansion, and how the full microscopic model can be included in the formalism with few approximations.

8.1 Circuit diagram and phenomenology



From the charge-boson model, we learned that the coupling capacitance should be replaced by a wire — effectively taking the $C_c \rightarrow \infty$ limit — in order to maximize coupling strength and avoid offset charge noise *via* decompactification. Such a circuit design is represented on Fig. 8.2. This circuit has been realized in the laboratory², so we can provide some orders of magnitude to better sketch its expected behavior. Its parameters are collected in Tab. 8.1. The circuit itself is shown on Fig. 8.1.

The circuit is composed of a long chain of $N = 4250$ superconducting Josephson junctions, in their linear regime ($E_J \gg E_c$), such that they behave effectively as inductors. The plasma frequency is estimated at $\omega_p/(2\pi) = 1/\sqrt{LC} = 18$ GHz. The chain is terminated by a SQUID³, galvanically coupled to the chain, that allows *in*

- ¹ Cross-sections analysis is ubiquitous in particle physics, but also is relevant for condensed matter and impurity models. *e.g.* the Kondo problem inquires about electron scattering of magnetic impurities. *cf.* J. Kondo. **1964**. *Prog. Theor. Phys.* **32**, 37.
- ² S. Leger, J. Puertas-Martinez, *et al.* **2019**. *Nat. Commun.* **10**, 5259; S. Léger. **2021**, *Electrodynamique Quantique d'une Jonction Josephson Couplée à Un Environnement Fortement Dissipatif*, Ph.D thesis, UGA.

Parameter	Value
N	4250
C	144 fF
C_J	14.5 fF
C_g	0.146 fF
L	0.53 nH
$f_0 \simeq f_p$	18 GHz
Z_c	1.9 k Ω
Z_{tl}	50 Ω

Table 8.1: Microscopic parameters of the circuit, and other important scales.

Figure 8.1: The experimental circuit, imaged by Scanning Electron Microscopy. **left panel.** Connection to the readout line. On the right starts the array of Josephson junctions. **right panel.** End of the chain and terminal SQUID ring.

- ³ U. Vool & M. Devoret. **2017**. *Int. J. Circuit Theory Appl.* **45**, 897.

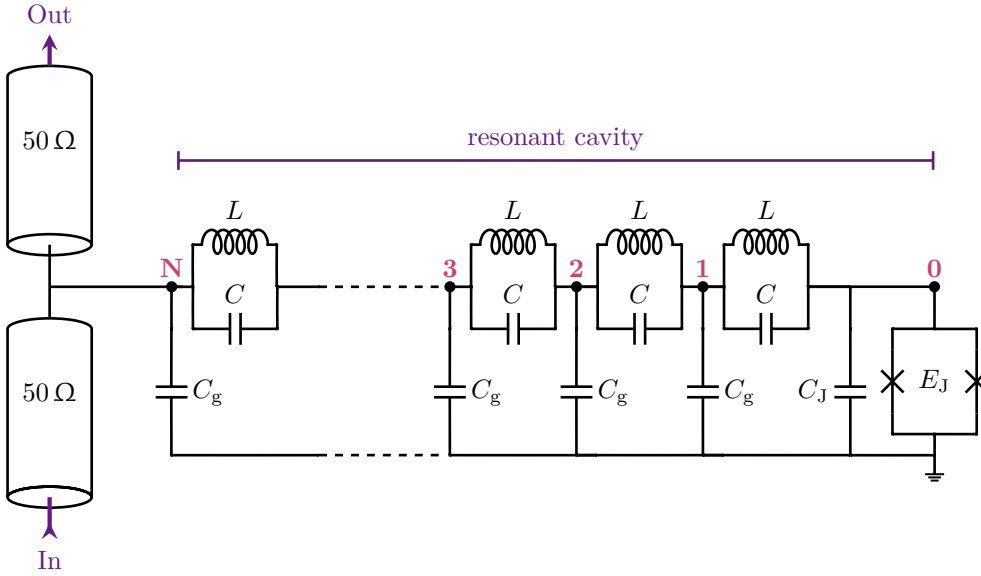


Figure 8.2: The boundary sine-Gordon circuit simulator. A long chain of N junctions forms a bosonic field, strongly coupled *via* a boundary Josephson term by the SQUID on site 0 , with tunable Josephson energy E_J . The chain is side-coupled to the probing $50\ \Omega$ pads.

situ control of E_J using an external magnetic flux threading the SQUID loop. The maximum Josephson energy accessible is $E_J^0/h \simeq 30\ \text{GHz}$. Due to asymmetry effects in the SQUID, the lowest accessible E_J value is not easily determined, and is used as a free parameter.

Phenomenology

The finite chain of junctions is long enough to be considered, in first estimate, as a transmission line of impedance $Z = \sqrt{L/C_g} = 1.9\ \text{k}\Omega$ ¹. The corresponding coupling strength is $\alpha = Z/(2\pi R_q) = 0.3$: according to Sec. 4.5, we should observe a localized phase, with a non-vanishing but strongly renormalized E_J^* scale.

This superconducting transmission line has a finite length, so it behaves like a cavity, with discrete resonances in frequency. When probed by a signal propagating in the $50\ \Omega$ pads, we expect a Fabry-Perot effect: transmission across the chain is only possible close to resonances. Away from a resonance, the chain behaves like an open breaker, so that the transmission between In and Out ports (*cf* Fig. 8.2) is unity. The corresponding Fabry-Perot transmission is sketched on Fig. 8.3. This observable is obtained by spectroscopy, a standard technique in microwave engineering². The two main characteristics of such a curve is the position and width of the resonances. We will see how these quantities are modified by the interactions due to the terminal Josephson junction.

Resonance shifts

In a simple Fabry-Perot experiment, the resonance peaks positions are given by constructive interference conditions: the wave must accumulate a phase of 2π during a round trip in the transmission line, including the phase at reflection. The equivalent circuit is represented on Fig. 8.4. On the left, at contact with the pads, since $25\ \Omega \ll Z_c$, we expect near-perfect reflection. The corresponding phase shift is π . On the right boundary, the reflection coefficient is given by

$$r_1 = \frac{Z_1 + Z_c}{Z_1 - Z_c}. \quad (8.1)$$

¹ As expected from a superconducting chain, the impedance is much higher than vacuum, $376\ \Omega$, reaching ultra-strong coupling.

² S. Leger, J. Puertas-Martinez, *et al.* **2019**. *Nat. Commun.* **10**, 5259; D. M. Pozar. **2011**. *Microwave Engineering*.

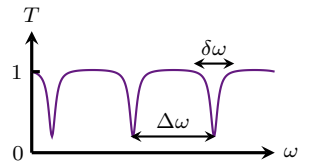


Figure 8.3: The expected transmission between In and Out ports based on Fabry-Perot effect. $\delta\omega$ denotes peak width, and $\Delta\omega$ the free spectral range.

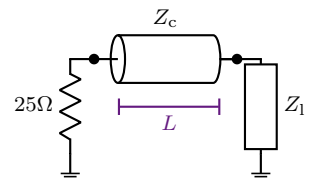


Figure 8.4: Effective circuit for Fabry-Perot effect.

Within quadratic approximation, the right end impedance is modeled by a parallel inductor and capacitor, $1/Z_1 = i\omega C_J + 1/(i\omega L_J)$. With $Z_J = \sqrt{L_J/C_J}$ and $\omega_J = 1/\sqrt{L_J C_J}$, the phase shift on the right is

$$\theta(\omega) = \text{Arg}(r_1) = 2 \arctan \left(\frac{Z_c}{Z_J} \left(\frac{\omega}{\omega_J} - \frac{\omega_J}{\omega} \right) \right). \quad (8.2)$$

The resonance condition is then spelled out as¹

$$k_\ell = \frac{\pi}{N}(\ell + 1/2) + \frac{1}{N}\theta(\omega_\ell). \quad (8.3)$$

Since the boundary condition can be controlled *in situ*, there is a simple way to measure the phase shift at mode ℓ , θ_ℓ , from resonances frequencies. When $E_J \rightarrow 0$, $L_J \rightarrow \infty$, so $\theta \rightarrow \pi$. Let us assume that the modes frequencies are smooth, slowly varying functions of the wavenumber: $\omega_\ell = \omega(k_\ell)$. Then,

$$\omega_\ell = \omega \left(\frac{\pi\ell}{N} + \frac{\theta(E_J=0)}{N} + \frac{\theta(E_J)}{N} \right) \simeq \omega_\ell(E_J=0) + \frac{\theta}{N} \frac{d\omega}{dk} \Big|_{E_J=0}. \quad (8.4)$$

A similar expression is reached if the mode number varies while E_J is kept at zero:

$$\omega_{\ell+1} = \omega \left(\frac{\pi\ell}{N} + \frac{\pi}{N} \right) \simeq \omega_\ell + \frac{\pi}{N} \frac{d\omega}{dk} \Big|_{E_J=0}. \quad (8.5)$$

Combining these results, we reach

$$\theta_\ell(E_J) = \pi \frac{\omega_\ell(E_J) - \omega_\ell(0)}{\omega_{\ell+1}(0) - \omega_\ell(0)}. \quad (8.6)$$

Since Eq. (8.2) provides a link between the phase shift and the boundary inductance $L_J = 1/E_J$, we have an experimental access to the renormalization of E_J when interactions are turned on. This connection between phase shifts of scattering states and properties of the impurity bound state is quite general².

Resonance widths

Still considering a simple, Fabry-Perot like computation, the widths of the resonances are known to be linked to energy losses during a round trip. The first source of losses is simply the energy emitted in the external pads packed together as a $Z_0 = 25 \Omega$ resistor. Let's roughly estimate the associated width. At first order in Z_0/Z_c , the reflection coefficient on the right is $R_r = |r_r|^2 \simeq 1 - 4Z_0/Z_c$. The Fabry-Perot finesse is then³ $\mathcal{F} = \pi Z_c/(2Z_0)$, which translates into a peak width of $\delta\omega \simeq Z_0/Z_c \Delta\omega \simeq 10^{-3}\Delta\omega$, with $\Delta\omega$ the free spectral range. This width is especially thin.

Other dissipation sources are present in superconducting devices, like dissipation in the insulating dielectric layers, called dielectric losses. It has been characterized for superconducting circuits⁴, and its reduction is an important technological factor for improvement of superconducting qBits coherence times⁵. The simplest model for dielectric loss consists in adding a real part to the impedance of a capacitance, $C \rightarrow C(1+i \tan \delta)$, $\tan \delta$ often called the tangent loss factor, a constant for many dielectrics. On our superconducting chain, it adds an imaginary part to the wavenumber. We adapt Sec. 3.2 results for continuous chains: Let a the chain unit cell size, $\kappa_\ell = k_\ell/a$ the dimensional wavenumber, $v = a/\sqrt{LC_g}$ the low-frequency wave velocity. Then, taking the tangent loss into account,

$$\kappa_\ell^2 \simeq \kappa_\ell'^2 + 2i\kappa_\ell'\kappa_\ell'' = \frac{\omega_\ell^2}{v^2} \frac{1}{1 - \frac{\omega_\ell^2}{\omega_p^2}(1 + i \tan \delta)}. \quad (8.7)$$

¹ We use adimensional wavenumber, k , related to the usual wavenumber κ by $k/a = \kappa$. Since $L = Na$, a the unit cell size, $\kappa L = kN$.

² B. S. DeWitt. **1956**. *Phys. Rev.* **103**, 1565.

³ The exact expression is

$$\mathcal{F} = \frac{\pi\sqrt{R}}{1-R}.$$

For more details on Fabry-Perot physics, the French reader can consult

Jolidon. **2021**. *Physique Expérimentale*.

⁴ C. R. H. McRae, R. E. Lake, *et al.* **2020**. *Appl. Phys. Lett.* **116**, 194003.

⁵ J. M. Martinis, K. B. Cooper, *et al.* **2005**. *Phys. Rev. Lett.* **95**, 210503.

We then separate real and imaginary parts of κ_ℓ , that are respectively responsible for propagation and attenuation. The quality factor of mode ℓ is formed as the number of oscillations of the mode during attenuation characteristic time:

$$Q_\ell = \frac{\kappa'_\ell}{\kappa''_\ell} = \frac{2}{\tan \delta} \frac{\omega_p^2}{\omega_\ell^2} \left(1 - \frac{\omega_\ell^2}{\omega_p^2}\right). \quad (8.8)$$

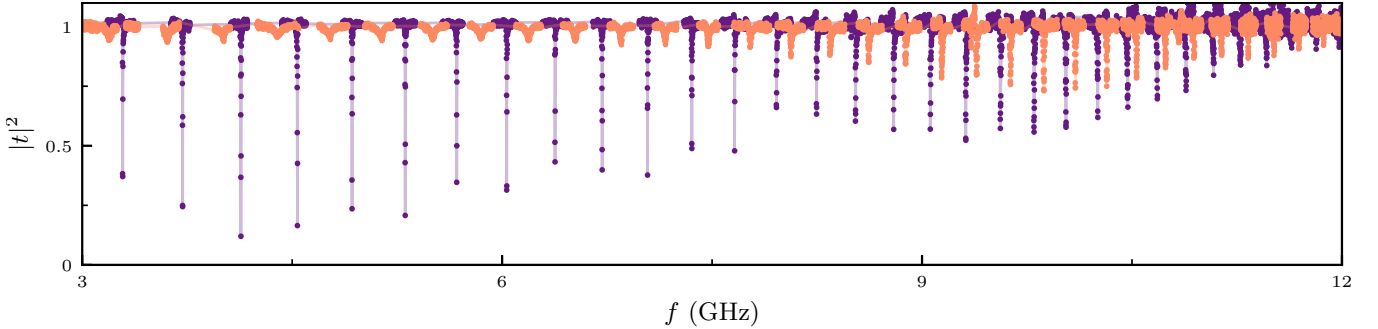
We then expect the quality factor to decrease at high frequency¹. For Al oxide, we estimate $\tan \delta \sim 10^{-3}$. Aside, in the measurement range, the maximum frequency is $\omega_\ell \sim \omega_p/2$. The peak width is then $\delta\omega = (\omega/Q\Delta\omega)\Delta\omega$, with $\Delta\omega$ the free spectral range, estimated at $\Delta\omega \simeq \omega_\ell/100$ in the measurement range. Altogether, $\delta\omega \simeq 10^{-2}\Delta\omega$. Dielectric losses are still a weak broadening mechanism.

A much more interesting broadening mechanism is provided by photon inelastic scattering off the boundary impurity. Expanding the interaction term into²

$$-E_J \cos(\hat{\phi}_0) = -1 + \frac{1}{2}\hat{\phi}_0^2 - \frac{1}{4!}\hat{\phi}_0^4 + \dots, \quad (8.9)$$

we deduce it authorizes photon frequency conversion in any event involving an even number of photons³: $1\gamma \rightarrow 3\gamma$, $2\gamma \rightarrow 2\gamma$, $1\gamma \rightarrow 5\gamma$, *etc.*, provided that the events conserve total energy. the photons scattered to other frequencies can be considered dissipated during a spectroscopy experiment, and contribute to the line width. We will not attempt to weight the order of magnitude of this contribution, since most of this part is devoted to its evaluation. Instead, directly have a look at the experimental data for peak widths.

Experimental resonances



The transmission measured experimentally between the In and Out pads of the sample is represented on Fig. 8.5, for two values of E_J . The calibration of E_J with the external magnetic flux controlling the SQUID is done in Sec. 10.5, where we perform the complete data analysis. For now, we simply notice that we observe the expected serie of well separated resonances, the width of which are strongly depending on E_J . The (●) curve only displays sharp resonances, dominated by dielectric and external losses⁴, while the (●) curve shows widths dramatically enhanced by a factor 10^2 . A close-up on this transmission curve is shown on Fig. 8.9, when we propose a simple model to extract the internal losses from the peak shape.

¹ Experiments seem to show that the $Q \sim 1/\omega^2$ law is too naive, *cf.* Supp. Mat. of: R. Kuzmin, R. Mencia, *et al.* **2019**. *Nat. Phys.* **15**, 930.

² Recall that expressed over eigenmodes,

$$\hat{\phi}_0 = \sum_k \gamma_k \hat{\phi}_k.$$

³ γ is symbol for photon.

Figure 8.5: The experimental transmission measured between In and Out pads for 2 magnetic fluxes in the SQUID loop:

- (●) : $E_J \simeq 27$ GHz,
- (●) : $E_J \simeq 7.7$ GHz.

⁴ As expected, dielectric losses slightly broaden the peaks at high frequency.

8.2 Transmission and Green's functions

Kubo formula

The strong variation of the line widths with E_J together with the high value of α advocates that first order perturbation theory cannot provide accurate results: we immediately prepare the formalism for more powerful methods. We will first reformulate the problem in the language of Green's function, since it is a very natural way to discuss the many-body problem.

Let's first package the whole chain into an admittance Y , as represented on Fig. 8.6. The transmission lines impedance is noted Z_{tl} . The transmission between In and Out ports is then

$$t = \frac{1}{1 + YZ_{tl}/2}. \quad (8.10)$$

We want to include the dissipative effects of the measurement lines onto our computation of the chain admittance, so we add and subtract them: $Y = 1/Z_{tot} - 2/Z_{tl}$. Reporting this in the transmission, we simply end up with

$$t = \frac{2Z_{tot}}{Z_{tl}}. \quad (8.11)$$

Representing the chain as an impedance is equivalent to working within the linear response framework¹. In quantum theory, the linear response is evaluated using the Kubo formula², which states that if a Hamiltonian is perturbed by a term like $\hat{H}_{probe} = \hat{B}f(t)$, the average of an observable \hat{A} is perturbed as

$$\langle \hat{A}(t) \rangle - \langle \hat{A} \rangle_0 = \int_{-\infty}^{\infty} d\tau G_{AB}^R(t - \tau) f(\tau) \quad (8.12)$$

where $\langle \cdot \rangle_0$ is thermal equilibrium average or non-interacting vacuum state average at $T = 0$, and

$$G_{AB}^R(t - \tau) = G_{AB}^R(t, \tau) = -i\theta(t - \tau) \langle [\hat{A}(t), \hat{B}(\tau)] \rangle \quad (8.13)$$

is the retarded Green's function between operators \hat{A} and \hat{B} . Moving to frequency space using a Fourier transform,

$$\langle \hat{A}(\omega) \rangle = G_{AB}^R(\omega) f(\omega), \quad (8.14)$$

which is the sought-after proportionality between probe and response. A current bias on a superconducting island n is represented by a driving term $-I(t)\hat{\phi}_n$ ³. The voltage between site n and ground is given by $U = \hat{\phi}$, such that

$$U(\omega) = -i\omega \langle \hat{\phi}_n \rangle = i\omega G_{\phi_n \phi_n}^R I(\omega). \quad (8.15)$$

From this equation, we read the impedance of the full chain in terms of the phase-phase Green's function of terminal site \mathbf{N} , so that the transmission is

$$t = \frac{2i\omega}{Z_{tl}} G_{\phi_N \phi_N}^R. \quad (8.16)$$

Equations of motion

The Green's function obeys equations of motion very similar to the ones obeyed by operators in Heisenberg's picture. Let's derive them for the model of Fig. 8.2. Let's

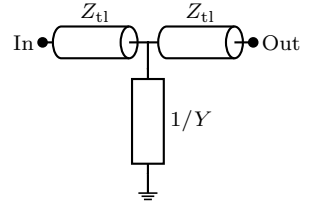


Figure 8.6: Full circuit, with the superconducting chain lumped into an admittance Y .

¹ Only the measurement line coupling to the system is treated as linear. This bears no assumption on the terminal Josephson junction non-linearity.

² H. Bruus & K. Flensberg. 2004. *Many-Body Quantum Theory in Condensed Matter Physics*.

³ One can check that the corresponding equation of motion is equivalent to adding a current generator in parallel between the site and ground.

first unplug the non-linear element by taking $E_J = 0$, and removing the external transmission lines. The complete capacitance and inductance matrices are \mathbf{C} and $1/L$, and the corresponding Hamiltonian writes

$$\hat{H}(E_J = 0) = \frac{1}{2} \hat{\mathbf{n}}^\top \mathbf{C}^{-1} \hat{\mathbf{n}} + \frac{1}{2} \hat{\phi}^\top 1/L \hat{\phi}. \quad (8.17)$$

The equation of motion is obtained by computing time derivatives¹:

$$\begin{aligned} i\partial_t G_{\phi_i \phi_j}(t, t') &= \delta(t) \left\langle \left[\hat{\phi}_i(t), \hat{\phi}_j(t) \right] \right\rangle - i\theta(t-t') \left\langle \left[i\partial_t \hat{\phi}_i(t), \hat{\phi}_j(t') \right] \right\rangle \\ &= i \sum_m (\mathbf{C}^{-1})_{im} G_{n_n \phi_j}. \end{aligned} \quad (8.18)$$

A second derivative yields the equation of motion. Since this last equation hints towards a matrix structure, we define a matrix of Green's functions as $\mathbf{G}_{ij} = G_{\phi_i \phi_j}$, and the equation of motion in frequency space is

$$(\omega^2 \mathbf{C} - 1/L) \mathbf{G} = \mathbf{1}. \quad (8.19)$$

There is a connection to the diagonalization procedure we followed in Sec. 3.1. Assume we find a change of basis \mathbf{P} such that $\mathbf{P}^\top \mathbf{C} \mathbf{P} = \mathbf{1}^2$ and $\mathbf{P}^\top 1/L \mathbf{P} = \boldsymbol{\omega}^2$, $\boldsymbol{\omega}$ a diagonal, positive matrix. Eq. 8.19 is rewritten in this base as

$$\begin{aligned} \mathbf{P}^\top (\omega^2 \mathbf{C} - 1/L) \mathbf{P} \mathbf{P}^{-1} \mathbf{G} \mathbf{C} \mathbf{P} &= \mathbf{P}^\top \mathbf{C} \mathbf{P} = \mathbf{1} \\ \Rightarrow (\omega^2 \mathbf{1} - \boldsymbol{\omega}^2) \bar{\mathbf{G}} &= \mathbf{1}, \end{aligned} \quad (8.20)$$

where we defined $\bar{\mathbf{G}} = \mathbf{P}^\top \mathbf{C} \mathbf{G} \mathbf{C} \mathbf{P}$ the matrix of modes Green's functions. Inverting the relation, we obtain $\mathbf{P} \bar{\mathbf{G}} \mathbf{P}^\top = \mathbf{G}$. This is coherent with a change of basis in the Green's function definition:

$$\mathbf{G}_{ij}(t, t') = -i\theta(t-t') \left\langle \left[\hat{\phi}_i(t), \hat{\phi}_j(t') \right] \right\rangle = \sum_{k\ell} \mathbf{P}_{ik} \mathbf{P}_{j\ell} \underbrace{\left(-i\theta(t-t') \left\langle \left[\hat{\phi}_k(t), \hat{\phi}_\ell(t') \right] \right\rangle \right)}_{\bar{\mathbf{G}}_{k\ell}(t, t')}. \quad (8.21)$$

Since $\bar{\mathbf{G}}$ inverse is clearly diagonal, we see that this change of basis solved the Green's function equation of motion. We deduce

$$\bar{\mathbf{G}}_{k\ell}(\omega) = \frac{\delta_{k\ell}}{\omega^2 - \omega_k^2} \quad \text{and} \quad \mathbf{G}_{ij}(\omega) = \sum_k \frac{\mathbf{P}_{ik} \mathbf{P}_{jk}}{\omega^2 - \omega_k^2}. \quad (8.22)$$

We recognize a harmonic oscillator/bosonic Green's function³.

Resistors and dissipation

Sec. 4.1 made the connection between infinite transmission lines of impedance Z and dissipation: energy emitted as waves in the line is effectively lost to the system. The transmission line then behaves as resistor of resistance $R = Z$. The elimination of the transmission line degrees of freedom we performed in the equation of motion can be repeated in the Green's function equation of motion. For $1/R$ a matrix of inverse resistances,

$$(\omega^2 \mathbf{C} - 1/L + i\omega 1/R) \mathbf{G}^R = \mathbf{1}. \quad (8.23)$$

Adding the dissipation provides a prescription for the Green's function. In this case, the retarded Green's function is computed. To see this, let us first inquire the simple case of dielectric losses, where the resistance matrix is assumed to take the same structure as the capacitance matrix: $1/R = \mathbf{C}/(R_0 C_0)$, with $R_0 C_0 = \tau$ a time constant.

¹ The R symbol is dropped, since this computation is valid for all Green's function prescriptions.

² Which allows to find inverses of \mathbf{P} and \mathbf{C} , useful in the following computation.

³ We see that the regularization prescription for poles is indeed lacking.

The equation of motion is then solved by the same change of basis \mathbf{P} , which results in

$$\bar{\mathbf{G}}_{k\ell}(\omega) = \frac{\delta_{k\ell}}{\omega^2 - \omega_k^2 + i\frac{\omega\omega_k}{Q_k}} \quad \text{and} \quad \bar{\mathbf{G}}_{\ell\ell}(t) = \int_{-\infty}^{\infty} \frac{d\omega}{2\pi} \frac{e^{-i\omega t}}{\omega^2 - \omega_\ell^2 + i\frac{\omega\omega_\ell}{Q_\ell}}, \quad (8.24)$$

We defined a quality factor for mode k by $\tau = Q_k/\omega_k$ ¹. The poles are represented on Fig. 8.7, their imaginary parts are always negative. Integration using residue theorem shows that $\bar{\mathbf{G}}_{\ell\ell}(t < 0) = 0$, as expected by causality for the retarded Green's function. It is noteworthy that choosing the Feynman prescription in Sec. 4.1² would have led to a dissipation term of the form

$$(\mathbf{G}^F)^{-1} = \omega^2 \mathbf{C} - 1/L + i|\omega|/R, \quad (8.25)$$

thus resulting in computing the Feynman Green's function, as we would expect. Finally, we can check that the retarded and Feynman Green's functions are related by³

$$G^F(\omega) = \text{Re } G^R(\omega) + i \text{sign}(\omega) \text{Im } G^R(\omega). \quad (8.26)$$

The 50 Ω pad have a resistance matrix with null entries everywhere except at (N, N) . Noting \mathbf{E}^{ij} the elementary matrices defined by $\mathbf{E}_{mn}^{ij} = \delta_{im}\delta_{jn}$, the corresponding inverse Green's function is

$$\left(\omega^2 \mathbf{C} - 1/L + i\frac{2\omega}{Z_{\text{tl}}} \mathbf{E}^{NN} \right) \mathbf{G}^R = \mathbf{1}. \quad (8.27)$$

Self-energy

The last equation of motion is still written for $E_J = 0$, and is thus linear. All the non-linearity can be factored in the self-energy, a complex function of frequency, using Dyson's equation: if G° is the Green's function associated to the linear part of some Hamiltonian, turning the interactions on corrects it by

$$G(\omega) = \frac{G^\circ(\omega)}{1 - G^\circ(\omega)\Sigma(\omega)}, \quad (8.28)$$

where Σ is the self-energy. We will demonstrate this equation and explain how to compute Σ in Chap. 9, using diagrammatic techniques. For now, we will simply give a simple interpretation of the self-energy: when added into \mathbf{G}^{-1} in Eq. (8.27), we obtain

$$\left(\omega^2 \mathbf{C} - 1/L + i\frac{2\omega}{Z_{\text{tl}}} \mathbf{E}^{NN} - \Sigma(\omega) \mathbf{E}^{00} \right) \mathbf{G}^R = \mathbf{1}. \quad (8.29)$$

A constant, real part in Σ simply renormalizes the inductance on site 0, while the linear dependence of its imaginary part acts as a resistor on the same site:

$$\Sigma(\omega) = \frac{1}{L_j^*} - i\frac{\omega}{R_j^*} + o(\omega). \quad (8.30)$$

This equation will be made rigorous in Chap. 9, where $\text{Re } \Sigma(\omega)$ will be shown to be even, and $\text{Im } \Sigma(\omega)$ odd, with negative slope.

8.3 Transmission spectroscopy

We have narrowed down the prediction of spectroscopy experiments to the determination of a single function of frequency, Σ . Before diving into its determination, we can first elaborate on how exactly the self-energy affects the transmission spectrum, and especially the position and width of transmission peaks. We will first parameterize the problem with an equivalent classical model, the hanging resonator, and then search for an analogous transmission expression as function of the self-energy.

¹ The model could be extended easily to $1/R$ co-diagonal with \mathbf{C} , resulting in τ depending on k .

² It corresponds to

$$\frac{1}{\nu^2 - \omega^2} \rightarrow \frac{1}{\nu^2 - \omega^2 + i\epsilon}$$

in the integrand.

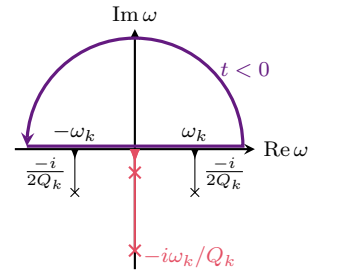


Figure 8.7: Green's function poles in complex ω plane. (●) $Q > 1/2$, (●) $Q < 1/2$. (●) Residue theorem contour. ³ R. D. Mattuck. 1976. *A Guide to Feynman Diagrams in the Many-body Problem*.

Hanging resonator

Around a peak, we mainly probe one mode of the system. The classical equivalent circuit¹ is represented on Fig. 8.8. With the usual definitions $Z_0 = \sqrt{L/C}$, $\omega_0 = 1/\sqrt{LC}$, the transmission assumes the form

$$t = \frac{1 + 2i \frac{Z_0}{R} \frac{\omega - \omega_0}{\omega_0}}{\left(1 + \frac{Z_{t1}}{2R}\right) + 2i \frac{Z_0}{R} \frac{\omega - \omega_0}{\omega_0}}. \quad (8.31)$$

We define internal and external quality factors as $Q_i = Z_0/R$ and $Q_e = Z_{t1}/(2R)$. $1 - |t|^2$ is a Lorentzian line shape, centered on ω_0 , of half-width $\delta\omega$

$$\frac{\Delta\omega}{\omega_0} = \frac{1}{Q_e} + \frac{1}{Q_i}. \quad (8.32)$$

The two quality factors respectively weight the losses due to the external pads, and internal losses.²

We can test this model on the experimental transmission. A close-up on a single transmission peak is shown on Fig. 8.9, together with the best fit to the hanging resonator transmission, with Q_i and Q_e as free parameters, while ω_0 is determined independently by locating the maximum. A small asymmetry is present in the data, especially for the weak losses case. This could be accounted for by adding parasitic inductances in the T-shaped connection to the external pad. More importantly, even if turning on the interaction spectacularly lowered the internal quality factor, the Lorentzian line shape is preserved.

Full chain resonator

We now want to compute \mathbf{G}_{NN}^R by inverting Eq. (8.29), and plugging it in the transmission, Eq. (8.16). We already saw that there exist a basis where chain eigenmodes decouple, which is signaled by the inverse Green's function being diagonal. We will postpone finding this change of basis \mathbf{P} until Chap. 9, since we only need to know its existence for now. We call $\mathbf{G}^{\circ\circ}$ the retarded green function³ computed without external dissipation of self-energy. The equation of motion is then

$$\left(\mathbf{G}^{\circ\circ-1} + i \frac{2\omega}{Z_{t1}} \mathbf{E}^{NN} - \Sigma(\omega) \mathbf{E}^{00}\right) \mathbf{G} = \mathbf{1}. \quad (8.33)$$

We are left with rank one corrections to the inverse of \mathbf{G} . Let's start by including external dissipation: we call \mathbf{G}° the solution of

$$\left(\mathbf{G}^{\circ\circ-1} + i \frac{2\omega}{Z_{t1}} \mathbf{E}^{NN}\right) \mathbf{G}^\circ = \mathbf{1}. \quad (8.34)$$

Multiplying by $\mathbf{G}^{\circ\circ}$ and writing elements $(0,0)$, $(0,N)$, (N,N) of this equation, we can always isolate \mathbf{G}° elements, to get

$$\begin{aligned} \mathbf{G}_{NN}^\circ &= \frac{\mathbf{G}_{NN}^{\circ\circ}}{1 + \frac{2i\omega}{Z_{t1}} \mathbf{G}_{NN}^{\circ\circ}}, & \mathbf{G}_{N0}^\circ &= \frac{\mathbf{G}_{N0}^{\circ\circ}}{1 + \frac{2i\omega}{Z_{t1}} \mathbf{G}_{NN}^{\circ\circ}}, \\ \mathbf{G}_{00}^\circ &= \frac{\mathbf{G}_{00}^{\circ\circ} + \frac{2i\omega}{Z_{t1}} (\mathbf{G}_{NN}^{\circ\circ} \mathbf{G}_{00}^{\circ\circ} - \mathbf{G}_{N0}^{\circ\circ 2})}{1 + \frac{2i\omega}{Z_{t1}} \mathbf{G}_{NN}^{\circ\circ}}. \end{aligned} \quad (8.35)$$

We made use of $\mathbf{G}_{N0}^{\circ\circ} = \mathbf{G}_{0N}^{\circ\circ}$ which implies $\mathbf{G}_{N0}^\circ = \mathbf{G}_{0N}^\circ$. Using the inverse of \mathbf{G}° , the complete equation of motion is then

$$\left(\mathbf{G}^{\circ-1} - \Sigma \mathbf{E}^{00}\right) \mathbf{G} = \mathbf{1}. \quad (8.36)$$

¹ D. M. Pozar. 2011. *Microwave Engineering*.

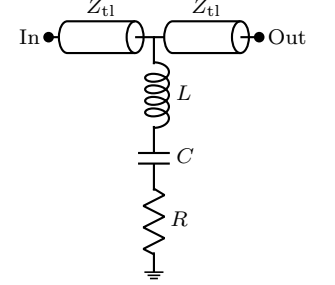


Figure 8.8: Hanging resonator model.

² One can especially check the $Q_i \rightarrow \infty$ limit: in that case,

$$1 - |t|^2 = \frac{1}{1 + (2Q_e)^2 \left(\frac{\omega - \omega_0}{\omega_0}\right)^2},$$

a Lorentzian with unit reflection at $\omega = \omega_0$, as expected.

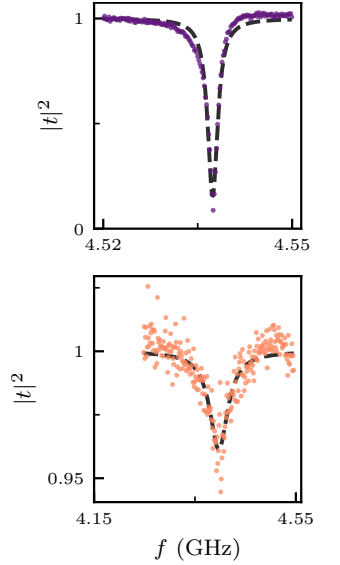


Figure 8.9: Detail of measured transmission, (●) $E_j \simeq 27$ GHz, $Q_i = 6100$, (●) $E_j \simeq 7.7$ GHz, $Q_i = 100$, (--) Adjustment to hanging resonator model.

³ We dropped again the R exponent, since the regularization choice is clear.

The same technique allows to isolate the sought-after Green's function:

$$\mathbf{G}_{NN} = \frac{\mathbf{G}_{NN}^{\circ\circ} + \Sigma (\mathbf{G}_{N0}^{\circ\circ 2} - \mathbf{G}_{NN}^{\circ\circ} \mathbf{G}_{00}^{\circ\circ})}{1 + \frac{2i\omega}{Z_{t1}} \mathbf{G}_{NN}^{\circ\circ} - \Sigma \left(\mathbf{G}_{00}^{\circ\circ} - \frac{2i\omega}{Z_{t1}} (\mathbf{G}_{N0}^{\circ\circ 2} - \mathbf{G}_{NN}^{\circ\circ} \mathbf{G}_{00}^{\circ\circ}) \right)}. \quad (8.37)$$

This last equation relates the self-energy with the transmission, all other quantities in the expression being known. For now, the interpretation is obscured by the size of the equation: we will make some approximations to highlight better the connection between transmission and self-energy.

Let's write the $\Sigma \rightarrow 0$ limit of the transmission:

$$t(\Sigma = 0) = \frac{2i\omega}{Z_{t1}} \frac{\mathbf{G}_{NN}^{\circ\circ}}{1 + \frac{2i\omega}{Z_{t1}} \mathbf{G}_{NN}^{\circ\circ}}. \quad (8.38)$$

Transmission vanishes at zeroes of $\mathbf{G}_{NN}^{\circ\circ}$ ¹. We will then develop Eq. (8.37) around such a zero, all other quantities being considered constant in the vicinity of the transmission peak. $\mathbf{G}_{NN}^{\circ\circ}$ is expressed as a sum over poles using Eq. (8.22). Zeros are located between poles, so we limit the expression of $\mathbf{G}_{NN}^{\circ\circ}$ at these two neighbouring poles:

$$\mathbf{G}_{NN}^{\circ\circ} = \frac{\mathbf{P}_{N1}^2}{\omega_1^2 - \omega^2} + \frac{\mathbf{P}_{N2}^2}{\omega_2^2 - \omega^2}. \quad (8.39)$$

ω_k and $\mathbf{P}_{0k}, \mathbf{P}_{Nk}$ are slowly varying functions of k . We define

$$\begin{cases} \bar{\omega} = (\omega_1 + \omega_2)/2 \\ \Delta\omega = (\omega_2 - \omega_1)/2 \end{cases}, \quad \begin{cases} \bar{p}_0 = (\mathbf{P}_{01} + \mathbf{P}_{02})/2 \\ \Delta p_0 = (\mathbf{P}_{02} - \mathbf{P}_{01})/2 \end{cases}, \quad \begin{cases} \bar{p}_N = (\mathbf{P}_{N1} + \mathbf{P}_{N2})/2 \\ \Delta p_N = (\mathbf{P}_{N2} - \mathbf{P}_{N1})/2 \end{cases}, \quad (8.40)$$

and the slow variation translate as $\Delta\omega/\bar{\omega}, \Delta p_0/\bar{p}_0, \Delta p_N/\bar{p}_N \ll 1$. In this approximation, the zero of $\mathbf{G}_{NN}^{\circ\circ}$ bracketed by the two poles is located at ω_0 given by

$$\omega_0^2 = \bar{\omega}^2 \left(1 + \left(\frac{\Delta\omega}{\bar{\omega}} \right)^2 - \left(\frac{\Delta\omega}{\bar{\omega}} \right) \left(\frac{\Delta p_N}{\bar{p}_N} \right) + \dots \right) \simeq \bar{\omega}^2. \quad (8.41)$$

Close to this zero, we expand $\mathbf{G}_{NN}^{\circ\circ}$ at first order,

$$\mathbf{G}_{NN}^{\circ\circ} \simeq (\omega - \omega_0) \left. \frac{d\mathbf{G}_{NN}^{\circ\circ}}{d\omega} \right|_{\omega_0}, \quad (8.42)$$

and with the same approximation, transmission takes the form

$$t = \frac{\mathbf{G}_{NN}^{\circ\circ} + \Sigma \mathbf{G}_{N0}^{\circ\circ 2}}{\frac{Z_{t1}}{2i\omega} (1 - \Sigma \mathbf{G}_{00}^{\circ\circ}) + \mathbf{G}_{NN}^{\circ\circ} + \Sigma \mathbf{G}_{N0}^{\circ\circ 2}}. \quad (8.43)$$

The real part of Σ can be absorbed in a displacement of ω_0 . At this point, we recognize the transmission shape of the hanging resonator: $\text{Re } \Sigma$ displace the transmission peak, while $\text{Im } \Sigma$ is responsible for the internal losses, Q_i . Quantitatively, the two effects are:

$$\omega_0 = \bar{\omega} - \mathbf{G}_{N0}^{\circ\circ 2} \left(\left. \frac{d\mathbf{G}_{NN}^{\circ\circ}}{d\omega} \right|_{\omega_0} \right)^{-1} \text{Re } \Sigma \quad \text{and} \quad Q_i = -\frac{\bar{\omega}}{2\mathbf{G}_{N0}^{\circ\circ 2} \text{Im } \Sigma} \left. \frac{d\mathbf{G}_{NN}^{\circ\circ}}{d\omega} \right|_{\omega_0}. \quad (8.44)$$

To conclude, we need to compute, still at lowest order in all our approximations, the $(N, 0)$ Green's function square and (N, N) Green's function derivative. For the first one, we have

$$\mathbf{G}_{N0}^{\circ\circ} = \sum_k (-1)^k \frac{P_{0k} P_{Nk}}{\omega^2 - \omega_k^2} \simeq \frac{P_{01} P_{N1}}{\omega^2 - \omega_1^2} - \frac{P_{02} P_{N2}}{\omega^2 - \omega_2^2} \simeq \frac{\bar{p}_0 \bar{p}_N}{\bar{\omega} \Delta\omega}. \quad (8.45)$$

¹ This can be understood, since connection to Z_{t1} drastically changes the boundary conditions of the chain, from free to almost pinned at the left end.

The $(-1)^k$ signs can be understood in the following way: the \mathbf{P} matrix is formed of eigenvectors, which are determined up to a sign. Only products like $\mathbf{P}_{0k}\mathbf{P}_{Nk}$ have a well defined sign. Since \mathbf{P}_{0k} and \mathbf{P}_{Nk} represents the weight of mode k on the first and last site respectively, the sign of the product indicates if chain ends oscillate in phase or in phase opposition. The Fig. 8.10 represents the situation. When k is increased by 1, one vibration node is added to the standing wave, and the sign alternates.

The previous result can be refined by including all poles beyond the two neighbors, assuming they are all equally separated by $2\Delta\omega$. Then¹,

$$\mathbf{G}_{N0}^{\circ\circ} \simeq \frac{\bar{p}_0\bar{p}_N}{\bar{\omega}\Delta\omega} \left(1 - \frac{1}{3} + \frac{1}{5} - \frac{1}{7} + \dots \right) = \frac{\pi\bar{p}_0\bar{p}_N}{4\bar{\omega}\Delta\omega}. \quad (8.46)$$

Similarly, the derivative of interest can be computed by²

$$\left. \frac{d}{d\omega} \left(\sum_k \frac{\mathbf{P}_{Nk}^2}{\omega^2 - \omega_k^2} \right) \right|_{\omega_0} \simeq -\frac{\bar{p}_N^2}{\omega_0\Delta\omega^2} \left(1 + \frac{1}{3^2} + \frac{1}{5^2} + \dots \right) = -\frac{\pi^2}{8} \frac{\bar{p}_N^2}{\omega_0\Delta\omega^2}. \quad (8.47)$$

These results are combined to provide the k^{th} mode peak displacement due to the self-energy:

$$\omega_0 - \bar{\omega} = \frac{\bar{p}_0^2}{2\bar{\omega}} \text{Re } \Sigma \quad \Rightarrow \quad D\omega_k = \gamma_k \text{Re } \Sigma(\omega_k). \quad (8.48)$$

In the last expression, we brought back the k dependence of relevant quantities, and defined, by analogy with Part. I, $\gamma_k = g_k/\omega_k = \mathbf{P}_{0k}/\sqrt{2\omega_k}$. Note that adding the contribution of all poles corrected the result by a factor of 2, crucial for quantitative comparison to experiment. Similarly, the internal dissipation contribution to k^{th} peak half-width is

$$\delta\omega_k = \frac{\omega_k}{Q_i} = 2\gamma_k \text{Im } \Sigma(\omega_k). \quad (8.49)$$

We retrieved the intuitive result that real part of the self-energy shifts the resonance peaks and its imaginary part contributes to their widths. The initial and resulting line shapes are represented on Fig. 8.11. Provided that Σ is constant over the line shape, the predicted profile stays Lorentzian.



Figure 8.10: The sign of $\mathbf{P}_{0k}\mathbf{P}_{Nk}$ indicates if ends of the chain oscillate in phase, or in phase opposition, in the mode k .

¹ We recognized the arctan power series.

² The corresponding series can be related to $\zeta(2)$, ζ the zeta Riemann function.

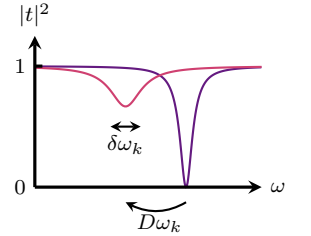


Figure 8.11:

(●) Line shape at $\Sigma = 0$. The width is finite, and minimum transmission is 0.

(●) Line shape displaced of $D\omega_k$ and broadened of $\delta\omega_k$ for $\Sigma \neq 0$.

9 | Analytical insights from the continuum limit

[En mathématiques,] la foi du charbonnier a donc ses périls; d'ailleurs, on ne peut être en contact avec des expérimentateurs sérieux sans être frappé du soin extrême qu'ils apportent à s'assurer de la correction de leurs mesures et à se garder d'interprétations fallacieuses; manier proprement les mathématiques demande un soin égal.

Dieudonné, *Calcul infinitésimal*.

Concerning mathematics, simple-minded faith does not go without risks. Similarly, one cannot talk with serious experimentalists without being struck by the extreme care they take to ensure their data's validity, and to avoid any misleading interpretations. The same care is required for handling mathematics.

In this chapter, we will inquire about the self-energy, focusing on analytical results. The Chap. 10 will lift most of the approximations used here to describe the circuit, at the cost of resorting to numerical computation. While more approximate, analytical approaches usually provide stronger understanding of the physics at play, by reducing the situation to a handful of important scales and adimensional numbers that set the qualitative behavior of the physics. Here, this role is played by two scales, the renormalized Josephson energy E_J^* and the ultraviolet cutoff ω_c , which drives the physics together with the interaction strength α . Temperature will be added to the picture in Sec. 10.2.

We will first establish the expression for the spectral function from the microscopic model, and then take the continuum limit. We detail next the diagrammatic expansion which properly defines the self-energy. We will finally discuss the first order approximation, which provides another route to the SCHA equation. In turn, the second order will provide the dissipative part of the self-energy.

9.1 BSG Spectral density

The goal of this section is to find an expression for the \mathbf{P}_{0k} in the BSG microscopic model proposed at Fig. 8.2, which will be used to build the continuous spectral density. To do so, we can rely on the similar work we did in Sec. 3.3. We will include in our modeling the inductance $L_J = 1/E_J$ approximating at quadratic order the terminal junction. This prepares the self-consistent approximation we will perform in the next section, Sec. 9.2.

The capacitance and inductance matrices corresponding to Fig. 8.2 are:

$$\mathbf{C} = \begin{bmatrix} C_J + C & -C & & & \\ -C & 2C + C_g & -C & & \\ & -C & 2C + C_g & -C & \\ & & & & \ddots \end{bmatrix}, \quad \mathbf{1/L} = \frac{1}{L} \begin{bmatrix} 1 + L/L_J & -1 & & & \\ -1 & 2 & -1 & & \\ & -1 & 2 & -1 & \\ & & & & \ddots \end{bmatrix}. \quad (9.1)$$

\mathbf{P} is the matrix of eigenvectors solution to the generalized eigenvalue problem $\mathbf{1/LP} = \mathbf{CP}\omega^2$, with ω the diagonal matrix containing the eigenfrequencies of the system. In the new basis $\vec{\phi} = \mathbf{P}\vec{\varphi}$, the system's Hamiltonian is diagonal plus boundary Josephson

energy:

$$\hat{H} = \frac{1}{2} (\hat{n}_i \mathbf{C}_{ij}^{-1} \hat{n}_j + \hat{\varphi}_i \mathbf{1}/L_{ij} \hat{\varphi}_j) - \frac{E_J}{2} \hat{\varphi}_0^2 - E_J \cos(\hat{\phi}_0). \quad (9.2)$$

Rewriting this expression with creation and annihilation operators¹, we get

$$\hat{H} = \omega_k \hat{a}_k^\dagger \hat{a}_k - \frac{E_J}{2} (\gamma_q (\hat{a}_q^\dagger + \hat{a}_q))^2 - E_J \cos(\gamma_\ell (\hat{a}_\ell^\dagger + \hat{a}_\ell)). \quad (9.3)$$

The mode-by-mode couplings, $\gamma_k = \mathbf{P}_{0k}/\sqrt{2\omega_k}$, have a consistent definition with Sec. 4.5, where they were defined from the BSG limit of the charge-boson Hamiltonian, and provided that $\gamma_k = g_k/\omega_k$. We now set aside the second and third term in the right hand side, which will be considered as interactions in the next sections. We want to compute the spectral density $A(\omega) = N\gamma^2(\omega)dk/d\omega^2$, and expect $A(\omega) \simeq 2\pi\alpha/\omega$ in the Ohmic limit³.

This eigenproblem is very similar to the one of Sec. 3.3. The bulk relation and the normalization of the plane wave ansatz are still valid, and only the boundary condition is modified,

$$\mathbf{P}_{1\ell} = \mathbf{P}_{0\ell} \left(1 + \frac{C_J}{C} \frac{\omega_J^2 - \omega_\ell^2}{\omega_0^2 - \omega_\ell^2} \right). \quad (9.4)$$

The characteristic frequencies are the half band-width $\omega_0 = 1/\sqrt{LC}$, the plasma frequency $\omega_p^2 = \omega_0^2/\sqrt{1 + C_g/4C}$, and the small junction frequency $\omega_J = 1/\sqrt{L_J C_J}$. We plug the ansatz $\mathbf{P}_{j\ell} = N_\ell \cos(jk_\ell + \delta_\ell)$ into this boundary equation to determine the phase shift⁴

$$\tan(\delta_\ell) = \tan\left(\frac{k_\ell}{2}\right) \left(2\frac{C_J}{C_g} - 1 + 2\frac{C_J}{C_g} \frac{\omega_J^2}{\omega_\ell^2} \right). \quad (9.5)$$

We use this result to compute $\cos^2 \delta_\ell$, using $\cos^2(\theta) = 1/(1 + \tan^2(\theta))$.

$$\cos^2(\delta_\ell) = \frac{1 - \omega_\ell^2/\omega_p^2}{1 - \omega_\ell^2/\omega_p^2 + Z_c^2 ((C_J - C_g/2)\omega_\ell - 1/(L_J\omega_\ell))^2}. \quad (9.6)$$

In the continuum limit, $C_g \rightarrow 0$, while $Z_c = \sqrt{L/C_g}$ stays constant. Together with the other results of Sec. 3.3, the spectral density writes

$$A(\omega) = \frac{Z_c}{\omega} \frac{\sqrt{1 - \omega^2/\omega_p^2}}{1 - \frac{\omega^2}{\omega_p^2} + \frac{Z_c^2}{Z_J^2} \left(\frac{\omega}{\omega_J} - \frac{\omega_J}{\omega} \right)^2} \theta(\omega_p - \omega). \quad (9.7)$$

The plasma pulsation provides a hard ultraviolet cutoff. Well below ω_p , we approximate the spectral density to

$$A(\omega) = \frac{Z_c}{\omega} \frac{1}{1 + \frac{Z_c^2}{Z_J^2} \left(\frac{\omega}{\omega_J} - \frac{\omega_J}{\omega} \right)^2}. \quad (9.8)$$

We recognize the expected Ohmic $2\pi\alpha/\omega$ behavior, with $2\pi\alpha = Z_c$, multiplied by a band-pass filter factor centered on the small junction characteristic frequency. Two regimes must be considered:

- $Z_c/Z_J \gg 1$: In this case, if $\omega > \omega_J$, $\omega > \omega_J Z_J/Z_c$ is also verified. There are only two frequency regions, of power laws $\omega A(\omega) \sim \omega^2$ and $\sim \omega^{-2}$ respectively, separated by a sharp resonance peak. In this case, the response of site 0 is similar to an isolated small junction.
- $Z_c/Z_J \ll 1$: Here, a third region appears. If $Z_c/L_J < \omega < 1/(Z_c C_J)$, the band-pass filter factor is flat. There is no resonance due to the small junction, which completely hybridizes with the continuum of modes from the array.

¹ Again,

$$\begin{cases} \hat{\varphi}_k = \sqrt{1/2\omega_k} (\hat{a}_k^\dagger + \hat{a}_k) \\ \hat{n}_k = i\sqrt{\omega_k/2} (\hat{a}_k^\dagger - \hat{a}_k) \end{cases}$$

² This spectral function includes the terminal junction, at least at quadratic order, so we employ a different symbol to differentiate it from J , the bath spectral density.

³ The litterature uses the same symbol for the density of g_k and the one of γ_k .

⁴ One can check that in the continuum limit, this equation agrees with Eq. 8.2.

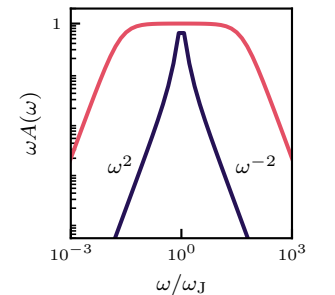


Figure 9.1: Band-pass filter effect in the spectral density. (•) $Z_c/Z_J \gg 1$, (•) $Z_c/Z_J \ll 1$.

We focus on the $Z_c/Z_J \ll 1$ case, which corresponds to low E_J and strong hybridization. The band-pass filter function then provides two cutoffs, one ultraviolet, linked to C_J , one infrared, linked to L_J . Since the plasma frequency already provides an ultraviolet cutoff, we only retain the infrared part of the filter, to reach a simplified expression for spectral density,

$$A(\omega) = \frac{2\pi\alpha\omega}{\omega^2 + (2\pi\alpha E_J)^2}. \quad (9.9)$$

9.2 Diagrammatic expansion

Chap. 8 has shown that all experimental observables can be linked to the Green's functions \mathbf{G}_{ij} , even in the presence of interactions. Crucially, these functions are the main object of one of the most standard tools of theoretical physics, Feynman diagrams. They were originally designed to keep track of the many terms that arise during perturbative expansions in quantum field theory¹. The pictorial representation helped make sense of each term as a specific process, bringing physical intuition into a maze of various contributions. Feynman's understanding of quantum mechanics, through its celebrated path integral, gave the final interpretation for the diagrammatic series: the quantum evolution "follows all the paths at once", and therefore they all must be summed up to provide the total probability amplitude.

Soon enough, theoreticians figured that Feynman's diagrams could be extended beyond the strictly perturbative realm. In this section, we will first remind the main results leading to Feynman's diagrams, and use them to derive exact relations between \mathbf{G}_{ij} and \mathbf{G}_{00} , the impurity Green's function. After that, we are in position to define the self-energy. Finally, a resummation technique, the self-consistent harmonic approximation, will lead us to introduce an emergent energy scale, E_J^* , as the Silbey-Harris ansatz and the perturbative renormalization group did in Part. I.

Dyson power series

Let us remind, without demonstrations, the main steps leading to Feynman's diagrams². The Feynman's Green function is defined as

$$\mathbf{G}_{ij}^F(t-t') = -i\langle 0|\mathcal{T}\hat{\phi}_i(t)\hat{\phi}_j(t')|0\rangle, \quad (9.10)$$

where the time ordering symbol \mathcal{T} implies that operators at early times are put on the right. Operators are written in Heisenberg's representation. The whole bracket can be expressed in interaction representation thanks to Gell-Mann & Low's theorem

$$\langle 0|\mathcal{T}\hat{\phi}_i(t)\hat{\phi}_j(t')|0\rangle = \frac{\langle 0|\mathcal{T}\hat{\phi}_i(t)\hat{\phi}_j(t')\exp\left(-i\int_{\mathbb{R}}d\tau\hat{H}_{\text{int}}(\tau)\right)|0\rangle}{\langle 0|\mathcal{T}\exp\left(-i\int_{\mathbb{R}}d\tau\hat{H}_{\text{int}}(\tau)\right)|0\rangle}. \quad (9.11)$$

All operators, here and in the following, are written in interaction picture. In the case at hand, $\hat{H}_{\text{int}}(\tau) = -E_J \cos(\hat{\phi}_0(\tau))$. The denominator is removed by suppressing disconnected diagrams, and expanding the numerator's exponential provides Dyson's power series,

$$i\mathbf{G}_{ij}^F(t-t') = i\mathbf{G}_{ij}^{cF}(t-t') + iE_J \int_{\mathbb{R}}d\tau \langle 0|\mathcal{T}\hat{\phi}_i(t)\hat{\phi}_j(t')\cos(\hat{\phi}_0(\tau))|0\rangle + \dots \quad (9.12)$$

\mathbf{G}_{ij}^{cF} is the Green's function at $E_J = 0$. The next step is usually to use Wick's theorem to relate the interacting correlation function to non-interacting Green's functions.

¹ For an historical perspective on Feynman's diagrams, cf. D. Kaiser. **2005**. *Drawing Theories Apart*.

² Many textbooks discuss quantum field theory. We give specific references along the text for precise topics and formulae, but for a modern and concise introduction, cf. H. Bruus & K. Flensberg. **2004**. *Many-Body Quantum Theory in Condensed Matter Physics*.

Wick's theorem applies only with monomials of the field. A solution is to expand the cosine, and retain all orders, such that the first order in E_J writes¹

$$iE_J \sum_{n=1} \frac{(-1)^n}{(2n)!} \int_{\mathbb{R}} d\tau \langle 0 | \mathcal{T} \hat{\phi}_i(t) \hat{\phi}_j(t') \hat{\phi}_0^{2n}(\tau) | 0 \rangle. \quad (9.13)$$

Wick's theorem then translate this expression into the Feynman rules for constructing the diagrams². The power to which the field appears gives the number of legs of the corresponding vertex in Feynman diagrams. We have to take into account all vertices with even number of legs, with their corresponding weights, as represented on Fig. 9.2³.

The m -legged vertex comes with a $1/m!$ factor. Therefore, the usual rules of symmetry factor counting apply. As usual, a first order approximation will take into account all diagrams with one vertex of any type. Second order draws all the two vertices diagrams, and so on. The infinite vertex number adds up with the fast increasing combinatorics of higher orders: it put us at risk of quickly drowning in diagrams. Fortunately, their number can be drastically cut by appropriate resummations.

Scattering ‘matrix’ and self-energy

In Feynman's diagrams, non-interacting Green's functions are represented by lines. Here, we define

$$i\mathbf{G}_{ij}^{\circ F}(t-t') = i \text{---}^j \quad \text{and} \quad i\mathbf{G}_{ij}^F(t-t') = i \text{---}^j. \quad (9.14)$$

Since the interaction Hamiltonian \hat{H}_{int} only contains the boundary field $\hat{\phi}_0$, only a line ending with index 0 can connect to a vertex. The Green's functions are then limited to⁴:

$$i\mathbf{G}_{ij}(t-t') = i \text{---}^j = i \text{---}^j + i \text{---}^j \text{---}^0 \text{---}^0 \text{---}^j \quad (9.15)$$

The T -blob represent the sum of all possible diagrams. It contains ---^0 lines only, such that T does not carry site indices. The corresponding equation is

$$\mathbf{G}_{ij}(t-t') = \mathbf{G}_{ij}^{\circ}(t-t') + i \iint_{\mathbb{R}^2} d\tau d\tau' \mathbf{G}_{i0}^{\circ}(t-\tau) T(\tau, \tau') \mathbf{G}_{0j}^{\circ}(\tau'-t'). \quad (9.16)$$

Since all Green's functions are invariant by time translation, this property translates to T , such that $T(\tau, \tau') = T(\tau - \tau')$. This equation has a convolution product structure. We can simplify it by taking the Fourier transform:

$$\mathbf{G}_{ij}(\omega) = \mathbf{G}_{ij}^{\circ}(\omega) + \mathbf{G}_{i0}^{\circ}(\omega) i T(\omega) \mathbf{G}_{0j}^{\circ}(\omega). \quad (9.17)$$

T is often called the scattering ‘matrix’ —even though the matrix structure is here lost— and used for its simple connection to the S -matrix and scattering properties in general⁵. We will rather connect it to the self-energy. Eq. (9.17) can be rewritten for \mathbf{G}_{0j} , and the result re-plugged into Eq. (9.17), to give

$$\begin{aligned} \mathbf{G}_{ij} &= \mathbf{G}_{ij}^{\circ} + \mathbf{G}_{i0}^{\circ} i T \mathbf{G}_{0j} - \mathbf{G}_{i0}^{\circ} i T \mathbf{G}_{00}^{\circ} i T \mathbf{G}_{0j}^{\circ} \\ &= \mathbf{G}_{ij}^{\circ} + \mathbf{G}_{i0}^{\circ} (iT - \mathbf{G}_{00}^{\circ} iT + \mathbf{G}_{00}^{\circ} i T \mathbf{G}_{00}^{\circ} iT + \dots) \mathbf{G}_{0j} \\ &= \mathbf{G}_{ij}^{\circ} + \mathbf{G}_{i0}^{\circ} \Sigma \mathbf{G}_{0j}. \end{aligned} \quad (9.18)$$

We defined Σ as the series in parentheses, and dropped ω dependencies for the sake of conciseness. The last equation can be recast, using matrix form, into

$$(\mathbf{G}^{\circ -1} - \mathbf{E}^{00} \Sigma) \mathbf{G} = \mathbf{1}, \quad (9.19)$$

¹ The constant part in the cosine is dropped by shifting the Hamiltonian.

² Many versions of Wick's theorem exist. In the context of canonical quantization, it is stated as a relation between time ordering and normal ordering. At finite temperature, one resorts to a heavier form using determinants. Path integral quantization makes it all clearer. *cf. resp.*

M. E. Peskin & D. V. Schroeder. **1995**. *An Introduction To Quantum Field Theory*;

H. Bruus & K. Flensberg. **2004**. *Many-Body Quantum Theory in Condensed Matter Physics*;

J. W. Negele & H. Orland. **1995**. *Quantum Many Particle Systems*.

³ Similar diagrammatic approach with many leg vertices was used for renormalization group analysis, *cf.*

D. J. Amit, Y. Y. Goldschmidt, & S. Grinstein.

1980. *J. Phys. A: Math. Gen.* **13**, 585;

V. Hakim, A. Muramatsu, & F. Guinea. **1984**. *Phys. Rev. B* **30**, 464.

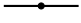


Vertex	Value
	$-iE_J/2!$
	$iE_J/4!$
	$-iE_J/6!$
\vdots	

Figure 9.2: The first vertices to include in Feynman's diagrams. The list goes to infinity.

⁴ Note that diagrammatic rules holds for Feynman Green's functions only. We now drop the F symbol, redundant for any diagrammatic equation.

⁵ G. Zaránd, L. Borda, *et al.* **2004**. *Phys. Rev. Lett.* **93**, 107204;

L. Borda, L. Fritz, *et al.* **2007**. *Phys. Rev. B* **75**, 235112;

M. Goldstein, M. H. Devoret, *et al.* **2013**. *Phys. Rev. Lett.* **110**, 017002.

which is precisely the Eq. (8.33), that we left unproven in Chap. 8. The series defining the self-energy is a simple geometric sum:

$$\Sigma = \frac{iT}{1 + \mathbf{G}_{00}^\circ iT} \Leftrightarrow iT = \frac{\Sigma}{1 - \mathbf{G}_{00}^\circ \Sigma} = \Sigma + \Sigma \mathbf{G}_{00}^\circ \Sigma + \dots \quad (9.20)$$

Moving back to the time domain, the last expression is spelled clearly in terms of diagrams:

$$\textcircled{T} = \textcircled{-i\Sigma} + \textcircled{-i\Sigma} \textcircled{-i\Sigma} + \textcircled{-i\Sigma} \textcircled{-i\Sigma} \textcircled{-i\Sigma} + \dots \quad (9.21)$$

The set of all diagrams on the left hand side is constructed as following. If a given diagram cannot be broken into disconnected pieces by cutting only one line, it belongs to the first term in the above series, *i.e.* to the self-energy. If it has one and only one line that could be broken to cut it into disconnected pieces, it belongs to the second term, and so on. **The self-energy is the sum of all one particle irreducible diagrams.** Note that all these results could have been obtained using equations of motion only, but only after tedious and model dependent computations.

Aside from this result, we also got rid of the matrix structure, the self-energy involving \mathbf{G}_{00} only. The effect of interactions are distributed on the other sites *via* the linear part of the equation of motion. This structure is characteristic of an impurity problem. From now on, we simply note $\mathbf{G}_{00} = G$.

Self-Consistent Harmonic Approximation

Let's compute the self-energy at first order. The corresponding set of diagrams is the following¹.

$$-i\Sigma = \textcircled{\text{---}} + \textcircled{\text{---}} \textcircled{\text{---}} + \textcircled{\text{---}} \textcircled{\text{---}} \textcircled{\text{---}} + \dots \quad (9.22)$$

$$= -iE_J \left(1 - \frac{iG^\circ(t=0)}{s_1} + \frac{(iG^\circ(t=0))^2}{s_2} - \dots \right) \quad (9.23)$$

s_n is the symmetry factor of n tadpole loops. Each loop comes with a symmetry of 2, due to exchange of its two legs, and exchange of the loops themselves add a factor of $n!$, such that $s_n = 2^n n!$. The infinite series of the first order can therefore be re-summed, as

$$\Sigma = E_J e^{-iG^\circ(t=0)/2}. \quad (9.24)$$

The non-interacting Green's function at $t = 0$ can be directly computed from its definition:

$$\begin{aligned} G^\circ(t) &= -i \langle 0 | \mathcal{T} \hat{\phi}_0(t) \hat{\phi}_0(0) | 0 \rangle \\ &= -i \gamma_k \gamma_\ell \langle 0 | \left(\hat{a}_k^\dagger e^{i\omega_k t} + \hat{a}_k e^{-i\omega_k t} \right) \left(\hat{a}_\ell^\dagger + \hat{a}_\ell \right) | 0 \rangle \quad (t > 0) \\ &= -i \gamma_\ell \gamma_\ell e^{-i\omega_\ell |t|}, \quad (\forall t \in \mathbb{R}). \end{aligned} \quad (9.25)$$

At $t = 0$, we simply have $G^\circ(0) = -i \gamma_\ell \gamma_\ell = -i \int_0^\infty d\omega A(\omega)$. The expression of $A(\omega)$ has been derived in Sec. 9.1, but its infrared divergence was cured by replacing the Josephson junction by an inductor, or equivalently, by approximating $-E_J \cos \hat{\phi}_0 \simeq E_J \hat{\phi}_0^2/2$. We can replicate this trick by adding the regularizing inductor as a counter-term in the Hamiltonian²:

$$\hat{H} = \omega_k \hat{a}_k^\dagger \hat{a}_k + \frac{E_J^*}{2} \hat{\phi}_0^2 - E_J \cos(\hat{\phi}_0) - \frac{E_J^*}{2} \hat{\phi}_0^2. \quad (9.26)$$

¹ The open circles indicate the in and outgoing lines. They do not appear in the self-energy expression but are needed to count vertices legs.

² The notion of counter-terms is ubiquitous in field theory for particle physics, *cf.* M. E. Peskin & D. V. Schroeder. 1995. *An Introduction To Quantum Field Theory.*

The quadratic part is diagonalized in the same way as in Sec. 9.1, simply replacing $E_J \rightarrow E_J^*$ (and correspondingly, $L_J \rightarrow L_J^*$). The counter-term added in the interaction part \hat{H}_{int} adds a diagram to the theory, represented on Fig. 9.3. The self-energy equation is now

$$-i\Sigma = \text{---}\star\text{---} + \text{---}\bullet\text{---} + \text{---}\text{---}\text{---} + \text{---}\text{---}\text{---} + \dots \quad (9.27)$$

$$= -i \left(E_J e^{-iG^\circ(0)/2} - E_J^* \right). \quad (9.28)$$

In this counter-term method, E_J^* is a free parameter. We determine it by asking that the self-energy cancels, which is equivalent to say that we absorbed all the effect of the interactions into a new energy scale introduced in the non-interacting Hamiltonian. The self-consistent equation for the self-energy is then

$$E_J^* = E_J e^{-iG^\circ(0)/2} = E_J e^{-\int_0^\infty \frac{d\omega}{2\pi} A(\omega)}. \quad (9.29)$$

The integral is evaluated using partial fraction decomposition,

$$-\alpha \int_0^\infty d\omega \frac{\omega}{\omega^2 + (2\pi\alpha E_J^*)^2} = -\frac{\alpha}{2} \ln \left(1 + \left(\frac{\omega_c}{2\pi\alpha E_J^*} \right)^2 \right), \quad (9.30)$$

where we cut the integral by an unspecified hard ultraviolet cutoff ω_c . In a real system, it is most probable that $\omega_c = \omega_p$. If $\omega_c \gg 2\pi\alpha E_J^*$, the self-consistent equation becomes $E_J^* = E_J (2\pi\alpha E_J^*/\omega_c)^\alpha$, which can be solved to find

$$E_J^* = E_J \left(\frac{\omega_c}{2\pi\alpha E_J} \right)^{\frac{\alpha}{\alpha-1}}. \quad (9.31)$$

This equation is closely related to Eq. 4.40, which was obtained by perturbative renormalization group analysis on a boundary sine-Gordon model with generic parameters. Self-consistent diagrammatic methods, perturbative renormalization group, and variational principle applied to a Gaussian state ansatz (*cf.* Eq. (4.27)), all capture the same physics and lead to the same scaling law.

9.3 Self-energy power law

In contrast with the variational method we mentioned, the diagrammatic expansion has a natural extension to the next orders. The imaginary part of the self-energy, and thus the inelastic scattering properties of the interacting model, are obtained by adding all diagrams with two vertices:

$$\begin{aligned} -i\Sigma = & 1^{\text{st}} \text{ order} + \text{---}\text{---}\text{---} + \text{---}\text{---}\text{---} + \dots \\ & + \text{---}\text{---}\text{---} + \text{---}\text{---}\text{---} + \dots \\ & + \text{---}\text{---}\text{---} + \text{---}\text{---}\text{---} + \text{---}\text{---}\text{---} + \text{---}\text{---}\text{---} + \dots \end{aligned} \quad (9.32)$$

The number of diagrams is once again getting out of hands. We have to organize this list. First, we single out a vertex. It can be dressed with any number of tadpoles, *i.e.* loops with a single propagator. We draw the rest of the diagram as a box, with any

Vertex	Value
	$iE_J^*/2!$

Figure 9.3: The counter-term vertex. Its sign makes it cancel the cos first order vertex when $E_J = E_J^*$.

Vertex	Value
	$iE_J^*/2!$
	$-\frac{iE_J}{2!} e^{-\frac{i}{2}G^\circ(0)}$
	$\frac{iE_J}{4!} e^{-\frac{i}{2}G^\circ(0)}$
	$-\frac{iE_J}{6!} e^{-\frac{i}{2}G^\circ(0)}$
	\vdots

Figure 9.4: The new set of vertices, dressed by tadpoles.

even number of lines between it and the singled out vertex. The sum over tadpoles writes

$$\begin{aligned}
 & \text{Diagram 1} + \text{Diagram 2} + \text{Diagram 3} + \dots \\
 &= \text{Diagram 4} \left(1 - \frac{iG^\circ(0)}{s_1} + \frac{(iG^\circ(0))^2}{s_2} - \dots \right) = \text{Diagram 5}, \quad (9.33)
 \end{aligned}$$

where the whole sum as been absorbed into a new vertex, represented colored. The new set of vertices is given on Fig. 9.4. The factorization above mainly worked because symmetry factors are multiplicative. If s is the symmetry factor of a diagram, the same diagram with n more tadpoles on some vertex will have symmetry $s \times 2^n n!$.

If we furthermore impose the self-consistent harmonic approximation, and adjust E_J^* to cancel Σ at first order, using dressed vertices only replaces $E_J \rightarrow E_J^*$ in the vertices values: we moved from an E_J expansion to an E_J^* expansion. The two first vertices in the Fig. 9.4 cancel each other, such that the vertex list begins at four legs.

Using vertex dressing, we reduced the list of second order diagrams to only two infinite lists,

$$\begin{aligned}
 -i\Sigma &= \text{Diagram 1} + \text{Diagram 2} + \dots \\
 &+ \text{Diagram 3} + \text{Diagram 4} + \dots \quad (9.34)
 \end{aligned}$$

The second line gives a local in time contribution, proportional to $\delta(t - t')$, which is flat in frequency and purely real. It contributes to a small displacement of E_J^* , which we discard for now. The first line will contribute to the imaginary part of the self-energy. This series too can be exactly summed, as

$$\begin{aligned}
 -i\Sigma(t) &= \text{Diagram 1} + \text{Diagram 2} + \dots \\
 &= (-iE_J^*)^2 \left(\frac{(iG^\circ)^3}{3!} + \frac{(iG^\circ)^5}{5!} + \dots \right) = -iE_J^{*2} (\sin(G^\circ(t)) - G^\circ(t)). \quad (9.35)
 \end{aligned}$$

Free Green's function expression

To push the computation further, we need an expression for $G^\circ(t)$. Let us start by its expression in the frequency domain. It was expressed in terms of the individual bosonic modes by Eq. (8.22). In the continuum limit, the dissipation induced by the pads can be neglected, since we do not separate discrete peaks anymore. In this limit,

$$G_F^\circ(\omega) = \sum_k \frac{2\omega_k \gamma_k^2}{\omega_k^2 - \omega^2} = 2\alpha \int_{\mathbb{R}} d\nu \frac{\nu^2}{(\nu^2 - \omega^2 + i\epsilon)(\nu^2 + (2\pi\alpha E_J^*)^2)}. \quad (9.36)$$

We do a partial fraction decomposition¹. One of the two parts is convergent, without poles. The result is simply

$$\int_{\mathbb{R}} d\nu \frac{1}{1 + (\nu/2\pi\alpha E_J^*)^2} = 2\pi\alpha E_J^* \arctan(x)|_{-\infty}^{\infty} = 2\pi^2\alpha E_J^*. \quad (9.37)$$

The second part is evaluated using Feynman's prescription to displace the poles, as indicated on Fig. 9.5. The sign of ϵ is the same as the one of ω . Finally, the integrand

¹ Explicitly,

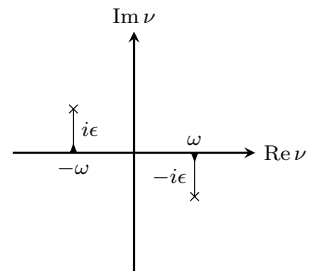
$$\frac{\nu^2}{(\nu^2 - \omega^2)(\nu^2 + V^2)} = \frac{1}{\omega^2 + V^2} \left(\frac{\omega^2}{\omega^2 - \nu^2} + \frac{V^2}{\nu^2 + V^2} \right).$$


Figure 9.5: Poles displacements with Feynman's prescription.

again undergo partial fraction decomposition, and is evaluated with Sokhotski-Plemelj formula¹

$$\int_{\mathbb{R}} d\nu \frac{\omega^2}{\nu^2 - \omega^2 + i\epsilon} = \frac{\omega}{2} \left(\int_{\mathbb{R}} \frac{d\nu}{\nu - \omega} - \int_{\mathbb{R}} \frac{d\nu}{\nu + \omega} - 2i\pi \text{sign}(\omega) \right). \quad (9.38)$$

The principal value integrals vanish. The end result is

$$G_F^\circ(\omega) = \frac{1}{\frac{i|\omega|}{2\pi\alpha} + E_J^*}. \quad (9.39)$$

The result is equivalent to a Dyson equation with $i|\omega|/(2\pi\alpha)$ as the inverse free Green's function, which is indeed the Green's function of a dissipative bath, and E_J^* as the self-energy. The next step is to get this expression to time domain, so we can use Eq. 9.35. We start by separating real and imaginary parts:

$$G_F^\circ(\omega) = 2\pi\alpha \left(\frac{2\pi\alpha E_J^*}{(2\pi\alpha E_J^*)^2 + \omega^2} - i \frac{|\omega|}{(2\pi\alpha E_J^*)^2 + \omega^2} \right), \quad (9.40)$$

and since both the real and imaginary parts are even functions of ω , their Fourier transforms are real. The real (imaginary) part of the Fourier transform is therefore the Fourier transform of the real (imaginary) part. For the real part,

$$\text{Re } G_F^\circ(t) = 2\pi\alpha^2 E_J^* \int_{\mathbb{R}} d\omega \frac{e^{-i\omega t}}{(\omega + i2\pi\alpha E_J^*)(\omega - i2\pi\alpha E_J^*)}. \quad (9.41)$$

The poles are located on the imaginary axis, as shown on Fig. 9.6. The residue theorem allows to conclude,

$$\text{Re } G_F^\circ(t) = \pi\alpha e^{-2\pi\alpha E_J^* |t|}. \quad (9.42)$$

Note that there seems to be a conflict at $t = 0$ with Eq. (9.30). This originates from a commutation of the two limits $\omega_c \rightarrow \infty$ and $t \rightarrow 0$, as can be checked by computing this $t = 0$ value from Kramers-Krönig relations and G^F imaginary part. When $\omega_c \rightarrow \infty$, $\lim_{t \rightarrow 0^+} G_F(t) = \lim_{t \rightarrow 0^-} G_F(t) \neq G_F(t = 0)$.

The imaginary part has no simple expression, mainly because of the absolute value that prevents us from drawing a useful contour for residue theorem. One could notice that the retarded Green's function has no absolute value, and therefore can be Fourier transformed analytically. Yet, diagrammatic rules only hold for Feynman's Green's function, which highlights the stark difference between the two prescriptions. We will separate the imaginary part into high and low frequency parts, equivalent to long or short times. We first rewrite it as

$$\begin{aligned} \text{Im } G_F^\circ(t) &= -\alpha \left(\int_0^\infty \frac{\omega e^{-i\omega t}}{\omega^2 + (2\pi\alpha E_J^*)^2} d\omega - \int_{-\infty}^0 \frac{\omega e^{-i\omega t}}{\omega^2 + (2\pi\alpha E_J^*)^2} d\omega \right) \\ &= -2\alpha \int_0^\infty \frac{\omega \cos(\omega t)}{\omega^2 + (2\pi\alpha E_J^*)^2} d\omega = -2\alpha \int_0^\infty \frac{x \cos(x)}{x^2 + (2\pi\alpha E_J^* t)^2} dx. \end{aligned} \quad (9.43)$$

In the last form, one can separate the integral into two regions,

$$\text{Im } G_F^\circ(t) \simeq \frac{-2\alpha}{(2\pi\alpha E_J^* t)^2} \int_0^{2\pi\alpha E_J^* |t|} x \cos(x) dx - 2\alpha \int_{2\pi\alpha E_J^* |t|}^\infty \frac{\cos(x)}{x} dx. \quad (9.44)$$

The first part contributes mainly for $2\pi\alpha E_J^* t \gg 1$, or for low frequencies $\omega \ll 2\pi\alpha E_J^*$, and the second part contributes at high frequencies. According to the renormalization group analysis, we expect perturbative analysis to hold above the energy scale E_J^* : the high frequencies are in the perturbative region and can be trusted, while the low-frequency part is doubtful. We analyze it first.

¹ W. Appel. 2007. *Mathematics for Physics and Physicists*.

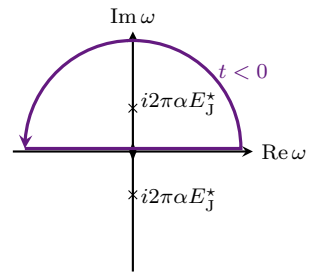


Figure 9.6: Poles on the imaginary axis, and (•) the integration contour for residue theorem.

Low frequencies

We gather the asymptotic behavior of Eq. (9.44). The first part is integrated as¹

$$\frac{1}{(\Omega^*t)^2} \int_0^{\Omega^*|t|} x \cos(x) dx = \frac{\sin(\Omega^*t)}{\Omega^*t} + \frac{\cos(\Omega^*t)}{(\Omega^*t)^2} - \frac{1}{(\Omega^*t)^2}. \quad (9.45)$$

The second part contains the integral cosine, $\text{Ci}(y) = \int_x^\infty dx \cos(x)/x$. There is no analytical expression for it, but we can extract its asymptotic behavior by successive integration by parts:

$$\text{Ci}(\Omega^*|t|) = \int_1^\infty \frac{\cos(x\Omega^*t)}{x} dx = -\frac{\sin(\Omega^*t)}{\Omega^*t} + \frac{\cos(\Omega^*t)}{(\Omega^*t)^2} - O((\Omega^*|t|)^{-3}). \quad (9.46)$$

The leading behavior is

$$G_F^\circ(t) = \pi\alpha e^{-\Omega^*|t|} + i \frac{2\alpha}{(\Omega^*t)^2}. \quad (9.47)$$

Since it goes to zero when $t \rightarrow \infty$, we can safely limit ourselves to the first diagram in the expansion Eq. (9.35). Likewise, we only keep the leading order of $G^{\circ 3} \sim 1/t^6$, and we Fourier transform again the expression to obtain the self-energy in the frequency domain²

$$\text{Im} \Sigma(\omega) \simeq \frac{E_J^*}{2\pi\alpha} \left(\frac{\omega}{2\pi\alpha E_J^*} \right)^5 \int_{-\infty}^\infty dx \frac{e^{ix}}{x^6}. \quad (9.48)$$

The inelastic scattering goes rapidly to 0 at low frequencies, following an ω^5 power law, and would make negligible corrections to experimental measurements.

The real part at low frequencies is also interesting, since it displays a constant that would add to peak displacements. When computing the n^{th} power of Eq. (9.47), we gather the only terms with no power dependence, since all others have power laws Fourier transforms, vanishing at $\omega = 0$. Then³,

$$\begin{aligned} \text{Re} \Sigma(t) &\simeq -E_J^{*2} \left(\frac{(\pi\alpha)^3}{3!} e^{-3\Omega^*|t|} - \frac{(\pi\alpha)^5}{5!} e^{-5\Omega^*|t|} + \dots \right) \\ \Rightarrow \text{Re} \Sigma(\omega = 0) &\simeq -\frac{2E_J^{*2}}{\Omega^*} \left(\frac{(\pi\alpha)^3}{3 \times 3!} - \frac{(\pi\alpha)^5}{5 \times 5!} + \dots \right). \end{aligned} \quad (9.49)$$

We need to re-sum the function $F(x) = x^3/(3!3) - x^5/(5!5) + \dots$. We notice that

$$x \frac{dF}{dx} = x - \sin(x) \quad \Rightarrow \quad F(y) = \int_0^y (\text{sinc}(x) - 1) dx = \text{Si}(y) - y. \quad (9.50)$$

The last step used the definition of the integral sine Si. The result for the constant contribution to the self-energy real part is

$$\text{Re} \Sigma(\omega = 0) \simeq -E_J^* \left(1 - \frac{\text{Si}(\pi\alpha)}{\pi\alpha} \right). \quad (9.51)$$

The prefactor is plotted as a function of α on Fig. 9.7. As α grows, this lowering of E_J^* can reach significant values. Since the perturbative expansion is not controlled below E_J^* , this effect is spurious, and is probably counter-balanced by higher orders corrections. In Sec. 10, this E_J^* lowering will be a serious limitation to the numerical prediction of resonance peaks displacements.

High frequencies

At high frequencies, we expect the perturbative approach to hold. Moreover, we will see that the self-energy develops an anomalous power law. In this regime, the main

¹ In this section, we use $2\pi\alpha E_J^* = \Omega^*$ as a shorthand in some computations.

² The last integral only contributes by a constant factor. It is related to the Γ function at Eq. (9.61).

³ We use the Fourier transform of a Lorentzian,

$$\int_{\mathbb{R}} e^{-A|t|} e^{i\omega t} dt = \frac{2A}{A^2 + \omega^2}.$$

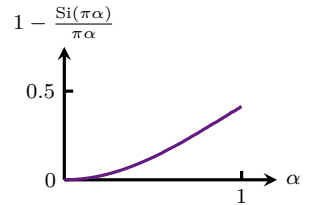


Figure 9.7: The adimensional prefactor to the self-energy real part.

contribution in Eq. (9.44) comes from the integral cosine, which has the short times asymptotic behavior^{1,2}

$$\int_{\Omega^*|t|}^{\infty} \frac{\cos(x)}{x} dx = \gamma + \ln(\Omega^*t) + O((\Omega^*t)^2). \quad (9.52)$$

The leading part is inserted into Eq. (9.35), together with the real part of G , and the complex sine is decomposed into real and imaginary part. It provides

$$\Sigma(t) \simeq i \frac{E_J^{*2}}{2} \left(\left(\frac{1}{\Omega^*|t|} \right)^{2\alpha} e^{-i\pi\alpha(1+O(t))} - (\Omega^*|t|)^{2\alpha} e^{i\pi\alpha(1+O(t))} \right) - E_J^{*2} G_F^c(t) \quad (9.53)$$

At short times, the $1/t^{2\alpha}$ contribution prevails. We then estimate the Fourier transform of the self-energy. After a rearrangement of the time integral into a dimensionless factor, we reach³

$$\Sigma(\omega) = ie^{-i\pi\alpha} \frac{E_J^*}{2\pi\alpha} \left(\frac{|\omega|}{2\pi\alpha E_J^*} \right)^{2\alpha-1} \int_0^{\infty} dx \frac{\cos(x)}{x^{2\alpha}} + iE_J^* \frac{2\pi\alpha E_J^*}{|\omega|}. \quad (9.54)$$

This expression of the self-energy is the main result of the section. It predicts that the high frequency self-energy is a power law, the exponent of which explicitly depends on the coupling strength. This is in sharp contrast with any result a bare perturbation theory could provide. In such a procedure, the self-energy is expressed as an integer power of the Green's function in time domain, resulting in integer power laws for $\Sigma(\omega)$. The low-frequency computation provided an example of such a normal power law. On the contrary, at high frequency, the resummation over processes involving any photon number changed drastically the computation, and provided this anomalous power law. This result has been obtained by different methods by Kane & Fisher⁴, who exploited a mapping between the boundary sine-Gordon model and a model of tunnel barrier in Luttinger liquids to evaluate the conductance through the barrier, with displays the same kind of anomalous power law. Their result has later been refined to fit in the framework of the SCHA⁵.

At $\alpha = 1/2$, the self-energy anomalous part is constant with respect to frequency, at least for high frequencies. Since⁶

$$\int_0^{\infty} \frac{\cos x}{x^{2\alpha}} = \sin(\pi\alpha)\Gamma(1-2\alpha), \quad (9.55)$$

its imaginary part is regular and finite at $\alpha = 1/2$, while its real part is diverging. A qualitative change is to be expected at this value of interaction strength, since, in the spin-boson model, it separates the under-damped from the over-damped regime⁷. This specific value is known as the Toulouse point, first known to be a solvable value for the Kondo Hamiltonian⁸.

Finally, at the transition point $\alpha = 1$, an Ohmic behavior is recovered, with $\Sigma \sim i|\omega|$. Our model cannot go higher in coupling strength, since perturbation around E_J^* loses its validity.

Ultraviolet cutoff and breakdown of power law

The anomalous power law we demonstrated is a striking consequence of the cosine diagrammatics, where the coupling strength directly controls the qualitative behavior of the system. At first glance, it seems that such an experimental observation would be a clear signal that we successfully emulated many-body physics, since most regular dissipation mechanism will provide a self-energy $\propto \omega$, or at least with a normal, integer power law.

¹ M. Abramowitz & I. A. Stegun. **1965**. *Handbook of Mathematical Functions*.

² Here, γ denotes the Euler-Mascheroni constant.

³ Again, the remaining integral is a mere constant, see Eq. (9.61).

⁴ C. L. Kane & M. P. A. Fisher. **1992**. *Phys. Rev. Lett.* **68**, 1220.

⁵ F. Guinea, G. G. Santos, *et al.* **1995**. *EPL* **30**, 561.

⁶ Yet again, the reader will find a proof at Eq. (9.61).

⁷ F. Guinea, V. Hakim, & A. Muramatsu. **1985a**. *Phys. Rev. B* **32**, 4410.

⁸ G. Toulouse. **1969**. *C. R. Acad. Sci. Paris* **268**, 1200.

The experimental relevance of this computation must nonetheless be questioned. We especially conducted the computation in the $\omega_c \rightarrow \infty$ limit. When introducing a ultraviolet cutoff in Eq. (9.52),

$$\int_{\Omega^*|t|}^{\omega_c|t|} \frac{\cos x}{x} dx = \text{Ci}(\omega_c|t|) - \text{Ci}(\Omega^*|t|) \simeq \ln\left(\frac{\omega_c}{\Omega^*}\right) + O(t^2). \quad (9.56)$$

The cutoff spoils the small times logarithmic dependence, at least for $t \ll 1/\omega_c$, such that the anomalous power law is lost above ω_c . Since a power law typically needs several decades to develop, and the experimental cutoff being approximately a decade above the other characteristic energies, it probably cannot be observed.

In this regime of finite ultraviolet cutoff, a small times interpolation is given by¹

$$\Sigma_F^o(t) \simeq -2\alpha \left(\gamma + \ln \left(\frac{\Omega^*}{\omega_c} e^{-\gamma} + \Omega^*|t| \right) \right). \quad (9.57)$$

Following the same line of demonstration, it results in the self-energy expression

$$\Sigma(\omega) = ie^{-i\pi\alpha} \frac{1}{2} \frac{E_J^*{}^2}{(2\pi\alpha E_J^*)^{2\alpha}} \int_{\mathbb{R}} dt \frac{e^{i\omega t}}{(|t| + \tau_0)^{2\alpha}}, \quad (9.58)$$

where $\tau_0 = e^{-\gamma}/\omega_c$. We focus on the last integral², denoted I . We extract the ω power law, cut the integral in half, and absorb τ_0 in the integral lower bound by a variable shift: we obtain

$$I(\omega) = \omega^{2\alpha-1} \left(e^{-i\omega\tau_0} \int_{\omega\tau_0}^{\infty} dy \frac{e^{iy}}{y^{2\alpha}} + e^{i\omega\tau_0} \int_{\omega\tau_0}^{\infty} dy \frac{e^{-iy}}{y^{2\alpha}} \right). \quad (9.59)$$

The second term is the complex conjugate of the first. We will link the first integral to the Γ function by rotating to imaginary y . We apply Cauchy theorem to the contour shown on Fig. 9.8. The integral on the outer circle vanishes when sent to infinity, such that

$$\int_{\omega\tau_0}^{\infty} dy \frac{e^{iy}}{y^{2\alpha}} = i^{1-2\alpha} \Gamma(1-2\alpha, \omega\tau_0) + i(\omega\tau_0)^{1-2\alpha} \int_0^{\pi/2} d\theta e^{i\theta(1-2\alpha)} e^{i\omega\tau_0(\cos\theta + i\sin\theta)}. \quad (9.60)$$

We used the definition of the incomplete Γ function. Bringing everything together, we obtain

$$\begin{aligned} \Sigma(\omega) = & ie^{-i\pi\alpha} \frac{E_J^*}{2\pi\alpha} \times \\ & \left(\left(\frac{|\omega|}{2\pi\alpha E_J^*} \right)^{2\alpha-1} \sin(\pi\alpha + \omega\tau_0) \Gamma(1-2\alpha, \omega\tau_0) \right. \\ & \left. - \left(\frac{\omega_c}{2\pi\alpha E_J^* e^{-\gamma}} \right)^{2\alpha-1} \int_0^{\pi/2} d\theta e^{-\omega\tau_0 \sin\theta} \sin(\omega\tau_0(\cos\theta - 1) + \theta(1-2\alpha)) \right). \end{aligned} \quad (9.61)$$

The last line, which comes from quarter circle integration, is negligible when $\omega_c \gg 2\pi\alpha E_J^*$, independently of frequency, due to its prefactor. The limit when $\omega \ll \omega_c$ is then coherent with our previous result; we retrieve the anomalous power law, while the incomplete Γ function converges, for $\alpha < 1/2$, to $\Gamma(1-2\alpha)$, which is a numerical prefactor only. Finally, we can examine the limit $\omega > \omega_c$, using the asymptotic form of $\Gamma(1-2\alpha, \omega\tau_0)$ ³:

$$\Sigma(\omega) \simeq ie^{-i\pi\alpha} E_J^* \left(\frac{\omega_c}{2\pi\alpha E_J^* e^{-\gamma}} \right)^{2\alpha} \left(\frac{E_J^*}{\omega} \right) e^{-\frac{\omega}{\omega_c} e^{-\gamma}}. \quad (9.62)$$

The self-energy is exponentially suppressed above the cutoff. When the scales ω_c and $2\pi\alpha E_J^*$ are not well separated, the integral over θ in the last line of Eq. (9.61) starts contributing. In this regime, we resort to numerical evaluation.

¹ This expression is a guess that bridge the constant at $t \rightarrow 0$ and the logarithmic decay at $t \gtrsim 1/\omega_c$.

² Unlike the $\omega_c \rightarrow \infty$ case, it is not possible to extract the ω dependence by a change of variable.

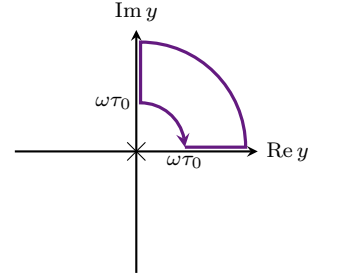
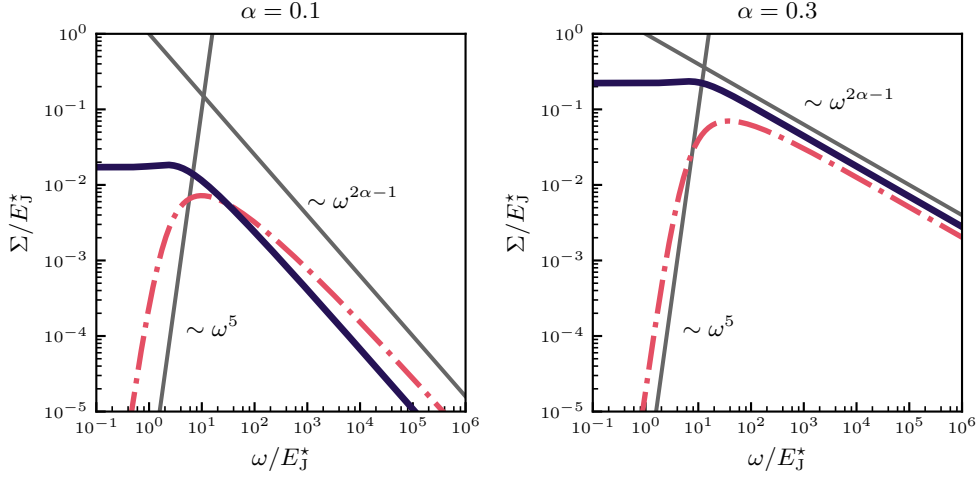


Figure 9.8: Cauchy contour for rotation to the imaginary axis. The cross indicates the pole.

³ When $x \rightarrow \infty$,

$$\Gamma(s, x) \sim x^{s-1} e^{-x}.$$

Numerical computation in the scaling limit



The previous analytical results were obtained using a fair amount of approximations. Alternatively, numerical computation of Σ using Eq. (9.35) and Eq. (9.39) could give the size of the crossover between high and low frequency behaviors, and elucidate the fate of the anomalous power law in the finite ultraviolet cutoff case, relevant for experiments. The main difficulty here comes from the limitations of the standard Fast Fourier Transform algorithm¹. It requires a function sampling on an evenly spaced grid. Power laws typically develops over many decades, and thus need huge amount of samples, while the function itself is rather smooth. An alternative FFT algorithm, based on the Hankel transform, exists². It allows to use logarithmic grids. With this tool, we numerically computed the self-energy in the scaling limit, as displayed on Fig. 9.9. The described power laws are correctly captured. The crossover region is quite broad, between one and two decades wide, which renders experimental measurements of the derived exponents difficult. The computation with finite ultraviolet cutoff is presented on Fig. 9.10. As expected, the anomalous power law needs a wide window to develop, at least 3 decades, between E_J^* and ω_c . When the ultraviolet cutoff comes close to $2\pi\alpha E_J^*$, we only observe a crossover regime between increase at small ω to exponential decay, with no clear law in between³.

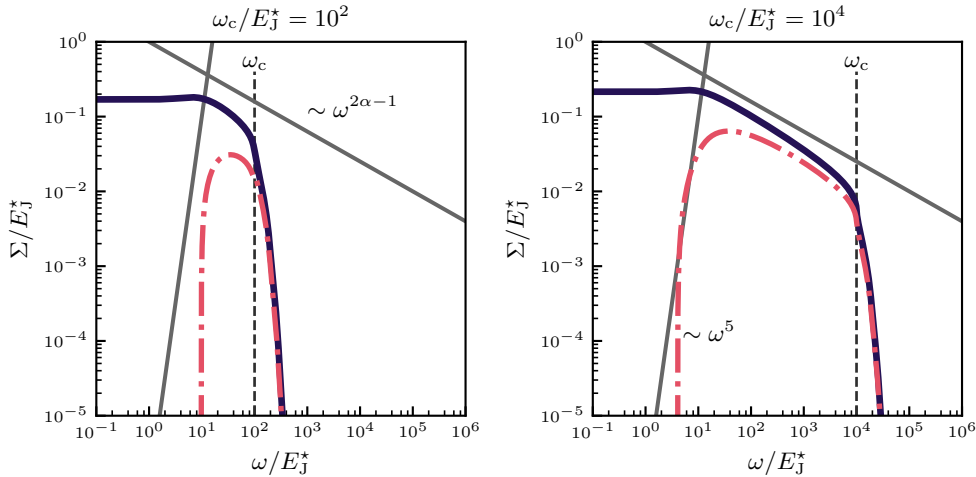


Figure 9.9: Self-energy in the scaling limit $\omega_c \gg E_J^*$, numerically computed on a logarithmic grid at two values of α below the Toulouse point. The high and low frequency power laws matches with analytical predictions.

(●): $\text{Im}\Sigma(\omega)$,
(●): $\text{Re}\Sigma(\omega)$,
(●): indicates power laws.

¹ E. O. Brigham & R. E. Morrow. **1967**. *IEEE Spectr.* 4, 63.

² A. J. S. Hamilton. **2000**. *Mon. Not. Roy. Astron. Soc.* 312, 257.

³ Alternative simulator technologies could offer a much broader window to observe scaling regime, cf. A. Anthore, Z. Iftikhar, *et al.* **2018**. *Phys. Rev. X* 8, 031075.

Figure 9.10: Self-energy with ultraviolet cutoff, numerically computed on a logarithmic grid at two values of ω_c and $\alpha = 0.3$. The power law behavior only develops for $\omega_c/E_J^* > 10^3$.

(●): $\text{Im}\Sigma(\omega)$,
(●): $\text{Re}\Sigma(\omega)$,
(●): indicates power laws,
(--): indicates ω_c scale.

10 | Microscopic analysis

Nel mezzo del cammin di nostra vita,
mi ritrovai per una selva oscura,
ché la diritta via era smarrita.

Dante, *Inferno*.

When half way through the
journey of our life, I found
that I was in a gloomy forest,
because the path which led
aright was lost.

transl. Courtney Langdon.

The analytical approach gave us useful insights on the physics of the problem. We concluded that the re-summation over all the multi-photons processes allowed by the Josephson term is crucial to capture the system behavior, at least above E_J^* , and that perturbation series in E_J naturally rearranges into a perturbation series in E_J^* . Nevertheless, the various scaling laws we derived are probably out of reach of spectroscopic experiments, that only access a frequency window between 2 and 12 GHz, one decade large. Furthermore, the cutoff, temperature, and E_J^* scales are close to each other, smearing even more the simple laws derived analytically.

It is then crucial to refine our analysis, to better match experimental predictions. The two main elements we put aside are the discrete mode structure of the Green's function, which should be mirrored in the self-energy, and the effect of temperature. Indeed, as we discussed in Sec. 2.2, the typical temperature of a dilution fridge is around 20 mK, but can be sensibly higher due to imperfect filtering of the measurement setup. It means that any mode below 400 MHz will be thermally populated. We estimate our lowest lying frequency around $f_{\min} = 1/(2\pi N \sqrt{LC_g}) \simeq 130$ MHz. The question of temperature relevance is then open, since there exist thermally populated modes in the system, but the temperature scale is still lower than E_J . We will detail how temperature influences this intermediate regime.

We start in Sec. 10.1 by deriving an exact expression for the Green's function that is also computationally cheap to evaluate. Adding temperature in self-energy computations is done in Sec. 10.2, where we resort to Keldysh formalism. Finally, we make connection to experimental data in Sec. 10.5.

10.1 Equations of motion inversion

The Green's function is computed by inverting the equation of motion (with a Dyson part for the self-energy)

$$\left(C\omega^2 - 1/L + \frac{2i\omega}{Z_{\text{tl}}} \mathbf{E}^{NN} - \Sigma(\omega) \mathbf{E}^{00} \right) \mathbf{G} = \mathbf{1}. \quad (10.1)$$

Up until now, we diagonalized the Green's function inverse on the left hand side. It provided a list of poles and weights. The resulting Green's function \mathbf{G}_{ij} was expressed as a sum over poles¹. For $N = 4250$ sites and poles, even if the diagonalization is performed analytically, the sum over the poles can be expensive, depending on the size of the sampling grid for Fourier transforms. This number of points ultimately

¹ Its exact form is

$$\mathbf{G}_{ij} = \sum_k \frac{\mathbf{P}_{ik} \mathbf{P}_{jk}}{\omega_k^2 - \omega^2}.$$

We can now add the boundary conditions, which also contain the pads broadening and the self-energy. We make use of the Sherman-Morrison formula¹, with $u = v$, u_0 the top boundary element, u_N the bottom boundary element, and $u_i = 0$ elsewhere. Then,

$$\mathbf{G}_{00} = \frac{\mathbf{G}_{00}^{\circ} + u_N (\mathbf{G}_{00}^{\circ 2} - \mathbf{G}_{0N}^{\circ 2})}{1 + (u_0 + u_N)\mathbf{G}_{00}^{\circ} + u_0 u_N (\mathbf{G}_{00}^{\circ 2} - \mathbf{G}_{0N}^{\circ 2})}. \quad (10.9)$$

With some trigonometry, we simplify the factor

$$(\mathbf{G}_{00}^{\circ 2} - \mathbf{G}_{0N}^{\circ 2}) = \frac{1}{(C(\omega_0^2 - \omega^2))^2} \frac{\sin((N-1)k)}{\sin(N+1)k}. \quad (10.10)$$

After some rearrangements, especially in the denominator², we finally reach

$$\mathbf{G}_{00} = \frac{\frac{2i\omega}{Z_{\text{tl}}} + C(\omega_0^2 - \omega^2)S(N, k)}{\frac{2i\omega}{Z_{\text{tl}}} (C_J \omega^2 - E_J^* - \Sigma) - C(\omega_0^2 - \omega^2)C_g \omega^2 + C(\omega_0^2 - \omega^2) \left(\frac{2i\omega}{Z_{\text{tl}}} + (C_J + C_g)\omega^2 - E_J^* - \Sigma \right) S(N, k)} \quad (10.11)$$

where $S(N, k) = 1 - \cos(k) - \sin(k)/\tan((N-1)k)$. A similar expression can be reached for \mathbf{G}_{NN} , needed to compute the transmission *via* Eq. (8.16). It reads

$$\mathbf{G}_{NN} = \frac{C_J \omega^2 - E_J^* - \Sigma + C(\omega_0^2 - \omega^2)S(N, k)}{\frac{2i\omega}{Z_{\text{tl}}} + C(\omega_0^2 - \omega^2)S(N, k)} \mathbf{G}_{00}. \quad (10.12)$$

These forms are difficult to read and interpret, but can be numerically evaluated with ease given a sampling of ω . The only missing element is $k(\omega)$. The dispersion relation provides this function; some care must nonetheless be taken, since complex values of k are reached above ω_p .

Complex wavenumber

The dispersion relation reads

$$\sin^2(k/2) = \frac{\omega^2 \omega_0^2 - \omega_p^2}{\omega_p^2 \omega_0^2 - \omega^2}. \quad (10.13)$$

ω_0 is the half band-width, while ω_p is the plasma pulsation. As a rule, $\omega_0 > \omega_p$. We then distinguish between three cases.

- If $\omega < \omega_p$, the wavenumber is purely real, and

$$k = 2 \arcsin \left(\frac{\omega}{\omega_p} \sqrt{\frac{\omega_0^2 - \omega_p^2}{\omega_0^2 - \omega^2}} \right). \quad (10.14)$$

- If $\omega_p < \omega < \omega_0$, k develops an imaginary part, since waves become evanescent above the plasma frequency. This is signaled by $\sin(k/2) > 1$. If $k = k' + i\Gamma$, we decompose into $\sin(k/2) = \sin(k'/2) \cosh(\Gamma/2) + i \cos(k'/2) \sinh(\Gamma/2)$. $k' = \pi$ at the edge of the Brillouin zone, and

$$\Gamma = 2 \operatorname{arccosh} \left(\frac{\omega}{\omega_p} \sqrt{\frac{\omega_0^2 - \omega_p^2}{\omega_0^2 - \omega^2}} \right). \quad (10.15)$$

- If $\omega_0 < \omega$, $\sin^2(k/2) < 0$, which signals an other boundary above which $k' = 0$ and

$$\Gamma = 2 \operatorname{arcsinh} \left(-\frac{\omega}{\omega_p} \sqrt{\frac{\omega_0^2 - \omega_p^2}{\omega_0^2 - \omega^2}} \right). \quad (10.16)$$

The complete function $k(\omega)$ is represented on Fig. 10.1. In the real system, the $[\omega_p, \omega_0]$ interval is narrower, $\simeq 1$ MHz. It must be noted that the function $S(N, k)$ can assume many expressions, but since k can take a large imaginary part, some of them can cause numerical overflow. The one proposed is regular at all frequencies.

¹ Which asserts that

$$(A^{-1} + uv^{\text{T}})^{-1} = A - \frac{Auv^{\text{T}}A}{1 + v^{\text{T}}Au}.$$

² One should collect all terms $\propto C(\omega_0^2 - \omega^2)$. Using trigonometry and dispersion relation, they are $\propto \sin(Nk)$.

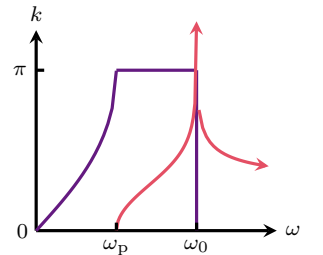


Figure 10.1: Wavenumber as a function of frequency. arrows indicate an asymptote to ∞ .
 (•) : $k' = \operatorname{Re} k$,
 (•) : $\Gamma = \operatorname{Im} k$.

Finally, an example of the transmission computed with this method is shown on Fig. 10.2. The peaks have been enlarged by $Z_{t1} = 100 \Omega$ for better visibility. As expected from the dispersion relation curvature, the peaks positions tighten at high frequencies. Above 16 GHz, they are not fully resolved.

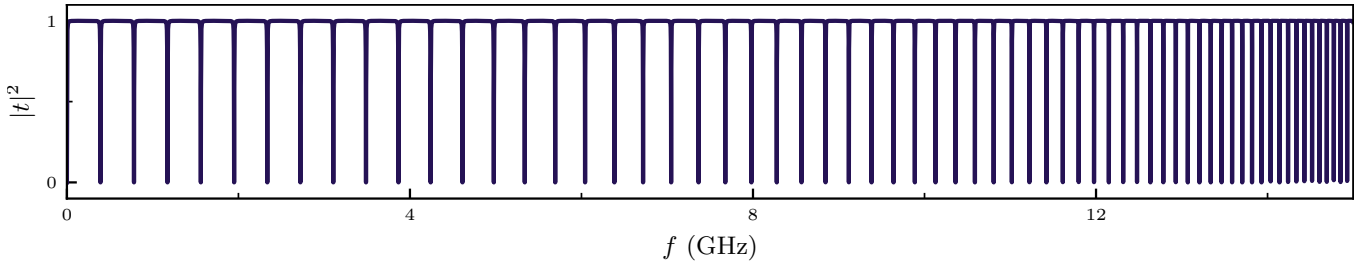


Figure 10.2: Transmission at $\Sigma = 0$ and $Z_{t1} = 100 \Omega$, for better peak visibility.

10.2 Finite temperature

Keldysh formalism

The main tool for quantum field theory at finite temperature is Matsubara's formalism¹. It introduces a new Green's function, the Matsubara Green's function, that is the retarded Green's function's analytic continuation to imaginary times. It has diagrammatic rules that holds at finite temperature, but response functions are all expressed in term of the retarded Green's function. Computing this retarded function from Feynman's function was easy, analytically and numerically, at least in the frequency domain (*cf.* Eq. (8.26)). If one rather obtained the Matsubara function, the retarded one is obtained by analytical continuation. The process is well defined analytically, but is difficult to perform numerically².

Keldysh's formalism provides another path towards the retarded Green's function. It was initially designed to tackle out-of-equilibrium situations at finite temperature. Yet, the method is easily restricted to the equilibrium case needed for linear response. It then provides a versatile tool to perform numerical computations at finite temperature.

We will not show proofs or derivations to establish Keldysh's formalism, and will simply state some important results³, showing the connection to zero temperature case when possible.

The main object of the Keldysh formalism is a 2×2 matrix formed out of the retarded, advanced, and Keldysh Green's functions,

$$\mathbb{G} = \begin{bmatrix} G_K & G_R \\ G_A & 0 \end{bmatrix}. \quad (10.17)$$

The Keldysh Green's function is given at equilibrium by the fluctuation-dissipation theorem,

$$G_K(\omega) = \coth\left(\frac{\beta\omega}{2}\right) (G_R(\omega) - G_A(\omega)). \quad (10.18)$$

$\beta = \hbar/k_B T$ is the inverse temperature. $\beta = 0.3 \text{ GHz}^{-1}$ at 20 mK. The temperature dependent term is linked to the Bose occupation factor, $n_B(\omega) = 1/(\exp(\beta\omega) - 1)$, by $\coth(\beta\omega/2) = 1 + 2n_B(\omega)$. It is sketched on Fig. 10.3.

¹ H. Bruus & K. Flensberg. **2004**. *Many-Body Quantum Theory in Condensed Matter Physics*.

² One must resort to the Padé approximant technique, *cf.* K. S. D. Beach, R. J. Gooding, & F. Marsiglio. **2000**. *Phys. Rev. B* **61**, 5147; Ž. Osolin & R. Žitko. **2013**. *Phys. Rev. B* **87**, 245135.

³ For a comprehensive review of the topic, *cf.* A. Kamenev. **2005**. arXiv:cond-mat/0412296.

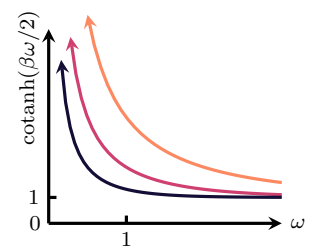


Figure 10.3: $\coth(\beta\omega/2)$ plotted for different β .
 (●) : $\beta = 2$,
 (●) : $\beta = 1$,
 (●) : $\beta = 1/2$.

The Dyson equation holds at the matrix level, as we will show shortly:

$$(\mathbb{G}^{\circ -1}(\omega) - \Sigma(\omega)) \mathbb{G}(\omega) = \mathbb{1}, \quad \Sigma = \begin{bmatrix} 0 & \Sigma_A \\ \Sigma_R & \Sigma_K \end{bmatrix}. \quad (10.19)$$

The structure of the self-energy 2×2 matrix, like the one of \mathbb{G} , is a consequence of causality¹. The consequence of the last equation is that the scalar Dyson equation holds for the retarded (and advanced) components,

$$G_R(\omega) = \frac{1}{G_R^{\circ -1}(\omega) - \Sigma_R(\omega)}. \quad (10.20)$$

This is not the case for the Keldysh component.

Again, no diagrammatic rules exist for the retarded function G_R alone. Instead, one must rotate the Green matrix to the ‘forward/backward’ basis², using a change of basis \mathbb{B} verifying³

$$\begin{bmatrix} G_{++} & G_{+-} \\ G_{-+} & G_{--} \end{bmatrix} = \mathbb{B} \mathbb{G} \mathbb{B}, \quad \mathbb{B} = \frac{1}{\sqrt{2}} \begin{bmatrix} 1 & 1 \\ 1 & -1 \end{bmatrix}. \quad (10.21)$$

The $G_{\pm\pm}$ have diagrammatic rules. We represent their propagators by

$$\begin{bmatrix} G_{++} & G_{+-} \\ G_{-+} & G_{--} \end{bmatrix} = \begin{bmatrix} \text{---} & \text{---} \text{---} \\ \text{---} \text{---} & \text{---} \end{bmatrix}. \quad (10.22)$$

The set of vertices is doubled. Every vertex we previously used now exist in two versions, with only solid lines attached, or only dashed lines attached. The second kind comes with an overall minus sign. The vertex list is represented on Fig. 10.4. Diagrammatic rules are often formulated directly in the advanced/retarded basis, but this approach is not well adapted to the resummation we want to perform. We will instead derive the expressions for the self-energy from the diagrammatics in the forward/backward basis, and then rotate back the the advanced/retarded basis.

The Dyson equation is rarely written in the forward/backward basis, so we check its validity. We construct the matrix self-energy as

$$\begin{bmatrix} \Sigma_{++} & \Sigma_{+-} \\ \Sigma_{-+} & \Sigma_{--} \end{bmatrix}, \quad (10.23)$$

where $\Sigma_{\sigma\sigma'}$ is the set of all one particle irreducible, amputated diagrams starting at a vertex $\sigma \in \{+, -\}$ and ending at a vertex $\sigma' \in \{+, -\}$. Dyson equation writes

$$\text{---} = \text{---} + \text{---} \circlearrowleft \Sigma_{++} \text{---} + \text{---} \circlearrowleft \Sigma_{-+} \text{---} + \text{---} \circlearrowright \Sigma_{-+} \text{---} + \text{---} \circlearrowright \Sigma_{--} \text{---}, \quad (10.24)$$

where the thick colored line indicates a full interacting propagator. Similar equation holds for the other propagators. The matrix structure is obvious: the four equations are summed up as

$$G_{\sigma\sigma'} = G_{\sigma\sigma'}^{\circ} + G_{\sigma\rho}^{\circ} \Sigma_{\rho\rho'} G_{\rho'\sigma} \Leftrightarrow (\mathbb{G}^{\circ -1} - \Sigma) \mathbb{G} = \mathbb{1}. \quad (10.25)$$

The last form has been obtained by rotating in the retarded/advanced basis, which confirms that

$$\mathbb{B} \begin{bmatrix} \Sigma_{++} & \Sigma_{+-} \\ \Sigma_{-+} & \Sigma_{--} \end{bmatrix} \mathbb{B} = \Sigma. \quad (10.26)$$

¹ It should be noted that the structure of Σ is not a definition, but a theorem.

² This name is transparent in a rigorous exposition of Keldysh formalism, where the system evolves on a closed time contour, with a forward and a backward part.

³ The change of basis is well defined, since $\mathbb{B} = \mathbb{B}^{-1}$.

Vertex	Value
	$iE_J^*/2!$
	$-iE_J/2!$
	$iE_J/4!$
	$-iE_J/6!$
⋮	
	$-iE_J^*/2!$
	$iE_J/2!$
	$-iE_J/4!$
	$iE_J/6!$
⋮	

Figure 10.4: The list of vertices in Keldysh formalism and for the forward/backward fields.

SCHA at finite temperature

At first order in the self energy, we see that no diagram connects solid and dashed external legs¹. The non-zero entries of the self-energy matrix are

$$\begin{aligned}
 -i\Sigma_{++} &= \text{---} \circ \text{---} \circ + \text{---} \circ \star \text{---} \circ + \text{---} \circ \text{---} \circ + \text{---} \circ \text{---} \circ + \dots \\
 -i\Sigma_{--} &= \text{---} \circ \text{---} \circ + \text{---} \circ \star \text{---} \circ + \text{---} \circ \text{---} \circ + \text{---} \circ \text{---} \circ + \dots
 \end{aligned} \tag{10.27}$$

The Keldysh rotation provides $\Sigma_R = (\Sigma_{++} - \Sigma_{--})/2$. Furthermore, $G_{++}(t=0) = G_{--}(t=0) = G_K(t=0)/2^2$, such that

$$\Sigma_R = E_J e^{-\frac{i}{4}G_K(0)} - E_J^* \tag{10.28}$$

The exponential argument is

$$-\frac{i}{4}G_K(0) = \frac{1}{2} \int_0^{\omega_c} \frac{d\omega}{2\pi} \cotanh\left(\frac{\beta\omega}{2}\right) \text{sign}(\omega) \text{Im} G_F(\omega). \tag{10.29}$$

When $\beta \rightarrow \infty$, *i.e.* $T \rightarrow 0$, $\cotanh(\beta\omega/2)\text{sign}(\omega) = \cotanh(\beta|\omega|/2) \rightarrow 1$. We recover the self-consistent equation we derived at zero temperature using Feynman's Green's functions, Eq. (9.29). It is noteworthy that the finite temperature self-consistent harmonic approximation could be reached in a different formalism, using the Gibbs-Helmholtz variational principle on the free energy.

At finite temperature, the hyperbolic cotangent function appearing in the integral prevents us from deriving an exact result. We rather cut the integral in half at the energy scale of the inverse temperature, to form a low and high frequency part³.

$$\begin{aligned}
 -\frac{i}{4}G_K(0) &\simeq -\alpha \left(\int_0^{\frac{1}{\beta}} + \int_{\frac{1}{\beta}}^{\omega_c} \right) \frac{\omega}{\omega^2 + \Omega^{*2}} \cotanh\left(\frac{\beta\omega}{2}\right) d\omega \\
 &\simeq -\alpha \left(\frac{2}{\beta} \int_0^{\frac{1}{\beta}} \frac{d\omega}{\omega^2 + \Omega^{*2}} + \frac{\alpha}{2} \int_{\frac{1}{\beta}}^{\omega_c} \frac{2\omega d\omega}{\omega^2 + \Omega^{*2}} \right) \\
 &\simeq -\frac{2\alpha}{\beta\Omega^*} \arctan\left(\frac{1}{\Omega^*\beta}\right) - \frac{\alpha}{2} \ln\left(\frac{(\beta\Omega^*)^2 + (\omega_c\beta)^2}{1 + (\beta\Omega^*)^2}\right).
 \end{aligned} \tag{10.30}$$

At low temperature, we suppose $1/\beta \ll 2\pi\alpha E_J^* \ll \omega_c$. The first term on the left hand side is $-1/(2\beta E_J^*) \ll 1$ and is neglected. We recover the zero temperature limit,

$$-\frac{i}{4}G_K(0) \simeq -\frac{\alpha}{2} \ln\left(\left(\frac{\omega_c}{\Omega^*}\right)^2 + 1 - O\left(\frac{1}{(\beta\Omega^*)^2}\right)\right). \tag{10.31}$$

As a result, we conclude that while $1/\beta \ll 2\pi\alpha E_J^*$, even if the low frequency modes are thermally populated, the SCHA result is not affected. Yet, this condition must be checked carefully, since E_J^* is going rapidly to zero because of renormalization. Furthermore, the real device has few modes at low frequencies, challenging the continuous approximation altogether. We postpone precise numerical computations to the end of the chapter.

The opposite limit of high temperature is also enlightening, even if it is not the regime we aim for experimentally. Assume $2\pi\alpha E_J^* \ll 1/\beta \ll \omega_c$. We use this limit in the result of Eq. (10.30), to obtain

$$-\frac{i}{4}G_K(0) \simeq -\frac{2\alpha}{(\beta\Omega^*)^2} - \alpha \ln(\beta\omega_c). \tag{10.32}$$

¹ *i.e.*, forward and backward Green's functions.

² The Keldysh rotation is slightly modified at $t=0$, *cf.* A. Kamenev. 2005. arXiv:cond-mat/0412296.

³ Again, in intermediate computations, $\Omega^* = 2\pi\alpha E_J^*$.

The self-consistency equation turns into

$$E_J^* = E_J e^{-\frac{1}{2\alpha(\pi\beta E_J^*)^2}} (\beta\omega_c)^{-\alpha} \simeq e^{-\frac{1}{2\alpha(\pi\beta E_J^*)^2}}. \quad (10.33)$$

The power law does not control E_J^* , and only contributes by an irrelevant constant. The remaining equation can see its solution expressed using the Lambert \mathcal{W} function, with little rearrangement:

$$\begin{aligned} \left(\frac{E_J^*}{E_J}\right)^2 &= \exp\left(-\frac{1}{\alpha(\pi\beta E_J)^2} \left(\frac{E_J}{E_J^*}\right)^2\right) \\ \Rightarrow \frac{E_J^*}{E_J} &= \frac{1}{\sqrt{\alpha\pi\beta E_J}} \left(\sqrt{-\mathcal{W}\left(-\frac{1}{\alpha(\pi\beta E_J)^2}\right)}\right)^{-1}. \end{aligned} \quad (10.34)$$

where \mathcal{W} is the first branch of the Lambert function¹. This function is represented on Fig. 10.5. Above the threshold temperature of $1/\beta = E_J\pi\sqrt{\alpha/e}$, the solution is lost: the self-consistent procedure breaks. This does not signal a transition. Note that the temperature scale is here compared to E_J , the bare value of the Josephson energy.

Second order at finite temperature

The extension of second order computations to finite temperature poses no conceptual problems. When examining the corresponding diagrams, we conclude that the vertex renormalization is not changed: since $G_{++}(t=0) = G_{--}(t=0)$, tadpole loops containing — lines do not differ from the ones containing - - - lines. Especially, vertex dressing does not interfere with the respective signs of + and - vertices. Then, the matrix structure of the self-energy is preserved, since the nature of the left and right vertices completely determines which type of propagator connects them. It writes

$$\begin{bmatrix} \Sigma_{++} & \Sigma_{+-} \\ \Sigma_{-+} & \Sigma_{--} \end{bmatrix} = \begin{bmatrix} \text{diagram 1} & \text{diagram 2} \\ \text{diagram 3} & \text{diagram 4} \end{bmatrix} + \dots, \quad (10.35)$$

where we only represented 3 intermediate legs terms. The resummation can be performed element-wise, and the vertex signs are packaged into matrices, such that

$$\begin{bmatrix} \Sigma_{++} & \Sigma_{+-} \\ \Sigma_{-+} & \Sigma_{--} \end{bmatrix} = E_J^*{}^2 \begin{bmatrix} 1 & 0 \\ 0 & -1 \end{bmatrix} \begin{bmatrix} \sin(G_{++}) - G_{++} & \sin(G_{+-}) - G_{+-} \\ \sin(G_{-+}) - G_{-+} & \sin(G_{--}) - G_{--} \end{bmatrix} \begin{bmatrix} 1 & 0 \\ 0 & -1 \end{bmatrix}. \quad (10.36)$$

This expression is enough for numerical computations, but the Keldysh rotation to the retarded/advanced basis can be done by hand:

$$\mathbb{Z} = E_J^*{}^2 \left(2 \begin{bmatrix} 0 & \cos \frac{G_K}{2} \sin \frac{G_A}{2} \cos \frac{G_R}{2} \\ \cos \frac{G_K}{2} \sin \frac{G_R}{2} \cos \frac{G_A}{2} & \sin \frac{G_K}{2} \cos \frac{G_A}{2} \cos \frac{G_R}{2} \end{bmatrix} - \begin{bmatrix} 0 & G_A \\ G_R & G_K \end{bmatrix} \right). \quad (10.37)$$

From this expression, we can read the retarded component of the self-energy, and use it in Dyson's equation and results from Sec. 10.1 to give the interacting Green's function at 2nd order.

We have benchmarked these results to a simple Matsubara calculation followed by analytical continuation using Padé approximants. However, the Matsubara approach cannot resolve the fine structure of the multi-photon peaks, contrary to the Keldysh version, as we will show. In the next section, we employ these techniques to analyse the fine structure of the self-energy at finite temperature.

¹ From its definition,

$$z = we^w \Leftrightarrow w = \mathcal{W}(z),$$

one can recover the expression of (10.34).

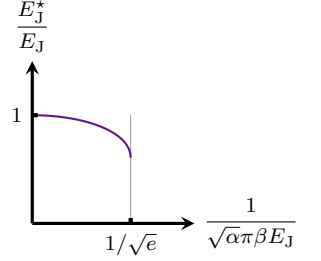


Figure 10.5: The renormalization at high temperature obtained *via* Lambert function. The solution is lost above $1/\sqrt{e}$.

10.3 High frequency and skeleton expansion

We first focus on results at $\omega > E_J^*$, since perturbation theory is most trusted in this region. The microscopic parameters are repeated on Tab. 10.1. The non-interacting Green's function is computed using Eq. (10.11), and the complex wavenumbers *formulae* of Sec. 10.1. Applying the right parity rules, we deduce the advanced, retarded, and Keldysh Green's function, build the corresponding Keldysh matrix, and rotate it to the forward/backward basis.

Here, Eq. (10.37) provides the retarded self-energy, and Dyson equation finally gives the interacting retarded Green's function. The transmission, the closest quantity to the experiment, is computed through \mathbf{G}_{NN} (Eq. (10.12)), plugged into Eq. (8.16). The numerical computation is performed using NumPy¹, in the Python language.

For now, we set the E_J^* scale by hand, at a fraction of E_J fixed at 1 GHz. Since we do not perform any self-consistency, we compute the vertex dressing separately from E_J^* , as

$$E_J^v = E_J \exp\left(-\frac{i}{4} \int_{\mathbb{R}} \frac{d\omega}{2\pi} G_K(\omega)\right). \quad (10.38)$$

We only consider the limit $E_J^* \ll E_J$, and check that the self-energy tends to a stable

Parameter	Value
N	4250
C	144 fF
C_J	14.5 fF
C_g	0.146 fF
L	0.53 nH
$f_0 \simeq f_P$	18 GHz
Z_c	1.9 k Ω
Z_{tl}	50 Ω

Table 10.1: Microscopic parameters of the circuit, and other important scales.

¹ C. R. Harris, K. J. Millman, *et al.* 2020. *Nature* 585, 357.

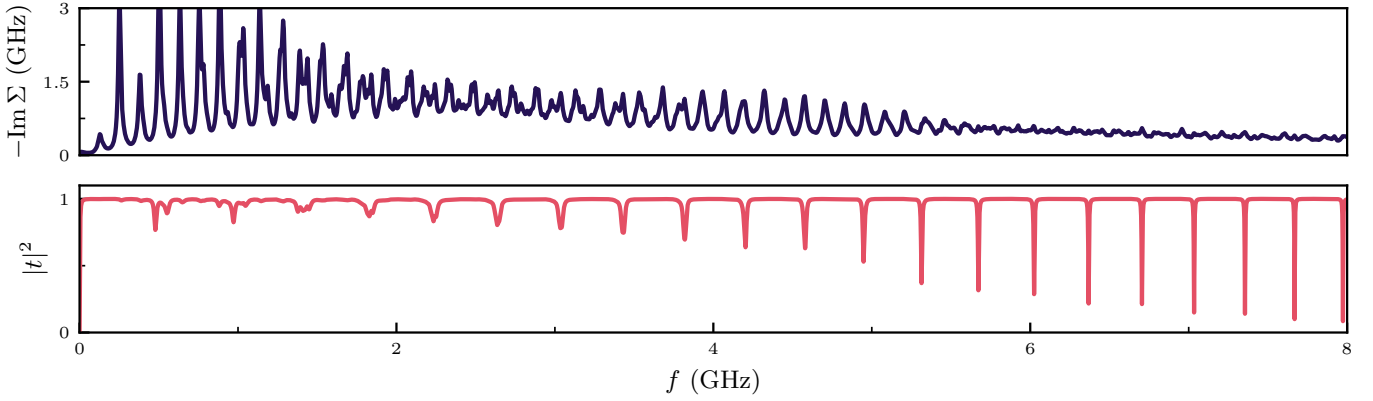


Figure 10.6: Order 2 computation at $T = 30$ mK and $E_J^* = E_J/20$.

result in this limit. The result is shown on Fig. 10.6 for $E_J^* = E_J/20$ and on Fig. 10.7 for $E_J^* = E_J/200$, both at $T = 30$ mK, a reasonable estimate of a dilution fridge temperature. We first observe a strong broadening of the transmission peaks, which

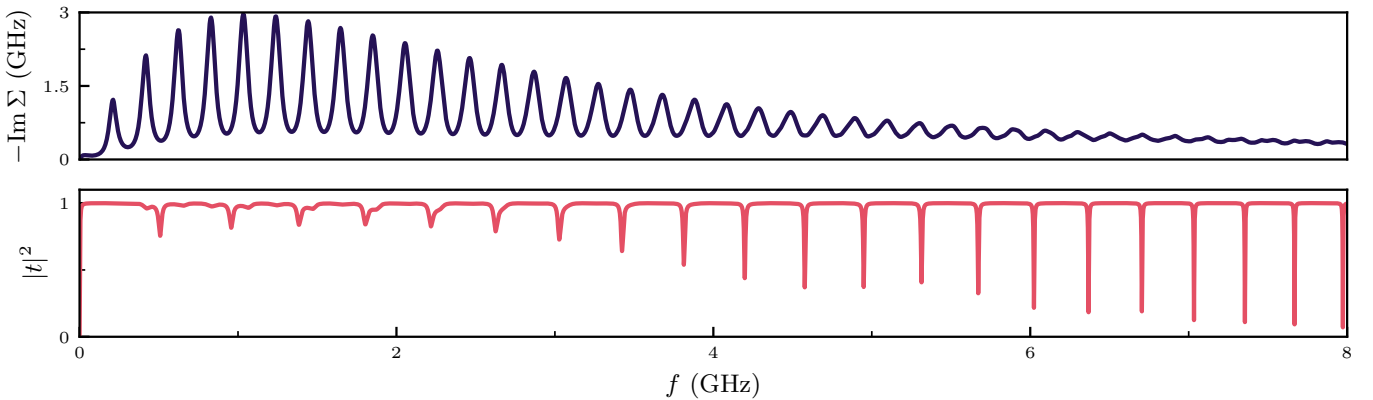


Figure 10.7: Order 2 computation at $T = 30$ mK and $E_J^* = E_J/200$.

corresponds to the experimental observations. The curve at $E_J^* = E_J/20$ presents a forest of peaks in the self energy, with corresponds to the various $2n + 1$ photon

resonances. We will detail the forest content in the low frequency case, where they are better separated. For now, we notice that they produce secondary peaks in the transmission, an effect that is not observed experimentally. When $E_j^* \rightarrow 0$, the self-energy is broadened, but not enough in order to suppress the secondary transmission peaks. The parameters influencing this peak forest effect are the temperature and the external losses, but none of them can smooth the self-energy within realistic values to reach agreement with the Lorentzian shape evidenced on Fig. 8.9. We turn instead to a new refining of the perturbative expansion.

Skeleton expansion

The failure to reproduce the correct spectroscopic structure is perhaps not surprising: the numerous resonant lines present in the self-energy are closely packed together, yet we did not include in any way the level repulsion between these lines. It can be added into the diagrammatic expansion thanks to a method known as the skeleton expansion, which can be seen as yet another resummation trick¹. In the self-energy list of diagrams, one can notice that the Green's function bare lines are dressed by more and more self-energy parts inserted into it:

$$\begin{aligned}
 -i\Sigma = & \text{diagram 1} + \text{diagram 2} + \text{diagram 3} + \dots \\
 & + \text{diagram 4} + \text{diagram 5} + \dots
 \end{aligned}
 \tag{10.39}$$

The first diagram is the one we already considered. The two others of the first line contain insertions of the self-energy into diagrams we already took into consideration. The two diagrams of the second line cannot be expressed as insertions of the 2nd order self-energy; they are neglected in the skeleton expansion. We omitted the Keldysh vertices here, as well as vertex dressing, both of which are discussed later.

The list of insertion diagrams is easily generated. Starting with the usual procedure $G^\circ \rightarrow \Sigma \rightarrow G^{(1)}$, we can re-compute Σ with $G^{(1)}$ instead of G° . It generates all diagrams with at most one self-energy inserted on each line. Iterating more and more will generate nested insertions, until the process converges to the bold Green's function, noted G^b ². Diagrammatically, we can summarize the situation by representing the dressed Green's function resulting from the process by a double line $iG^b(t-t') = \underline{\underline{t}} \text{---} \underline{\underline{t'}}$. It obeys the relationships:

$$G^b(\omega) = \frac{1}{G^{\circ-1}(\omega) - \Sigma(\omega)}
 \tag{10.40}$$

and

$$-i\Sigma(t-t') = \text{diagram 1} + \text{diagram 2} + \dots
 \tag{10.41}$$

The diagrams appearing in Σ are called the skeleton diagrams, since all the diagrams taken into account are only dressed versions of these bare skeletons. Akin to the Dyson equation resummation, the exact self-energy still contains an infinity of skeleton diagrams, and we limit ourselves to second order. Solving this set of equation is equivalent to the iterative process we described above, provided it converges. It can be considered as a self-consistent procedure.

Historically, the skeleton expansion has been useful in several instances. For the Fermi liquid problem, it provided a diagrammatic proof of the existence of the Fermi surface at zero temperature for the interacting system³, as it was anticipated long

¹ In the context of quantum chemistry, the method is known as self-consistent GW. It is a crucial tool to finely describe complex spectroscopic structures, cf. D. Golze, M. Dvorak, & P. Rinke. **2019**. *Front. Chem.* **7**, 377.

² It must not be confused with the interacting Green's function, G , that can be found by summing all the diagrams. Here, we still selected a sub-class of relevant diagrams.

³ J. M. Luttinger. **1960**. *Phys. Rev.* **119**, 1153.

ago by phenomenological theories of the Fermi liquid. It reappeared for the X-ray problem¹, and latter for the more involved Kondo problem², where it was used to extend the domain of validity of perturbation theory below the Kondo temperature.

We introduce it in the BSG problem because the Green's function is clearly widely perturbed by the introduction of interactions, with strong broadening of its initially narrow resonance peaks. We hope that iterating the skeleton expansion will pile up this broadening on itself, densifying the forest of resonance peaks, and thus smoothing the self-energy.

Skeleton expansion and SCHA

Before computing the second order, we can make a quick detour to the first order. The self-energy skeleton diagrams are

$$-i\Sigma(\tau) = \text{diagram 1} + \text{diagram 2} + \text{diagram 3} + \dots = -i\delta(\tau)E_J e^{-\frac{1}{2} \int_{\mathbb{R}} \frac{d\omega}{2\pi} G_F^b(\omega)}. \quad (10.42)$$

The skeleton expansion at 1st order reduces to the self-consistent harmonic approximation³. E_J^* role is here played by $\Sigma(\omega)$, a real constant at this approximation level. Note that we did not need to introduce a counter-term, since G^b already contains Σ , and is thus free of infrared divergences. When Σ develops a frequency dependence and imaginary part, E_J^* can be defined as $\text{Re}\Sigma(\omega_0)$, the regulator for G infrared divergence.

Skeleton expansion at 2nd order

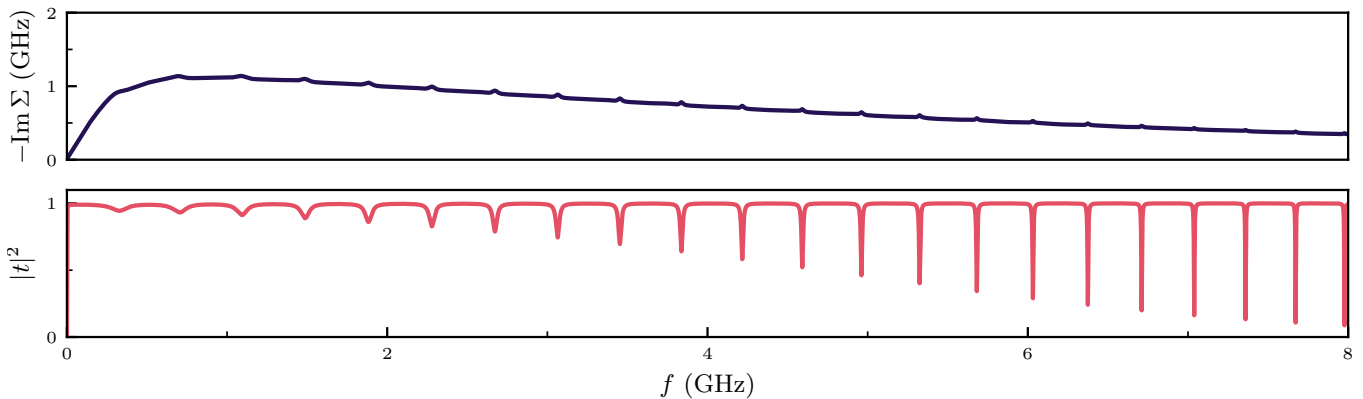


Figure 10.8: 2ndorder skeleton expansion, at $T = 30$ mK and $E_J^* = E_J/20$.

We now apply the skeleton expansion to the experimental situation at hand, implementing directly the recursive algorithm in the numerical routine, and waiting for point-wise convergence of G^b . At each step, we impose the value of E_J^* by shifting the real part of the self-energy, which does not violate Kramers-Krönig relations. The results are shown on Fig. 10.8. As expected, the self-energy is smoothed by the skeleton self-consistency. Since the self-energy is slowly varying, we recover Lorentzian peaks, as observed experimentally. We can expect that the self-energy is now closer to the predictions of Sec. 9.3 continuous limit. Our algorithm is now too resolved in frequency to perform computations over many decades, so we refrain ourself to produce log/log plots. Fig. 10.9 shows two exponential decay laws, with slightly different slopes. The one above the plasma frequency $\omega_p/2\pi = 18.08$ GHz is expected. The

¹ B. Roulet, J. Gavoret, & P. Nozières. **1969**. *Phys. Rev.* **178**, 1072.

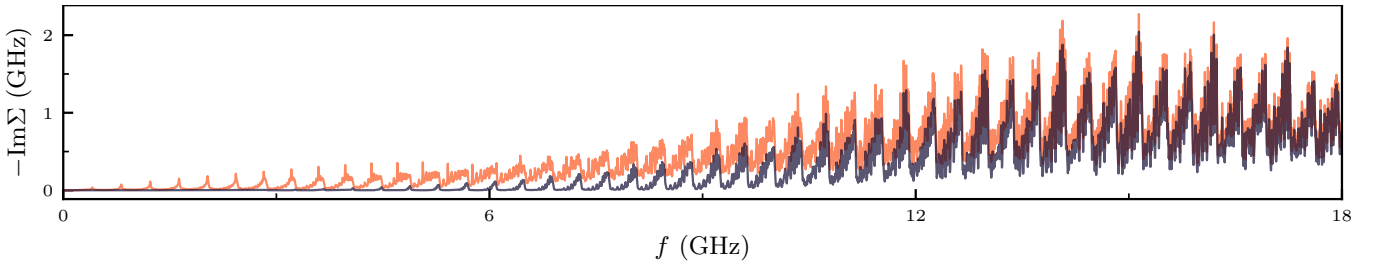
² R. D. Mattuck, L. Hansen, & C. Y. Cheung. **1971**. *J. Phys. Colloques* **32**, 1.

³ One could argue that the SCHA provides an fixed point equation, $E_J^* = f(E_J^*)$, while the skeleton expansion provides a recursion algorithm, $E_{J_{n+1}}^* = f(E_{J_n}^*)$. The two coincide only if the fixed point is attractive. It could be interesting to find physical examples where f does not verify this property, or have a more involved fixed point structure.

one below corresponds to the situation we highlighted on Fig. 9.10; the ultraviolet cutoff prevents the high frequency power law to develop, and we instead observe a crossover regime. It results in this approximate exponential decay.

10.4 Peak forests at low frequency

We now turn our attention to the low frequency part, in the $\omega \lesssim E_J^*$ sense. We compute the self-energy in the same manner than before, but we suppress renormalization, setting $E_J^* = E_J$ by hand. This is enough to bring E_J^* in the measure range, 2 – 12 GHz, and transit from high to low frequency regime. The resulting self-energy is represented on Fig. 10.10.



We observe a forest of resonance peaks, that seems organized into well separated groves of densely packed peaks, forming large resonance bands. A peak at frequency ω mainly corresponds to a 3-photon resonance, *i.e.* there exist 3 modes the frequencies of which check energy conservation, $\omega = \omega_1 + \omega_2 + \omega_3$ ¹. This detailed spectroscopy can be realized on the self-energy curve at lower Z_{t1} , which lowers the external dissipation, and hence the peak width. A close-up on a specific grove is plotted on Fig. 10.11.

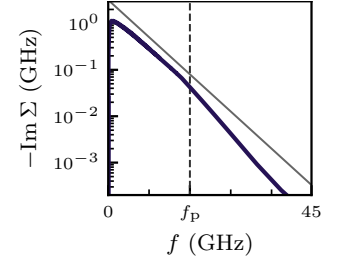
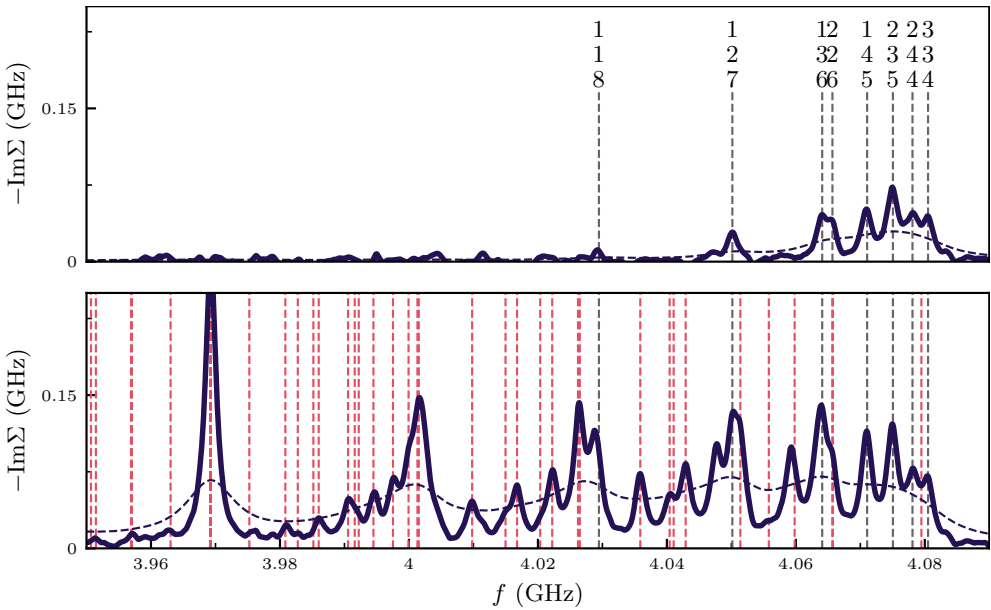


Figure 10.9: Same result in log/lin scale.
 (●) : self-energy,
 (○) : exponential fit below f_P .

Figure 10.10: 2nd order self-energy for $E_J = E_J^* = 3$ GHz, at different temperatures.
 (●) : $T = 0$ mK,
 (○) : $T = 50$ mK.

¹ This physically motivated statement can be proven by noticing $\Sigma(\omega)$ is $G(\omega)$ self-convoluted three times.

Figure 10.11: Close-up on (●) 2nd order self-energy, computed at
 (—) $Z_{t1} = 10 \Omega$,
 (- -) $Z_{t1} = 50 \Omega$.
Top panel. $T = 0$ mK. Grey lines (■) predict resonances, numbers indicate the index of the resonant modes.
Bottom panel. $T = 30$ mK. Pink lines (■) indicate temperature assisted resonances.

The resonances are labeled by the number of the modes involved, *e.g.* (1,2,7) peak corresponds to a splitting in 3 photons occupying modes number 1, 2 and 7. We see that this peak grove is composed of $\omega \sim 10\omega_{\min}$ resonances, ω_{\min} the fundamental frequency of the array. For a linear dispersion relation, all these resonances would be

degenerate. The dispersion relation is here slightly curved, resulting in a degeneracy lift, and the formation of a large grove of peaks¹.

At finite temperatures, modes are thermally populated, which allows new processes involving absorption of thermal photon instead of emission only. The conservation law turns into $\omega = \pm\omega_1 \pm \omega_2 \pm \omega_3$. This raise drastically the combinatoric number of allowed resonances, broadening further the peak grove at finite temperature. This effect is demonstrated on the bottom panel of Fig. 10.11, by plotting the temperature assisted resonances.

Third order

The renormalization group argument we laid down in Sec. 4.5 warned us on the validity of perturbation theory below the E_J^* scale. This is a manifestation of the boundary sine-Gordon model asymptotic freedom in the superconducting phase. A similar situation has been widely studied in the case of the Kondo problem, where the emergent scale is given by the Kondo temperature. In this context, the set of relevant diagrams change at the T_K scale². To test the quality of our diagram set choice, we can augment it to third order, and monitor the weight of the next order in Σ . The list of 3rd order diagrams is³

$$-i\Sigma = (\text{2nd order}) \tag{10.43}$$

(i)

(ii)

(iii)

Lines (i) and (ii) are the new diagrams with frequency dependence and imaginary parts. Line (ii) is a diagram we already computed, with further dressing of the vertex. Line (iii) contains all the new contributions to vertex dressing. They are constant in frequency (or local in time), and purely real.

These diagrams fall into the non-crossing category, which means that they can be computed quite systematically. Lines in parallel correspond to Green's functions, or any correlation function, multiplied together in the time domain. Lines in series correspond to functions convoluted together in the time domain, so they are also multiplied in frequency domain. Fourier transforming back and forth is thus enough to conclude any computation.

As an example, we define the even and odd bubbles as

$$\begin{aligned}
 i\chi_e(t-t') &= \text{bubble} + \text{bubble} + \dots = \cos(G^b(t-t')) - 1, \\
 i\chi_o(t-t') &= \text{bubble} + \text{bubble} + \dots = i(\sin(G^b(t-t')) - G^b(t-t')). \tag{10.44}
 \end{aligned}$$

These correlation functions play a prominent role in the random phase approximation, a standard diagrammatic technique for the electron gas⁴. The first diagram

¹ The five photon resonances do not appear in this regime. We deduce that they are less relevant, contrary to the high frequency regime.

² R. D. Mattuck, L. Hansen, & C. Y. Cheung. 1971. *J. Phys. Colloques* 32, 1.

³ We only represent the minimal number of line between each vertex: one could add a pair of lines between any pair of vertex, and sum over these possibilities to generate sines or cosines. Aside, note that the second and third diagram on line (iii) are equal but have different symmetry factors, as well as the fourth and the fifth. Finally, all vertices are dressed by 1st order diagrams, and at finite temperature, the list is extended by using the two vertex types.

⁴ H. Bruus & K. Flensberg. 2004. *Many-Body Quantum Theory in Condensed Matter Physics*.

in Eq. (10.43) is then decomposed on a top part, written as $-iE_J^y(i\chi_e(\omega))^2$, to be Fourier transformed, and a bottom part, $(-iE_J^y)^2 iG^b$. Both are multiplied to provide the diagram value, up to vertices and symmetry factors. The first crossing diagram, that cannot be reduced by such a procedure, only appears at 4th order¹. At finite temperature, the two species of vertices inserts smoothly into this picture: we define a 2×2 matrix of vertices,

$$\mathbb{V} = -iE_J^y \begin{bmatrix} 1 & 0 \\ 0 & -1 \end{bmatrix} \tag{10.45}$$

as well as matrices of correlation functions \mathbb{X}_e and \mathbb{X}_o by analogy with Green's function Keldysh matrix, \mathbb{G} . Correlation functions in parallel are multiplied element-wise², while correlation functions in series are multiplied as matrices:

$$\text{Diagram} = \mathbb{X}_e(\omega) \mathbb{V} \mathbb{X}_e(\omega). \tag{10.46}$$

At last, we perform the skeleton recursion, together with first and second order diagrams. The resulting self-energy is represented on Fig. 10.12 at $T = 30$ mK, and compared to 2nd order. Neither the skeleton expansion, nor the 3rd order managed

¹ One crossing diagrams representative is:



² i.e. with Hadamard's matrix product.

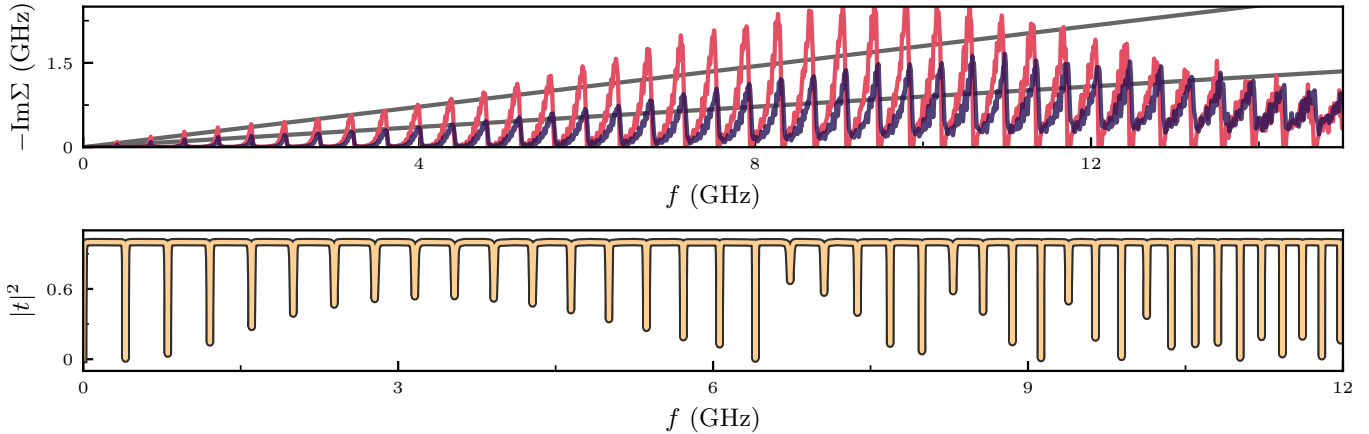


Figure 10.12:
Top panel. Self-energy for $T = 30$ mK, computed at (●) 2nd and (●) 3rd orders. Lines (—) show linear approximation of peak value at small frequency.
Bottom panel. Transmission computed with 3rd order self-energy.

to smooth the self-energy. We still observe relatively broad peak groves. The self-energy varies slowly enough, so the transmission dips are approximately Lorentzian. The computation shows only minor deviations, that are not relevant to experimental measures.

More concerning is the amplitude of 3rd order, comparable to 2nd order. Perturbation theory is not satisfactorily converged, and the result must be interpreted with care. The overall shape seems more stable, so we could hope that we are only lacking some global amplitude factor. Overall, the many-body dissipation is weaker here than in the high-frequency regime.

Finally, we notice that the weak ω^5 low frequency power law disappears at finite temperature, to be replaced by a stronger but more conventional ω power law. In this regime, many-body losses thus behave like an effective resistor.

We now have a strong analytical and numerical understanding of the many-body behavior of the system. We already signaled the qualitative agreements between our theory and the experiments. It is now time to systematically compare the two.

10.5 Adjusting to experimental data

Free parameters and SQUID asymmetry

An important advantage of a careful microscopic modelization of the circuit is that the number of free parameters is low, and well controlled. The various capacitances and inductances, C, C_g, C_J and L are measured independently of the many-body spectroscopy experiments. The large size of the chain junctions allows to estimate C by measuring the junctions size¹, and L and C_g are measured by fitting the dispersion relation. C_J can either be estimated by junction size, or left as a free parameter for the adjustment of the phase shifts we detailed in Sec. 8.1. These experimental values are given in Tab. 10.1.

The value of E_J is controlled *in situ*, by an external magnetic flux threading the loop of a SQUID². The SQUID circuit is represented on Fig. 10.13. The phases across each junctions are denoted φ_1 and φ_2 . Their respective Josephson energies are E_1 and E_2 . The total SQUID Hamiltonian is then $\hat{H} = -E_1 \cos \hat{\varphi}_1 - E_2 \cos \hat{\varphi}_2$. Kirchhoff's loop rule then asserts $\varphi_1 + \varphi_2 = \Phi_{\text{ext}}$. We define the variable $\varphi = \varphi_2 - \varphi_1$, such that $\varphi_1 = (\Phi_{\text{ext}} - \varphi)/2$ and $\varphi_2 = (\Phi_{\text{ext}} + \varphi)/2$. The Hamiltonian is factorized into³

$$\begin{aligned} \hat{H} &= -(E_1 + E_2) \cos(\Phi_{\text{ext}}/2) \left(\cos(\varphi/2) - \frac{E_2 - E_1}{E_1 + E_2} \sin(\varphi/2) \tan(\Phi_{\text{ext}}/2) \right) \\ &= -E_J^0 \sqrt{\cos^2(\Phi_{\text{ext}}/2) + d^2 \sin^2(\Phi_{\text{ext}}/2)} \cos(\hat{\varphi}'), \end{aligned} \quad (10.47)$$

where $E_J^0 = E_1 + E_2$, $d = (E_2 - E_1)/(E_2 + E_1)$, and $\varphi' = \varphi - \arctan(d \tan(\Phi_{\text{ext}}))$. $\hat{\varphi}'$ is the degree of freedom of the SQUID. We see that the Hamiltonian reduces to the one of a single junction, with a tunable Josephson energy depending on the external flux. d is its asymmetry: it vanishes when the two junctions are exactly identical. Else, it is essentially relevant for external flux near π , where it prevents the effective Josephson energy to vanish. The effect is represented on Fig. 10.14.

The calibration of E_J with respect to Φ_{ext} thus requires two parameters, E_J^0 and d . The first one can be estimated by Ambegaokar & Baratoff's relation, Eq. (2.11). The normal resistance is measured independantly on an array of similar SQUIDS, nanolithographed on the same sample, and measured at room temperature. It provides the estimate $E_J^0 = 25.8$ GHz. We consider this measure an estimate only, given the fabrication uncertainty, an will keep E_J^0 as a free parameter. The SQUID asymmetry is small by design, and hard to estimate by the junction sizes only.

Finally, the sample temperature is also considered a free parameter, given the important experimental uncertainty on thermalization between the dilution fridge and the sample itself. The free parameters are then E_J^0 , d and T .

Adjustment procedure

The most reliable comparison between theory and experiment is provided by the transmission peak widths at high-frequency, or equivalently at low E_J^* . This result is especially independent of temperature, and allows to adjust the values of E_J^0 and d . The experimental and computed peak widths for Φ_{ext} close to π are represented on Fig. 10.15. We assume perfect experimental knowledge of Φ_{ext} : then, at $\Phi_{\text{ext}} = \pi$, $E_J = E_J^0 d$. We adjust the corresponding numerical curve to extract $E_J^0 d = 0.6$ GHz. The determination of these two values separately is less precise: with adjustment to the experimental curves at $\Phi_{\text{ext}} = 0.98 \pi$ and $\Phi_{\text{ext}} = 0.96 \pi$, we estimate $d = 2.4(4)\%$

¹ Orders of magnitude are obtained by assuming simple, approximate geometries. The result can be greatly refined by finite element simulation of the exact circuit electromagnetic response.

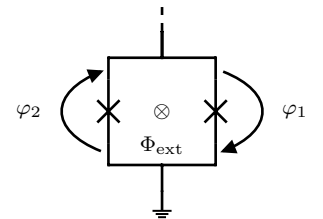


Figure 10.13: The SQUID circuit, formed by two junctions, and threaded by the external magnetic flux Φ_{ext} .

² U. Vool & M. Devoret. 2017. *Int. J. Circuit Theory Appl.* 45, 897.

³ The factorization can be tedious. We want to find B and C such that

$$\cos \varphi + d \tan \Phi \sin \varphi = C \cos(\varphi + B),$$

which provides $C \cos B = 1$ and $C \sin B = -d \tan \Phi$. We add the squares to conclude: $C = \sqrt{1 + (d \tan \Phi)^2}$.

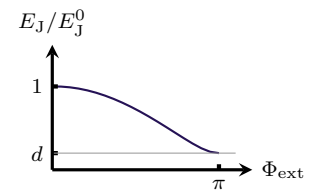
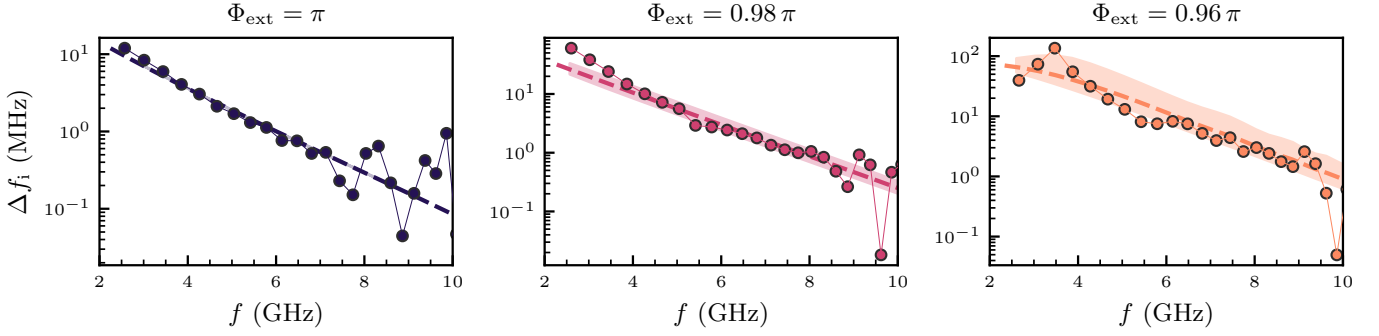


Figure 10.14: The Josephson energy controlled by Φ_{ext} at finite asymmetry.



and $E_J^0 = 25(3)$ GHz, with good agreement with Ambegaokar & Baratoff estimate $E_J^0 = 25.8$ GHz. Similarly, the 2% asymmetry is compatible with the tolerances of microfabrication.

Besides the numerical values, the qualitative agreement is quite remarkable, the experiment confirming the approximate exponential decay of the many-body losses across the spectrum we observed in the crossover regime (*cf.* Sec. 10.3). This behavior is in stark contrast with standard loss mechanisms, which usually provide integer power-laws dependence for losses, and also with the scaling limit anomalous power law. Note that the slope is controlled by ω_p , and is thus indeed constant with respect to E_J , as seen on Fig. 10.15. Finally, the low end of the spectrum reveals a deviation from the theoretical prediction, which is interpreted as the influence of finite E_J^* . For higher E_J — and lower Φ_{ext} — the scale E_J^* enters the measurement window. Computation based on the $E_J^* \ll E_J$ limit thus fails.

Figure 10.15: Peak widths due to internal dissipation, (●) Experiment, (---) Numerical estimate, (■) $\pm 0.4\%$ error margin on d , with fixed $E_J^0 d = 0.6$ GHz, for small E_J values: (●) $\Phi_{\text{ext}} = \pi$, (●) $\Phi_{\text{ext}} = 0.98\pi$, (●) $\Phi_{\text{ext}} = 0.96\pi$.

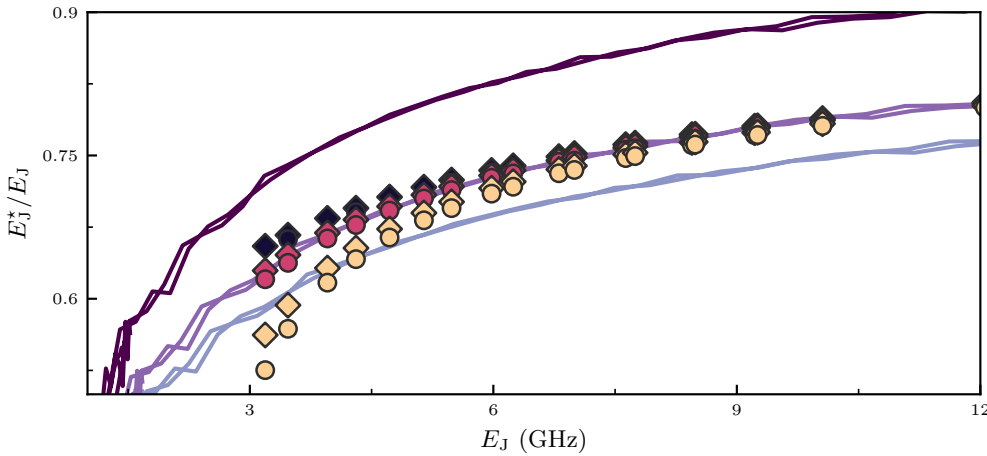


Figure 10.16: E_J^* scale renormalization as a function of its bare value E_J , computed at (●) 2nd order, (◊) 3rd order in perturbation theory, and for a temperature (●) 10 mK, (●) 30 mK, (●) 50 mK. Compared to (—) experimental result, with E_J calibrated with parameters (●) $d = 2.4\%$, (●) $d = 2.15\%$, (●) $d = 2.05\%$, and $E_J^0 d = 0.6$ GHz fixed.

In this intermediate E_J^* regime, we can test our E_J^* prediction, obtained by letting E_J^* defined as $E_J^* = \text{Re} \Sigma(\omega = 0)$ follow the renormalization flow of the skeleton self-consistency equation. The comparison to experimental values, extracted by phase shift measurement as detailed in Sec. 8.1, is presented on Fig. 10.16. We first ensure that the result is satisfactorily converged, by comparing 2nd and 3rd order results. They broadly agree, with discrepancy appearing at high temperature and strong renormalization. Accordingly, at E_J too low compared to $1/\beta$, we expect the self-consistency to break, *cf.* Sec. 10.2. Quantitatively, we match experimental and numerical results for $T = 30$ mK and $d = 2.15\%$, the former of which is in agreement with the dilution fridge temperature, and the latter with our previous estimation of

the asymmetry. Again, the qualitative agreement is noteworthy, since the many-body computation correctly captures an important renormalization factor, of order 1/2 of the bare value.

Our last observable is the peak widths, and thus the inelastic losses, in this same regime of $\omega \sim E_J^*$. As represented on Fig. 10.12, the self-energy is rougher, which translates into small deviations from the Lorentzian shape for the transmission peaks. To extract the width, we first numerically locate the peak in transmission, and then fit the transmission dip using the hanging resonator model (*cf* Eq. (8.31)), limiting ourselves to a frequency range of $\Delta\omega/5$, $\Delta\omega$ the local free spectral range, using a non-linear fit procedure. The result for one peak is presented on Fig. 10.17, where we check that the deviation to the Lorentzian shape is small, and irrelevant for experimental measurements because well below the noise level.

With the Lorentzian model validated, we compare the experimental and theoretical inelastic losses in the $\omega \sim E_J^*$ region on Fig. 10.18. As expected from Sec. 10.4, the predicted losses are below the experimental ones (note that theoretical prediction is plotted with a $\times 4$ factor on Fig. 10.18). This is to be correlated with the important weight of 3rd order terms in the self-energy imaginary part, which indicates that more contributions are to be found in higher orders. Interestingly, the overall amplitude of losses is very sensitive to temperature. It is especially clear that $T = 0$ estimations cannot capture the many-body losses in this regime. We could adjust the temperature parameter to fit these internal losses, which would lead to $T \simeq 80$ mK. Even if this value is experimentally credible, it would contradict the adjustment of Fig. 10.16 on E_J^* , which is more sound given its good convergence with respect to the perturbation series.

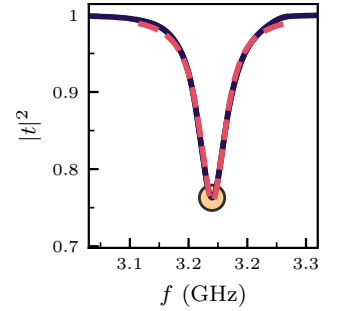


Figure 10.17: Close-up of (—) a transmission peak, and (---) its Lorentzian fit. (○) signals the numerically detected peak position.

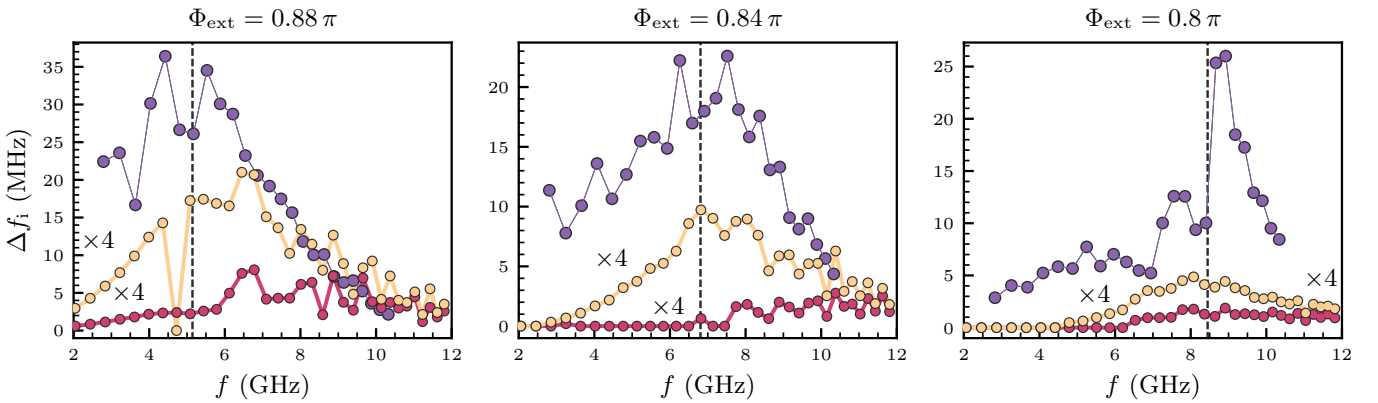


Figure 10.18: (●) Experimental peak widths due to internal dissipation, (○) $4\times$ theoretical result at $T = 50$ mK, (●) $4\times$ theoretical result at $T = 30$ mK, all represented for several Φ_{ext} , and calibrating E_J with $d = 2.2\%$ and $E_J^0 d = 0.6$ GHz. (||) indicates E_J on the frequency axis.

Besides the global numerical factor, we see that the qualitative shape is reproduced, especially with a broad maximum at the E_J scale. Furthermore, the effect of the self-energy peak forest is patent on the computed curve: it results in strong variability in the peak widths values. This is in strong contrast with the high frequency, $E_J^* \rightarrow 0$ case of Fig. 10.18. It must be noted that the experimental curves display a similarly strong variability, that cannot be explained by experimental noise alone, based on the comparison with Fig. 10.15. On the latter, we observe noise around 0.1 MHz of amplitude, while it can be as strong as 10 MHz on Fig. 10.18. This could indicate a peak forest effect, image of discrete nature of the chain modes, in the experimental results.

Overall, we found good qualitative and quantitative agreement between experiment and theory everywhere the perturbation series shows good convergence, and extracted free parameters $d = 2.2\%$, $E_j^0 = 27$ GHz and $T = 30$ mK that are coherent with their expectations and independent measurements. It revealed the many-body nature of the important inelastic losses observed, since only self-consistent skeleton expansion could reproduce it, by mixing together the resonances of a large number of modes. Furthermore, outside of its bounds, the theoretical prediction still hints towards an explanation of the strong variability in peak widths by a peak forest effect in the self-energy. It also underlines the crucial role of finite temperature in this regime.

Conclusion

11 | Perspectives on many-body simulation

Antinoüs flétris, dandys à face glabre,
Cadavres vernissés, lovelaces chenus,
Le branle universel de la danse macabre
Vous entraîne en des lieux qui ne sont pas connus !

Baudelaire, *Danse Macabre*.

Withered Antinoi, shaven
fools with stinking breath,
pale varnished corpses, grey
decrepit beaux, the world-
wide rhythm of the Dance
of Death is sweeping you to
shores no mortal knows!

transl. L. P. Shanks.

The outstanding properties of superconducting circuits make them an ideal tool to explore the most intriguing aspects of quantum mechanics. They present reasonable coherence times, high — and tunable — values of interaction strengths, and circuit designs scalable towards the many-body regime, for impurity and bulk models. This thesis attempted to demonstrate how this richness can be practically harnessed in the laboratory to uncover many-body phenomena. To do so, we clarified the various accessible regimes for a very generic superconducting impurity model simulator, designed new theoretical tools to predict its qualitative and quantitative behavior in the pertinent aforementioned regimes, and compared our results to experimental evidences of many-body physics taken from one of the first few experimental superconducting simulator.

During this work, we obtained several novel results. Some concerned the exploration of the newly formulated charge boson model¹ phase diagram². We found a parametric bound on the coupling strength due the underlying microscopic circuit³, showed the limited resilience of the spin-boson transition with NRG, and discussed the role of decompactification with the compact wavefunction ansatz. The latter in on itself an important contribution of this thesis; we provided its complete framework, and derived its key quantity, the vacuum energy expectation value⁴, for the charge-boson model. It made clear the role of charge fluctuations to weight the winding numbers importance. In this regard, Eq. (6.32) showed that, contrary to the superconducting phase fluctuations that underpins the well known Schmid transition, the charge fluctuations are not driven by the model ultraviolet cutoff. The analysis of this last equation allowed to provide a simple physical picture for decompactification at strong coupling.

Concerning the boundary sine-Gordon simulator analysis, we brought light on the ultraviolet cutoff influence on the anomalous power laws known from Tomonaga-Luttinger liquids, both analytically and numerically⁵. We described its departure from scaling regime, which is crucial to understand experimental results. We obtained good agreement between the prediction and observation of a surprising exponential decay in the self-energy frequency dependence. Our last original contribution is the demonstration that only an interplay of finite temperature and the self-consistent diagrammatic method of the skeleton expansion — imported, *inter alia*, from Abrikosov's theory on the Kondo problem — could produce a smooth dissipative response from the

¹ Defined at Eq. (3.28).

² sketched on Fig. 6.1 and traced thanks to the NRG on Fig. 4.6.

³ *cf.* Eq. (3.46).

⁴ *cf.* Eq. (6.16).

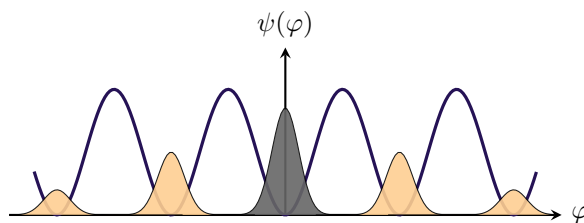
⁵ *cf.* Eq. (9.62) for analytical evidence, Fig. 9.10 for numerical confirmation, and Fig. 10.15 for confrontation to the experiment.

discrete Fabry-Perot resonances of the superconducting chain¹. This study highlights the microscopic origin of internal dissipation for quantum systems in the mesoscopic size range, comprising $\sim 10^3$ well separated degrees of freedom.

As engaging as it is, the road to textbook many-body physics is still narrow. As examples, the scaling regime proved itself hard to reach experimentally, the influence of finite temperature appeared far from negligible, and the microscopic structure of resonances is believed to play an important, yet not fully understood role in the $\omega \sim E_J^*$ regime. Experiments are currently scratching the surface of the unconventional effects, phase transitions and new phenomenologies promised by the models we attempt to probe, and important efforts will be required to fully uncover them. On the theoretical side, the careful work of modelization must obviously be continued, on a case-by-case basis, to provide precise predictions to guide experiments and confront them. Beyond that, some open questions remains to be explored, on theoretical as well as experimental grounds. We now sketch two of these research lines opened by the present thesis².

Patching the breakdown of the self-consistent method

The self-consistent harmonic approximation has proven to be a powerful tool, not only to sketch the qualitative physics and predict the Schmid transition, but also to provide numerically accurate results. Its re-derivation from diagrammatic methods allowed its extension to capture its dissipative properties, and suggested a good deal of old and new resummation techniques. Yet, it had the shortcoming of an instability at finite temperature, more precisely when $T \simeq E_J$, as we highlighted in the continuum limit on Fig. 10.5. This can be linked to the building up of 3rd order corrections seen on Fig. 10.16. The structure of cosine diagrammatics tends to an overflow of contributions at higher orders, as it has been noticed already in renormalization group analysis of the 2 dimensional sine-Gordon model³. One could be tempted to look for the right resummation. Our numerous attempts in this direction, *e.g.* by formulating a version of the random phase approximation for multi-legs vertices, did not provide significant results, and a firmer understanding of the breakdown might be needed to progress further in that direction.



A change of strategy might as well be necessary. Upon closer examination, the harmonic description fails when fluctuations of $\hat{\varphi}_0$ are comparable to 1. While staying in the superconducting phase, which implies that the phase is localized — even loosely — this could indicate that the structure of the ground state changes drastically from a Gaussian picture. It is likely that the superconducting phase starts exploring the neighboring minima of the cosine potential, as represented on Fig. 11.1. The perturbation around a Gaussian state cannot capture this qualitative change, which could explain the breakdown, and the excessive renormalization of E_J predicted for high $\langle \hat{\varphi}_0^2 \rangle$. This guesswork calls for a different method; in path integral formalism,

¹ *cf.* Fig. 10.8.

² An emphasis on the compact ansatz, with some future development avenues, have been given in Chap.7.

³ D. J. Amit, Y. Y. Goldschmidt, & S. Grinstein. 1980. *J. Phys. A: Math. Gen.* 13, 585.

Figure 11.1: (●) : Josephson potential, (●) Gaussian state assumed by self-consistent harmonic approximation, (●) expected wavefunction spill out to neighboring sites.

this tunneling effect is typically dealt with instantons, well known for providing non-perturbative results. They have been employed recently on the same model to describe inelastic scattering in the insulating phase of the boundary sine-Gordon model¹. A lighter approach could be to postulate a variational state as a sum of the main Gaussian state together with multi minima satellites contributions, the various satellites' weights in the total ansatz state being used as a variational parameters. The close resemblance with the compact ansatz could allow us to import some computations and methods from our previous work.

On the same note, making a rigorous connection between the compact ansatz and the path integral formulation of the compactness problem² could shed light on the compact ansatz inner workings, and suggest new developments of the technique.

Extension to out-of-equilibrium protocols

We presented in Sec. 10.2 how the finite temperature cosine diagrammatics was managed by Keldysh's formalism. We used it as a trick to avoid the problem of Eq. (9.35) analytical continuation in Matsubara's formalism. Yet, its scope is much broader: it was originally designed to tackle out-of-equilibrium problems. The study of transient dynamics fall into this category, which have been studied at length for waveguide QED implementation of the spin-boson model³. Another prototypical example is the case of driven systems, where Kubo's formula⁴ is no longer valid to derive the drive influence on the system.

A corresponding experimental situation is a two-tone measurement, where a probe pumps the system at a frequency ω_1 while a different frequency ω_2 is monitored. This allows to isolate the inelastic contribution, and resolve it in frequency⁵. Such an experiment would bring a definitive proof that the internal broadening mechanism is indeed linked to the inelastic response of the boundary non-linear Josephson junction. Frequency resolved cross-sections have been computed at $T = 0$ ⁶, but our analysis clearly demonstrated that temperature is a crucial ingredient of these scattering protocols. Keldysh formalism could allow to extend the analysis to provide quantitative cross-section predictions.

Generally speaking, formulating a theory of strongly driven, interacting many-body systems is still mostly an open problem. Dynamical phase transitions are expected with strong enough pumps⁷. This already incited experiments on driven superconducting simulators⁸. The question is especially acute for superconducting devices, since it is known that a driven pendulum, the classical limit for the non-linear Josephson junction, presents instabilities during which the pendulum escapes its potential well. Such an effect has been recently studied experimentally in the quantum case of a single Josephson junction⁹. It is noteworthy that for the quantum system, escaping the wells of the Josephson potential is equivalent to accessing highly excited states of the Josephson spectrum. These states are known to be more sensitive to the compactness of the superconducting phase¹⁰. The question is then open to know if strong drives could counterbalance decompactification mechanism of the many-body system, and lead to a revival of compact effects, such as offset charge sensitivity.

¹ A. Burshtein, R. Kuzmin, *et al.* **2021**. *Phys. Rev. Lett.* **126**, 137701; R. Kuzmin, N. Grabon, *et al.* **2021**. *Phys. Rev. Lett.* **126**, 197701.

² The influence of the compactness of φ has a clear formulation in path integral formalism, *cf.* L. S. Schulman. **2012**. *Techniques and Applications of Path Integration*.

³ N. Gheeraert, S. Bera, & S. Florens. **2017**. *New J. Phys.* **19**, 023036; N. Gheeraert, X. H. H. Zhang, *et al.* **2018**. *Phys. Rev. A* **98**, 043816.

⁴ *cf.* Eq. (8.12).

⁵ One could wonder how a linear response experiment allowed us to capture inelastic processes in the first place. This is thanks to unitarity of the evolution, expressed in the form of the optical theorem, *cf.*

M. E. Peskin & D. V. Schroeder. **1995**. *An Introduction To Quantum Field Theory*.

⁶ M. Goldstein, M. H. Devoret, *et al.* **2013**. *Phys. Rev. Lett.* **110**, 017002.

⁷ For an example of dynamical phase transition exhibited with Keldysh's formalism, *cf.* G. Biroli & O. Parcollet. **2002**. *Phys. Rev. B* **65**, 094414.

⁸ L. Magazzù, P. Forn-Díaz, *et al.* **2018**. *Nat. Commun.* **9**, 1403; B. Peropadre, D. Zueco, *et al.* **2013**. *Phys. Rev. Lett.* **111**, 243602.

⁹ R. Lescanne, L. Verney, *et al.* **2019**. *Phys. Rev. Applied* **11**, 014030.

¹⁰ *cf.* Fig. 7.1.

Bibliography

- V. Ambegaokar & A. Baratoff, *Tunneling Between Superconductors*. **1963**. *Phys. Rev. Lett.* **10**, 486.
- D. J. Amit, Y. Y. Goldschmidt & S. Grinstein, *Renormalisation group analysis of the phase transition in the 2D Coulomb gas, Sine-Gordon theory and XY-model*. **1980**. *J. Phys. A: Math. Gen.* **13**, 585.
- P. W. Anderson, *Localized Magnetic States in Metals*. **1961**. *Phys. Rev.* **124**, 41.
- P. W. Anderson. **1964**. in *Lectures on the Many-body Problems*, ed. E. R. Caianiello, 113.
- P. W. Anderson, *A poor man's derivation of scaling laws for the Kondo problem*. **1970**. *J. Phys. C: Solid State Phys.* **3**, 2436.
- G. M. Andolina, F. M. D. Pellegrino, V. Giovannetti, A. H. MacDonald, M. Polini, *Cavity quantum electrodynamics of strongly correlated electron systems: A no-go theorem for photon condensation*. **2019**. *Phys. Rev. B* **100**, 121109.
- A. Anthore, Z. Iftikhar, E. Boulat, F. D. Parmentier, A. Cavanna, A. Ouerghi, U. Gennser, F. Pierre, *Circuit Quantum Simulation of a Tomonaga-Luttinger Liquid with an Impurity*. **2018**. *Phys. Rev. X* **8**, 031075.
- A. Anthore, D. M. Kennes, E. Boulat, S. Andergassen, F. Pierre, V. Meden, *Universality at work – the local sine-Gordon model, lattice fermions, and quantum circuits*. **2020**. *Eur. Phys. J. Spec. Top.* **229**, 663.
- S. Ashhab & F. Nori, *Qubit-oscillator systems in the ultrastrong-coupling regime and their potential for preparing nonclassical states*. **2010**. *Phys. Rev. A* **81**, 042311.
- C. Aslangul, N. Pottier & D. Saint-James, *Quantum ohmic dissipation: Particle on a one-dimensional periodic lattice*. **1985**. *Phys. Lett. A* **111**, 175.
- V. Barzykin & I. Affleck, *The Kondo Screening Cloud: What Can We Learn from Perturbation Theory?* **1996**. *Phys. Rev. Lett.* **76**, 4959.
- D. M. Basko & F. W. J. Hekking, *Disordered Josephson junction chains: Anderson localization of normal modes and impedance fluctuations*. **2013**. *Phys. Rev. B* **88**, 094507.
- D. M. Basko, F. Pfeiffer, P. Adamus, M. Holzmann, F. W. J. Hekking, *Superconductor-insulator transition in Josephson junction chains by quantum Monte Carlo calculations*. **2020**. *Phys. Rev. B* **101**, 024518.
- K. S. D. Beach, R. J. Gooding & F. Marsiglio, *Reliable Padé analytical continuation method based on a high-accuracy symbolic computation algorithm*. **2000**. *Phys. Rev. B* **61**, 5147.
- M. T. Bell, W. Zhang, L. B. Ioffe, M. E. Gershenson, *Spectroscopic Evidence of the Aharonov-Casher Effect in a Cooper Pair Box*. **2016**. *Phys. Rev. Lett.* **116**, 107002.
- A. Bezryadin, C. N. Lau & M. Tinkham, *Quantum suppression of superconductivity in ultrathin nanowires*. **2000**. *Nature* **404**, 971.
- G. Biroli & O. Parcollet, *Out-of-equilibrium dynamics of a quantum Heisenberg spin glass*. **2002**. *Phys. Rev. B* **65**, 094414.

- A. Blais, A. L. Grimsmo, S. M. Girvin, A. Wallraff, *Circuit Quantum Electrodynamics*. **2021**. *Rev. Mod. Phys.* **93**, 025005.
- A. Blandin & J. Friedel, *Propriétés magnétiques des alliages dilués. Interactions magnétiques et antiferromagnétisme dans les alliages du type métal noble-métal de transition*. **1959**. *J. Phys. Radium* **20**, 160.
- A. Boca, R. Miller, K. M. Birnbaum, A. D. Boozer, J. McKeever, H. J. Kimble, *Observation of the Vacuum Rabi Spectrum for One Trapped Atom*. **2004**. *Phys. Rev. Lett.* **93**, 233603.
- A. L. Boité, *Theoretical Methods for Ultrastrong Light–Matter Interactions*. **2020**. *Adv. Quantum Technol.* **3**, 1900140.
- L. Borda, L. Fritz, N. Andrei, G. Zaránd, *Theory of inelastic scattering from quantum impurities*. **2007**. *Phys. Rev. B* **75**, 235112.
- I. V. Borzenets, J. Shim, J. C. H. Chen, A. Ludwig, A. D. Wieck, S. Tarucha, H.-S. Sim, M. Yamamoto, *Observation of the Kondo screening cloud*. **2020**. *Nature* **579**, 210.
- V. Bouchiat, G. Chardin, M. Devoret, D. Esteve, *Measurement method of the antiproton gravitational mass using the single electron transistor*. **1997**. *Hyperfine Interact.* **109**, 345.
- V. Bouchiat, D. Vion, P. Joyez, D. Esteve, M. H. Devoret, *Quantum coherence with a single Cooper pair*. **1998**. *Phys. Scr.* **1998**, 165.
- D. Braak, *Integrability of the Rabi Model*. **2011**. *Phys. Rev. Lett.* **107**, 100401.
- R. M. Bradley & S. Doniach, *Quantum fluctuations in chains of Josephson junctions*. **1984**. *Phys. Rev. B* **30**, 1138.
- E. O. Brigham & R. E. Morrow, *The fast Fourier transform*. **1967**. *IEEE Spectr.* **4**, 63.
- P. Brooks, A. Kitaev & J. Preskill, *Protected gates for superconducting qubits*. **2013**. *Phys. Rev. A* **87**, 052306.
- M. Brune, E. Hagley, J. Dreyer, X. Maître, A. Maali, C. Wunderlich, J. M. Raimond, S. Haroche, *Observing the Progressive Decoherence of the “Meter” in a Quantum Measurement*. **1996a**. *Phys. Rev. Lett.* **77**, 4887.
- M. Brune, F. Schmidt-Kaler, A. Maali, J. Dreyer, E. Hagley, J. M. Raimond, S. Haroche, *Quantum Rabi Oscillation: A Direct Test of Field Quantization in a Cavity*. **1996b**. *Phys. Rev. Lett.* **76**, 1800.
- H. P. Büchler, V. B. Geshkenbein & G. Blatter, *Quantum Fluctuations in Thin Superconducting Wires of Finite Length*. **2004**. *Phys. Rev. Lett.* **92**, 067007.
- S. Bulgadaev, *Phase diagram of a dissipative quantum system*. **1984**. *ZhETF Pisma Redaktsiui*.
- R. Bulla, H.-J. Lee, N.-H. Tong, M. Vojta, *Numerical renormalization group for quantum impurities in a bosonic bath*. **2005**. *Phys. Rev. B* **71**, 045122.
- R. Bulla, N.-H. Tong & M. Vojta, *Numerical Renormalization Group for Bosonic Systems and Application to the Sub-Ohmic Spin-Boson Model*. **2003**. *Phys. Rev. Lett.* **91**, 170601.
- A. Burshtein, R. Kuzmin, V. E. Manucharyan, M. Goldstein, *Photon-instanton collider implemented by a superconducting circuit*. **2021**. *Phys. Rev. Lett.* **126**, 137701.
- S. Camalet, J. Schrieffer, P. Degiovanni, F. Delduc, *Quantum impurity approach to a coupled qubit problem*. **2004**. *EPL* **68**, 37.
- K. Cedergren, R. Ackroyd, S. Kafanov, N. Vogt, A. Shnirman, T. Duty, *Insulating Josephson Junction Chains as Pinned Luttinger Liquids*. **2017**. *Phys. Rev. Lett.* **119**, 167701.
- I. Chiorescu, Y. Nakamura, C. J. P. M. Harmans, J. E. Mooij, *Coherent Quantum Dynamics of a Superconducting Flux Qubit*. **2003**. *Science* **299**, 1869.

- C. Ciuti & P. Nataf, *Comment on “Superradiant Phase Transitions and the Standard Description of Circuit QED”*. **2012**. *Phys. Rev. Lett.* **109**, 179301.
- P. Coleman, *Local moment physics in heavy electron systems*. **2002**. *AIP Conf. Proc.* **629**, 79.
- J. da Providencia & C. Fiolhais, *Variational principles in quantum statistical mechanics*. **1987**. *Eur. J. Phys.* **8**, 12.
- S. De Liberato, *Light-Matter Decoupling in the Deep Strong Coupling Regime: The Breakdown of the Purcell Effect*. **2014**. *Phys. Rev. Lett.* **112**, 016401.
- M. H. Devoret, D. Esteve & C. Urbina, *Single-electron transfer in metallic nanostructures*. **1992**. *Nature* **360**, 547.
- B. S. DeWitt, *Transition from Discrete to Continuous Spectra*. **1956**. *Phys. Rev.* **103**, 1565.
- G. W. F. Drake & Z.-C. Van, *Variational eigenvalues for the S states of helium*. **1994**. *Chem. Phys. Lett.* **229**, 486.
- M. I. Dykman & E. I. Rashba, *The roots of polaron theory*. **2015**. *Phys. Today* **68**, 10.
- R. Fazio & H. van der Zant, *Quantum phase transitions and vortex dynamics in superconducting networks*. **2001**. *Phys. Rep.* **355**, 235.
- R. Feynman. **1965**, *The Development of the Space-Time View of Quantum Electrodynamics (Nobel lecture)*.
- R. P. Feynman & F. L. Vernon, *The theory of a general quantum system interacting with a linear dissipative system*. **1963**. *Ann. Phys.* **24**, 118.
- M. P. A. Fisher & W. Zwerger, *Quantum Brownian motion in a periodic potential*. **1985**. *Phys. Rev. B* **32**, 6190.
- S. Florens, A. Freyn, D. Venturelli, R. Narayanan, *Dissipative spin dynamics near a quantum critical point: Numerical renormalization group and Majorana diagrammatics*. **2011**. *Phys. Rev. B* **84**, 155110.
- P. Forn-Díaz, J. J. García-Ripoll, B. Peropadre, J.-L. Orgiazzi, M. A. Yurtalan, R. Belyansky, C. M. Wilson, A. Lupascu, *Ultrastrong coupling of a single artificial atom to an electromagnetic continuum in the nonperturbative regime*. **2017**. *Nat. Phys.* **13**, 39.
- P. Forn-Díaz, L. Lamata, E. Rico, J. Kono, E. Solano, *Ultrastrong coupling regimes of light-matter interaction*. **2019**. *Rev. Mod. Phys.* **91**, 025005.
- J. R. Friedman, V. Patel, W. Chen, S. K. Tolpygo, J. E. Lukens, *Quantum superposition of distinct macroscopic states*. **2000**. *Nature* **406**, 43.
- J. W. Gadzuk, *Localized vibrational modes in Fermi liquids. General theory*. **1981**. *Phys. Rev. B* **24**, 1651.
- J. J. García-Ripoll, B. Peropadre & S. De Liberato, *Light-matter decoupling and A 2 term detection in superconducting circuits*. **2015**. *Sci. Rep.* **5**, 16055.
- M. Gell-Mann & F. E. Low, *Quantum Electrodynamics at Small Distances*. **1954**. *Phys. Rev.* **95**, 1300.
- N. Gheeraert, S. Bera & S. Florens, *Spontaneous emission of Schrödinger cats in a waveguide at ultrastrong coupling*. **2017**. *New J. Phys.* **19**, 023036.
- N. Gheeraert, X. H. H. Zhang, T. Sépulcre, S. Bera, N. Roch, H. U. Baranger, S. Florens, *Particle Production in Ultra-Strong Coupling Waveguide QED*. **2018**. *Phys. Rev. A* **98**, 043816.
- T. Giamarchi, *Theory for 1D Quantum Materials Tested with Cold Atoms and Superconductors*. **2017**. *Physics* **10**, 115.

- H. M. Gibbs, *Spontaneous Decay of Coherently Excited Rb*. **1972**. *Phys. Rev. Lett.* **29**, 459.
- H. M. Gibbs, *Incoherent Resonance Fluorescence from a Rb Atomic Beam Excited by a Short Coherent Optical Pulse*. **1973**. *Phys. Rev. A* **8**, 446.
- M. Goldstein, M. H. Devoret, M. Houzet, L. I. Glazman, *Inelastic Microwave Photon Scattering off a Quantum Impurity in a Josephson-Junction Array*. **2013**. *Phys. Rev. Lett.* **110**, 017002.
- D. Golze, M. Dvorak & P. Rinke, *The GW Compendium: A Practical Guide to Theoretical Photoemission Spectroscopy*. **2019**. *Front. Chem.* **7**, 377.
- J. A. González & M. A. del Olmo, *Coherent states on the circle*. **1998**. *J. Phys. A: Math. Gen.* **31**, 8841.
- X. Gu, A. F. Kockum, A. Miranowicz, Y.-x. Liu, F. Nori, *Microwave photonics with superconducting quantum circuits*. **2017**. *Phys. Rep.* **718**=719, 1.
- J. E. Gubernatis, J. E. Hirsch & D. J. Scalapino, *Spin and charge correlations around an Anderson magnetic impurity*. **1987**. *Phys. Rev. B* **35**, 8478.
- F. Guinea, V. Hakim & A. Muramatsu, *Bosonization of a two-level system with dissipation*. **1985a**. *Phys. Rev. B* **32**, 4410.
- F. Guinea, V. Hakim & A. Muramatsu, *Diffusion and Localization of a Particle in a Periodic Potential Coupled to a Dissipative Environment*. **1985b**. *Phys. Rev. Lett.* **54**, 263.
- F. Guinea, G. G. Santos, M. Sasseti, M. Ueda, *Asymptotic Tunnelling Conductance in Luttinger Liquids*. **1995**. *EPL* **30**, 561.
- V. Gurarie & A. M. Tsvelik, *A Superconductor-Insulator Transition in a One-Dimensional Array of Josephson Junctions*. **2004**. *J. Low Temp. Phys.* **135**, 245.
- D. Gusenkova, M. Spiecker, R. Gebauer, M. Willsch, D. Willsch, F. Valenti, N. Karcher, L. Grünhaupt, I. Takmakov, P. Winkel, D. Rieger, A. V. Ustinov, N. Roch, W. Wernsdorfer, K. Michielsen, O. Sander, I. M. Pop, *Quantum Nondemolition Dispersive Readout of a Superconducting Artificial Atom Using Large Photon Numbers*. **2021**. *Phys. Rev. Applied* **15**, 064030.
- V. Hakim, A. Muramatsu & F. Guinea, *Two-state system coupled to phonons: A renormalization-group analysis of the transition*. **1984**. *Phys. Rev. B* **30**, 464.
- A. J. S. Hamilton, *Uncorrelated modes of the non-linear power spectrum*. **2000**. *Mon. Not. Roy. Astron. Soc.* **312**, 257.
- S. Haroche, *Nobel Lecture: Controlling photons in a box and exploring the quantum to classical boundary*. **2013**. *Rev. Mod. Phys.* **85**, 1083.
- C. R. Harris, K. J. Millman, S. J. van der Walt, R. Gommers, P. Virtanen, D. Cournapeau, E. Wieser, J. Taylor, S. Berg, N. J. Smith, R. Kern, M. Picus, S. Hoyer, M. H. van Kerkwijk, M. Brett, A. Haldane, J. F. del Río, M. Wiebe, P. Peterson, P. Gérard-Marchant, K. Sheppard, T. Reddy, W. Weckesser, H. Abbasi, C. Gohlke, T. E. Oliphant, *Array programming with NumPy*. **2020**. *Nature* **585**, 357.
- S. He, L. Duan & Q.-H. Chen, *Improved Silbey-Harris polaron ansatz for the spin-boson model*. **2018**. *Phys. Rev. B* **97**, 115157.
- N. Jakovčević Stor, I. Slapničar & J. L. Barlow, *Accurate eigenvalue decomposition of real symmetric arrowhead matrices and applications*. **2015**. *Linear Algebra Appl.* **464**, 62.
- E. Jaynes & F. Cummings, *Comparison of quantum and semiclassical radiation theories with application to the beam maser*. **1963**. *Proc. IEEE* **51**, 89.

- P. Jung, A. V. Ustinov & S. M. Anlage, *Progress in superconducting metamaterials*. **2014**. *Supercond. Sci. Technol.* **27**, 073001.
- A. Kamenev, *Many-body theory of non-equilibrium systems*. **2005**. arXiv:cond-mat/0412296.
- C. L. Kane & M. P. A. Fisher, *Transport in a one-channel Luttinger liquid*. **1992**. *Phys. Rev. Lett.* **68**, 1220.
- K. Kaur, T. Sépulcre, N. Roch, I. Snyman, S. Florens, S. Bera, *Spin-Boson Quantum Phase Transition in Multilevel Superconducting Qubits*. **2021**. *Phys. Rev. Lett.* **127**, 237702.
- J. Koch, V. Manucharyan, M. H. Devoret, L. I. Glazman, *Charging Effects in the Inductively Shunted Josephson Junction*. **2009**. *Phys. Rev. Lett.* **103**, 217004.
- J. Koch, T. M. Yu, J. Gambetta, A. A. Houck, D. I. Schuster, J. Majer, A. Blais, M. H. Devoret, S. M. Girvin, R. J. Schoelkopf, *Charge-insensitive qubit design derived from the Cooper pair box*. **2007**. *Phys. Rev. A* **76**, 042319.
- A. F. Kockum, A. Miranowicz, S. D. Liberato, S. Savasta, F. Nori, *Ultrastrong coupling between light and matter*. **2019**. *Nat. Rev. Phys.* **1**, 19.
- J. Kondo, *Resistance Minimum in Dilute Magnetic Alloys*. **1964**. *Prog. Theor. Phys.* **32**, 37.
- K. Kowalski, J. Rembielinski & L. C. Papaloucas, *Coherent states for a quantum particle on a circle*. **1996**. *J. Phys. A: Math. Gen.* **29**, 4149.
- Y. Krupko, V. D. Nguyen, T. Weißl, É. Dumur, J. Puertas, R. Dassonneville, C. Naud, F. W. J. Hekking, D. M. Basko, O. Buisson, N. Roch, W. Hasch-Guichard, *Kerr nonlinearity in a superconducting Josephson metamaterial*. **2018**. *Phys. Rev. B* **98**, 094516.
- R. Kuzmin, N. Grabon, N. Mehta, A. Burshtein, M. Goldstein, M. Houzet, L. I. Glazman, V. E. Manucharyan, *Inelastic Scattering of a Photon by a Quantum Phase Slip*. **2021**. *Phys. Rev. Lett.* **126**, 197701.
- R. Kuzmin, R. Mencia, N. Grabon, N. Mehta, Y.-H. Lin, V. E. Manucharyan, *Quantum electrodynamics of a superconductor–insulator phase transition*. **2019**. *Nat. Phys.* **15**, 930.
- W. E. Lamb & R. C. Retherford, *Fine Structure of the Hydrogen Atom by a Microwave Method*. **1947**. *Phys. Rev.* **72**, 241.
- W. E. Lamb, R. R. Schlicher & M. O. Scully, *Matter-field interaction in atomic physics and quantum optics*. **1987**. *Phys. Rev. A* **36**, 2763.
- K. Le Hur, *Kondo resonance of a microwave photon*. **2012**. *Phys. Rev. B* **85**, 140506.
- S. Léger. **2021**, *Electrodynamique Quantique d'une Jonction Josephson Couplée à Un Environnement Fortement Dissipatif*, Ph.D thesis, UGA.
- S. Leger, J. Puertas-Martinez, K. Bharadwaj, R. Dassonneville, J. Delaforce, F. Foroughi, V. Milchakov, L. Planat, O. Buisson, C. Naud, W. Hasch-Guichard, S. Florens, I. Snyman, N. Roch, *Observation of quantum many-body effects due to zero point fluctuations in superconducting circuits*. **2019**. *Nat. Commun.* **10**, 5259.
- A. J. Leggett. **1992**. in *Quantum Tunnelling in Condensed Media*, ed. Y. Kagan & A. J. Leggett.
- A. J. Leggett. **2019**. in *Fundamentals and Frontiers of the Josephson Effect*, ed. F. Tafuri, 63.
- A. J. Leggett, S. Chakravarty, A. T. Dorsey, M. P. A. Fisher, A. Garg, W. Zwerger, *Dynamics of the dissipative two-state system*. **1987**. *Rev. Mod. Phys.* **59**, 1.
- R. Lescanne, L. Verney, Q. Ficheux, M. H. Devoret, B. Huard, M. Mirrahimi, Z. Leghtas, *Escape of a Driven Quantum Josephson Circuit into Unconfined States*. **2019**. *Phys. Rev. Applied* **11**, 014030.

- J. M. Luttinger, *Fermi Surface and Some Simple Equilibrium Properties of a System of Interacting Fermions*. **1960**. *Phys. Rev.* **119**, 1153.
- L. Magazzù, P. Forn-Díaz, R. Belyansky, J.-L. Orgiazzi, M. A. Yurtalan, M. R. Otto, A. Lupascu, C. M. Wilson, M. Grifoni, *Probing the strongly driven spin-boson model in a superconducting quantum circuit*. **2018**. *Nat. Commun.* **9**, 1403.
- M. Malekakhlagh, A. Petrescu & H. E. Türeci, *Cutoff-Free Circuit Quantum Electrodynamics*. **2017**. *Phys. Rev. Lett.* **119**, 073601.
- V. E. Manucharyan, J. Koch, L. Glazman, M. Devoret, *Fluxonium: Single Cooper pair circuit free of charge offsets*. **2009**. *Science* **326**, 113.
- R. A. Marcus, *On the Theory of Oxidation-Reduction Reactions Involving Electron Transfer. I*. **1956**. *J. Chem. Phys.* **24**, 966.
- J. M. Martinis, K. B. Cooper, R. McDermott, M. Steffen, M. Ansmann, K. D. Osborn, K. Cicak, S. Oh, D. P. Pappas, R. W. Simmonds, C. C. Yu, *Decoherence in Josephson Qubits from Dielectric Loss*. **2005**. *Phys. Rev. Lett.* **95**, 210503.
- J. M. Martinis & K. Osborne, *Superconducting Qubits and the Physics of Josephson Junctions*. **2004**. arXiv:cond-mat/0402415.
- R. D. Mattuck, L. Hansen & C. Y. Cheung, *Removing the divergence at the Kondo temperature by means of self-consistent perturbation theory*. **1971**. *J. Phys. Colloques* **32**, 1.
- C. R. H. McRae, R. E. Lake, J. L. Long, M. Bal, X. Wu, B. Jugdersuren, T. H. Metcalf, X. Liu, D. P. Pappas, *Dielectric loss extraction for superconducting microwave resonators*. **2020**. *Appl. Phys. Lett.* **116**, 194003.
- D. M. Meekhof, C. Monroe, B. E. King, W. M. Itano, D. J. Wineland, *Generation of Nonclassical Motional States of a Trapped Atom*. **1996**. *Phys. Rev. Lett.* **76**, 1796.
- H. Meier, R. T. Brierley, A. Kou, S. M. Girvin, L. I. Glazman, *Signatures of quantum phase transitions in the dynamic response of fluxonium qubit chains*. **2015**. *Phys. Rev. B* **92**, 064516.
- M. Mirhosseini, E. Kim, V. S. Ferreira, M. Kalaei, A. Sipahigil, A. J. Keller, O. Painter, *Superconducting metamaterials for waveguide quantum electrodynamics*. **2018**. *Nat. Commun.* **9**, 3706.
- A. Mizel & Y. Yanay, *Right-sizing fluxonium against charge noise*. **2020**. *Phys. Rev. B* **102**, 014512.
- J. E. Mooij & Y. V. Nazarov, *Superconducting nanowires as quantum phase-slip junctions*. **2006**. *Nat. Phys.* **2**, 169.
- A. Murani, N. Bourlet, H. le Sueur, F. Portier, C. Altimiras, D. Esteve, H. Grabert, J. Stockburger, J. Ankerhold, P. Joyez, *Absence of a Dissipative Quantum Phase Transition in Josephson Junctions*. **2020**. *Phys. Rev. X* **10**, 021003.
- Y. Nakamura, Y. A. Pashkin, T. Yamamoto, J. S. Tsai, *Charge Echo in a Cooper-Pair Box*. **2002**. *Phys. Rev. Lett.* **88**, 047901.
- P. Nataf & C. Ciuti, *Vacuum Degeneracy of a Circuit QED System in the Ultrastrong Coupling Regime*. **2010**. *Phys. Rev. Lett.* **104**, 023601.
- T. Niemczyk, F. Deppe, H. Huebl, E. P. Menzel, F. Hocke, M. J. Schwarz, J. J. Garcia-Ripoll, D. Zueco, T. Hümmer, E. Solano, A. Marx, R. Gross, *Circuit quantum electrodynamics in the ultrastrong-coupling regime*. **2010**. *Nature Phys.* **6**, 772.
- S. E. Nigg, H. Paik, B. Vlastakis, G. Kirchmair, S. Shankar, L. Frunzio, M. H. Devoret, R. J. Schoelkopf, S. M. Girvin, *Black-Box Superconducting Circuit Quantization*. **2012**. *Phys. Rev. Lett.* **108**, 240502.

- Ž. Osolin & R. Žitko, *Pad\`e approximant approach for obtaining finite-temperature spectral functions of quantum impurity models using the numerical renormalization group technique.* **2013.** *Phys. Rev. B* **87**, 245135.
- I. V. Pechenezhskiy, R. A. Mencia, L. B. Nguyen, Y.-H. Lin, V. E. Manucharyan, *The superconducting quasischarge qubit.* **2020.** *Nature* **585**, 368.
- B. Peropadre, D. Zueco, D. Porras, J. J. García-Ripoll, *Nonequilibrium and Nonperturbative Dynamics of Ultrastrong Coupling in Open Lines.* **2013.** *Phys. Rev. Lett.* **111**, 243602.
- N. R. Poniatowski, *Superconductivity, Broken Gauge Symmetry, and the Higgs Mechanism.* **2019.** *Am. J. Phys.* **87**, 436.
- I. M. Pop, I. Protopopov, F. Lecocq, Z. Peng, B. Pannetier, O. Buisson, W. Guichard, *Measurement of the effect of quantum phase slips in a Josephson junction chain.* **2010.** *Nat. Phys.* **6**, 589.
- J. Puertas Martínez, S. Léger, N. Gheeraert, R. Dassonneville, L. Planat, F. Foroughi, Y. Krupko, O. Buisson, C. Naud, W. Hasch-Guichard, S. Florens, I. Snyman, N. Roch, *A tunable Josephson platform to explore many-body quantum optics in circuit-QED.* **2019.** *npj Q. Info.* **5**, 1.
- E. M. Purcell, H. C. Torrey & R. V. Pound, *Resonance Absorption by Nuclear Magnetic Moments in a Solid.* **1946.** *Phys. Rev.* **69**, 37.
- J. Rammer & H. Smith, *Quantum field-theoretical methods in transport theory of metals.* **1986.** *Rev. Mod. Phys.* **58**, 323.
- R.-P. Riwar, *Charge quantization and detector resolution.* **2021.** *SciPost Phys.* **10**, 093.
- B. Roulet, J. Gavoret & P. Nozières, *Singularities in the X-Ray Absorption and Emission of Metals. I. First-Order Parquet Calculation.* **1969.** *Phys. Rev.* **178**, 1072.
- A. Roy, D. Schuricht, J. Hauschild, F. Pollmann, H. Saleur, *The quantum sine-Gordon model with quantum circuits.* **2021.** *Nucl. Phys. B* **968**, 115445.
- A. Schmid, *Diffusion and Localization in a Dissipative Quantum System.* **1983.** *Phys. Rev. Lett.* **51**, 1506.
- G. Schön & A. Zaikin, *Quantum coherent effects, phase transitions, and the dissipative dynamics of ultra small tunnel junctions.* **1990.** *Phys. Rep.* **198**, 237.
- J. R. Schrieffer & P. A. Wolff, *Relation between the Anderson and Kondo Hamiltonians.* **1966.** *Phys. Rev.* **149**, 491.
- E. Schrödinger, *Are there quantum jumps?: Part ii*.* **1952.** *Br. J. Philos. Sci.* **3**, 233.
- T. Shi & C. P. Sun, *Lehmann-Symanzik-Zimmermann reduction approach to multiphoton scattering in coupled-resonator arrays.* **2009.** *Phys. Rev. B* **79**, 205111.
- R. Silbey & R. A. Harris, *Variational calculation of the dynamics of a two level system interacting with a bath.* **1984.** *J. Chem. Phys.* **80**, 2615.
- I. Snyman & S. Florens, *Robust Josephson-Kondo screening cloud in circuit quantum electrodynamics.* **2015.** *Phys. Rev. B* **92**, 085131.
- O. D. Stefano, R. Stassi, L. Garziano, A. F. Kockum, S. Savasta, F. Nori, *Feynman-diagrams approach to the quantum Rabi model for ultrastrong cavity QED: Stimulated emission and reabsorption of virtual particles dressing a physical excitation.* **2017.** *New J. Phys.* **19**, 053010.
- A. E. Svetogorov & D. M. Basko, *Effect of disorder on coherent quantum phase slips in Josephson junction chains.* **2018.** *Phys. Rev. B* **98**, 054513.

- G. Toulouse, *Expression exacte de l'énergie de l'état de base de l'hamiltonien de Hondo pour une valeur particulière de J* . **1969**. *C. R. Acad. Sci. Paris* **268**, 1200.
- J. Ulrich & F. Hassler, *Dual approach to circuit quantization using loop charges*. **2016**. *Phys. Rev. B* **94**, 094505.
- C. H. van der Wal, A. C. J. ter Haar, F. K. Wilhelm, R. N. Schouten, C. J. P. M. Harmans, T. P. Orlando, S. Lloyd, J. E. Mooij, *Quantum Superposition of Macroscopic Persistent-Current States*. **2000**. *Science* **290**, 773.
- M. Vanević & Y. V. Nazarov, *Quantum Phase Slips in Superconducting Wires with Weak Inhomogeneities*. **2012**. *Phys. Rev. Lett.* **108**, 187002.
- O. Viehmann, J. von Delft & F. Marquardt, *Superradiant Phase Transitions and the Standard Description of Circuit QED*. **2011**. *Phys. Rev. Lett.* **107**, 113602.
- J. J. Viennot, X. Ma & K. W. Lehnert, *Phonon-Number-Sensitive Electromechanics*. **2018**. *Phys. Rev. Lett.* **121**, 183601.
- D. Vion, A. Aassime, A. Cottet, P. Joyez, H. Pothier, C. Urbina, D. Esteve, M. H. Devoret, *Manipulating the Quantum State of an Electrical Circuit*. **2002**. *Science* **296**, 886.
- N. Vogt, R. Schäfer, H. Rotzinger, W. Cui, A. Fiebig, A. Shnirman, A. V. Ustinov, *One-dimensional Josephson junction arrays: Lifting the Coulomb blockade by depinning*. **2015**. *Phys. Rev. B* **92**, 045435.
- M. Vojta, *Impurity quantum phase transitions*. **2006**. *Phil. Mag.* **86**, 1807.
- J. von Delft & H. Schoeller, *Bosonization for beginners — refermionization for experts*. **1998**. *Ann. Phys. (Berlin)* **7**, 225.
- U. Vool & M. Devoret, *Introduction to quantum electromagnetic circuits*. **2017**. *Int. J. Circuit Theory Appl.* **45**, 897.
- S. Weinberg, *Superconductivity for Particular Theorists*. **1986**. *Prog. Theor. Phys. Supp.* **86**, 43.
- P. Werner. **2005**, *Dissipative Quantum Phase Transitions*, Ph.D thesis, ETH Zurich.
- K. Wilson & J. Kogut, *The renormalization group and the ϵ expansion*. **1974**. *Phys. Rep.* **12**, 75.
- K. G. Wilson, *The renormalization group: Critical phenomena and the Kondo problem*. **1975**. *Rev. Mod. Phys.* **47**, 773.
- B. Yurke & J. S. Denker, *Quantum network theory*. **1984**. *Phys. Rev. A* **29**, 1419.
- G. Zaránd, L. Borda, J. von Delft, N. Andrei, *Theory of Inelastic Scattering from Magnetic Impurities*. **2004**. *Phys. Rev. Lett.* **93**, 107204.
- G. Zhu, D. G. Ferguson, V. E. Manucharyan, J. Koch, *Circuit QED with fluxonium qubits: Theory of the dispersive regime*. **2013**. *Phys. Rev. B* **87**, 024510.
- W. Zwerger, A. T. Dorsey & M. P. A. Fisher, *Effects of the phase periodicity on the quantum dynamics of a resistively shunted Josephson junction*. **1986**. *Phys. Rev. B* **34**, 6518.